



Leibniz-Institut für
Astrophysik Potsdam

Forschungsabteilung “The Milky Way and the Local Volume”

Models of the Galaxy and the massive spectroscopic stellar survey RAVE

**Dissertation
zur Erlangung des akademischen Grades
“doctor rerum naturalium”
(Dr. rer. nat.)
in der Wissenschaftsdisziplin “Astrophysik”**

**eingereicht an der
Mathematisch-Naturwissenschaftlichen Fakultät
der Universität Potsdam**

**von
Tilman Piffl**

Potsdam, 25.10.2013

This work is licensed under a Creative Commons License:
Attribution - Noncommercial - Share Alike 3.0 Germany
To view a copy of this license visit
<http://creativecommons.org/licenses/by-nc-sa/3.0/de/>

Betreuer: Prof. Matthias Steinmetz (Leibniz-Institut für Astrophysik Potsdam (AIP))

Published online at the
Institutional Repository of the University of Potsdam:
URL <http://opus.kobv.de/ubp/volltexte/2014/7037/>
URN [urn:nbn:de:kobv:517-opus-70371](http://nbn-resolving.org/urn:nbn:de:kobv:517-opus-70371)
<http://nbn-resolving.org/urn:nbn:de:kobv:517-opus-70371>

Abstract

Numerical simulations of galaxy formation and observational Galactic Astronomy are two fields of research that study the same objects from different perspectives. Simulations try to understand galaxies like our Milky Way from an evolutionary point of view while observers try to disentangle the current structure and the building blocks of our Galaxy. Due to great advances in computational power as well as in massive stellar surveys we are now able to compare resolved stellar populations in simulations and in observations. In this thesis we use a number of approaches to relate the results of the two fields to each other. The major observational data set we refer to for this work comes from the Radial Velocity Experiment (RAVE), a massive spectroscopic stellar survey that observed almost half a million stars in the Galaxy.

In a first study we use three different models of the Galaxy to generate synthetic stellar surveys that can be directly compared to the RAVE data. To do this we evaluate the RAVE selection function to great detail. Among the Galaxy models is the widely used Besançon model that performs well when individual parameter distribution are considered, but fails when we study chemodynamic correlations. The other two models are based on distributions of mass particles instead of analytical distribution functions. This is the first time that such models are converted to the space of observables and are compared to a stellar survey. We show that these models can be competitive and in some aspects superior to analytic models, because of their self-consistent dynamic history. In the case of a full cosmological simulation of disk galaxy formation we can recover features in the synthetic survey that relate to the known issues of the model and hence proof that our technique is sensitive to the global structure of the model. We argue that the next generation of cosmological galaxy formation simulations will deliver valuable models for our Galaxy. Testing these models with our approach will provide a direct connection between stellar Galactic astronomy and physical cosmology.

In the second part of the thesis we use a sample of high-velocity halo stars from the RAVE data to estimate the Galactic escape speed and the virial mass of the Milky Way. In the course of this study cosmological simulations of galaxy formation also play a crucial role. Here we use them to calibrate and extensively test our analysis technique. We find the local Galactic escape speed to be 533_{-41}^{+54} km s⁻¹ (90% confidence). With this result in combination with a simple mass model of the Galaxy we then construct an estimate of the virial mass of the Galaxy. For the mass profile of the dark matter halo we use two extreme models, a pure Navarro, Frenk & White (NFW) profile and an adiabatically contracted NFW profile. When we use statistics on the concentration parameter of these profile taken from large dissipationless cosmological simulations we obtain an estimate of the virial mass that is almost independent of the choice of the halo profile. For the mass M_{340} enclosed within $R_{340} = 180$ kpc we find $1.3_{-0.3}^{+0.4} \times 10^{12}$ M_⊙. This value is in very good agreement with a number of other mass estimates in the literature that are based on independent data sets and analysis techniques.

In the last part of this thesis we investigate a new possible channel to generate a population of Hypervelocity stars (HVSs) that is observed in the stellar halo. Commonly, it is assumed

that the velocities of these stars originate from an interaction with the super-massive black hole in the Galactic center. It was suggested recently that stars stripped-off a disrupted satellite galaxy could reach similar velocities and leave the Galaxy. Here we study in detail the kinematics of tidal debris stars to investigate the probability that the observed sample of HVSs could partly originate from such a galaxy collision. We use a suite of N -body simulations following the encounter of a satellite galaxy with its Milky Way-type host galaxy. We quantify the typical pattern in angular and phase space formed by the debris stars and develop a simple model that predicts the kinematics of stripped-off stars. We show that the distribution of orbital energies in the tidal debris has a typical form that can be described quite accurately by a simple function. The main parameters determining the maximum energy kick a tidal debris star can get is the initial mass of the satellite and only to a lower extent its orbit. Main contributors to an unbound stellar population created in this way are massive satellites ($M_{\text{sat}} > 10^9 M_{\odot}$). The probability that the observed HVS population is significantly contaminated by tidal debris stars appears small in the light of our results.

Deutsche Zusammenfassung

Ein häufig verfolgter Ansatz Galaxien wie unsere Milchstraße besser zu verstehen, sind numerische Simulationen, d.h. das Nachvollziehen ihrer Entstehung und Entwicklung mit Hilfe von Computern. Dieses Vorgehen erlaubt das Betrachten solcher Objekte von einem evolutionären Standpunkt aus. Eine andere Herangehensweise verfolgt die Galaktische Astronomie, welche über Sternbeobachtungen den aktuellen Zustand der Milchstraße untersucht. Hier wird versucht, die konstitutiven Bestandteile unserer Galaxie zu erkennen, um dadurch ein besseres Verständnis ihrer Struktur zu erlangen. Die enorme Rechenleistung moderner Supercomputer und die Entwicklungssprünge im Bereich der digitalen Himmelsdurchmusterungen haben dazu geführt, dass inzwischen mit beiden Ansätzen vergleichbare Populationen von einzeln beobachtbaren Sternen studiert werden können.

In der vorliegenden Arbeit werden verschiedene Möglichkeiten untersucht, die Ergebnisse dieser beiden astrophysikalischen Disziplinen, welche bislang weitgehend getrennt von einander betrieben wurden, sinnvoll zu kombinieren. Der überwiegende Teil der Beobachtungsdaten, die dabei verwendet werden, wurde im Zuge des Radial Velocity Experiments (RAVE) gesammelt, einer spektroskopischen Durchmusterung der Sterne fast des gesamten Südhimmels. Um die Daten des RAVE-Projekts statistisch auswerten zu können, musste zuerst die detaillierte Auswahlfunktion der Durchmusterung rekonstruiert werden, d.h. die Wahrscheinlichkeit, dass ein Stern von RAVE beobachtet wurde, musste, in Abhängigkeit von den Eigenschaften des Sterns, bestimmt werden. Der Hauptteil der Dissertation gliedert sich in drei weitgehend unabhängige Studien.

Im ersten Teil wird die oben erwähnte Auswahlfunktion benutzt, um voraus zu sagen, was das RAVE Projekt beobachtet hätte, falls bestimmte theoretische Modelle unserer Milchstraße zu träfen. Auf diese Art und Weise umgehe ich das problematische Unterfangen, die Beobachtungsdaten zu einem physikalischen Modell zu verallgemeinern. Die Problematik hierbei liegt darin, dass astronomische Beobachtungen nicht direkt physikalisch relevante Größen, wie Massen oder Alter der Sterne, liefern, sondern scheinbare Helligkeiten oder Winkelpositionen. In dieser Studie wird der umgekehrte Weg beschritten und synthetische Beobachtungen aus den Modellen generiert. Untersucht wurden dabei sowohl klassische analytische Modelle als auch Modelle, die aus numerischen Simulationen resultieren. Letztere wurden zu ersten Mal überhaupt auf diese Art und Weise getestet und es zeigt sich, dass solche Modelle den klassischen in bestimmten Aspekten, die mit der Entwicklungsgeschichte der Milchstraße verknüpft sind, überlegen sind.

Im zweiten Teil der Arbeit werden die RAVE-Daten benutzt um die Masse der Milchstraße, bzw. die Masse der in ihr enthaltenen dunklen Materie, abzuschätzen. Zur Eichung der Analysemethode wird dabei wieder auf Ergebnisse von Simulationen zurück gegriffen, die die Entwicklung von ähnlichen Galaxien wie der Milchstraße verfolgt haben. Zuerst wird die lokale Entweichgeschwindigkeit, d.h. die Mindestgeschwindigkeit, die ein Körper benötigt, um unsere Galaxie zu verlassen, bestimmt. Die beste Abschätzung beträgt 533_{-41}^{+54} km s⁻¹. Anhand dieser Schätzung kann, in Kombination mit vereinfachten analytischen Modellen der Materieverteilung in unserer Galaxie, die Masse der Milchstraße auf $1,3_{-0,3}^{+0,4} \times 10^{12} M_{\odot}$ be-

stimmt werden. Dieses Ergebnis bestätigt frühere unabhängige Massenschätzungen, die auf anderen Beobachtungsdaten und anderen Analysestrategien basieren.

Im letzten Teil der Arbeit wird eine spezielle Population von Sternen im Außenbereich unserer Galaxie untersucht, sogenannte Hyperschnellläufersterne (HSS). Diese wurde in einer weiteren Himmelsdurchmusterung, dem Sloan Digital Sky Survey (SDSS), gefunden. Die Besonderheit dieser Sterne besteht in ihren extrem hohen Geschwindigkeiten oberhalb der Entweichgeschwindigkeit. Allgemein wird angenommen, dass die Sterne ihre Geschwindigkeiten im Zuge der Spaltung eines Doppelsternsystems durch Gezeitenkräfte nahe des supermassereichen Schwarzen Lochs im Zentrum der Milchstraße erreichen. Vor Kurzem wurde jedoch ein alternatives Szenario vorgeschlagen. Nach diesem können solche Sterne auch während des Einfalls einer Satellitengalaxie auf die Milchstraße entstehen. Diese Hypothese wird anhand von numerischen Simulationen, die diese Situation nachbilden, getestet. Es zeigt sich, dass HSS auf diese Weise entstehen können, aber dass die beobachtete Population höchstwahrscheinlich einen anderen Ursprung hat.

Contents

| | | |
|----------|---|-----------|
| 1 | Introduction | 9 |
| 2 | Scientific background | 15 |
| 2.1 | The RAVE survey and its selection function | 15 |
| 2.1.1 | Overall completeness compared to 2MASS | 18 |
| 2.1.2 | Spatially resolved completeness | 19 |
| 2.2 | Theoretical models of galaxy evolution | 20 |
| 2.3 | The stellar synthesis code GALAXIA | 23 |
| 2.3.1 | Stellar population synthesis from analytic distribution functions | 24 |
| 2.3.2 | Stellar population synthesis from an N-body model | 25 |
| 2.3.3 | Modifications to GALAXIA | 26 |
| 2.3.4 | Computation of the smoothing parameters | 27 |
| 3 | Mock RAVE surveys from models of the Galaxy | 29 |
| 3.1 | Creating a synthetic RAVE survey | 30 |
| 3.1.1 | Application of the selection function | 31 |
| 3.1.2 | Introduction of observational errors | 32 |
| 3.1.3 | Stellar parameter dependent selections | 35 |
| 3.2 | The GALAXIA/Besançon model | 36 |
| 3.2.1 | General description of the model | 37 |
| 3.2.2 | Comparison to RAVE | 38 |
| 3.2.3 | Correlating dynamics and chemistry | 42 |
| 3.3 | The chemodynamic MCM model | 44 |
| 3.3.1 | General description of the model | 45 |
| 3.3.2 | The effect of different processing options | 47 |
| 3.3.3 | The effect of the RAVE selection function | 51 |
| 3.3.4 | Comparison to 2MASS | 52 |
| 3.3.5 | Comparison to RAVE | 53 |
| 3.3.6 | Modeling the giant sample of Boeche et al. (2013) | 57 |
| 3.4 | A full cosmological simulation | 63 |
| 3.4.1 | General description of the model | 63 |
| 3.4.2 | Comparison to RAVE | 65 |
| 3.4.3 | Effects of the selection function | 67 |
| 3.5 | Excursion: designing a selection function for 4MOST | 69 |
| 3.6 | Discussion | 73 |
| 4 | The Galactic escape speed and the mass of the Galaxy | 74 |
| 4.1 | Methodology | 75 |
| 4.1.1 | Non-local modeling | 76 |
| 4.1.2 | General behavior of the method | 77 |

| | | |
|----------|---|------------|
| 4.2 | Constraints for k from cosmological simulations | 77 |
| 4.2.1 | The velocity threshold | 79 |
| 4.3 | Data | 83 |
| 4.3.1 | Sample selection in RAVE | 83 |
| 4.3.2 | Including other literature data | 85 |
| 4.4 | Results | 88 |
| 4.4.1 | Comparison to Smith et al. (2007) | 88 |
| 4.4.2 | The local escape speed | 89 |
| 4.4.3 | Binning in Galactocentric distance | 90 |
| 4.5 | Discussion | 91 |
| 4.5.1 | Influence of the input parameters | 91 |
| 4.5.2 | A critical view on the input assumptions | 91 |
| 4.5.3 | Estimating the mass of the Milky Way | 93 |
| 4.5.4 | Fitting the halo concentration parameter | 94 |
| 4.5.5 | Relation to other mass estimates | 96 |
| 4.5.6 | On the dark matter halo profile | 97 |
| 4.5.7 | Future prospects | 97 |
| 5 | An alternative origin for hyper-velocity stars | 99 |
| 5.1 | Simulation set-up | 100 |
| 5.2 | Observable properties from the simulations | 103 |
| 5.2.1 | Angular distribution | 104 |
| 5.2.2 | The radial velocity-distance plane | 105 |
| 5.2.3 | Maximum velocities | 106 |
| 5.3 | A model for tidal stripping | 106 |
| 5.4 | The energy distribution | 111 |
| 5.5 | Discussion | 113 |
| 5.5.1 | The bound HVS population and the outer stellar halo | 115 |
| 5.5.2 | An intragalactic stellar population | 115 |
| 6 | Summary and conclusions | 117 |
| 6.1 | Synthetic stellar surveys | 117 |
| 6.2 | The Galactic escape speed and the mass of the Milky Way | 120 |
| 6.3 | Hypervelocity stars in galactic tidal tails | 121 |
| 6.4 | Closing remarks | 122 |
| | Bibliography | 124 |

1 Introduction

With the new Millennium industrialization has finally reached Astronomy. Not in the sense of a scientific proletariat doing shift work in astronomical facilities under precarious conditions, but in the sense of mass production and automation. Endeavors like the 2dF Galaxy Redshift Survey and the Hipparcos astrometric satellite set the scene in the late 1990s for massive data taking projects with the Sloan Digital Sky Survey (SDSS) being their currently most prominent and successful representative. Advanced CCD detectors allow efficient and precise photometry and astrometry over large areas of the sky. Multi-object and integral field spectroscopy enable the simultaneous measurement of hundreds or even thousands of spectra in a single exposure. Globalization and greatly reduced travel costs allow the operation of telescopes at sites with optimal observing conditions. All this combined has made the massive acquisition of data a relatively cheap and predictable affair. Efficient access to this inconceivable amount of data that is growing ever more quickly appears not to pose a serious problem because computational power and storage capabilities are growing even faster (Schlegel 2012).

There are new challenges arising in this era of large projects that lie on different grounds. Two major aspects of such grand endeavors have to be considered as many problems arise because of their simultaneous occurrence: (1) the raw data output of these projects has to be processed via fully automated analysis pipelines (AAP) because of the sheer number of data and (2) the observations are always of interest for a large number of scientists and it is thus logical to make the data available to the astronomical community. The latter is often a requirement by the funding agencies. The development of an AAP is a difficult task and it is clearly not practical that every user develops her or his own program. On the other hand, even for a perfect AAP the analysis products will be in most cases non-trivial to use, because there might be degeneracies, a decreased sensitivity of spectral features in some regions in the parameter space or the inability to measure certain types of objects. This problem is not new, nor is the situation that the analysis of a data set and the interpretation of the results is not done by the same person. New, however, is the frequent lack of personal interaction between the performers of these tasks and the accompanying alienation of the scientific worker from the data product. The result is a necessity to explicitly evaluate and comprehensively document the capabilities and limits of the data products. To do this effectively for a large data set is a yet ongoing struggle.

Uncertainty distributions or – in the Bayesian nomenclature – posterior probability distributions $p(\Omega)$ of a parameter Ω are in many cases non-Gaussian, significantly skewed or even multi-peaked. Sometimes there are degeneracies between different parameters Ω_i . This is not a fundamental problem for an individual measurement as there are straightforward ways to incorporate $p(\Omega)$ in a subsequent analysis (e.g. as a prior in a maximum likelihood analysis), but problems arise for big data sets. Here the efficient storage and communication of $p(\Omega)$ to and use by the general community becomes an issue, because the detailed keeping of $p(\Omega)$ might result in data expansion instead of data reduction (Hogg & Lang 2011).

Another aspect of importance is the question, which targets are (successfully) observed by

and enter the data base of a survey. Despite the overwhelming observing capabilities of modern telescopes we are far from being able to observe all objects of interest, be they galaxies, stars in the Milky Way or something else. At best all objects brighter than a given apparent magnitude are measured, but in the case of spectroscopic surveys often only a sub-set of all possible targets can be observed. To preserve the statistical value of such an experiment the criteria, why a target was observed, have to be well defined and recorded. They form the selection function S of a survey. The detailed knowledge of S will most likely be of increasing priority when more sophisticated observing strategies are applied for future spectroscopic surveys, like 4MOST (de Jong et al. 2012), WEAVE (Dalton et al. 2012) or DESI (formerly BigBOSS) (Schlegel et al. 2011), that can build upon the wealth of already available information about their potential targets (see also Rix & Bovy 2013).

Apart from the targeting algorithm there is a more subtle issue affecting S . After the observations the data have to be analyzed and the parameters of interest have to be extracted. That might not be possible for all observations, either because of the low quality of the measurement or, more problematic, because the analysis method is not suited for a specific type of object. Reasons for the latter can be, inter alia, that a star is too cool or too hot to allow a sensible analysis. Or its spectrum exhibits features that are not included in available stellar models. This leads directly back to the AAPs that through this back door leave their signature in S .

Stellar surveys and their analysis In Galactic Astronomy the massive spectroscopic stellar surveys RAVE and SEGUE observed hundreds of thousands of stars and thereby increased the number of available stellar spectra by more than a magnitude within one decade. Together with the Geneva-Copenhagen survey they also for the first time provided *homogeneous* data sets. In the photometric domain we find a large variety of surveys, the currently most widely used of which are 2MASS and the SDSS. With APOGEE and the Gaia-ESO survey – that will both soon publish their first data releases – this development has reached the high-resolution domain. The astrometric space mission Gaia and the Large Synoptic Survey Telescope (LSST) will probably present the next climax of this process by surveying one billion stars in the Galaxy (see Ivezić et al. (2012) for a recent review on present and future stellar surveys).

With the rapidly growing amount of stellar data collected by these projects the full complexity of our Galaxy becomes visible (e.g. Belokurov et al. 2006; Williams et al. 2011; Antoja et al. 2012; Bovy et al. 2012b; Widrow et al. 2012). Already in the data available to date significant non-equilibrium features are detectable, most notably the moving groups in the Hipparcos data (Dehnen 1998) and the velocity gradients found in the RAVE data (Siebert et al. 2012; Williams et al. 2013). In the Gaia era precise geometric parallaxes will most likely prohibit neglecting the presence of spiral arms in the Galactic disk or the clumpy structure of the stellar halo. This complexity will make it extremely difficult to extract the underlying physical properties and distribution functions directly. Considering the additional complications introduced by the survey selection functions it might be completely futile except for very specific cases.

An alternative venue is presented by inverse modeling. Instead of correcting the data for observational biases to facilitate a comparison to physical models, we can apply the selection function to the physical models, in order to predict what would have been observed if the model was true. The uncertainty distributions $p(\Omega)$ of the data can then be used to compute the likelihood of the data given the model in a Bayesian analysis. One problematic aspect of this technique is that there is not a standard way to evaluate the quality of a model

except in relation to other models. Alternatively, the model prediction can be equipped with observational errors according to $p(\Omega)$ and compared directly to the data. A positive side-effect of this inverse modeling approach is that the selection function and the uncertainties in the data can be handled independently to a large degree and correlated errors can be implemented in a straightforward manner.

There is an important obstacle that has to be overcome for a direct comparison of models and data. Physical models usually describe a system in terms of distributions of fundamental physical quantities like mass density, age and 6D phase space coordinates. Astronomical observations yield information about completely different quantities like apparent brightness, spectral energy distributions, proper motions, line-of-sight velocities or stellar parameters. A detour over the fields of stellar evolution and stellar atmospheres is hence unavoidable to transform one set of quantities into the other. Attempts to solve this classical problem of stellar population synthesis were made by, e.g., Bruzual & Charlot (2003) for unresolved stellar populations in distant galaxies or Robin et al. (2003) and Girardi et al. (2005) for models of our Galaxy based on analytic distribution functions. Sharma et al. (2011) and Pasetto et al. (2012a) provided a code framework that also allows for the conversion of mass distributions that are represented by a finite number of tracer particles, i.e. an N -body distribution, to the space of observables.

Cosmological simulations An interesting type of Galaxy model that has become available only recently is a numerical simulation of disk galaxy formation at a resolution that allows for the analysis of the distribution functions of stellar populations. In principle, a comparison to such a model allows one to test the implemented fundamental physics directly with local observations and thereby tackle the major question whether the Galaxy is consistent with the Λ CDM cosmology.

With the advent of computers a new branch emerged in the astronomical community: numerical simulations. After initial successes in the explanation of the morphology of interacting galaxies (Toomre & Toomre 1972) large parts of the new field focused on the implications of the newly formed dark matter paradigm and thereby left behind the observable domain. Only in the last decade more efforts have been put into simulations that also follow the evolution of the baryonic component as for example the works of Navarro & Steinmetz (1997, 2000) who showed that the inclusion of pure hydrodynamics does not lead to the formation of realistic galaxy disks and that further physical process must play a role. It turned out that galaxies like our own are the result of a non-linear interplay of star formation and energy feedback in form of supernovae, stellar winds and super-massive black holes (e.g. Governato et al. 2004; Piontek & Steinmetz 2011; Springel 2012). These processes act on small scales, but nevertheless have a profound impact on the global structure of massive galaxies, in part because of the hierarchical nature of their formation process. This is problematic, because all of the above-mentioned processes can currently not be resolved even in state-of-the-art simulations so they can only be considered in a phenomenological way. This can be done in various (numerical) ways and the respective realization can influence the global result (see Piontek & Steinmetz (2011) and Scannapieco et al. (2012) for systematic studies).

Despite these difficulties, recently, several groups have reported successful simulation runs that formed a realistic disk galaxy (Governato et al. 2010; Guedes et al. 2011). Other studies have illustrated the possibility to obtain the large variety of galaxy morphologies within the Λ CDM paradigm (e.g. Scannapieco et al. 2009; Aumer et al. 2013; Marinacci et al. 2014). The “success” of a galaxy simulation is currently evaluated considering the global structure of the resulting systems. Typical measures are the Tully-Fisher relation or the disk-to-total mass

or light ratio. More detailed knowledge is almost exclusively available for our own Galaxy. Hence it is a next logical step is to facilitate a comparison to surveys of the stellar content of the Milky Way. In this way we can probe the simulations on scale where the impact of feedback processes is most direct. However, the Milky Way is just one galaxy and it might not be an average galaxy in every aspect. An interesting approach to this problem is followed by the CLUES project (Gottlöber et al. 2010) that attempts to re-simulate the *local* Universe and the Milky Way with its specific environment. Despite all these advancements a direct comparison to observations of resolved stellar populations remains a challenge, in particular, because even in current state-of-the-art simulations one mass particle represents $\sim 10^3$ stars. As mentioned above the comparison of the physical quantities in the simulations with observations involves stellar population synthesis. For unresolved stellar populations this is already commonly applied for simulation analysis, mostly to evaluate the global structure of the galaxies (e.g. Guedes et al. 2011; Scannapieco et al. 2011; Martig et al. 2012). Confronting such simulations to resolved stellar observations can have several positive outcomes. First, we can test our current perception of galaxy formation on local observations. This is, however, complicated through the large influence of numerical implementation of physical processes that are not resolved in the simulations (star formation, feedback, etc.). Secondly, we can explore the models to find features that should be detectable by observations. A famous example for this approach is the missing satellite problem (Klypin et al. 1999) that triggered the search and discovery of a whole new population of Galactic satellite galaxies. Finally, these models can provide realistically complex mass distributions in configuration space¹. Because of this, such models play an important role for testing analysis approaches under realistic conditions.

A disadvantage of full cosmological simulations is that they are computationally extremely expensive. It is hence not possible to run a large number of simulations and do a systematic study or fit a data set. In the context of the strong stochasticity of the galaxy formation process this is an important caveat. Suites of simulations as provided as provided by Scannapieco et al. (2009) or Aumer et al. (2013) can alleviate the problem and so can hybrid modeling techniques as presented by Minchev et al. (2013a).

This thesis Galactic astronomy and numerical simulations of disk galaxies have finally reached similar scales for their spatial volumes under study. Simulations have advanced and are now able to resolve structures of sizes below a kiloparsec while modern stellar surveys have extended their observable regions to distances of one to several kiloparsecs. It thus appears almost imperative to confront these results with each other. In this thesis we attempt to construct links between the two fields and show that this can be fruitful for both sides.

We will, for the first time, convert fully discretized models of a disk galaxy into the space of observables to see them through the eyes of an internal observer. We will generate synthetic RAVE surveys based on these models that can be directly compared to the real data set. For this purpose we have to evaluate in great detail the selection function of the RAVE survey, the knowledge of which is crucial for many applications. We will, on the other hand, use cosmological simulations to test and calibrate an analysis technique that extracts an estimate of the total mass of the Milky Way from the kinematics of halo stars in the RAVE data. In a third study, we use numerical simulations to explore a possible origin of a specific population of stars observed in the Galactic halo, so-called Hypervelocity stars. This generation channel, the accreted satellite scenario, is linked to the hierarchical formation history of the stellar

¹Phase space combined with other properties like metal abundances, ages, etc. .

halo.

Structure of the thesis After the general introduction in this chapter, in Chapter 2 we give a more detailed description of the major data sets and the tools we use for our studies. Here we also lay out how we evaluated the RAVE selection function and how we generally transform N -body distributions into observable populations of stars using the code GALAXIA. In the spirit of inverse modeling this is then applied in Chapter 3 to three different Galaxy models of very different type and capability. Next, in Chapter 4, we follow the opposite approach and attempt to estimate the virial mass of the Galaxy directly from the RAVE data. Cosmological simulations are again an important ingredient for this study, because the additional constraints extracted from them allow to break a degeneracy in the parameters of interest. In Chapter 5 we present our study concerning the alternative generation scenario for Hypervelocity stars (HVSs). By means of dedicated N -body simulations we attempt to explain a number of peculiar features of the observed population of HVSs. We conclude and summarize in Chapter 6.

Additional remarks on the authorship Of this dissertation Chapter 5 has been published in the journal *Astronomy & Astrophysics* (Piffl, Williams, & Steinmetz 2011). The project further presents a continuation of a study that I submitted as a Diploma thesis at Leipzig University (Piffl 2009, advisers: Matthias Steinmetz and Tilman Butz). The complete study was repeated in a more sophisticated manner, both in terms of the simulations performed and in terms of the analysis. One major improvement is the modeling of the satellite galaxies. In Piffl (2009) these were modeled as simple Plummer (1911) spheres while for the present study we use the superposition of a dark matter halo with an NFW mass profile and a Hernquist (1990) sphere for the baryonic component. The mass ratios and scale parameters of these components are depended on the total mass of the satellite galaxy and are observationally motivated. Subsequently, we could drop the clearly over-simplifying assumption that stars and dark matter are distributed equally in phase space. The increased realism of the simulation led to much more differentiated results that partly contradict the findings of Piffl (2009). I set up and ran all simulations, developed the analysis and wrote the paper (with comments from my co-authors). Thereby I used a code for the generation of N -body initial conditions for a disk galaxy in equilibrium that was provided by Matthias Steinmetz.

Chapter 4 has been submitted on 23rd August 2013 to *Astronomy & Astrophysics* and is currently under review by an anonymous referee who recommended the article for publication after revisions². For the present content of the chapter the comments of the referee were already taken into account. The article was also co-authored. I extended the analysis (in discussion with my co-authors) that was introduced in Leonard & Tremaine (1990) and Smith et al. (2007), implemented and executed it. Cecilia Scannapieco provided the simulations and the basic coordinate transformations to shift and rotate the galaxies into a suitable coordinate system. She also wrote a short paragraph describing the simulations. James Binney provided comments on an advanced draft version of the article and wrote the major part of Section 4.5.2, namely the comments on the conceptual underpinning of the method. Both, the contributions by C. Scannapieco and by J. Binney, are again marked at the respective places in the main body of the text. The other co-authors in the non-alphabetical part of

²At the time this final version of the manuscript was prepared, the article was already published (Piffl et al. 2014).

the author list gave advice at various stages of the project while the co-authors in the alphabetical author list gave minor comments on the final manuscript and owe the authorship to their status as 'builders' in the RAVE collaboration, i.e. to their general contributions to the realization of the RAVE survey.

In Section 3.5 I describe parts of my contribution to the (successful) proposal of the 4MOST instrument to ESO. The results of this chapter developed in constant discussion with members of the 4MOST consortium, mainly Cristina Chiappini and Ivan Minchev. I further implemented and tested the selection functions and created the mock input catalogs, and contributed a number of paragraphs for the scientific report (Chiappini et al. 2013) in the proposal.

In Section 3.2.3 I describe a project I took part in and that was published as Boeche et al. (2013b). My contribution was to provide a mock RAVE data set based on the GALAXIA/Besançon model, discussing the results and their implications as well as a small paragraph describing the mock data. The article is mainly focused on the gradients derived from the actual data while in this thesis I focus more the differences found in the mock data. For the sake of completeness I should mention that some of my investigations presented in Section 2.1, in particular Figure 2.2 and an adapted version of Figure 2.3, were used in the description of the fourth data release of the RAVE survey (Kordopatis et al. 2013, their Figures 18 and 3, respectively).

2 Scientific background

In this chapter we will introduce the data sets and tools that form the basis of our research. One aim of this work is to connect two largely independent lines of astronomical research. In this chapter we will provide brief introductions to these quite disparate fields and do some preparatory investigations. The attentive reader will realize that we first describe our observational data of the Galaxy, then numerical models of the Galaxy and finally the code frame-work, GALAXIA, that forms an interface between the two.

2.1 The RAVE survey and its selection function

The Radial Velocity Experiment (RAVE) is a massive spectroscopic stellar survey of the southern hemisphere conducted using the 6dF multi-object spectrograph on the 1.2-m UK Schmidt Telescope at the Siding Springs Observatory (Australia). A general description of the project can be found in the previously published data release papers: Steinmetz et al. (2006); Zwitter et al. (2008); Siebert et al. (2011); Kordopatis et al. (2013). The project started in April 2003 and finished the observational phase in April 2013. In total 574 630 spectra were secured on 483 330 individual stars. The latest public data release (DR4; Kordopatis et al. 2013) contains information from 483 849 measurements of 426 945 individual stars. The median signal-to-noise ratio (S/N) is 52.

The spectra were taken in the Ca II-triplet region (8410 – 8795 Å) with an effective spectral resolution of $R = 7000$. The strong Calcium absorption lines allow a robust determination of the line-of-sight velocities via the Doppler effect even with low S/N ($\gtrsim 10$ per pixel). The region further coincides with the wavelength window which will be observed by the spectrograph of the upcoming Gaia satellite (e.g. Prusti 2012).

In order to provide an unbiased velocity sample the survey selection function was kept as simple as possible: it is magnitude limited ($9 < I < 12$) and has a weak color-cut of $J - K_s > 0.5$ for stars near the Galactic disk and the Bulge. We will discuss the detailed selection function below.

In addition to the very precise line-of-sight velocities, v_{los} , with typical uncertainties of a few km s^{-1} , several other stellar properties could be derived from the spectra. The astrophysical parameters, effective temperature (T_{eff}), surface gravity ($\log g$), an overall metallicity ($[M/H]$) and a limited range of individual elemental abundances were multiply estimated from the spectra using different analysis techniques (Zwitter et al. 2008; Siebert et al. 2011; Kordopatis et al. 2013; Boeche et al. 2011). Note that throughout this work we will use the bracket notation we dealing with elemental abundances:

$$[X/Y] = \log_{10} \frac{N(X)}{N(Y)} - \log_{10} \frac{N_{\odot}(X)}{N_{\odot}(Y)}, \quad (2.1)$$

where $N(X)$ is the number of atoms/molecules of element X in the star and $N_{\odot}(X)$ is the corresponding number of the Sun.

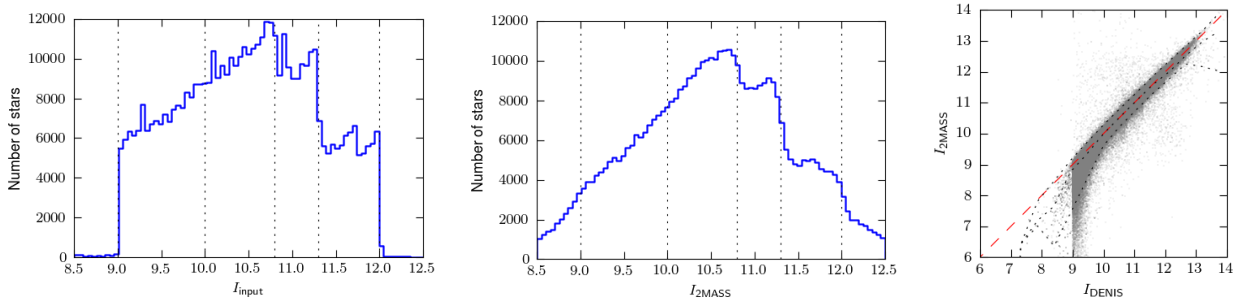


Figure 2.1: Distribution of input I -magnitudes in the full RAVE catalog. Dotted lines mark the border of the magnitude bins used for the observation runs. The left panel shows the input magnitudes on which the initial target selection was based. It is a compilation of a number of different source catalogs. The middle panel shows the $I_{2\text{MASS}}$ magnitude which are computed via the 2MASS J and K_s magnitude, but present a homogeneous data base. The right panel compares the DENIS I magnitudes with the approximated $I_{2\text{MASS}}$ (gray dots). The red dashed line marks equality and the dotted black lines show the median and the region containing 90% of the data.

Breddels et al. (2010), Zwitter et al. (2010) and Burnett et al. (2011) independently used these estimates to derive spectro-photometric distance estimates for a large fraction of the stars in the survey. Binney et al. (2014) improved on the method by Burnett et al. (2011) and there is a consensus in the RAVE collaboration that these distances are currently the most reliable values. Matijević et al. (2012) used a genetic algorithm to do a morphological classification of the spectra and in this way we identified binaries and other peculiar stars in the sample. Finally Boeche et al. (2011) developed an independent analysis pipeline to derive individual chemical abundances from the spectra. All targets in the DR4 were also cross-matched with other data bases to be augmented with additional information like apparent magnitudes in other filter pass-bands and proper motions. If not stated differently, throughout this work we adopt the parallax¹ estimates, ϖ , provided by Binney et al. (2014) and the proper motions from the UCAC4 catalog (Zacharias et al. 2013).

In any statistical analysis it is fundamental to understand the relation between the data sample to be analyzed and the underlying population from which the sample was drawn. This relation is called the selection function of the sample. Without this knowledge inferences on the general properties of the population are impossible.

The RAVE survey was designed to have a very simple selection function. In order to avoid any biases in kinematics or chemistry the initial target selection was based only on the apparent I -band magnitude and angular position of the stars. Later in the course of the survey the angular footprint of the survey was increased to include also regions close to the Galactic disk and bulge. In these new regions a color criterion $J - K_s \geq 0.5$ was imposed to select for cool giant stars (Kordopatis et al. 2013).

Another fact to consider is that the input catalog was divided into bins in I -magnitude. This was done because the individual stellar spectra measured by RAVE are projected close to each other on the CCD chip in the fiber-fed spectrograph. Thereby some light of a spectrum is scattered onto the adjacent spectrum and vice versa (“cross-talk”). This becomes a problem when the spectra of stars of very different brightnesses are projected next to each other on the CCD chip. Hence only stars within a certain magnitude range were observed simultaneously.

¹According to Binney et al. (2014) the parallax estimates are more robust than the direct distance estimates.

Table 2.1: Quality criteria for the 2MASS mother sample.

| Criterion | Requirement | Description |
|-------------------|--------------|--|
| $\sigma(J)/J$ | ≤ 0.01 | high photometric precision in J -band |
| $\sigma(K_s)/K_s$ | ≤ 0.01 | high photometric precision in K_s -band |
| ph_flag $_J$ | A, B, C or D | good photometric quality in J -band |
| ph_flag $_{K_s}$ | A, B, C or D | good photometric quality in K_s -band |
| cc_flag $_J$ | 0 | not contaminated by an artifact/confusion in J -band |
| cc_flag $_{K_s}$ | 0 | not contaminated by an artifact/confusion in K_s -band |
| gal_contam | 0 | not contaminated by extended source |
| pm_flag | 0 | not positionally associated with asteroid/comet |

The stars from the brighter bins were preferentially observed. This results in jumps and breaks in the overall I -magnitude distribution of the observed stars as illustrated in the left panel of Figure 2.1. We can thus assume that the probability, S , for a star for being observed by the RAVE survey is

$$S = S(l, b, I, J - K_s), \quad (2.2)$$

with l and b denoting the Galactic coordinates of the star.

When the observations of the RAVE survey started in 2003 there was no comprehensive photometric infrared survey available to serve as an input catalog. Instead approximate I -magnitudes were calculated from the Tycho-2 catalog (Høg et al. 2000) and at the faint end of the magnitude range stars from the SuperCOSMOS Sky Survey (Hambly et al. 2001) could be used. Later the DENIS catalog (Epchtein et al. 1997) was used as a source for I -magnitudes and for brighter targets an estimate for I computed from J and K_s magnitudes from 2MASS (Skrutskie et al. 2006) (see Siebert et al. (2011) and Kordopatis et al. (2013) for more details). From this it is clear that the input data carries some inhomogeneity and it is nearly impossible to construct a valid mother sample from this variety of data sets.

Therefore, we decided to use only 2MASS to assess the completeness of the RAVE survey. 2MASS provides accurate J , H and K_s photometry for all RAVE targets and, equally important, also for *all* other stars which could have potentially entered the input catalog. Unfortunately, it does not provide I -band photometry, but we can compute an approximate $I_{2\text{MASS}}$ magnitude via the following formula (T. Zwitter, private communication):

$$I_{2\text{MASS}} - J = (J - K_s) + 0.2 \exp \frac{(J - K_s) - 1.2}{0.2} + 0.12 \quad (2.3)$$

The right-most panel in Figure 2.1 compares the DENIS magnitudes with our approximated values. For the majority of cases the deviation is smaller than 0.3 mag. At bright magnitudes the 2MASS magnitudes become systematically brighter than the DENIS values. This comes mainly from the fact that the DENIS magnitudes suffer from saturation effects above $I \simeq 10$ mag (Kordopatis et al. 2013).

We compute an $I_{2\text{MASS}}$ value for each entry of the 2MASS point-source catalog and clean the data from spurious measurements (our adapted requirements for a “good” measurement are given in Table 2.1). Finally we apply the aforementioned color cut to the 2MASS data:

$$J - K_s > 0.5 \quad \text{for} \quad |b| < 25^\circ. \quad (2.4)$$

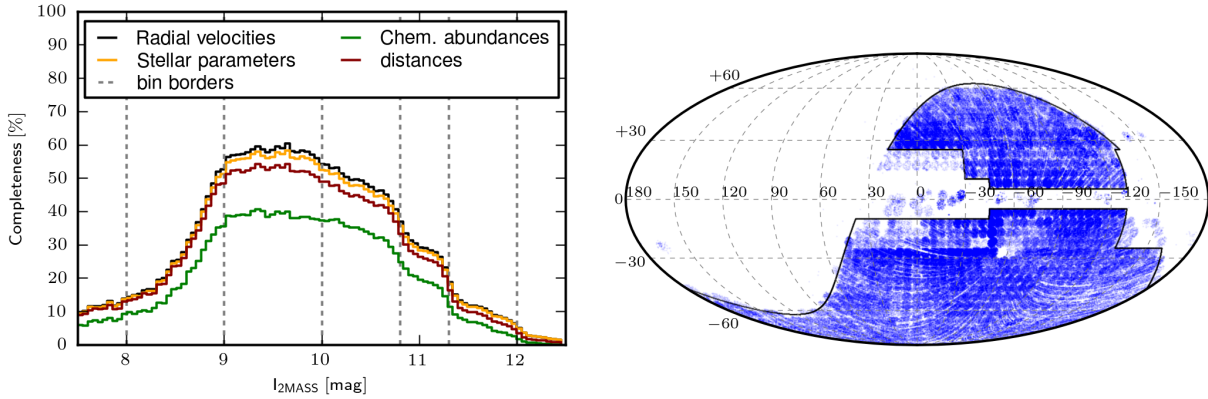


Figure 2.2: *Left panel*: Integral completeness of the RAVE survey w.r.t. the 2MASS catalog as a function of apparent magnitude. The different lines represent sub-samples for additional data products are available. *Right panel*: Mollweide projection of the simple survey footprint within which we estimate the completeness of the RAVE catalog w.r.t. 2MASS (black line). For comparison all RAVE targets are plotted as well (blue points). Axes are in Galactic coordinates.

2.1.1 Overall completeness compared to 2MASS

As a first step we can compare the number of RAVE targets with those in 2MASS as function of magnitude. We need to determine which 2MASS objects have ever been in the field of view of a RAVE observation. To do this we take each pointing of the RAVE survey and find those stars that fall in to the field of view, i.e., which have an angular distance smaller than the angular radius of the RAVE fields, $\alpha_{\text{field}} = 2.85^\circ$. It is important to do it in this way instead of simply taking all stars falling into the region of the survey footprint on the sky, because the tiling of RAVE leaves non-negligible gaps between the fields. These arise because (1) the circular fields are arranged such that they overlap², but leave small gaps between them and (2) there is a large gap around the equatorial South pole that was left out because of technical issues in the star tracking system of the telescope.

The left panel in Figure 2.2 plots the resulting completeness distributions for several data sub-sets for which additional data products are available. For the estimate a few RAVE pointings were omitted which are located outside the main survey area and were taken for calibration purposes or other specific science cases. Figure 2.2 (right panel) illustrates what we define as the core survey area of RAVE for which the completeness was evaluated. In particular the (neglected) fields in the Galactic plane (near $l \simeq 0^\circ$) are located in the most densely populated region of the sky and thus would dramatically reduce the completeness estimate. This would not reflect the properties of the RAVE survey correctly as these fields were observed for calibration purposes and will not be used for a statistical analysis. Note that empty areas within the footprint will not reduce the completeness, because 2MASS stars in these regions are automatically removed by the field-by-field selection described above.

²This overlap poses a further complication if one would attempt to evaluate the completeness on a field-by-field basis.

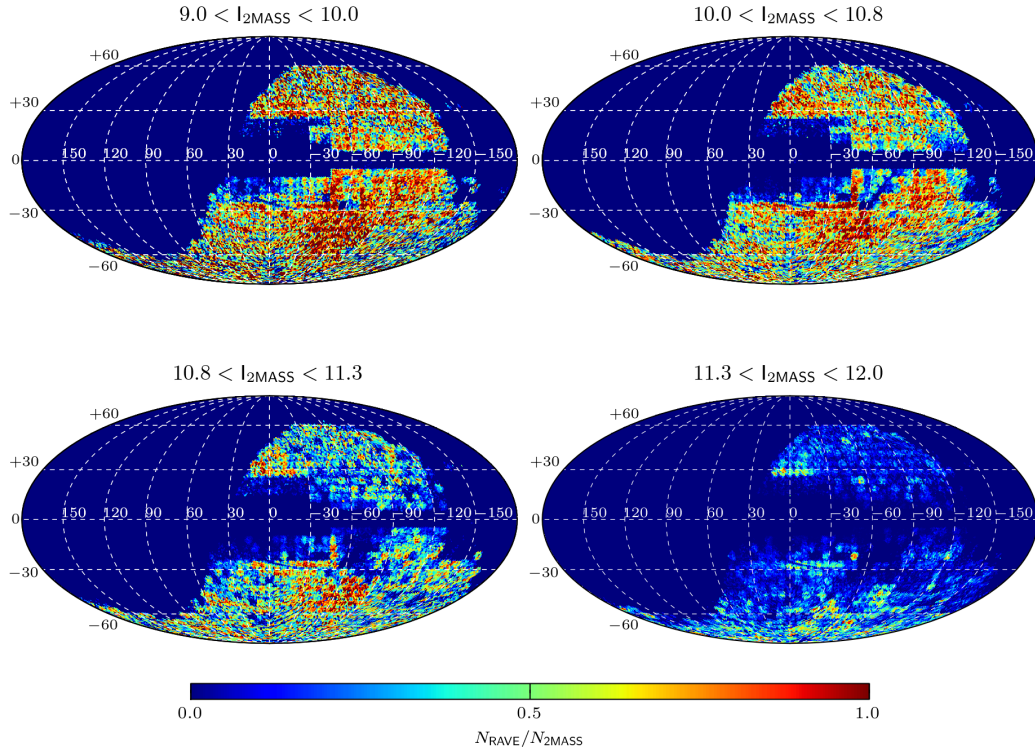


Figure 2.3: Mollweide projections of completeness distribution of the RAVE survey w.r.t. 2MASS as a function of angular position in Galactic coordinates. The pixel size is 0.84 deg^2 . The four panels correspond to the four magnitude bins into which the input target were grouped for observations. The brightest bin (upper left panel) was observed preferentially and contains less potential targets. As a result the completeness is much higher in this bin than, e.g., in the faintest bin (lower right).

2.1.2 Spatially resolved completeness

The RAVE target distribution on the sky is not homogeneous as illustrated, e.g. in the right panel of Figure 2.2. Some RAVE fields were visited more often than others, primarily because they are located at high altitude for the Siding Spring Observatory and had thus a higher probability to be observable. Another reason is that target densities vary strongly as one moves closer or away from the Galactic disk and the Galactic center. Therefore it is important to compute the selection function as a function of position on the sky.

We do this by dividing the celestial sphere into equally sized pixels using the HEALPix³ routines (Górski et al. 2005). The latter also provide an efficient algorithm to sort the stars into the pixels. We chose a pixel area of 0.84 deg^2 which is much smaller than a RAVE field ($\simeq 25.5 \text{ deg}^2$). In this way we accurately map out the gaps between the fields and also the empty strips in the RAVE coverage which were inherited from the DENIS survey.

To compute the completeness S_i in the i th pixel we divide the number of RAVE stars $N_{\text{RAVE},i}$ by the number of 2MASS objects $N_{2\text{MASS},i}$ falling into the pixel area, respectively, i.e.,

$$S_i(I_{\min}, I_{\max}) = \frac{N_{\text{RAVE},i}(I_{\min}, I_{\max})}{N_{2\text{MASS},i}(I_{\min}, I_{\max})}. \quad (2.5)$$

³<http://healpix.jpl.nasa.gov>

Here I_{\min} and I_{\max} are the lower and upper limiting magnitudes for which the completeness is evaluated. Figure 2.3 shows the resulting completeness maps for all RAVE measurements which have a radial velocity estimate (multiple observations were removed) for the four I magnitude bins [9,10] (upper left panel), [10,10.8] (upper right), [10.8,11.3] (lower left) and [11.3,12] (lower right) into which the input catalog was divided for observations. The brighter bins naturally contain less potential targets and, in addition, were preferentially observed so yield a higher completeness than the fainter bins.

For the general application of the completeness function $S(I)$ we will choose a finer binning in the I -magnitude and a more coarse grid in the (l, b) plane. Mapping out the empty strips and patches in the RAVE coverage is feasible, but not necessary, because the width of these areas is much smaller than the angular scales on which the properties of the observable population are reasonably expected to change.

The maps in Figure 2.3 were produced considering all RAVE targets for which at least one radial velocity measurement with uncertainty lower than 10 km s^{-1} is available. We can choose a different sub-sample of RAVE targets as an input. However, such sub-samples have to be selected with care in order to yield valid results for the completeness. The parameters used in the selection criteria must be correlated with the properties of the stars only through measurements available in the 2MASS catalog, i.e. angular coordinates l, b and apparent magnitudes J, K_s ($I_{2\text{MASS}}$) or not at all correlated, like, e.g., spectrum quality criteria. The signal-to-noise ratio, S/N, belongs to the first category, because it likely is related to the apparent magnitude of the star. Hence, a S/N cut will change the input distribution of $I_{2\text{MASS}}$ magnitudes and so the completeness distribution of the sample will be affected.

2.2 Theoretical models of galaxy evolution

An often repeated sentence about the currently most widely accepted model of the content and evolution of the Universe, the Λ CDM cosmology, is that its fundamental parameters and laws can be written down on a single sheet of paper. The fact that such a simple model should be able to account for the complexity of astronomical objects observed in the real universe (not to speak of variety of phenomena observable here on Earth) already points to the highly non-linear nature of the evolution predicted by this model. This high degree of non-linearity makes it very difficult to assess the implications of the model for our present epoch.

The conceptually most straightforward way to test our picture of the formation and evolution of the Universe are cosmological simulations of structure formation. On large scales ($> 1 \text{ Mpc}$) it is sufficient to only follow the evolution of the dark matter to successfully reproduce and explain the filamentary structure of the Universe as found in galaxy redshift surveys (e.g. Springel et al. 2006). On smaller scales physical processes other than gravity become important as well and so the baryonic component has to be considered as well. There are two fundamental approaches to implement the baryonic physics: either the luminous matter is included as a post-process to a dark matter-only simulation run using scaling laws and semi-analytic models (Kauffmann et al. 1999), or a direct simulation that models all relevant physical processes from the beginning. We will focus on the latter approach for this work.

Ideally, such simulations take as an input only fundamental physical laws and a set of initial conditions and provide as an output snapshots of a statistically significant part of the Universe at different times of its history up to the present epoch. In this strict sense, such

a simulation is currently infeasible to perform due to the limited computing power available and will also most likely never be possible. Therefore, a number of approximations are made that largely reduce the numerical effort. Many of these approximations are conceptually and physically well motivated, like, e.g., the tree-algorithm (Barnes & Hut 1986) for the evaluation of the gravitational field, smoothed particle hydrodynamics (SPH) (Lucy 1977; Gingold & Monaghan 1977; Steinmetz & Müller 1993) to model gas dynamics, or radiative cooling of gas clouds (e.g. Scannapieco et al. 2005).

However, the computational effort is not the only problem. Much of the physics acting on smaller scales are currently not only not resolved, they are not yet well understood. These processes can be implemented only in a phenomenological way as “sub-grid” physics. The most important among these are the UV-background and reionization, star formation, energy feedback from supernovae (e.g. Scannapieco et al. 2005, 2006) and massive stars (Aumer et al. 2013; Stinson et al. 2013). Owing to the hierarchical scenario of galaxy formation in the cold dark matter (CDM) paradigm (which we use as our basic framework throughout this work) such events can have a profound impact on larger scales, e.g. through the suppression of star formation in low mass galaxies (e.g. Ferrara & Tolstoy 2000). This situation leads to the problem that slight differences in the numerical implementation can translate into huge differences in the simulation result. Code comparisons like the Aquila (Scannapieco et al. 2012) or the AGORA projects (Kim et al. 2014) are therefore important to identify robust results.

Currently, the next major task is to simulate the formation of realistic galaxies and galaxy populations with statistical properties as found in observations. It turned out that the formation of massive disk-dominated galaxies as our own Galaxy are particularly difficult to obtain with current simulation techniques unless the above-mentioned sub-grid physics are treated properly. Recently, several groups reported successful attempts to form realistic disk-dominated galaxies (Governato et al. 2010; Guedes et al. 2011). However, as these are studies of single objects their significance remains unclear.

This problem was tackled by Scannapieco et al. (2009) who performed a suite of eight simulations with initial conditions picked randomly using the last snapshot of a dark matter-only simulation of a much larger volume⁴. The only selection criteria were that at $z = 0$ the dark matter halo has a virial mass similar to the mass of the Milky Way and the final halo has no similarly massive neighbor closer than 1.4 Mpc. Among these candidates are also the six halos that were studied in much higher resolution, but as dark matter only simulations, in the Aquarius project (Springel et al. 2008). This suite of simulations allowed the authors to study the processes that lead to the formation and destruction of a galactic disk.

To refer to the individual simulations we adopt the naming convention (A – H) of Scannapieco et al. (2009). The galaxies have virial masses between $0.7 - 1.6 \times 10^{12} M_{\odot}$ and span a large range of morphologies (Figure 2.4), from galaxies with a significant disk component and/or a central bar (e.g. simulations C and G) to pure elliptical galaxies (simulation F). The mass of the gas and stellar particles is $0.22 - 0.56 \times 10^6 M_{\odot}$ and the softening parameters for the gravity were set to 0.7 – 1.4 kpc. A detailed description of the simulations can be found in Scannapieco et al. (2009, 2010), Scannapieco & Athanassoula (2012) and Tissera et al. (2012) while the simulation code is presented in Scannapieco et al. (2005, 2006) and Springel (2005).

In this work we will use these simulations for two separate studies. In Chapter 3 we will use their final mass, age and metallicity distributions to create mock stellar surveys that can be

⁴see also Aumer et al. (2013) and Marinacci et al. (2014) who partly re-simulated the same initial conditions with different codes.

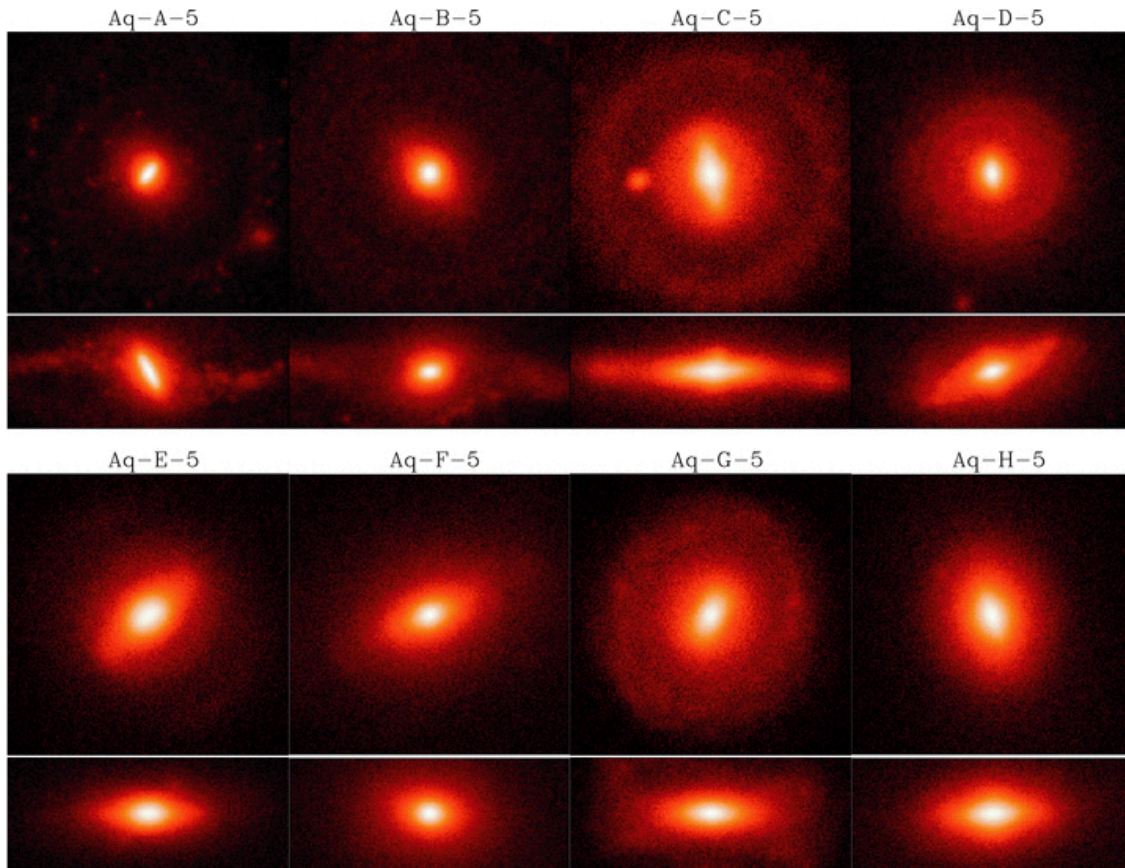


Figure 2.4: Face-on and edge-on view of the eight galaxies simulated by Scannapieco et al. (2009). Color-coding is reflecting the projected stellar luminosity (i band). The images are 50 kpc across, and the edge-on views have a vertical height of 20 kpc. The figure was taken from Scannapieco et al. (2011).

directly compared to the real observations in the RAVE survey. Doing this we will concentrate more on their disk components. In Chapter 4 we will explicitly pick mass particles not belonging to the disk population to gain an understanding of the velocity distribution in the stellar halo.

Re-scaling the simulations In both studies we will explore the galaxies from the perspective of an observer that is situated *inside* the system at a position equivalent to the position of the Sun in the Milky Way. To find this position we first define a Cartesian coordinate system in which the rotation axis of the galaxies is parallel to the z -axis and the center of mass is at the origin. In velocity space we fix the rest-frame by requiring a zero net-velocity for all particles within 20 kpc from the center.

The galaxies in the simulations have different structural parameters than the Milky Way. It is therefore not immediately clear where we should place the Sun in these galaxies. If applicable, we first fix the azimuthal position by requiring that the line between the Sun and the galactic center lags the bar major axis by 20° in the direction of rotation. The orientation of the bar we take from Scannapieco & Athanassoula (2012). Otherwise we pick a random angle.

For the solar distance R_0 to the galactic center there are several options: (1) we simply set a value for R_0 , e.g. 8 kpc, assuming that the simulated galaxy is a detailed twin of the Milky

Table 2.2: Virial radii, R_{340} , masses, M_{340} , and velocities, V_{340} , after re-scaling the simulations to have a circular speed of 220 km s^{-1} at the solar radius $R_0 = 8.28 \text{ kpc}$. We define R_{340} to be the galactocentric radius encompassing a mean mass density of 340 times the critical density for closure in the Universe.

| Simulation | R_{340} (kpc) | M_{340} ($10^{10} M_{\odot}$) | V_{340} (km s^{-1}) | scaling factor |
|------------|--------------------|--------------------------------------|-------------------------------------|----------------|
| A | 154 | 77 | 147 | 1.20 |
| B | 179 | 120 | 170 | 0.82 |
| C | 157 | 81 | 149 | 1.22 |
| D | 176 | 116 | 168 | 1.05 |
| E | 155 | 79 | 148 | 1.07 |
| F | 166 | 96 | 158 | 0.94 |
| G | 165 | 94 | 157 | 0.88 |
| H | 143 | 62 | 137 | 1.02 |

Way in terms of scale length, bar length, etc. . (2) Another option would be to fix the value of R_0 in units of the radial disk scale length R_d . This would ensure that we are located in a similar environment as the Sun in the Milky Way. Estimates for R_d in the literature range between 2 – 4 kpc, so this would still leave considerable freedom. Finally, (3) we could consider the kinematics of the galaxy to fix the position. Since we want to compare to the RAVE survey – the major data product of which are velocities – this seems a plausible choice. We re-scale the simulation in such a way that the circular speed at R_0 is 220 km s^{-1} . For this we use the following coordinate transformations for radial distance, r , velocity, v and mass, m , of the stellar particles:

$$\begin{aligned}
 r' &= r/f, \\
 v' &= v/f, \\
 m' &= m/f^3.
 \end{aligned}
 \tag{2.6}$$

These transformations leave the numerical values of the gravitational constant G and the mass density invariant. This is important because these quantities are used in the simulation code with their absolute values for the gravity solving and in the star formation recipe. Note, however, that these transformations also change the energy scale in the simulation and thereby we effectively change the amount of energy feedback from supernovae by a factor f^{-2} . The scale factors and resulting virial masses, radii and velocities for all 8 simulations are given in Table 2.2. The factors are close to unity so the changes in the feedback energy are well inside the uncertainties of this parameter and the numerical realization of energy injection into the surrounding ISM.

2.3 The stellar synthesis code GALAXIA

In the last decades several attempts have been made to produce a detailed model of the Milky Way comprising as much of the current knowledge as possible. There are simple mass models (e.g. Dehnen & Binney 1998; McMillan 2011; Irrgang et al. 2013) mainly used for orbit calculations for single stars or satellite galaxies and there are very complex models describing also the expected stellar kinematics and the spatial distribution of stellar ages and chemical abundances. The latter allow to derive detailed predictions of stellar observations that can be

statistically compared to real observations. The most widely used of these models are the so-called Besançon model (Robin et al. 2003) and the TRILEGAL model (Girardi et al. 2005). Recently, Sharma et al. (2011) developed a new numerical framework to create such models and – as a test case – implemented the density profiles of the Besançon model. Such a model generally consists of analytic expressions for the mass density profile, the age, metallicity and velocities distribution as well as an assumption about the initial mass function (IMF) and a set of stellar isochrones that are used to map from physical into observational space. While the density profiles can be fitted against deep photometric observations, the other ingredients are often less well constrained or are still under debate (for example the IMF, see e.g. (Kroupa 2007)). The velocity distribution is mostly set to reproduce local measurements and can be made consistent with the gravitational potential implied by the mass density profile (Bienaymé et al. 1987). Often these models are constructed as a super-position of several sub-components, as e.g. a Galactic bulge, a dark and a stellar halo and often several Galactic disks.

Such models are often useful and sometimes even necessary tools to analyze and interpret large sets of data. Here we list some examples of typical applications without claiming it to be exhaustive: Reylé et al. (2009) used the Besançon model to constrain the Galactic warp in the 2MASS catalog by studying the differences of an un-warped Galaxy model and the data. Gao et al. (2013) tested the TRILEGAL model, the Besançon model and in addition the less comprehensive model by Just & Jahreiß (2010) against the SDSS photometric star counts to find the most informative data projections. Williams et al. (2011) used the GALAXIA code to evaluate the statistical significance of a stellar stream in the RAVE data. Miglio et al. (2013) used again TRILEGAL predictions to disentangle intrinsic features in their data from selection effects. Similarly, Boeche et al. (2013b) use the GALAXIA model to investigate the influence of selection effects on the chemical radial gradients in the Galactic disk. Finally, Cioni et al. (2014) used GALAXIA to model the proper motions of the foreground stars in their observations of the Large Magellanic cloud.

Also for the planning of new observing facilities a forecast of the observable objects presents important information. The analysis software for the space-born mission Gaia (e.g. Prusti 2012) is developed and tested using an extended version of the Besançon model (Robin et al. 2012). Another example is the 4MOST telescope (de Jong et al. 2012), the full 5-year operations of which were simulated using a GALAXIA output as a mock input catalog, in order to evaluate the science capabilities of the planned instrument. The code is also used for a similar purpose in the planning of the GALAH survey using the HERMES spectrograph (Zucker et al. 2013).

2.3.1 Stellar population synthesis from analytic distribution functions

This work makes extensive use the GALAXIA code and derivations from it. In the following we briefly introduce the principal concepts of the GALAXIA framework. The full details and a suite of basic test applications can be found in Sharma et al. (2011). The code models the Galaxy as a superposition of a set of stellar components. These could be the Galactic disk(s), a central bulge/bar and a stellar halo, but also individual stellar streams or in-falling satellite galaxies. Each component is described by its phase space distribution function (DF)

$$f_j = f_j(\mathbf{r}, \mathbf{v}, \tau, Z, m), \quad (2.7)$$

which is assumed to be a function of position (\mathbf{r}), velocity (\mathbf{v}), age (τ), metallicity (Z) and stellar mass (m). The index j stands for the individual components.

It is further assumed that the DF can be written as a product of several basic functions describing different physical aspects of the component:

$$f_j = \frac{\Psi(\tau)}{\langle m \rangle} \xi(m, \tau) f_{\text{pos}}(\mathbf{r}, \tau) f_{\text{vel}}(\mathbf{v}, \mathbf{r}, \tau) f_Z(Z, \mathbf{r}, \tau). \quad (2.8)$$

Here $\Psi(t)$ is the star formation rate as a function of look-back time or age. The parameter $\langle m \rangle$ represents the mean mass of the stars of a simple stellar population with present-day mass distribution $\xi(m, \tau)$, which is a convolution of the initial mass function (IMF) with stellar evolutionary models predicting the range of stellar masses still observable after the time τ . The spatial and kinematic DFs, f_{pos} and f_{vel} , are assumed to be functions of age only as is the metallicity DF, f_Z . This latter approximation of the metallicity being uncorrelated with the kinematics of a star is common in all currently available stellar evolution models, but too simplistic in the light of newly available data, as we will discuss later in Section 3.2.3.

Once all these distribution laws are fixed, a random realization of the DF is created using either the inverted cumulative distributions or the von Neumann rejection technique (e.g. Press et al. 2007). This step is generally the bottle neck of the stellar synthesis codes and GALAXIA is using a particularly efficient algorithm to do the sampling making it a very powerful tool to study to fit global Galaxy models to large data sets (e.g. Sharma et al. 2013).

The observable properties of the resulting mock stars can then be obtained from stellar evolutionary models. These provide the basic stellar parameters, namely surface gravity ($\log g$), effective temperature (T_{eff}), bolometric luminosity L , and absolute magnitudes in a variety of astronomical filter systems. Currently, GALAXIA is using the Padova stellar atmosphere models (Marigo et al. 2008).

A further important ingredient to mock observations is dust extinction along the line of sight. GALAXIA has a basic scheme implemented which assumes a double exponential dust disk which is fit to the extinction maps provided by Schlegel et al. (1998). It is well known that these maps are problematic near the Galactic disk and we apply the ad hoc correction factor

$$E_{B-V, \text{corr}} = E_{B-V} \left(0.6 + 0.2 \left(1 - \tanh \left[\frac{E_{B-V} - 0.15}{0.3} \right] \right) \right) \quad (2.9)$$

proposed by Sharma et al. (2013) to lessen this effect. Note however, since for this work we want to model the RAVE survey, this is not a major concern as RAVE by construction avoids the highly extinguished regions in the plane. With these extinction estimates $E(B-V)$ at hand it is then straightforward to compute the apparent magnitude of the mock stars via

$$m_i = M_i + 5 \log_{10}(d[\text{kpc}]) + 10 + A(i), \quad (2.10)$$

where d is the heliocentric distance to the star and $A(i) = R(i)E(B-V)$ is the extinction in a given filter i computed using the conversion factors $R(i)$. We use the values $R(J) = 0.72$ and $R(K_s) = 0.306$ given by Yuan et al. (2013).

2.3.2 Stellar population synthesis from an N-body model

The major part of the GALAXIA code has the purpose to produce discrete realizations of an analytically described Galaxy model in observational space. However, with the advancement of numerical simulations of structure formation it became clear recently that the (outer) stellar halo is not well described by a smooth relaxed population. It is rather a combination

of large number of stellar streams resulting from merging and accretion of minor neighboring galaxies over past cosmic history. Therefore Sharma et al. included a section in the GALAXIA code that allows to include a stellar halo from an N -body simulation that could provide the lumpiness expected in a Λ CDM universe.

In this case, the spatial and kinematic DFs taken from the mass particle distributions. The particles are discrete tracers of the underlying smooth mass distribution and a softening kernel has to be applied to recover this density field. GALAXIA uses a so-called Epanechnikov kernel for the smoothing:

$$W(u) = \begin{cases} N_W (1 - u^2) & \text{for } u \leq 1 \\ 0 & \text{otherwise,} \end{cases} \quad (2.11)$$

where $u^2 = (|\mathbf{r}|/h_r)^2 + (|\mathbf{v}|/h_v)^2$ and N_W is a normalization constant, which is defined through

$$\int d^6u W(u) \stackrel{!}{=} 1 \quad (2.12)$$

and has the value $N_W \simeq 0.77403670$ (Sharma & Steinmetz 2006).

For the standard Galaxy model described in Sharma et al. (2011) the simulations by Bullock & Johnston (2005) served as a halo model. This simulation was a pure N -body simulation of dark matter and star particles which were accreted in form of satellite galaxies onto a Milky Way-like galaxy represented by an analytic potential. Ages and metallicities were assigned to the star particles only as a post-processing step. Sharma et al. decided not to use these individual age and metallicity of a certain particle in order to spawn a stellar population from it, because they were not connected to their individual positions in phase space, but to the initial properties of the satellite galaxy they belonged to. Instead, the code generates an age-metallicity function for each individual satellite and based on this randomly assigns age and chemistry.

In practice, this means that each mass particle represents a simple stellar population that is distributed in a phase space volume around the particle. The mass is according to the IMF split up into individual stars that have all the same age and chemical abundances as the host particle.

2.3.3 Modifications to GALAXIA

For this work we want to be able to process an N -body realization of a complete galaxy including disk(s), bulge and stellar halo. Clearly, for such a large system the approximation that the age-metallicity relation is the same globally is not valid anymore. Therefore, we had to make modifications to the code to ensure that each mock star inherits the age and chemical properties of its parent particle.

The original version of GALAXIA uses the exponential IMF proposed by Chabrier (2001) for all N -body input. We implemented the IMF by Scalo (1986) (see Eq. 3.6) as a second option in order to be consistent with the MCM model (see Section 3.3) which we will study in the course of this work.

On the suggestion of L. Girardi (private communication) we modified the way how the appropriate isochrone is selected given the age τ , the iron abundance $[\text{Fe}/\text{H}]$ and the α -enhancement $[\alpha/\text{Fe}]$ of a star particle. Instead of adopting the isochrone with a metallicity closest the metallicity of the particle, we compute a modified metallicity

$$[\text{M}/\text{H}]_{\text{mod}} = [\text{Fe}/\text{H}] + [\alpha/\text{Fe}] \quad (2.13)$$

and select the isochrone which is tagged closest to this value to generate the stellar population. The reason for this obviously inconsistent course is that we want to correct, at least approximately, for the fact that all stellar tracks in GALAXIA were computed with $[\alpha/\text{Fe}] = 0$. According to Girardi the α -enhanced isochrones currently available in the literature are all suffering from an error in an opacity table and should therefore not be used. Finally, we had to apply some minor changes to the original code mainly concerning in- and output routines to facilitate to use of our N -body models and we added the Padova isochrones in the 2MASS filter system to the code.

2.3.4 Computation of the smoothing parameters

As already done by Sharma et al. for the Bullock & Johnston (2005) halos in the original version of GALAXIA we use the publicly available code EnBiD (Entropy based Binary Decomposition; Sharma & Steinmetz (2006)) to compute individual smoothing lengths \mathbf{h}_i for the mass particles. As for kernel softening in smoothed-particle hydrodynamics (SPH) the smoothing length are defined as the distance to the N_{ngb} -th nearest neighboring particle, however, in this case in six-dimensional phase space. The difficulty in this process is to find a suitable metric to compute distances in phase space. EnBiD evaluates a local metric for each particle so that the local variance of phase space density is about equal in positional and velocity space.

The code yields erroneous results if two particles are sitting on the exact same phase space position which happens in one of the models we will use later on (the MCM model, see Section 3.3). In this case we circumvent the problem by randomizing the particles' azimuthal positions for the softening computation and rotate their velocities accordingly⁵. This has the effect that the softening becomes a function of (cylindrical) radius R and height above the Galactic plane z only, while without the randomization we should see, e.g., marginally decreased softening in the spiral arms where the number density of particles is slightly increased. The effect would be negligible, however, since the azimuthal density variations are very small except, maybe, for the central bar region. But these regions are too distant from the Sun to be observed by the RAVE survey and so this issue is not of concern for this study.

The GALAXIA standard value of N_{ngb} is 64 for the softening estimates. A smaller value would increase our resolution (and the shot noise in the density field). Decreasing N_{ngb} by a factor f will decrease the resulting softening length on average by a factor $f^{\frac{1}{6}}$. So if we drastically decrease N_{ngb} to 16 the softening lengths will shrink only to $\sim 80\%$ of their original value.

This is problematic because the softening in 6D phase space leads to very large spatial softening length. Figure 2.5 shows the spatial and kinematic softening parameters for particles in the solar annulus computed for a disk configuration with more than 2 million particles. If we consider only the three spatial dimensions we find softening lengths around 200 pc which is even somewhat smaller than the canonical scale height of 300 pc for the thin disk. However, in the full 6D case the spatial softening is around 1 kpc, erasing all information about a possible thin and thick disk dichotomy.

⁵The existence of 2 particles at the same phase space point is actually a numerical artifact arising during the construction of the MCM model. The increased mass density at these points is hence not physically motivated and moving these particles away from each other does actually improve the model in this specific aspect.

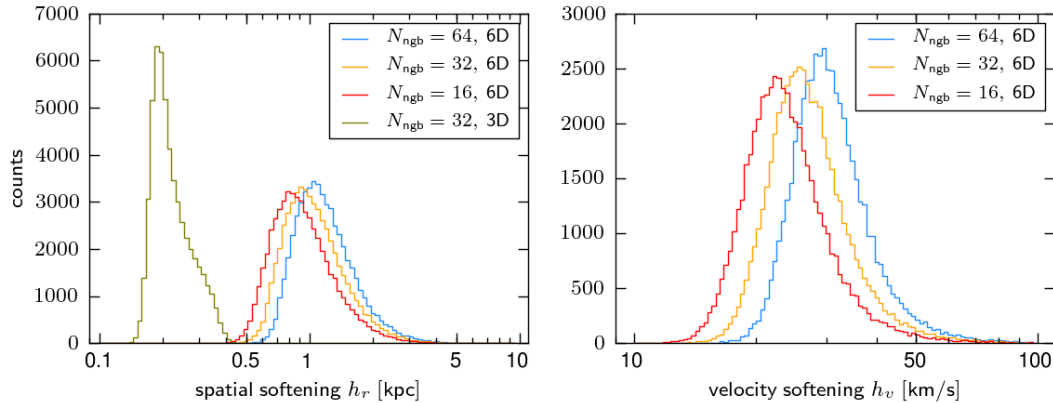


Figure 2.5: Softening parameters computed for an N -body disk with more than 2 million particles in total. The left and right panels show the distribution of the spatial and kinematic softening parameters for particles in the solar annulus for various values of N_{ngb} . For the spatial softening we show also the softening lengths if we smooth only in positional space as is typically done in SPH simulations. Only particles with $7.5 < R < 8.5$ kpc and $|z| < 1$ kpc were considered.

One of the underlying problems is that GALAXIA cannot distinguish between different spatial directions for the softening. While this is fine for the spherical or moderately flattened distributions of satellite galaxies, in highly anisotropic configurations a lot of information is lost. For thin stellar streams as found in the halo Sharma et al. (2011) improved the situation by ensuring that – if possible according to the observational constraints – one mock star gets assigned the exact phase space position of the parent particle. This improves the resolution significantly if only one or a few stars are spawned per mass particle, i.e. for particles which are distant from the Sun.

In the case of the Galactic disk, parts of which are very close, this approach does not work anymore because particles get heavily over-sampled. In order to conserve as much information as possible we decided to use spatial softening lengths computed without considering the velocity space. For the velocity smoothing we use a constant value h_v , which we set to be the median value of distribution of velocity softening length computed with EnBiD in 6D phase space with $N_{\text{ngb}} = 32$. For this we only consider particles in the solar annulus, which we define as $7.5 < R < 8.5$ kpc and $|z| < 1$ kpc, because these are the most relevant particles for our study. We test the effect of this somewhat arbitrary decision in Section 3.3.2.

3 Mock RAVE surveys from models of the Galaxy

An empirical measurement is usually influenced by a great multitude of minor effects that results in a stochastic scattering of the observed value around the actual value of the quantity of interest. The large number of different influences usually drives the scattering distribution towards a Gaussian function, the width of which can be easily evaluated by several repetitions of the experiment. For astronomical observations such influences can be stochastic photon emission of the source, the current state of the atmosphere above the telescope, temperature variations in the telescope or read-out noise on the CCD detector to name just a few. Things get more complicated when the observations are used in a further analysis, which is often equivalent to a non-linear transformation. This can severely alter the shape of the uncertainty distributions.

A further level of complexity is added if the measurements that enter the data set are not entirely randomly selected, i.e. if the data set has a selection function. A typical example for such a complication is the Malmquist bias that describes the fact that a magnitude-limited survey is biased towards intrinsically brighter objects. There are however, also more subtle effects like a metallicity bias that can be easily introduced by a color cut in a stellar survey. Even if the effects of a selection function are well understood it is sometimes extremely difficult to correct for them.

A very simple illustration of the problems that can arise during such a correction is offered by the case of a stellar sample of a completeness (w.r.t. all potentially observable targets) that varies as a function of magnitude. This can be achieved by weighting each star in the sample by the inverse completeness of its magnitude region. As a result it can happen that very few stars get extremely high weights and thereby introduce a large statistical uncertainty in the results. Typically this happens at the faint end of the magnitude range where potential target numbers are high and signal-to-noise ratios of the measurements are low so many targets are lost due to quality issues. Together with possibly non-Gaussian uncertainty distributions the evaluation of the uncertainty in the final result of such an analysis becomes non-trivial.

In the study presented in this chapter we follow a different approach. Instead of trying to remove the selection effects from the data we ask what would we observe using a given survey selection function if a given model was true. This allows us to repeat the target selection and observing process in the same order as for the real survey and thereby successively introduce the same measurement uncertainties and selection criteria (see also Bovy et al. 2012c). A great advantage of this approach is that we (have to) deal with observational quantities which have relatively simple uncertainty distributions (e.g. line-of-sight velocities and proper motions instead of the computed Cartesian coordinates U, V, W). The downside of the approach is that we have to apply very comprehensive and hence complex models which require many assumptions that then are all tested simultaneously.

In the course of this work we will explore three different Galaxy models for their consistency with the results of the RAVE survey. Depending on the type of the input model we are able to

study different aspects of the survey data. First (Section 3.2) we will use the standard model implemented in the original version of GALAXIA. As this model is a close twin of the well-tested Besançon model (Robin et al. 2003), this exercise will firstly provide an independent test of this model, in particular the implemented kinematics and chemistry and secondly establish a benchmark for a good Galaxy model to which other models can be compared to. The model is also the only one based on analytic distribution functions that we will study. We will then move over to models based on discrete mass particle distributions. Here we will initially (Section 3.3) use the chemodynamical MCM model of the Milky Way (Minchev et al. 2013a) that consists of a pseudo-cosmological simulation of the evolution of a disk galaxy. Stellar ages and chemical abundances were added in a sophisticated post-processing step using a chemical evolution model of the Milky Way. Finally (Section 3.4), we will explore a fully cosmological simulation of the formation of a disk galaxy from the simulation suite of Scannapieco et al. (2009), following self-consistently also the chemical evolution of the inter-stellar medium.

Our study is meant to be a pilot study in the sense that we do not try to improve or modify these models in the light of our results. Although it would be possible to develop a new Milky Way model with a more comprehensive use of our method, this is beyond the scope of this thesis.

3.1 Creating a synthetic RAVE survey

Before we can actually evaluate the RAVE selection function in the way described in Section 2.1 we have to decide about the part of the RAVE data we want to compare with. The measurements have to be of good quality or at least their uncertainties have to be well understood otherwise a comparison to the resulting mock survey is meaningless.

First of all we have to sort out the repeat observations, which amount to $\sim 10\%$ of the RAVE measurements. We keep always the observation with the highest S/N value. Further we remove all measurements that are flagged to have a problem in the spectrum (any `SpectraFLAG` is present). For similar reasons we discard all measurements for which a radial velocity correction larger than 10 km s^{-1} (`correctionRV`) was applied or that have an uncertainty in the radial velocity (`eHRV`) larger than 7 km s^{-1} . A large value in one of these quantities could point to problems in the spectrum. The RAVE analysis pipeline returns estimates for the line-of-sight velocities for all measurements regardless of the quality of the spectrum or the fit of the synthetic spectrum. The Tonry & Davis (1979) correlation coefficient (`CorrelationCoeff`) is provided for each spectrum fit that reflects the compatibility of the observed and the selected synthetic spectrum. We select all measurements where this coefficient is larger than 10. As we use the 2MASS catalog to evaluate the completeness of the selected sample we use only those targets which have a secure counter-part in 2MASS (Cross-identification flag `XIDquality2MASS` is A). We also restrict our targets to have an $I_{2\text{MASS}}$ between 8 and 13 mag.

As already mentioned before, below a Galactic latitude of $b = 25^\circ$ RAVE observed only stars with $J - K_s > 0.5$ mag to favor of cool giant stars over hot dwarfs. However, there are a couple of calibration observations which do not follow this selection criterion. We discard all stars which violate the criterion for the sake of a clear selection function. The Schlegel et al. (1998) extinction maps are known to be inaccurate in regions of high extinction and we therefore avoid such regions. The RAVE survey did the same, but for the reason that highly extinguished spectra pose large difficulties for the analysis pipelines. We follow the footprint

of the second input catalog (see Kordopatis et al. 2013, their Figure 1). This means that we exclude stars with $|b| < 10^\circ$ and $|l| < 45^\circ$ in both hemispheres and – on the Northern Hemisphere only – stars with $b < 25^\circ$ and $|l| < 30^\circ$ (see, e.g., Figure 2.2 for an illustration). Finally, we want to get a handle on the uncertainties in the stellar parameter estimates of the input data. We do this by imposing a lower limit on the S/N of the measurements. By default we set this limit to 40, but depending on the parameters we want to compare we will sometimes choose a higher value. The relatively high default threshold anticipates already an additional data quality cut connected to the RAVE DR4 analysis pipeline that we cannot perform at this stage, but has to be done on the mock data (see Section 3.1.3). By imposing a strong cut in S/N at this point leads to a clearer selection function. After applying all these selection criteria we obtain a sample of $\sim 225\,000$ stars. This is about 53% of the $\sim 425\,000$ unique stars in the RAVE DR4 catalog.

3.1.1 Application of the selection function

Together with the RAVE selection function and the modified GALAXIA code we have now all the tools in hand to create a sample of mock stars which resembles the original RAVE sample as close as possible for a given model of the Galaxy. We have to define a tiling of the sky (via HEALPix) and bins in $I_{2\text{MASS}}$ (bin width 0.2 mag) to compute the completeness S as a function of angular position and magnitude. In the following we use HEALPix pixels of size $\simeq 3.35 \text{ degree}^2$ (HEALPix parameter NSIDE = 32). This is larger than the pixel size used for Figure 2.3 which served illustrative purposes. A larger pixel area reduces stochastic noise in the mock survey, but has the consequence that we do not recover the empty stripes along equatorial declination in the RAVE inherited from the DENIS survey. Instead we obtain a reduced completeness in pixels intersecting with the stripes. Since there are no significant variations on scales comparable to the widths of the stripes this does not affect our results¹. Then we apply the same HEALPix tiling and magnitude binning to the GALAXIA output, which we use as the mock equivalent of the 2MASS catalog, except that we have, in addition to the positional and magnitude information, the full phase space, chemical and age information about every single entry. To be consistent we do not use the I magnitudes provided by the code, but again compute $I_{2\text{MASS}}$ from the J and K_s magnitudes. We also add extinction to the apparent magnitudes in the way described in Section 2.3.2. Note that we thus neglect the photometric uncertainties in the data.

In each $(l, b, I_{2\text{MASS}})$ -bin we randomly select the same fraction of total number of available mock stars as given by S^2 . We use statistical rounding to fix the (integer) number of stars to be picked: for each bin we draw a random number X between zero and unity. If X is smaller than the floating point part of the product of the completeness of the bin and the number of available targets in the bin, we round up otherwise we round down. The resulting mock sample is an equivalent model realization of the input RAVE sample and can be treated exactly in the same way.

¹The same argument generally applies for the statistical usability of the RAVE survey itself.

²Alternatively we could assign a weight to each mock star equal to the completeness of the bin in which it is located. In this way we could reduce the scatter to the mock data. We leave this approach for future investigations

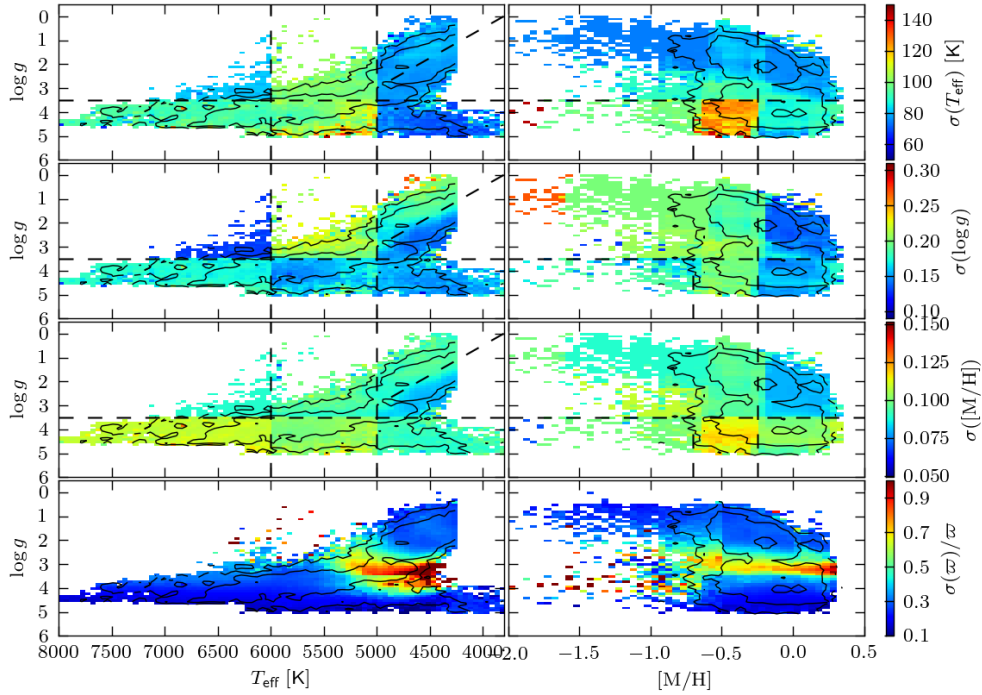


Figure 3.1: Mean uncertainties of the RAVE stellar parameter estimates of T_{eff} (first row), $\log g$ (second row) and $[M/H]$ (third row) as well as of the parallax estimates, ϖ (bottom row), as a function of the star’s location in the parameter space. The dashed black lines mark the borders of the regions with similar uncertainties which we defined to introduce errors of the mock data. The black contours show the number density distribution of the RAVE data and mark locations with 10, 100 and 1000 stars per bin.

3.1.2 Introduction of observational errors

Observational data sets never contain the “true” values of the physical quantities listed, but the most likely values given the observations (and the analysis pipeline). The precision of the measurements is usually expressed as an uncertainty which indicates a range of values which contains the true value to a certain confidence level α . If we want to compare our artificial data set, which contains the true values predicted by the underlying model, with real data we have to add similar errors to the mock data. We distinguish between the uncertainty or precision, $u(X)$, of a measured quantity X , which is a property of the probability distribution of this quantity, and an error $e(X)$ which is a random value drawn from this probability distribution. In order to do this we will assume that the probability distribution follows a Gaussian in each parameter. To obtain a similar uncertainty distribution as in the real RAVE data we randomly associate the set of uncertainty values of a real RAVE measurement (from our input sample) to each mock star.

This is possible because the DR4 pipeline provides individual uncertainties (68% confidence) for each measurement. How well a parameter can be constrained by the RAVE spectrum depends also on the type of star, i.e. where it is located in parameter space. As illustrated in Figure 3.1 different regions in the parameter space allow different precisions in the estimate. The reason for this is that for some parameter combinations certain features in the spectrum are more sensitive to small changes in the parameters than for other combinations. The abrupt jumps visible in Figure 3.1, e.g. at $\log g = 3.5$ dex, do result from discontinu-

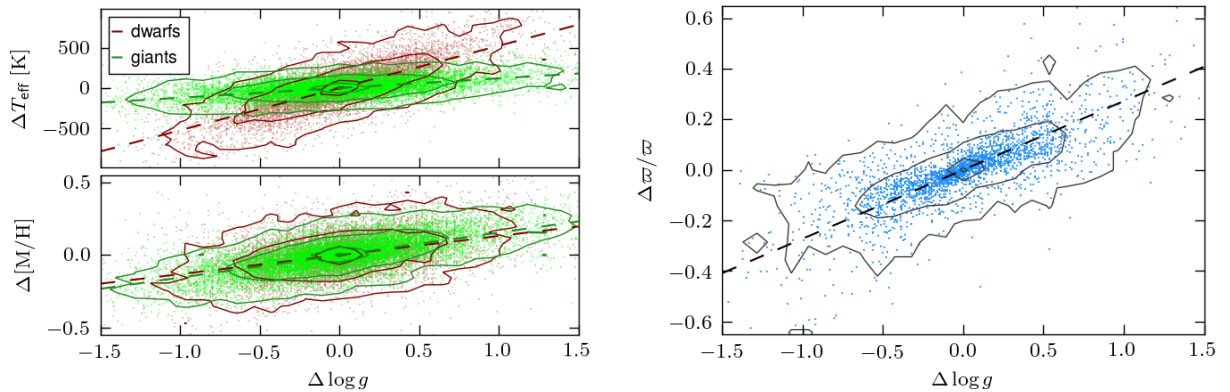


Figure 3.2: *Left panel:* Distribution of the differences ΔX between the astrophysical parameter estimates, X , coming from RAVE repeat observations of the same star. The stars were separated into dwarfs ($\log g > 3.5$, red color) and giants ($\log g \leq 3.5$, green color). The contour lines mark positions where the number density dropped to 1%, 10%, 50% and 90% of the maximum value (located at $(0, 0)$). The dashed lines highlight the orientation of the major axis of the distributions as computed from the covariance matrix. *Right panel:* Distribution of the differences in the parallax, $\Delta\varpi$, and surface gravity, $\Delta \log g$, estimates coming from RAVE repeat observations of the same star. The contour lines are the same as in the left panel.

ous changes in the stellar model atmospheres that are compared to the data by the analysis pipeline. To take this into account we divide the parameter space into regions in which the variation of the uncertainties is small, i.e. the regions that are marked with black dashed lines in Figure 3.1. Then, we choose a suite of uncertainties for each mock star from a single RAVE star located in the same region as the mock star. The choice of the borders was mainly determined by the aforementioned jumps in the uncertainty distributions. Note that this procedure is somewhat inconsistent as we use the *measured* location of the RAVE star and associate it with the *unaltered* location of the mock star in the parameter space. This is unavoidable since we cannot know the real location of the RAVE stars. However, because the uncertainties in the parameters are usually small compared to the sizes of the regions of similar uncertainty values we consider this a minor problem.

A further issue to investigate is whether there are degeneracies for measurements of different astrophysical quantities. Such correlations can arise if several parameter combinations yield very similar spectra. The stars with repeat observations in RAVE offer the possibility to identify such correlations, because we can study the differences ΔX of the measured parameters X coming from two measurements of the same star. Figure 3.2 reveals that an over-estimated value for the stellar surface gravity $\log g$ leads to a too high value for the effective temperature T_{eff} and the metallicity $[M/H]$. We treat dwarfs and giants separately by cutting the sample at $\log g = 3.5$ and approximate these correlations by shifting T_{eff} and $[M/H]$ according to the following formula:

$$e_{\text{bias}}(X) = S_X e(\log g), \quad (3.1)$$

where the correlation coefficient S_X is computed via the covariance matrix σ of ΔX and $\Delta \log g$ obtained from the RAVE data:

$$S_X = \frac{\sigma_{12}^2}{\sigma_{11}^2} = \frac{d\Delta X}{d\Delta \log g}. \quad (3.2)$$

We find $S_{T_{\text{eff,dwarfs}}} = 531$ K, $S_{T_{\text{eff,giants}}} = 122$ K, $S_{[M/H],dwarfs} = 0.132$ and $S_{[M/H],giants} = 0.155$. We have to take into account that these correlations already went into the uncertainties of the parameter estimates. We therefore reduce the uncertainties by multiplying with the ratio of the standard deviations of ΔX that we find before and after subtracting the correlations. For giants (dwarf) stars the scatter in the effective temperature is reduced to 87% (67%) and in metallicity to 76% (93%) of the original value. The computed shifts $e_{\text{bias}}(X)$ are then combined to the random value $e(X)$ drawn from the Gaussian distribution of width $u(X)$ and added to the original value of X .

In addition to the internal uncertainties which reflect the analysis pipeline’s ability to chose the correct linear combination of model spectra, there are external uncertainties which are determined by comparing the derived parameters with external reference estimates obtained via different observations and analysis techniques. Kordopatis et al. (2013) quantify the deviations for different types of stars (see their Table 3) with an additional standard deviation σ_{ext} . However, for the surface gravity estimates systematic shifts can be found (Figures 6 & 10 in Kordopatis et al. (2013)) which imply a general underestimation of ~ 0.5 dex for giants (reference $\log g \lesssim 3$) and a more complex systematic behavior for stars with higher surface gravity. The sample of reference observations is a compilation of (inhomogeneously analyzed) literature values, but the behavior is consistently observed in all homogeneous sub-sets. A further hint that this systematic is intrinsic to the RAVE data comes from a comparison with APOGEE observations of a number of RAVE stars revealing very similar trends in $\log g$ (M. Steinmetz, C. Chiappini & F. Anders, private communication).

We also add errors to the phase space coordinates of the stars. We consider the uncertainties in the angular positions to be negligible and the three velocity components to have uncorrelated Gaussian errors. The deviations in the distances, d , are more complicated to model, however, since these are derived on the basis of the stellar parameters (and apparent magnitudes) of the stars. Therefore the distance errors are strongly correlated with the errors in these parameters. Ideally, the distances of the mock stars would be recomputed using the error-prone stellar parameters and the same methodology of Binney et al. (2014) as the distance estimates in RAVE. Here, we use the simple approach we already used for the stellar parameters: we assume Gaussian errors in the parallaxes $\varpi = 1/d$ of the stars and use the individual uncertainties provided by Binney et al. (2014). Note that the authors explicitly showed via a comparison to a sample of Hipparcos stars that the probability distributions are close to Gaussian for the *parallaxes*. As the bottom panel of Figure 3.1 illustrates the relative uncertainties are predominantly below 30%, except for the sub-giants with high metallicities. To reproduce this behavior we bin the RAVE data in the $T_{\text{eff}} - \log g$ -plane with bin widths of 500 K and 0.25 dex. Then we associate uncertainties of RAVE stars to the mock stars in corresponding bins.

We again searched for correlations of the parallax and stellar parameter estimates using the RAVE repeat observations. Only for the surface gravity, we found a significant correlation (cf. Figure 3.2, right panel) of $0.272\% \text{ dex}^{-1}$ for the relative parallax differences. We take this into account by shifting the parallax values accordingly and rescaling the uncertainties by a factor of 0.67, which is, as above, the ratio of the standard deviations in the parallax differences before and after removing the correlation.

3.1.3 Stellar parameter dependent selections

The RAVE sample described above is used to evaluate the completeness $S(l, b, I_{2\text{MASS}}, J - K_s)$ w.r.t. the 2MASS catalog. As a next step we have to take into account that the RAVE spectral analysis pipeline does not deliver reliable results for all types of stars. For the estimates of the stellar parameters from the DR4 pipeline clear limits were defined beyond which the derived values are not reliable anymore (Kordopatis et al. 2013) and hence should not be used for our purposes. The limits are

$$\begin{aligned} 0.5 &\leq \log g \leq 5 \text{ dex}, \\ 3800 &\leq T_{\text{eff}} \leq 8000 \text{ K}, \\ -5 &\leq [\text{M}/\text{H}] \leq 0.3 \text{ dex}. \end{aligned} \tag{3.3}$$

Furthermore all stars with

$$\begin{aligned} T_{\text{eff}} &\leq 4250 \text{ K} \quad \text{and} \quad \log g \leq 4.5 \text{ dex} \\ &\quad \text{or} \\ T_{\text{eff}} &\geq 6250 \text{ K} \quad \text{and} \quad \log g \geq 4.5 \text{ dex} \end{aligned} \tag{3.4}$$

were removed from the mock stellar sample, because these parameter combination were excluded from the solution space of the RAVE spectral analysis pipeline (Kordopatis et al. 2013). These restrictions can not be included in the photometric selection function, because they require knowledge on the targets which is not provided by the photometric input catalogs, but is available only *after* the observation is made. Therefore we cannot include it in the selection procedure described in Section 2.1. However, these limits have to be taken into account when comparing a mock catalog to the RAVE data and so we have to remove them from the mock stellar sample after the completeness matching.

First, we identify all stars that were classified to be 'normal' stars according to the classification scheme by Matijević et al. (2012) (c1 – c6 are all 'n'). This excludes objects with peculiar spectra which are likely not well fit with the RAVE synthetic spectral library. Reasons for this range from trivial things like problems in the continuum fit of the spectrum, over double-peaked absorption lines implying a spectroscopic binary to more problematic cases like spectra with emission lines at the centers of the absorption lines, so-called chromospheric activity. The last point is problematic in the sense that chromospheric activity is believed to correlate with the stellar age (Mamajek & Hillenbrand 2008). This implies that by selecting against these stars we might introduce an age bias into our sample. For the moment there is, however, not enough information to do a detailed selection, e.g. as a function of age, for these stars and we have to accept this source of uncertainty for the time being. We refer the reader to Žerjal et al. (2013) and Matijević et al. (2012) for more extensive studies of these stars. Preliminary tests (e.g. removing a fraction of the youngest stars from the mock samples) indicated that there is no clear way to include this effect into the modeling, but also that this effect does not present a major uncertainty. More comprehensive investigations are planned for future work. We evaluate the fraction of 'normal' stars in each $(l, b, I_{2\text{MASS}})$ -bin of our RAVE sample and randomly reduce the number of stars by this factor in the corresponding bin in the mock survey.

The DR4 pipeline uses two methods to derive the astrophysical parameters of a spectrum: DEGAS and MATISSE. The former is a decision tree algorithm that searches for the closest point on a discrete grid of model spectra and is used to provide starting values for MATISSE. The latter is a machine-learning algorithm that interpolates between the spectral grid points

via a projection method to provide more accurate stellar parameters. A more detailed description of the pipeline can be found in Kordopatis et al. (2013) and references therein. If the DEGAS estimate lies outside of the MATISSE learning grid of synthetic spectra or $S/N \leq 35$, the DEGAS values are listed in the data base. We want to use only observations for which MATISSE converged (`Algo_conv_k = 0`), because the DEGAS values are concentrated on discrete points in the parameter space at the points of the grid of synthetic spectra. We introduce this selection into our mock survey in the same way as we did for the spectral classification criterion by reducing the number of mock stars in each $(l, b, I_{2\text{MASS}})$ -bin to the fraction of successful MATISSE estimates in the corresponding bin for the RAVE data. We can summarize our generation process as follows:

1. Definition of the RAVE input sample using photometric and data quality criteria.
2. Evaluation of the completeness in $(l, b, I_{2\text{MASS}})$ -bins.
3. Application of the $J - K_s$ color cut to the all-sky survey of mock stars generated via GALAXIA
4. Random selection of mock stars matching the completeness in the same $(l, b, I_{2\text{MASS}})$ -bins.
5. Adding observational errors on the stellar parameters of the mock stars.
6. Removing real and mock stars from the samples in those regions in the parameter space than cannot be reliably analyzed by the RAVE analysis pipeline.
7. Identification of those RAVE stars in each $(l, b, I_{2\text{MASS}})$ -bin for which the MATISSE part of the RAVE analysis pipeline did not converge or that are not 'normal' according to Matijević et al. (2012) and randomly remove the same fraction of mock stars in this bin.

The ordering of these selection steps is important while modeling the impact of the analysis pipeline as closely as possible. The final number of stars in our RAVE sample after all these cuts is almost 150 000 or 35% of all stars observed by RAVE.

3.2 The GALAXIA/Besançon model

The GALAXIA code is, generally speaking, a frame-work for the generation of stellar populations according to any model of the Galaxy and the user is free to provide her or his own model. The original version of GALAXIA also provides a Galaxy model, which is in most aspects identical to the popular Besançon model by Robin et al. (2003). Sharma et al. (2011) illustrate that the model reproduces well the magnitude distributions of the Besançon model as well as the properties of the Hipparcos stars and gives a reasonable fit to the kinematics of the Geneva-Copenhagen survey (Nordström et al. 2004).

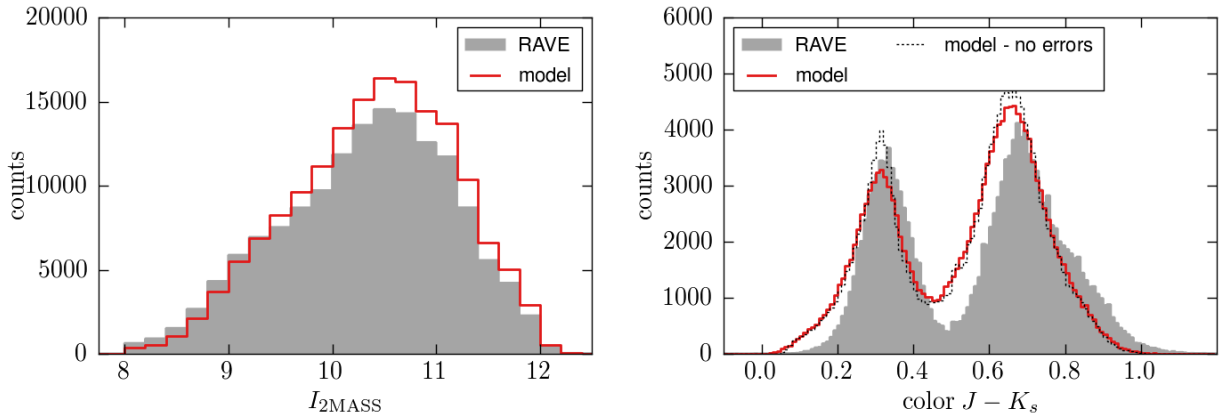


Figure 3.3: *Left panel:* $I_{2\text{MASS}}$ distribution in the mock survey (red line) and the RAVE input sample (gray area). The mock sample was selected to follow the $I_{2\text{MASS}}$ distribution of the input sample using the same bins in $I_{2\text{MASS}}$ as in the figure. Deviations appear because we are matching the completeness of the sample instead of the exact number counts in each bin. *Right panel:* Comparison of the $J - K_s$ color distributions in the model (red line) and the real RAVE input sample (gray area). No observational errors were added to the mock data, because the uncertainties in the 2MASS photometry are better than 1% in the relevant magnitude range and hence negligible for our purposes.

3.2.1 General description of the model

The Galaxy model is described in detail in Sharma et al. (2011) and Robin et al. (2003). In particular, the details of the distribution functions in the model can be found in the Tables 1 – 3 in Sharma et al. (2011). Here we provide only a brief summary and highlight a few details that we will refer to in the later analysis.

The Galactic disk is modeled as a superposition of isothermal populations with flattening, velocity dispersion and mean metallicity being functions of age. The model also contains a discrete thick disk component with a constant scale height and age, a spheroidal component, representing the stellar halo and the classical bulge, and a central bar. The metallicity distributions are modeled as Gaussian functions. The thin disk population spans over mean metallicities from +0.03 dex down to -0.37 dex at the solar radius. It is the only component with a Galactocentric radial metallicity gradient ($d[M/H]/dR = -0.07$ dex). The thick disk and the halo have mean metallicities of -0.78 dex and -1.78 dex, respectively. The circular velocity at the solar radius is 226.84 km s^{-1} . It is important to mention that the velocities are assigned without regard of the metallicity of the stars. The latter has important effects when we look for correlations between more general orbital properties of the stars and the chemistry (see at the end of this section).

We will now use this model to generate a mock RAVE survey as described in the previous section. The distribution functions are based on Robin et al. (2003), so the model could be seen as the summary of the knowledge of the Galaxy at the time when the first RAVE spectra were taken. It is thus very interesting to check whether the model correctly predicts the general properties of the RAVE data.

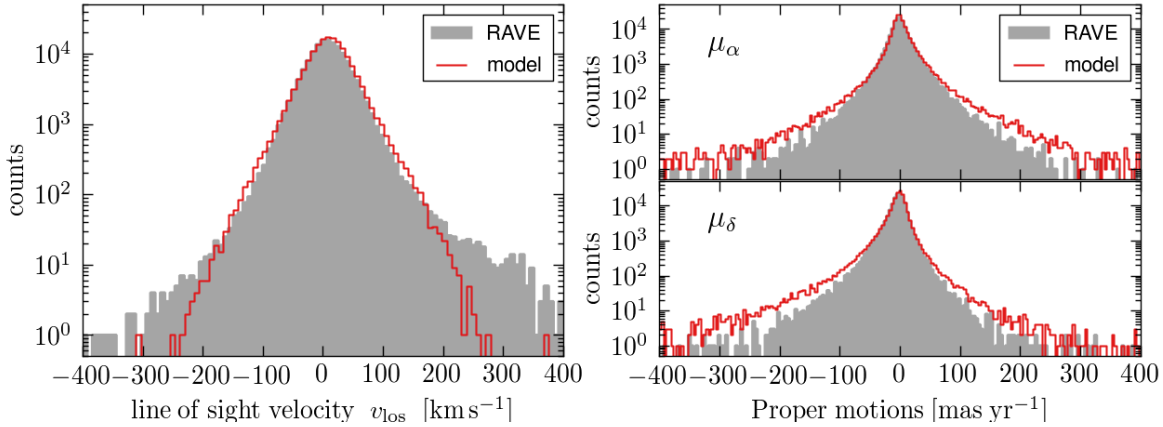


Figure 3.4: Comparison of the velocity distributions in the model (red line) and the real RAVE input sample (gray area). The medians of the v_{los} distributions are 9.3 km s^{-1} and 7.4 km s^{-1} and the regions containing 90% of the data are $[-51, 70] \text{ km s}^{-1}$ and $[-50, 69] \text{ km s}^{-1}$, respectively. The right panels show the proper motions.

3.2.2 Comparison to RAVE

For a faint (un-reddened) magnitude limit $I < 14 \text{ mag}$ and all-sky coverage GALAXIA produces a catalog with 86 million stars. This is our mock input catalog equivalent to 2MASS for the real RAVE survey. Applying our selection procedure as described above we obtain a list of almost 165 000 mock stars which compares very well to the number of RAVE stars in the input sample. Note that this is a non-trivial result, because the GALAXIA model was not tuned to match the 2MASS data.

Figure 3.3 compares the $I_{2\text{MASS}}$ magnitudes and colors $J - K_s$ of the mock and the real data sets. These two quantities are not measured by RAVE, but come from the input catalog. The magnitude distribution should be similar by construction, but does not necessarily match perfectly, because we selected our mock sample to reproduce the completeness and not the exact number counts in each magnitude bin. The $J - K_s$ color distributions of the real and the mock survey also agree relatively well. The deviations suggest that the model is deficient of cool stars with $J - K_s \gtrsim 0.8$ and an over-abundance at intermediate temperatures around $J - K_s \simeq 0.5$ and of very hot stars with $J - K_s < 0.25$.

Velocities The most robustly measured quantities in the RAVE survey itself are the line-of-sight velocities, v_{los} , and in addition we have proper motions from the UCAC4 catalog Zacharias et al. (2013) for almost all RAVE stars. To directly compare the velocities in the mock and real data sets we need to define the solar motion. For the solar peculiar motion we use the values from Schönrich et al. (2010): $U_{\odot} = 11.1 \text{ km s}^{-1}$, $V_{\odot} = 12.24 \text{ km s}^{-1}$ and $W_{\odot} = 7.25 \text{ km s}^{-1}$. The local standard of rest, v_{LSR} , is the circular speed at the solar radius. For the Besançon mass model we have $v_{\text{LSR}} = 226.84 \text{ km s}^{-1}$.

In the left panel of Figure 3.4 we examine the line-of-sight velocities. Their distributions agree well for small absolute velocities, but the model under-predicts the number of stars for $|v_{\text{los}}| > 160 \text{ km s}^{-1}$. Note that the model exhibits a similar trend in the skewness of the distribution showing a slightly extended tail at positive v_{los} . The RAVE stars with $v_{\text{los}} > 300 \text{ km s}^{-1}$ are mainly counter-rotating or non-rotating metal-poor giant stars. These features identify them clearly as halo stars and we hence conclude that the stellar halo is

under-represented in the model.

The median v_{los} of the mock and the real sample differ by about 2 km s^{-1} . With the large sample sizes this difference is likely not the result of Poisson noise (the uncertainty of the mean value is 0.14 km s^{-1}), but reflects a mismatch between the model and the data. The value is comparable to the total uncertainties on the solar peculiar motion Schönrich et al. (2010) and considering the large uncertainties on the value of v_{LSR} we see it as a good match. If we only vary V_{\odot} , which is because of the asymmetric drift the most uncertain component of the solar peculiar velocity, we find a best match for $V_{\odot} \simeq 16 \text{ km s}^{-1}$, or a total azimuthal velocity of the Sun w.r.t. the Galactic center, $V_{\text{LSR}} + V_{\odot}$, of 243 km s^{-1} . We note, however, that this estimate relies on the circular speed curve to be correct, because of the large spatial volume covered by the RAVE stars. There are already several attempts to constrain the solar motion from RAVE data (Coşkunoğlu et al. 2011; Pasetto et al. 2012b; Golubov et al. 2013) that use a more dedicated analysis technique and that find lower values for V_{\odot} than ours. Our value is however still smaller than the 26 km s^{-1} recently reported by Bovy et al. (2012a) and broadly consistent with the value of 14 km s^{-1} by Schönrich (2012).

The proper motion distributions (right panels in Figure 3.4) are matching equally well with the median values differing by less than 0.01 mas yr^{-1} in μ_{α} and 0.45 mas yr^{-1} in μ_{δ} . Here the model produces broader distributions in both directions for $|\mu_i| > 50 \text{ mas yr}^{-1}$. Such large proper motions can only arise from nearby stars and this is confirmed by the stellar parameters revealing that these are relatively metal-rich dwarf stars. Deviations for the velocities of the giant stars as observed for the line-of-sight velocities are hidden in the peak at zero proper motion, because of the typically large distances of these stars.

Stellar parameter distributions We now move on to higher order analysis products, namely the stellar parameters estimated by the RAVE spectral analysis pipeline. In Figure 3.5 we compare the mock and distributions of the effective temperature T_{eff} and the surface gravity $\log g$.

The mock temperature distribution fit the data quite well at low and very high values, but the central minima do not agree. It is important to note that the positions of the peaks in the mock data are determined to a large degree by the stellar isochrones used during the generation of the stars. Especially the low temperature peak is strongly constrained by the location of the giant branch. Significant shifts can only result from drastic changes in the metallicity distribution. The high temperature peak has an additional dependency on the age distribution in the sample. It is thus not surprising that we find good agreement for the location of the low temperature peak. The real data shows a much broader peak with the center slightly shifted to lower temperatures by about 200 K. Interestingly, there is a known difference in the temperature scale between RAVE DR4 temperatures and the temperatures measured for the same stars in the Geneva-Copenhagen survey (Kordopatis et al. 2013). The RAVE estimates are on average lower by 170 K, which is broadly consistent with the shift we observe here. The common stars in the two surveys are all dwarf stars, so it is not clear whether this discrepancy is constant for all T_{eff} and $\log g$ values. On the other hand, the comparison of stellar parameter estimates for stars measured in RAVE and in the APOGEE survey (Allende Prieto et al. 2008) reveal an off-set of the RAVE DR4 temperatures to higher values by $\sim 100 \text{ K}$ s (F. Anders & C. Chiappini, private communication).

The mock surface gravity distribution (right panel) appears to be generally shifted with respect to the RAVE distribution by $\sim 0.3 \text{ dex}$. When we correct for the shift we find only relatively small discrepancies. The real distribution has a pronounced tail at low $\log g$ that is not matched by the model. Besides the nearby explanation that the model is not

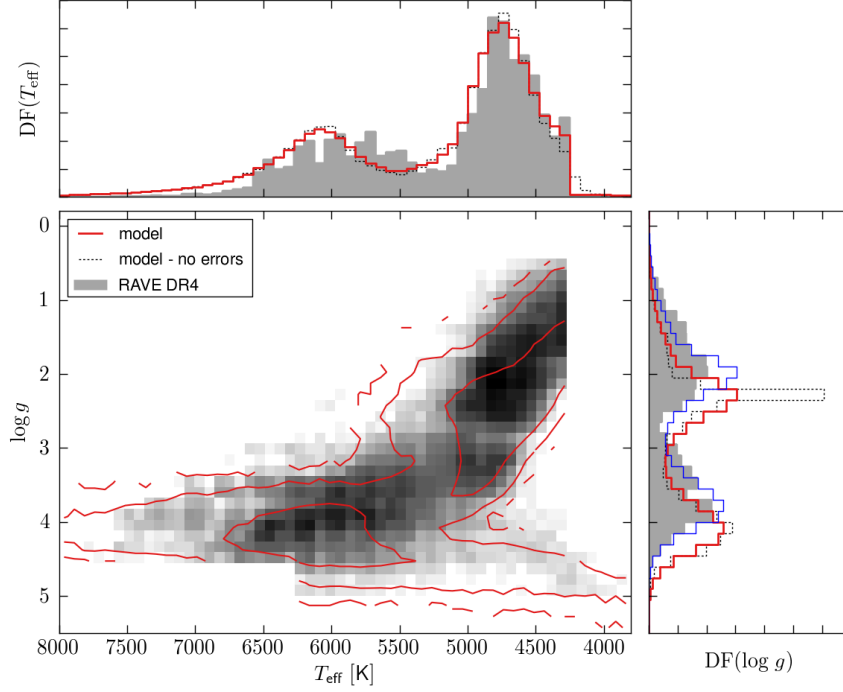


Figure 3.5: Hess diagram of the mock survey (gray scales) and the real data (orange and green contours). The smaller panels show the distribution marginalized over T_{eff} (right panel) and over $\log g$ (top panel). The contour lines in the large lower left panel illustrate the density distributions of the two RAVE parameter sets. The lines mark locations with 3, 30 and 300 stars per $(100 \text{ K} \times 0.1 \text{ dex})$ -bin. The black dotted lines in the two side panels show the mock data before observational errors are added. The thin blue line is the same as the red line, but shifted by -0.3 dex .

correct, this tail could also be an artifact induced by the RAVE analysis pipeline that shows a systematic shift for low $\log g$ values towards even lower values (see Kordopatis et al. (2013), their Figure 10). There is further secondary peak in the RAVE distribution around $\log g \sim 3.3$ is located in the region of cool sub-giants (cf. large panel of Figure 3.5). The gap between this peak and the giant branch is most likely a result of the discretization of the RAVE parameter estimates that is introduced by the DEGAS part of the pipeline (Kordopatis et al. 2013). This gap is most likely also the reason for the shifted location of the central minimum between the giant and the dwarf star peak, even after we corrected for the general shift between model and data.

Metallicity distribution In Figure 3.6 we compare the overall metallicity distributions. The model peaks at too high metallicities, predicts too many stars with metallicities between -0.5 and -1.5 dex and fails to produce the tail to very metal-poor stars with $[M/H]$ below -2 dex . In the right panels we plot the metallicity distributions for two sub-samples of the catalogs, a giant sample and a dwarf sample, that were selected avoiding the overlap $\log g$ zone between 3 and 4 dex. In this way we are not affected by the different $\log g$ scales in the data and the model.

Consistently the giants extend to lower metallicities than the dwarfs. Giant stars are intrinsically brighter stars and are therefore observed at larger distances than the dwarfs in our magnitude limited survey. With increasing distance to the Galactic plane the fraction

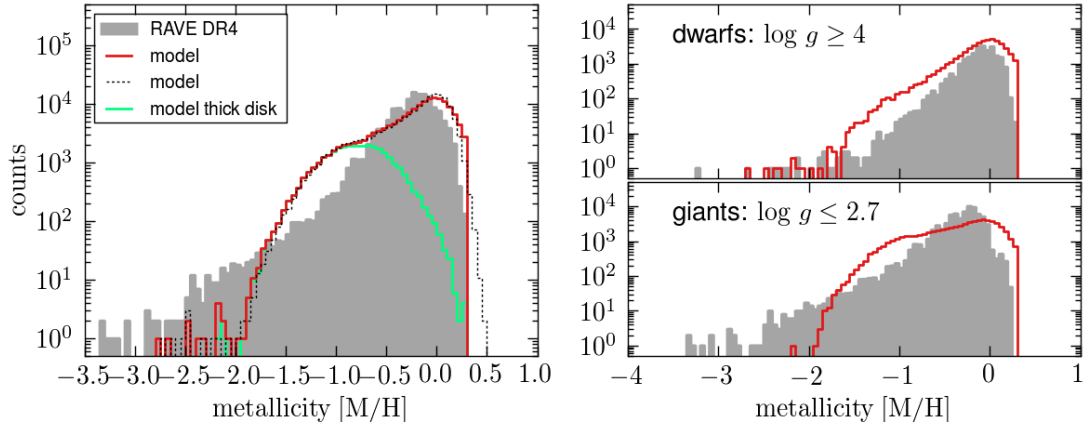


Figure 3.6: Metallicity distributions of the model (red line) and the RAVE input sample (gray area). In the model we have knowledge of the host population of each star. The thick green line shows the metallicity distribution of the stars belonging to the Thick disk population. The dashed black line shows the model before observational error were included.

of Thick disk and halo stars increases. In contrast, the dwarfs sample is confined to regions where the thin disk dominates the population and therefore it becomes less likely that a metal-poor star enters the survey sample. The RAVE giant sample exhibits a qualitatively similar behavior as the model. Both exhibit a more pronounced tail to low metallicities than the dwarf sample.

By construction of the model practically all metal-poor stars belong to either the Thick disk or the halo population (cf. Figure 3.6). A reduction of the mass in these components or a shift of their metallicity distributions to higher values would thus also reduce the disagreement between model and data. The mean metallicity generally appear a bit to low compared to results from observations (Soubiran et al. 2003). More generally we could speculate that the discrepancy could be a hint that the division into a thick and thin disk component might be too simplistic as proposed recently by Schönrich & Binney (2009) and Bovy et al. (2012b). The aim of this work is the evaluation of the existing model, which was adjusted to and is fitting many other observational constraints (Sharma et al. 2011; Robin et al. 2003; Reylé et al. 2009), so we do not attempt to improve it at this stage.

However, the distribution functions of the model are not the only uncertain ingredients to our mock sample. In particular the Thick disk and the stellar halo host predominantly old populations (age > 10 Gyr). Both, observations (e.g. Fuhrmann 2011) and the theoretical considerations on chemical evolution of the inter-stellar medium show that such old stars usually have enhanced abundances of α -process elements and follow different evolutionary tracks than stars with solar chemical composition. GALAXIA neither assigns values for $[\alpha/\text{Fe}]$ to the mock stars nor would such values have an effect, because the stellar evolutionary tracks implemented into GALAXIA were all computed for zero α enhancement.

Distances Finally we can also compare the distance distributions in the two samples. The distances for the real RAVE sample are spectro-photometric parallaxes derived by Binney et al. (2014). This method takes the star’s apparent magnitudes in the J , H and K_s bands and the astrophysical stellar parameters as the input. Therefore we deal with a *secondary* data analysis product. The two panels in Figure 3.7 compare the mock and the real distance and parallax distributions. While the RAVE data shows a slight dip around 500 pc (2 mas),

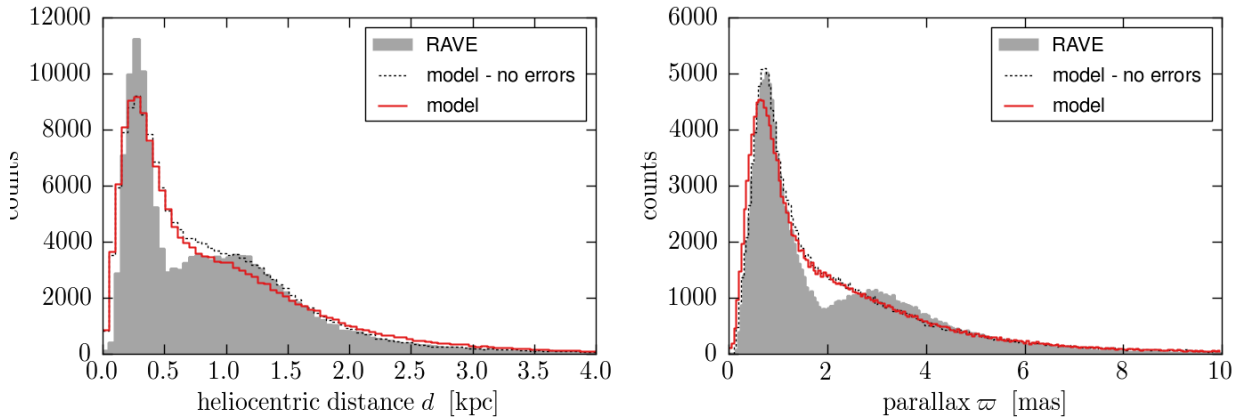


Figure 3.7: *Left panel:* Comparison of the heliocentric distance distributions in the model (gray) and the real RAVE input sample (blue line). The black histogram show the mock data without observational errors added. *Right panel:* Same as the left panel, but with the parallaxes, $\varpi = 1/d$.

this dip is degraded to a kink of the mock data. The fact, that the dip is visible in the RAVE data, even though these data are also carrying observational errors, could be caused by two problems: (1) the dip is actually much more prominent and simply not accurately reproduced by the model or (2) the dip is a result of the discretization of the RAVE stellar parameter estimates. Since the distances and their uncertainties were confirmed by Binney et al. (2014) by comparing the spectro-photometric parallaxes to parallaxes directly measured by the Hipparcos satellite, a combination of both issues seems to be the most likely explanation.

3.2.3 Correlating dynamics and chemistry

Boeche et al. (2013b) used RAVE measurements of dwarf stars with high S/N to investigate radial metallicity gradients in the Galactic disk as a function of height above the Galactic plane. To interpret the result it was crucial to understand the role of the selection effects in the data. For this an equivalent mock sample based on the GALAXIA/Besançon model was used. The generation of the mock data was the contribution of the author of this thesis to the paper and the focus will hence lie on the comparison of the model with the data. Through this comparison insights on the relation of the measured and the intrinsic gradient of the stellar population were be obtained and the limits of the Besançon model were brought to the surface.

The vast majority of the stars observed by RAVE have a heliocentric distance < 2 kpc (cf. Figure 3.7). Among those, the dwarfs stars peak at a distance of ~ 300 pc and do not reach further than 1 kpc. To be able to measure gradients more robustly Boeche et al. computed the guiding radii, R_g , for all stars in their sample. The guiding radius of a star is defined as the radius of circular orbit around the Galactic center that has the same (specific) angular momentum L_z as the star. The idea was thus to use the available information about the kinematics of the stars to infer the mean properties of regions in the disks outside the survey volume.

The RAVE sample was further divided to study the evolution of the gradients as a function of height above the Galactic plane. For the same reasons as above this division was done according to Z_{\max} , the maximum distance of the star to the Galactic plane along the orbit,

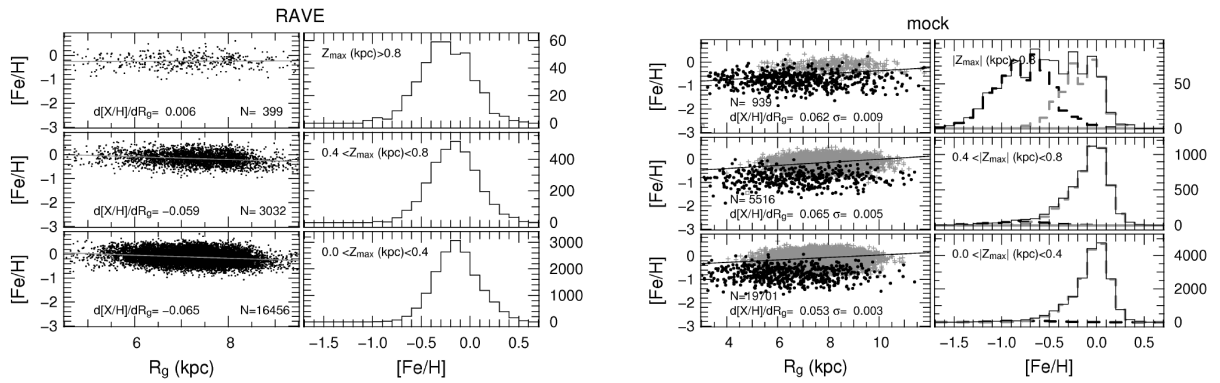


Figure 3.8: *Upper panels:* Distributions of dynamically selected RAVE samples of dwarf stars in the $([Fe/H], R_g)$ plane (left column) and marginalized over R_g (right column). The different rows show samples selected in intervals of Z_{\max} as indicated in the panels in the right column. In the left column the number of data points, N in the panel and the best fitting abundance gradients are given. *Lower panels:* Same as the upper panel, but for a mock stellar sample based on the GALAXIA/Besançon model. The gray and black symbols in the left column distinguish stars belonging to the thin and thick disk, respectively. Both figures were taken from Boeche et al. (2013b), their Figure 3, bottom panels.

instead of the present-day z -coordinate of the stars. The upper set of panels in Figure 3.8 shows the resulting gradients for three intervals in Z_{\max} .

The mock sample was created the same way as described above. Two additional quality criteria on the spectra were imposed that were not taken into account for the mock sample. These relate to the RAVE chemical pipeline (Boeche et al. 2011) and ensure that the pipeline provided a reasonable fit ($\text{chisq}_c < 2000$) and that a large enough fraction of the spectrum could be used for the fit ($\text{frac}_c > 0.7$). Since these criteria are not related to the intrinsic properties of the stars, neglecting them should not have a significant effect on the results.

The lower set of panels in Figure 3.8 shows the mock data and the gradient fitting results. The measured gradients are positive for all Z_{\max} interval and thus clearly incompatible with the results from the real data. It is important to note, that the intrinsic abundance gradients in the model are *negative* (thin disk) or zero (other components). A positive gradient therefore cannot be attributed to an erroneous metallicity distribution function in the model, but must be the result of more subtle effects in the target selection and the analysis strategy.

In the model it is possible to trace back which Galactic component which each star belongs to. As expected almost all stars in the sample are associated with either the thin or the thick disk. In Figure 3.8 this is illustrated by gray (thin disk) and black dots (thick disk and stellar halo). Dissecting the model data into thin and thick disk stars reveals that the total positive gradient is the outcome of a combination of selection effects and the usage of the guiding radius R_g , or, more generally spoken, the finite survey volume and the usage of a dynamical quantity: the increase in radial coverage gained by using R_g instead of the actual positions of the stars reflects the internal (radial) velocity dispersion of the stellar population. For a spatially confined population we further expect a systematic shift to R_g lower than the mean radial position of the stars for the same reasons that give rise to the asymmetric drift, namely that more stars visit the solar neighborhood from the inner Galaxy than from out regions, simply because of the decrease of the mass density with radius. In fact, we see this effect in the model, because the asymmetric drift is explicitly taken into

account during the assignment of velocities in the modeling process. This systematic shift is increasing with the velocity dispersion of the population, i.e. is larger for thick disk stars than for the dynamically cooler thin disk population. In combination with the lower metallicity of the thick disk population this produces a rising metallicity as a function of R_g . Note that the velocity dispersion-metallicity relation within the thin disk population leads to the same effect on a smaller scale.

The question remains why this is not observed in the real data? The most likely explanation for this is that there are correlations between the dynamics and the metallicities of the real stellar population that weaken or even prevent the effects described above and that are not taken into account in the model. A major weakness of the GALAXIA/Besançon model is that the metallicities are assigned randomly to the stars without considering their kinematics. This means that a star has the same metallicity probability DF irrespective of whether it originates (kinematically) from the inner or the outer Galaxy.

In the real data we expect such correlations as a result of the (negative) chemical abundance gradient in the ISM. If we neglect radial migration, for stars on close to circular orbits R_g could be identified with the birth radius of the star. A measurement of the radial abundance gradient as a function of R_g would then directly provide the abundance gradient in the ISM at the time of birth of these stars. However, in the presence of radial migration (Sellwood & Binney 2002) the measured gradient in the stellar component is most likely flatter than the initial gradient in the ISM. The reason for this is that stellar migration is a stochastic process and as such has to increase the entropy of the system.

The GALAXIA/Besançon model as well as the original model provide an excellent description of the Galaxy in terms of mass and light distributions. Also the velocity distributions generated by the model present reasonable approximations to observations. However, if it comes to more subtle properties of the stellar populations such as the chemodynamical correlations discussed above, the model clearly fails. With large number of massive spectroscopic surveys like RAVE and SEGUE that are already available today and even more ambitious projects like Gaia and 4MOST on the horizon there's a clear need for a more sophisticated model. In the next section we will explore a new model of the Galaxy that promises to naturally incorporate correlations of age, metallicity and kinematics. This model, however, comes with the price that we have to leave the domain of analytic distribution functions.

3.3 The chemodynamic MCM model

In the last section we reached the limits of the Besançon model while examining correlations between dynamics and chemistry of the model stars. With the advent of massive spectroscopic surveys like RAVE, the Gaia-ESO survey, SEGUE or APOGEE and in the near future HERMES and Gaia, such a model is clearly insufficient. Minchev, Chiappini, & Martig (2013a) presented a new type of model of the Galaxy which combines a cosmological simulation of disk galaxy formation with a semi-analytic model of the chemical evolution of the Milky Way. We refer to this as the MCM model. The general idea behind the approach is to profit from the realistic modeling of the dynamical processes in spatially resolved simulations of galaxy formation and evolution as well as from the flexibility of semi-analytic models in which the influence of the input parameters are well understood and which are computationally very cheap. In particular, the effects of radial migration (Sellwood & Binney 2002; Minchev & Quillen 2006; Minchev & Famaey 2010) on the distribution of chemical elements

in the Galaxy should be well taken into account by this technique.

The model has been shown to be compliant with a range of observations, for example, the metallicity distributions of data at different proximity to the Sun or the mean metallicity variation with distance from the disc plane (Minchev et al. 2013a). However, these comparisons were done taking into account the selection effects in a very rough way and, in particular, without selecting on observational quantities. Here we test and analyze the model for the first time in a more sophisticated manner.

3.3.1 General description of the model

The technique to produce the MCM model can be summarized as follows: a simulation of the formation and evolution of a Milky-Way like disk galaxy is run using a numerical scheme which at minimum has to include star formation. Then, as a post-processing step, the star particles get assigned metallicities according to their birth time and place in the galaxy according to an independent theoretical distribution function $f_Z([X_0/H], \dots, [X_N/H], \mathbf{r}_{\text{birth}}, \tau)$, where X_i is an arbitrary chemical element, or isotope, out of the N chemical elements one might consider. So, ideally the (stellar) mass distribution function, i.e., the mass density of stars as a function of position (\mathbf{r}), velocity (\mathbf{v}), age (τ) and metal abundances ($[X/H]$) could be written like

$$\begin{aligned} f &= f(\mathbf{r}, \mathbf{v}, \tau, [X_0/H], \dots, [X_N/H]) \\ &= f_{\text{pos}}(\mathbf{r}, \tau) f_{\text{vel}}(\mathbf{r}, \mathbf{v}, \tau) f_Z([X_0/H], \dots, [X_N/H], \mathbf{r}_{\text{birth}}, \tau), \end{aligned} \quad (3.5)$$

in analogy to the last three terms in Eq. 2.8 for the GALAXIA code. The phase space distribution $f_{\text{pos}} f_{\text{vel}}$ represents the simulation results. The knowledge and consistent use of the birth time and birth place $\mathbf{r}_{\text{birth}}$ of each star over models like the Besançon model or TRILEGAL.

In practice, f_Z is the outcome of the chemical evolution model for the Galactic thin disk by Chiappini (2009), which was designed to recover the chemical trends observed in the Milky Way. This model computes the chemical evolution of the inter-stellar medium (ISM) as a function of time and projected Galactocentric radius $R = \sqrt{x^2 + y^2}$. It assumes exponentially declining smooth gas accretion and a star formation law which is dependent of the local gas surface density and R . The latter account for the effect of an inside-out formation of the disk. For the computation of the chemical feedback by the stars to the ISM a stellar initial mass function had to be assumed. Chiappini opted for the functional form proposed by Scalo (1986),

$$\xi(M) = \begin{cases} A_1 M^{-2.35} & \text{for } M \leq 2 M_{\odot}, \\ A_2 M^{-2.70} & \text{otherwise,} \end{cases} \quad (3.6)$$

where $A_1 = 0.19$ and $A_2 = 0.24$ are normalization constants. Chiappini (2009) also present a model for the thick disk, but this was ignored in MCM model to test whether the dynamic evolution in the simulation already results in a thickened low-metallicity component without explicitly including it in the modeling.

Both, the chemical evolution model and the cosmological simulation provide a star formation history (SFH). Minchev et al. opted for the SFH of the chemical evolution model and choose a simulation with a reasonably similar SFH. In cases where the star formation rate (SFR) is too high in the simulation, only a random subset gets ages and metallicities assigned while

the excess particles are ignored. In the opposite case, if the SFR in the simulation is too low at a given radius R , star particles at similar R and with similar kinematics as the newly born star particles, are selected and get a new age, metallicities (and also a new birth radii) assigned. This means that some particles in the simulation are used multiple times during the process. These are then treated as two independent particles. In other words, the exact SFH of the model is implemented into the simulation outcome and as a result the phase space distribution is slightly altered. This should not have a major affect, because if the system is close to equilibrium, i.e. evolving only slowly, to a good approximation stellar and gas mass can be exchanged in the simulation without changing the dynamics (I. Minchev, private communication).

The simulation used in the model contains a barred late-type spiral galaxy taken from the suite of 33 simulations presented by Martig et al. (2012). The authors report a gravitational softening of 150 pc as the spatial resolution and a stellar particle mass of $7.5 \times 10^4 M_\odot$ as mass resolution. The simulations are “resimulations” of a dark matter-only simulation of a much larger volume. More details concerning the simulation technique are described in Martig et al. (2009, 2012) and references therein.

The simulation was re-scaled according to the following transformations

$$\begin{aligned} \mathbf{r}' &= \mathbf{r}/f_1, \\ \mathbf{v}' &= \mathbf{v} \times \sqrt{f_1/f_2}, \end{aligned} \quad (3.7)$$

with $f_1 = 1.67$ and $f_2 = 1.38$, in order to match the size of the Galactic bar and the circular velocity at the position of the Sun, $v_{\text{LSR}} = 220 \text{ km s}^{-1}$. Generally, scaling transformations are defined in such a way that they preserve the numerical value of the gravitational constant G . To achieve this we would need to downscale the mass of each particle dividing by f_2 . However, because in the metallicity assignment process some particles are ignored and some are use more than once, it does not make sense to use the original particles masses. This was not an issue for Minchev et al., because they did not use the masses, but for our processing with GALAXIA we need an absolute mass for each particle as the normalization of the IMF. In the metallicity assignment process all particles are treated to have the same mass and thus we do the same and define

$$m_{\text{particle}} = \frac{M_{\text{tot},\star}}{N_{\text{tot}}}, \quad (3.8)$$

where $M_{\text{tot},\star}$ and N_{tot} is the total stellar mass and the total number of stellar particles in the model, respectively. We adopt $M_{\text{tot},\star} = 7.8 \times 10^{10} M_\odot$ because, as we will see later, for this value we obtain roughly the right number of stars in our mock survey. Note that because the model is most likely incorrect at small Galactocentric radii, i.e., in the Bulge region, we should not interpret $M_{\text{tot},\star}$ as the actual stellar mass of the Galaxy. A more robust measure would be the stellar surface density Σ_\star in the solar annulus. We find $\Sigma_\star \simeq 42 M_\odot \text{ pc}^{-2}$, which is too large compared to the typical literature value of $30 - 35 M_\odot \text{ pc}^{-2}$ (Bovy et al. 2012b; Flynn et al. 2006, and references therein). We do not consider this a major problem, because $M_{\text{tot},\star}$ only acts as a scaling factor determining the total number of stars entering the mock survey.

Minchev et al. only used mass particles which had a maximum distance $|z|$ to the plane defined by the Galactic disk smaller than 5 kpc in the final snapshot. The chemical evolution model does not account for the stellar halo and thus it would not be appropriate to assign metallicities to particles clearly belonging to this component. Further only particles with a maximum (not yet re-scaled) projected radius $R < 30 \text{ kpc}$ were selected. For our study this latter restriction has an effect only for the mass assignment, because the RAVE survey does

Table 3.1: Processing options for our test mock surveys. The second columns gives the IMF applied, the third column indicates which metallicity was used for the isochrone selection and the last column contains the options for the EnBiD code to compute the softening parameters.

| Label | IMF | Metallicity | Smoothing |
|-----------------|-----------------|-------------|-------------|
| Chabrier | Chabrier (2001) | [M/H] | 6D, 64 ngbs |
| Scalo86 | Scalo (1986) | [M/H] | 6D, 64 ngbs |
| alpha-corrected | Scalo (1986) | [M/H]* | 6D, 64 ngbs |
| 3D-smoothing | Scalo (1986) | [M/H]* | 3D, 32 ngbs |

not observe stars at such large distances.

The original MCM model provided contains 2014 301 stellar particles, some of them located on common phase space positions. RAVE observed only a small fraction of the Galaxy, not only by number of stars, but also by volume. According to Binney et al. (2014) 99% of the RAVE stars have a distance to the Sun below 5 kpc. This implies that also only a small fraction of the particles in the simulation will be considered during the creation of the mock survey and, in particular, only particles from the side of the model galaxy facing the Sun’s position. We can thus increase the resolution of the model by superposing the particle distribution with a copy of itself which was rotated by 180° around the z -axis. In principle, we could stack even more copies by rotating around smaller angles (e.g. 2 copies rotated by 120° and 240°), but this would erase the effect of (even) non-axis-symmetries like the Bar or two- and four-armed spiral patterns.

After this superposition the model contains twice the number of stellar particles and the mass of a single particle, m_{particle} , becomes $1.94 \times 10^4 M_{\odot}$. We can now compute the softening parameter for each particles as described in Section 2.3 and then use our modified version of GALAXIA to produce mock observations equivalent to those already used in Section 3.2 based on the analytic DFs of the Besançon model.

Finally we fixed the position of the Sun, i.e. of the observer, at $R_0 = 8$ kpc with an azimuthal position such that it rotationally lags the central bar by 30°.

3.3.2 The effect of different processing options

As described in Sections 2.3.3 and 2.3.4, for the process of generating the mock survey there are several choices to be made and we want to investigate the effect of our decisions. In particular, we want to understand the effects of our choice of the IMF, the modified law to select the isochrones and the influence of the phase space smoothing. To test this we produced a suite of mock surveys for which we successively move away from the standard GALAXIA routines. The changes in the processing are listed in Table 3.1.

For these test runs we used the original model data without increasing the resolution as described in the last section and the $M_{\text{tot},*}$ was set to $5 \times 10^{10} M_{\odot}$, i.e. a lower value than what was mentioned above. The first difference does not have any influence on the results in this section, while the effect of the second is discussed below.

Influence of the IMF We constructed mock RAVE catalog exactly in the same way as described in Section 3.1. The mock survey based on the Chabrier (2001) IMF contains about 156 000 stars which is too to the 150 000 stars in the RAVE input sample. The rest of the

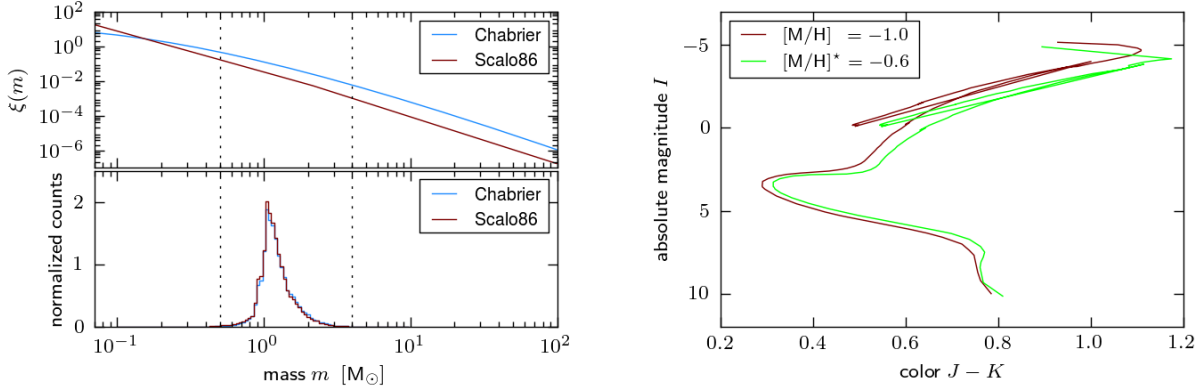


Figure 3.9: *Upper left panel:* The exponential Chabrier (2001) IMF originally used in GALAXIA for the stellar halo and the Scalo (1986) IMF used in our modified version and in the chemical evolution model of Chiappini (2009). The latter was used for our input model. *Lower left panel:* Normalized distribution of stellar masses in the mock surveys. *Right panel:* Stellar isochrones from the Padova set of isochrones in an color-magnitude diagram. Both tracks have an age of 10 Gyr. For a star with $[\text{Fe}/\text{H}] = -1$ and $[\alpha/\text{Fe}] = 0.4$, the original version of GALAXIA would choose the maroon curve while with the new pseudo-metallicity the green curve would be adopted.

test runs are based on the Scalo (1986) IMF and contain only 100 000 stars. Since we are matching the completeness of the RAVE survey in the selection process, this means that the observable stellar densities in the Scalo (1986) case are too low. The reason for the different results can be seen in the left panel of Figure 3.9. For the Scalo (1986) IMF a larger fraction of the mass is in very low mass stars which do not enter the survey sample as can be seen from the bottom panel where the stellar mass distributions for the two cases are displayed. The latter are nearly identical, since the age and metallicity distributions are the same and therefore the same types of stars have the appropriate apparent magnitudes to enter the survey. As a result applying the Scalo (1986) IMF effectively lowers the observable mass fraction of each mass particle in the model. The effect can be balanced by increasing the stellar mass of the Galaxy as a whole.

The stellar parameter distributions for the two cases do not exhibit any significant differences (Figure 3.10). This implies that we suffer from a degeneracy between the choice of the IMF and the total stellar mass $M_{\text{tot},\star}$. In order to be consistent with the assumptions of our input model we stick to the IMF by Scalo (1986) and increase $M_{\text{tot},\star}$ to the value of $7.8 \times 10^{10} M_{\odot}$ for all investigations in later sections. We could optimize $M_{\text{tot},\star}$ in more detail to obtain an estimate for the local stellar surface density, but such an estimate would be highly model dependent and so of limited value.

Influence of the new metallicity criterion As a next step we replace the metallicities with our pseudo-metallicity given in Equation 2.13. We expect significant changes only for the metal-poor stars which typically have a large $[\alpha/\text{Fe}]$ value. Effectively this change results in adopting a stellar track with a higher metallicity. This leads to an increased brightness for main-sequence dwarfs and a decreased brightness for giant stars as can be seen in the right panel of Figure 3.9. The distributions of the effective temperature and the surface gravities remain almost unchanged, except that there are now slightly more dwarfs in the sample.

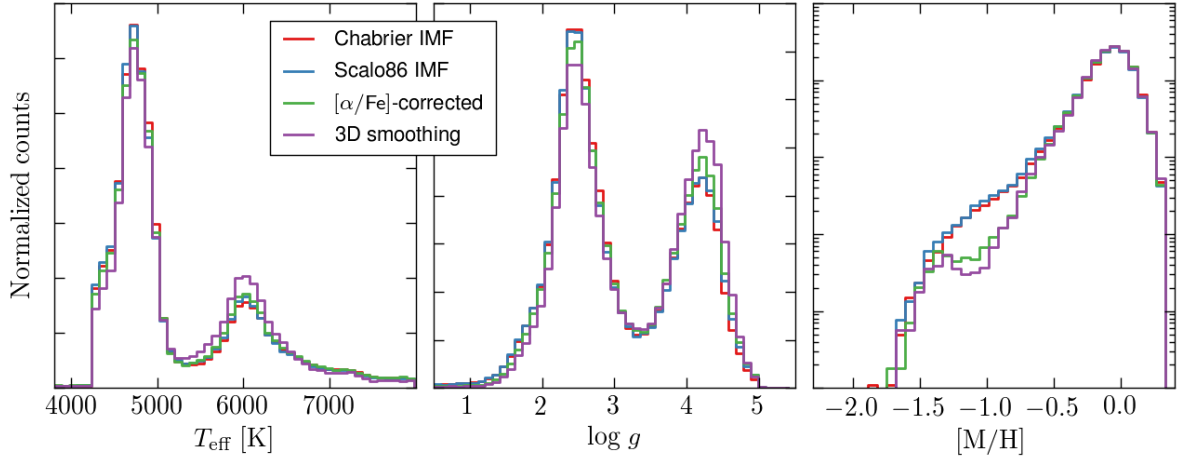


Figure 3.10: Normalized stellar parameter distributions of mock RAVE surveys obtained using different features during the processing. Please refer to the main text and Table 3.1 for a detailed explanation of the differences in the individual set-ups.

We find a significant deviation in the metallicity distribution (see Figure 3.10). There are less stars below $[M/H] = -0.5$ in the 'alpha-corrected' run. A likely explanation for this is that a fraction of the metal-poor giants are moved out of the observable parameter space due to their decreased brightness. This shifts the balance in the mother sample slightly towards dwarf stars which appear thus more abundant in the survey sample.

Influence of the smoothing parameters Finally, we address the effects of the phase space smoothing. Clearly, this processing step leads to a decreased spatial resolution, which is most severe in the direction perpendicular to the Galactic disk, where the scale lengths are comparable or even lower than the spatial softening parameter h_r . This also means that the youngest populations which are also the most flattened ones are affected most.

The effect that matters most for our experiment is that stars might enter the survey sample, which were spawned from particles which are located in regions that were on purpose avoided by the RAVE survey, in particular the immediate disk plane³.

To develop an idea of the extent of this effect we produced a new mock survey '3D-smoothing' for which we used the much lower softening length arising when we only smooth in positional space (cf. Figure 2.5, left panel). Otherwise the survey is equivalent to the 'alpha-corrected' run. The upper panels of Figure 3.11 illustrate the results. We find large discrepancies at low $|z|$ where in the 6D phase space smoothed case (left panels) many host particles are located outside the actual survey volume near $z = 0$ kpc. On the other hand, at large $|z|$ we find a lower but comparable number of host particles outside the survey volume. This is easy to explain if we re-call that in regions with low spatial densities the densities in velocity space must be high (in order to fulfill the collisionless Boltzmann equation). For this reason in such regions the velocity smoothing is negligible and we find similar spatial smoothing length as in the 3D case.

As explained in Section 2.3.4 we use a fixed value for the smoothing in velocity space for all

³Except for some special purpose observations which we neglect for our experiment, RAVE did not observe stars with Galactic latitudes below 5°

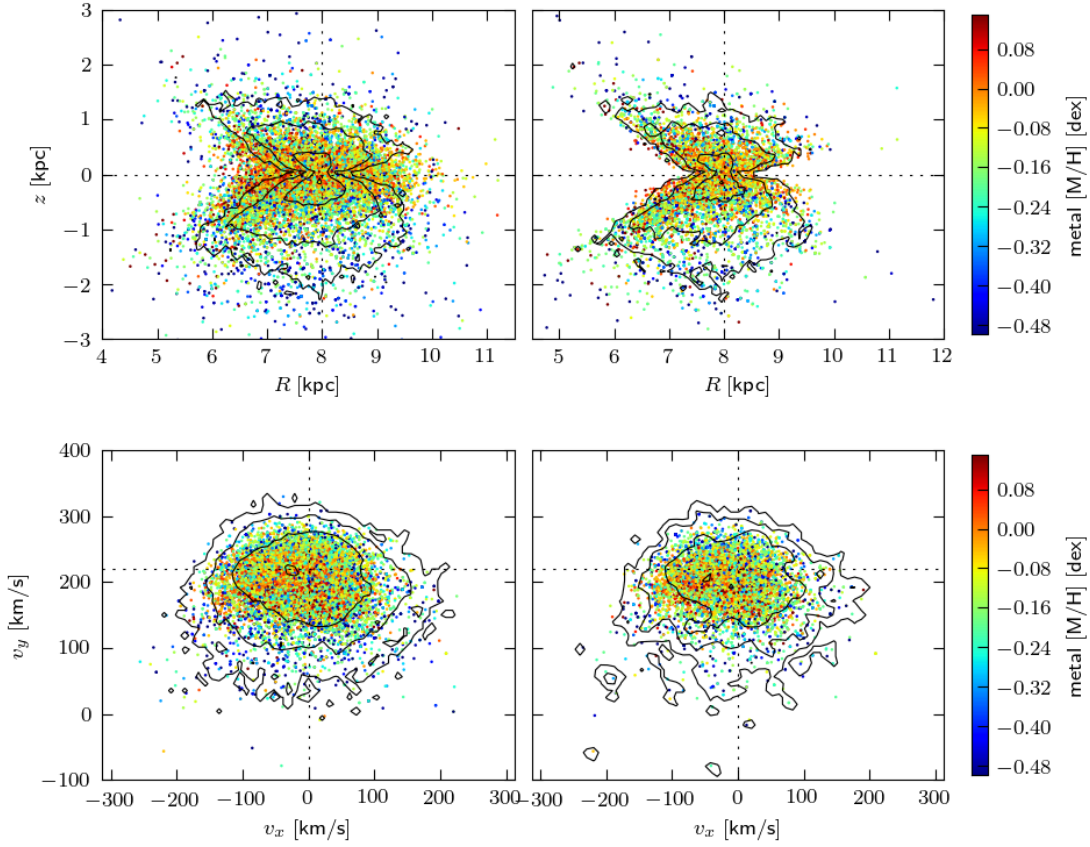


Figure 3.11: The mock RAVE survey volume in the R - z plane (top) and in the v_x - v_y plane (bottom). The black contour lines indicate the number density of mock stars marking locations where the density dropped to 90%, 10%, 1% and 0.1% of the maximum value. The colored dots represent the mass particles from which the stars in the survey sample were spawned. Color-coding represents metallicity. The left panels show the data from a survey created with smoothing in 6D phase space while the data in the right panel was smoothed only in positional space, i.e. with much lower softening lengths.

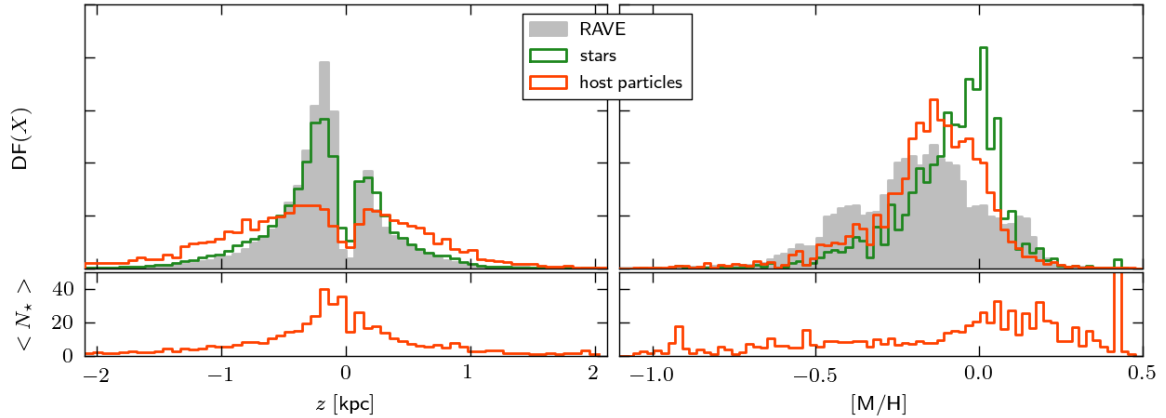


Figure 3.12: Comparison of the distributions of the mock RAVE stars and their host particles (upper panels). The left side shows the distributions vertical to the galaxy disk and the right side shows the metallicity distributions. The equivalent distributions found in the real RAVE data are also plotted for comparison. The lower panels show the mean number of mock stars spawned from a particle in a given z or metallicity bin.

particles. A too low value of h_v would lead to a decomposition of the mock stars into discrete stellar streams, each corresponding to a single mass particle. Similarly, a large value for h_v erases all velocity sub-structure. The lower panels of Figure 3.11 illustrate that the velocity distribution shows much more features in the '3D-smoothing' case than for the full phase space smoothing. The velocities clumps far from the bulk of the survey stars are clearly the result of shot noise. Most of them are due to a single mass particle. This just confirms our expectation that the resolution of the N -body input is too low to allow a study of velocity sub-structure, e.g. induced by non-axis-symmetries as found by Antoja et al. (2012) in the RAVE data. Note that the model is generally not suited for an investigation on stellar streams, because the metallicity assignment process does not differentiate between stars born in the disk from those coming from accreted satellite galaxies.

Our expectation, that the general metallicity distribution would shift to lower values with the smaller softening was not met as can be seen in the right-most panel of Figure 3.10. The metallicity distribution seems to be robust against the softening. Nevertheless, we find significant changes in the $\log g$ and T_{eff} distributions. Clearly, the balance has shifted to dwarf stars for the '3D-softening' case. A large softening length as in the 'alpha-corrected' case flattens out the vertical disk profile. This effectively moves mass away from low $|z|$ to higher values. As a result the density of observable giant stars, which are generally more distant, is increased on the cost of the density of observable dwarf stars. With the smaller softening in the '3D-softening' case this effect is weakened and thus more dwarf stars enter the survey on the cost of the giant population. Since giants are generally cooler stars than dwarfs, this also translates into the effective temperature distribution.

3.3.3 The effect of the RAVE selection function

We have to distinguish the selection function of a survey and the resulting selection effects. The first quantifies the probability for a star to enter the survey sample and should only depend on properties known prior to the actual observations for all possible targets or at least to a clearly defined sub-set of those. The selection effects represent the consequences of

the selection function in terms of biases in the quantities not known or not considered during the sample selection.

One simple way to understand the effects of the RAVE selection function is to compare the properties of the mock RAVE sample with the properties of the particles from which the mock star originated. In this way we compare the statistical properties of the RAVE stars with the statistical properties of the full population residing in the survey volume⁴. Studying these differences is not strictly necessary for our analysis approach, because by comparing the survey data directly with their mock equivalents the effects are automatically taken into account. Yet, uncovering explicitly the relation to the underlying model and what a survey detects from this, helps to sharpen one’s intuition and understanding why a model is successful or why it fails.

When we examine the distribution of heights z above and below the Galactic plane (Figure 3.12, left panel), we immediately see that the mock stars are much more concentrated to lower distances than their host particles⁵. If the same fraction of mass per unit volume was observable over the whole survey volume we would find coinciding distributions. A natural explanation for the discrepancy is coming from the IMF. Most of the mass of a (simple) stellar population is deposited in intrinsically faint low-mass main-sequence stars which are only observable close to the Sun. Our choice of the functional form of the IMF by Scalo (1986) plays only a minor role in this issue, because the RAVE stars are covering only a small interval of the full stellar mass range, where at least the IMFs from Scalo (1986) and Chabrier (2001) have similar slopes (cf. Figure 3.9).

This over-representation of nearby stars strongly influences the metallicity distribution of the survey stars (right panel of Figure 3.12). While the abundance distribution of the particles seems to match well the peak found in the real RAVE data, the distribution of the mock stars is clearly shifted to higher metallicities, similar to what we found for the Besançon model. This strikingly demonstrates the necessity to carefully take into account the selection effects when comparing (or even fitting) a model to survey data. In particular, it is not sufficient to consider only the survey volume without accounting for the type of stars in the sample.

3.3.4 Comparison to 2MASS

The direct output of the GALAXIA processing is an all-sky stellar survey. With the appropriate filter bands this data is ideally suited to do a comparison with the 2MASS catalog. This exercise reveals whether the model also matches the Milky Way in terms of photometric star counts.

The 2MASS survey is an photometric all-sky survey in three infrared filter bands, J , H and K_s . We will use only the K_s band for our comparison, because this should be least affected by extinction. Using the other filter bands give in similar results. In the K_s band 2MASS is complete down to an apparent magnitude of 14.3 mag (Skrutskie et al. 2006). We first look at the magnitude functions in different regions of the sky (Figure 3.13, left panel). Except for the Galactic center region we find good agreement between the model and the data,

⁴This is an approximation. To be exact we would need to weight the particles according to the fraction of their spatial smoothing volume overlapping with the RAVE survey volume. The latter is not trivial to define, however.

⁵Note that the particle distribution does not reflect the real vertical structure of the disk, because the RAVE survey volume has a conical structure growing narrower towards the disk (cf. upper left panel of Figure 3.11). The asymmetry of the stellar distribution with respect to zero is further a result of the varying completeness of RAVE.

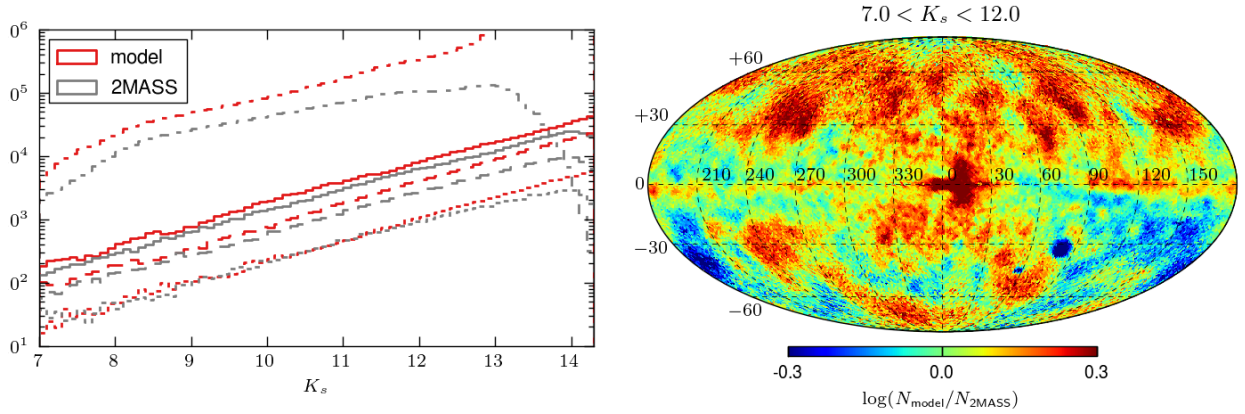


Figure 3.13: *Left panel:* K_s magnitude distribution in four regions of 10 degree diameter on the sky: the Galactic center at $(l, b) = (0^\circ, 0^\circ)$ (dot-dashed lines), the Galactic anti-center at $(l, b) = (180^\circ, 0^\circ)$ (solid lines), a superposition of the two Galactic poles at $b = \pm 90^\circ$ (dotted lines) and a superposition of four intermediate regions at $(l, b) = (\pm 90^\circ, \pm 45^\circ)$ (dashed lines). *Right panel:* Ratio of the star counts in the mock survey and in the 2MASS catalog as a function of position on the sky. Axes are a Mollweide projection of a Galactic coordinate system with the Galactic center $((l, b) = (0^\circ, 0^\circ))$ in the center of the plot. The color scaling is in logarithmic units going from $\log 0.5$ to $\log 2$. Only stars with K_s magnitudes within the limits indicated above the map were considered.

even though the model slightly over-predicts the star counts. In the Galactic center region the model produces 2–3 times too many stars for most magnitude bins. At the faint end ($K_s > 13$) the 2MASS counts drop, most likely because of extinction and crowding issues. The model does not reproduce this behavior which points to the inaccurate modeling of extinction in this region and neglected crowding issues.

The right panel of Figure 3.13 plots the angular distribution of star count ratios of the model and the 2MASS catalog for stars in a small K_s magnitude range. A very patchy structure is visible which originates from the discrete sampling of the mass density distribution by the mass particles in the model. The patchy structure is consistently observable in fainter magnitude ranges (not shown). The two sharp blue spots in the southern hemisphere near $(l, b) = (80^\circ, -30^\circ)$ and $(l, b) = (60^\circ, -45^\circ)$ are the two Magellanic clouds which are not present in the model. This illustrates that a higher mass resolution for an N -body model to compete with star count predictions from a smooth analytic model like the Besançon model if predictions for specific regions on the sky are needed. For similar comparisons of the Besançon model with 2MASS and other photometric data sets we refer the reader to Robin et al. (2003) and Reylé et al. (2009).

3.3.5 Comparison to RAVE

In this section we will again compare the distributions of observables in the model with the real RAVE data. We will specifically focus on the differences seen to the Besançon model, which we use as a reference for a widely used standard model of the Galaxy.

We start again examining the apparent magnitude and color distributions (Figure 3.15).

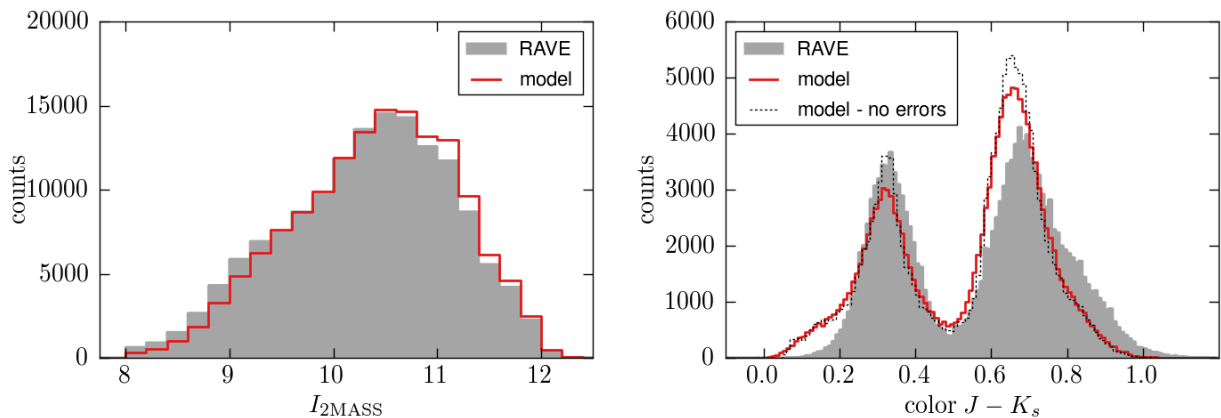


Figure 3.14: *Left panel:* $I_{2\text{MASS}}$ distribution in the mock survey (gray area) and the RAVE input sample (orange line). The mock sample was selected to follow the $I_{2\text{MASS}}$ distribution of the input sample using the same bins in $I_{2\text{MASS}}$ as in the figure. Deviations appear because we are matching the completeness of the sample instead of the exact number counts in each bin. *Right panel:* Comparison of the $J - K_s$ color distributions in the model (gray) and the real RAVE input sample (orange line). No observational errors were added to the mock data.

We find a slight over-abundance of faint targets in the model, but generally a still good agreement. The $J - K_s$ color distribution matches the observed distribution even closer than the Besançon model with the central minimum at the right position. This better agreement mainly comes from the red peak ($J - K_s > 0.5$) which has a less extended tail on its blue side compared to the Besançon data and has a higher peak value instead. Otherwise the two model distributions are nearly identical.

Velocities Even though the MCM model has a focus on reproducing the dynamics in the solar vicinity, the corresponding velocity distributions (Figure 3.14) compare worse to the real RAVE velocities as e.g. the ones coming from the Besançon model. We have to remember though that this model is based on a N -body simulation with limited spatial *and* velocity resolution. The small peaks in the proper motion distributions of the giant stars consist of stars originating almost all from the same host particle. It is thus not completely clear what the model would predict for these velocity regions. In the GALAXIA/Besançon model we saw a similar lack of high $|v_{\text{los}}|$ stars, so this deficiency cannot be solely attributed to the absence of a stellar halo component in the MCM model – at least not if the halo is modeled as in the Besançon model.

We can further see that the velocities for the giants are matched better than those of the dwarf stars. The broad wings in the proper motion distributions of the dwarf stars can be attributed to the velocity softening and can be reduced via a more aggressive (smaller) values for the softening parameter h_v .

We can quantify the different shapes of the v_{los} distributions by computing their moments. For Figure 3.16 we computed the excess kurtosis (γ_2), the second moment minus 3, as a function of limiting velocity for the line-of-sight velocity distributions. The GALAXIA/Besançon model closely follows the real data up to $\sim 170 \text{ km s}^{-1}$ while the MCM model exhibits flatter distribution for all velocities.

It is important to note, however, that the advantage in the MCM model does not lie in the absolute match of the kinematics of the Galaxy, but in the realistic *correlations* between the

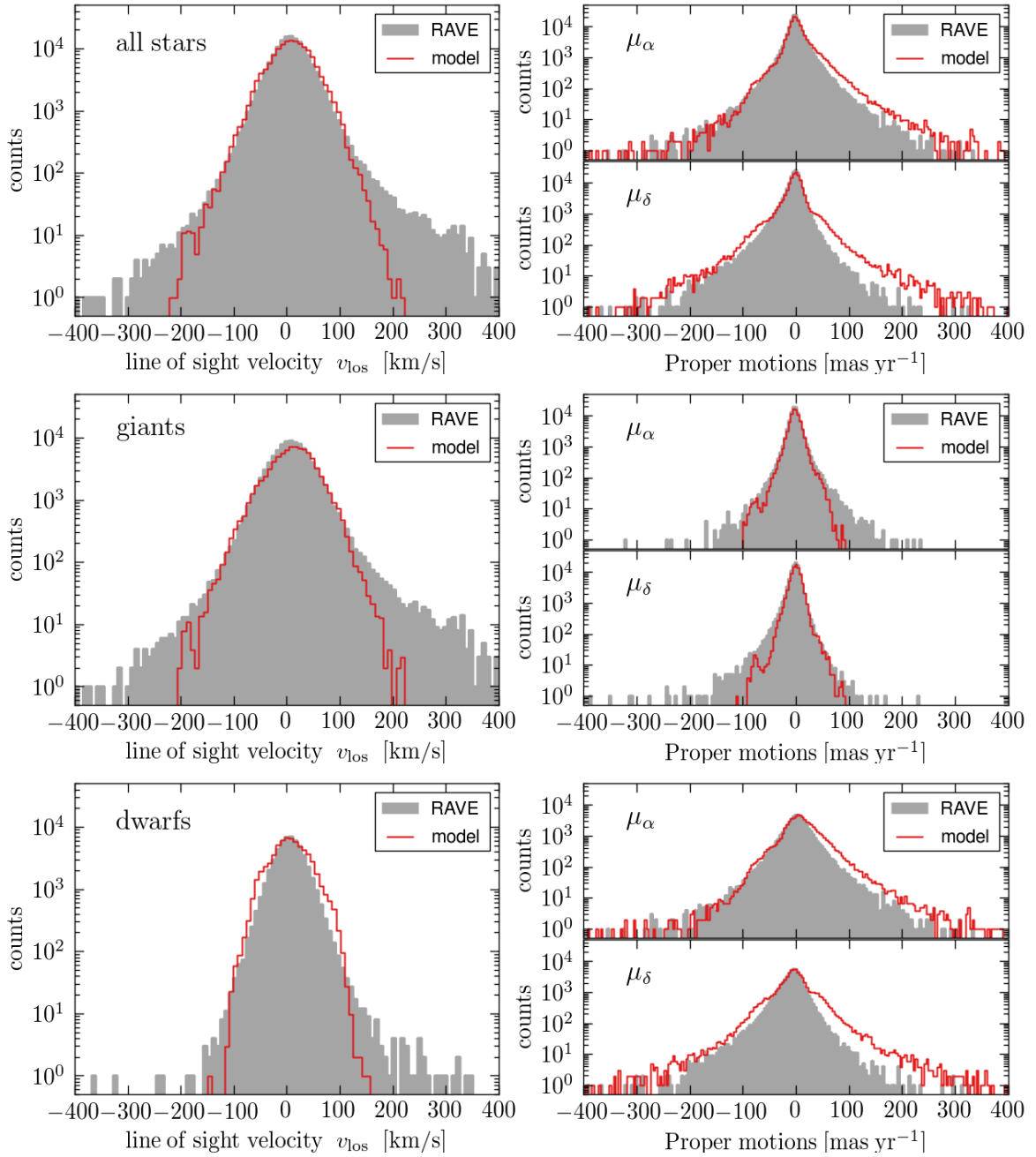


Figure 3.15: Comparison of the velocity distributions in the model (red line) and the real RAVE input sample (gray shaded area). The three rows show the distributions for all stars in the surveys (top row), for the giant stars ($\log g < 2.7$, middle row) only and for dwarf stars only (bottom row).

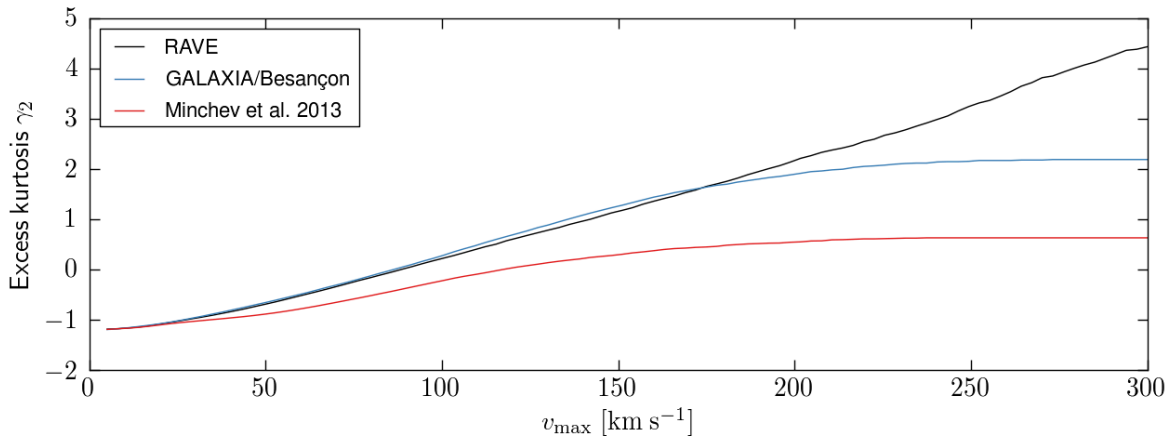


Figure 3.16: Excess kurtosis of the line-of-sight velocity distributions as function of the maximum velocity modulus considered for the computation. The three lines correspond to the real RAVE data and to mock surveys based on the GALAXIA/Besançon model and the MCM model. A value of zero for excess kurtosis corresponds to Gaussian shape of the distribution.

kinematics and the chemical abundances of the stars. This aspect of the model is investigated later in Section 3.3.6.

Stellar parameter distribution Similar to the Besançon model we find a qualitative agreement between the model prediction for the stellar parameter distributions in RAVE with those of the mock sample. In Figure 3.17 we compare directly the RAVE data and the two models. In all three cases we find the double peaked structure for $\log g$ and T_{eff} , only with different relative heights of the peaks. In the temperature distributions the central minimum shifted for the two models, a feature that was already implied by the differing color distributions.

Plotting the two models on top of each other confirms that there is a general shift of ~ 0.3 dex between the peak locations of the surface gravity values in the model predictions and the RAVE DR4 data. In the figure we shifted the both model distributions by this amount to allow a better comparison. This shift points to a difference in the surface gravity scales encoded into the isochrones used for the modeling and the model atmospheres used in the RAVE spectral analysis pipeline. The different locations of the central minimum is most likely an artifact coming from the RAVE analysis pipeline as was already discussed in Section 3.2.2. Generally, it can be said that the $\log g$ estimates are the most uncertain of the three stellar parameters, because the wave length region observed by RAVE contains only little information about this quantity (e.g. G. Gilmore, RAVE collaboration meeting 2013). The metallicity distributions reveal significant differences between the models. The prominent tail to low metallicities visible in the Besançon model data is absent in the MCM model which in turn is deficient at these low metallicities. The main peak is shifted with respect to the real RAVE data to higher metallicities by a similar amount in both models. The bump in the $[M/H]$ distribution in the MCM model data can not be attributed to shot noise in the N -body model. The population of stars with metallicity below -1.2 dex originates from 326 different mass particles and is thus an intrinsic feature of the model which not visible in the data.

None of the two models recovers the extended tail to metallicities below -2 dex present in the RAVE giant star sample (bottom right panel). However, for the MCM model this is

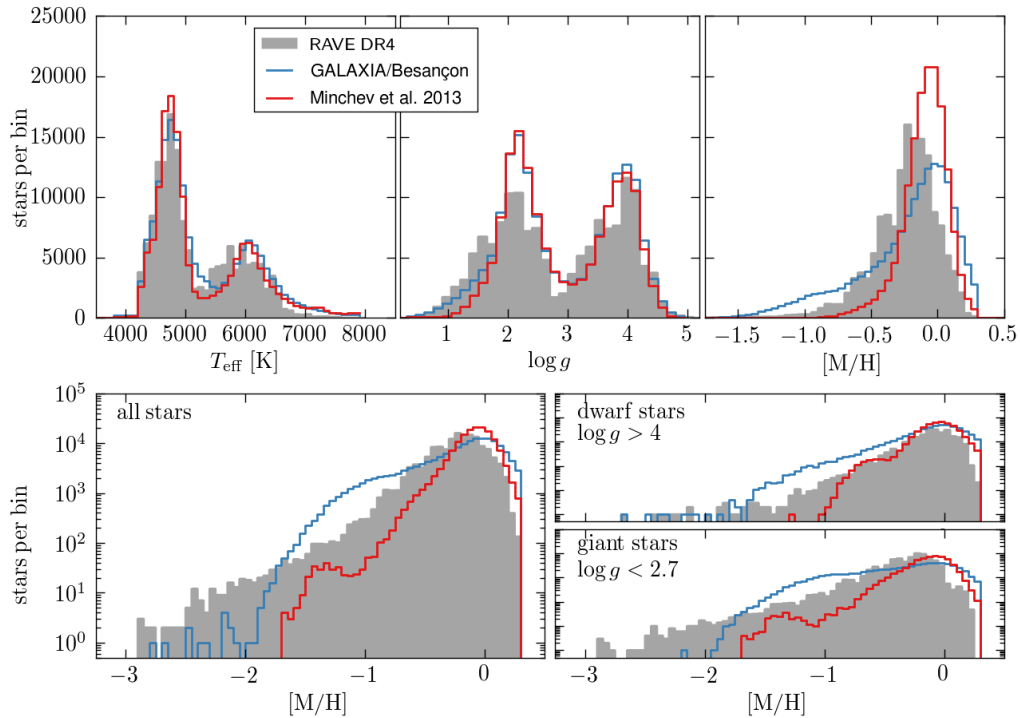


Figure 3.17: Distributions of the stellar parameters effective temperature, T_{eff} , surface gravity $\log g$ and metallicity $[M/H]$ for the real RAVE stars (gray shaded area) and two mock catalogs created from the chemodynamical MCM model by (red lines) and the GALAXIA/Besançon model (blue lines), respectively. The upper row shows the distributions in linear scale, while in the lower row the $[M/H]$ distributions for all stars (left) and for dwarf and giant subsamples are plotted in logarithmic scale to visualize the low metallicity tails. The model distributions for $\log g$ were both shifted by -0.3 dex to correct for a difference in the $\log g$ scales in the model isochrones and the RAVE data.

expected, because the model does not include a stellar halo population by construction. An additional stellar halo component would have to be substantially more massive or differently structured than the halo model in the GALAXIA/Besançon model to explain the quantities of very metal-poor stars found in RAVE. The deficiency of high $|v_{\text{los}}|$ stars observed in both models points in a similar direction as do various observational reports in the literature (Carollo et al. 2007; Schuster et al. 2012; An et al. 2013).

3.3.6 Modeling the giant sample of Boeche et al. (2013)

The truly unique feature of the MCM model by are the naturally arising correlations between the chemical composition of the stars and their present dynamics. As we have seen in Section 3.2.3 such correlations cannot be neglected when analyzing chemodynamical data. In this section we will try to reproduce the results of a study that directly aimed to discover the relations between chemical abundances and the orbital properties of a sample of RAVE stars, namely the study by Boeche et al. (2013a).

Boeche et al. selected a high quality sample of RAVE giant stars and computed their orbits in a Galactic model potential. In this they followed a study using high-resolution spectroscopy

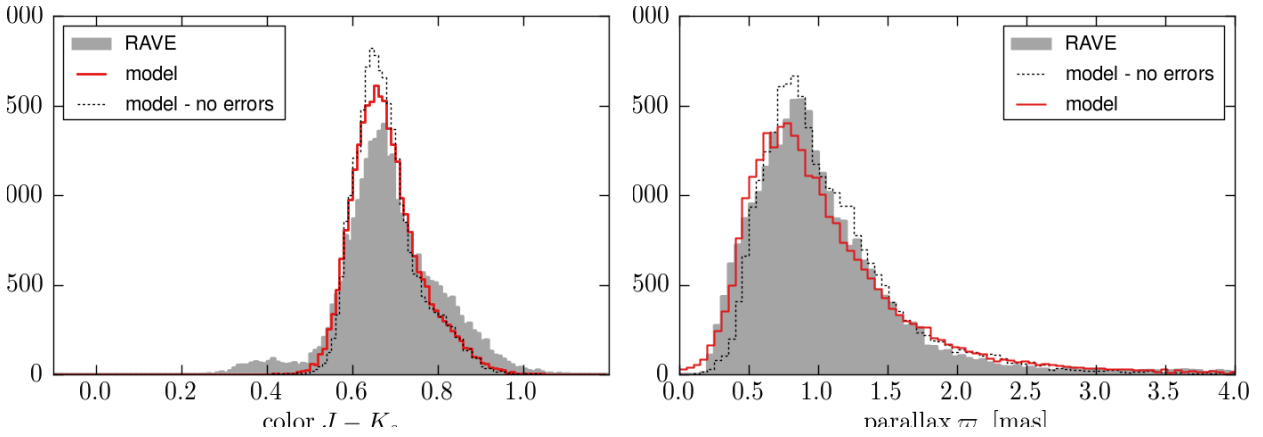


Figure 3.18: Color and parallax distribution of a high quality RAVE giant star sample selected in the same way as in Boeche et al. (2013a) (gray shaded histogram) and a mock equivalent based on the MCM model (red line). The black dotted line shows the model results without our error model applied.

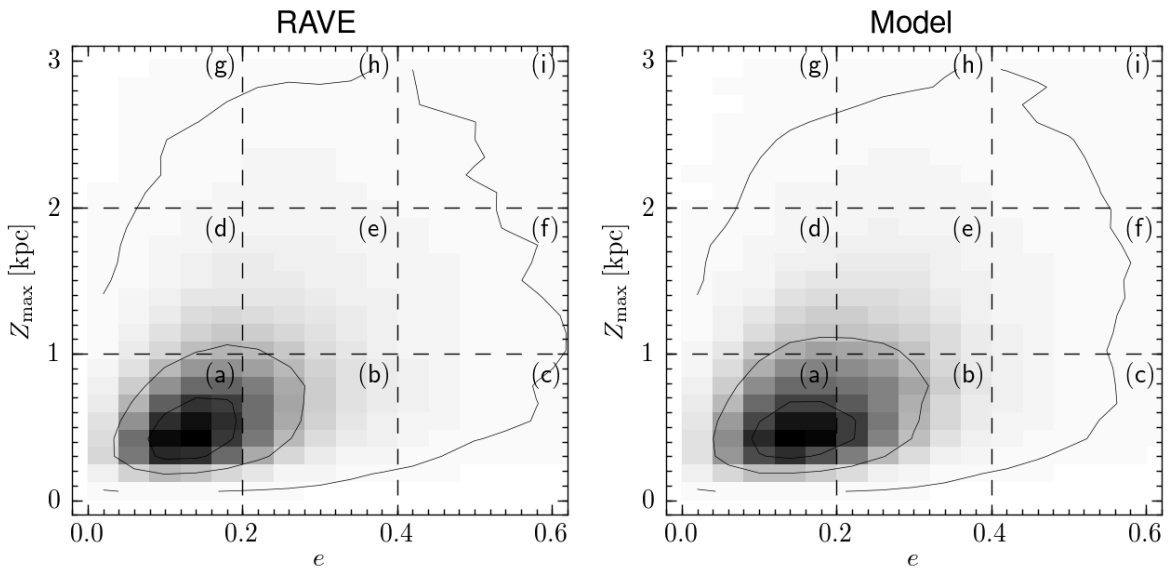


Figure 3.19: Distribution of a giant star sample with $S/N \geq 60$ in the (e, Z_{\max}) -plane. The contour lines mark locations where the number density dropped by a factor of $e^{-1/4}$, e^{-1} and e^{-4} from the maximum value. The dashed lines divide the nine regions defined by Boeche et al. (2013a). The left panel shows the original RAVE sample and the right panel the results from the model.

by Gratton et al. (2003) who tested dynamic against chemical selection criteria to distinguish thin and thick disk stars. The stellar orbits are characterized by their eccentricity, e , and the maximum distance to the Galactic plane, Z_{\max} , and their Galactocentric tangential velocity, V_{ϕ} . The eccentricity is defined as follows:

$$e = \frac{R_{\text{apo}} - R_{\text{peri}}}{R_{\text{apo}} + R_{\text{peri}}}, \quad (3.9)$$

where R_{apo} and R_{peri} are the Apogalacticon and Perigalacticon of the orbit, respectively. Nearly circular co-rotating orbits that never moved far from the Galactic plane were defined as thin disk orbits, while the rest was associated with the thick disk and the non- or counter-rotating stellar halo. Boeche et al. (2013a) generalized this approach by sub-dividing the (e, Z_{\max}) -plane into nine panels and analyzing these sub-populations separately.

With our machinery it is now straightforward to produce a sample of mock stars selected in the same way as the sample of Boeche et al. (2013a). The authors applied two additional data quality criteria based on the parameters computed by the RAVE chemical pipeline (Boeche et al. 2011) that ensure that the derived chemical abundances are reliable. Namely, the χ^2 value of the pipeline fit has to be low (`chisq_c` < 1000) and the star spectrum has to be usable over practically the whole RAVE wavelength range (`frac_c` > 0.99). The requirements are not related to the intrinsic properties of the stars and we applied them together with the S/N cut. Boeche et al. used the high threshold of 60 for their minimum S/N, which we consequently adopted as well. A giant sample is then produced by selecting for the following criteria

$$\begin{aligned} 0.5 &\leq \log g \leq 3.5 \text{ dex} \\ 4000 &\leq T_{\text{eff}} \leq 5500 \text{ K} \end{aligned} \quad (3.10)$$

With these criteria we find a RAVE sample with 28 551 stars⁶ and obtain a mock sample of 25 416 stars. We compare the resulting $J - K_s$ color and parallax distributions of the original and the mock sample and find excellent agreement (Figure 3.18). The real data exhibits a very small population of stars with $J - K_s < 0.5$ that points to an under-estimation of the effective temperature for these stars. Whether we remove this population or not does not influence any of the further results and so we decided to keep it for consistency with the original paper. The mock stars further peak at slightly larger distances (smaller parallax values) than the real stars. The distributions of the line-of-sight velocities and the proper motions compare similarly as for the giant sample with S/N > 40 shown in the middle row of Figure 3.14.

We compute the orbital properties of the stars using a simple test particle computation in a rigid Galaxy potential. We use a very simple mass model with a Miyamoto & Nagai (1975) disk (scale length $R_d = 4$ kpc and scale height $Z_d = 0.3$ kpc), a Hernquist (1990) bulge with scale radius $r_b = 0.6$ kpc and a spherical NFW halo (Navarro et al. 1996) with scale radius $r_h = 36$ kpc. The masses were chosen such that the circular speed at the solar radius is 220 km s^{-1} with disk, bulge and halo contributing 60%, 35% and 5% of the circular speed, respectively. The specifics of the mass model are not a major concern for our study, because we use the orbital parameters only to categorize the orbits relative to each other, so that the absolute values are not in the main focus. Figure 3.19 illustrate the distribution of the sample stars in the (e, R_{\max}) plane. We see a generally very similar structure, but the model shows a broader peak than the real data consistent with the less peaked shape of the line-of-sight velocity distribution in the model (Figure 3.14). The samples are then sub-divided into nine

⁶This is a much larger sample than the one used by Boeche et al. (2013a), because we use the later, more complete version of the RAVE survey than what was available when the original study was done.

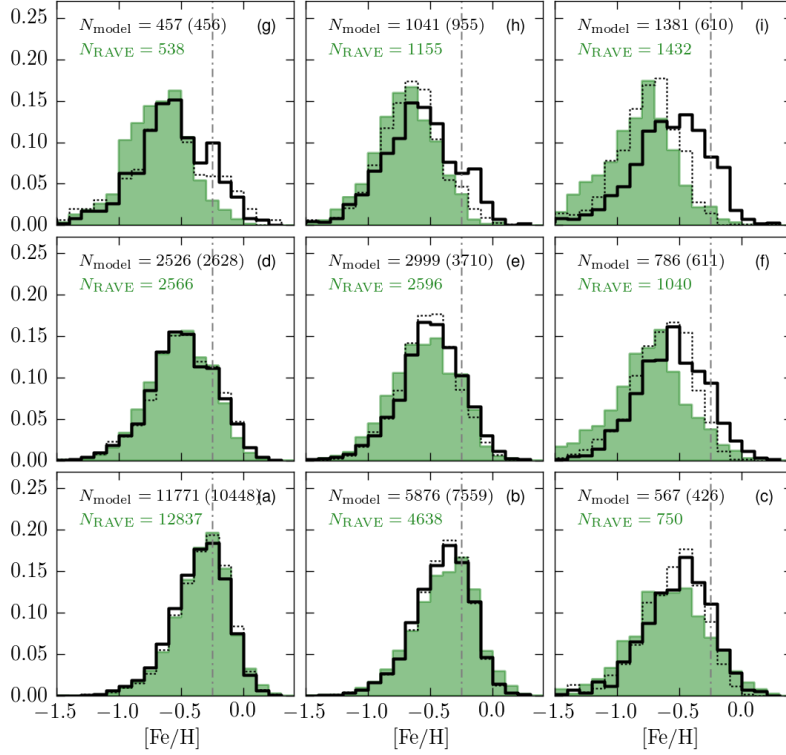


Figure 3.20: Normalized metallicity distribution of the nine sub-populations defined in Figure 3.19. The original RAVE data is shown as filled green histograms and the model is over-plotted as a black line. The thin dotted histograms show the model results when no errors on the phase space positions are applied. In the upper left corners are the numbers of stars in the corresponding sub-populations, in parenthesis are the numbers for the error-free model data. The $[\text{Fe}/\text{H}]$ values of the mock data were shifted by -0.25 dex to allow a better comparison of the variations of the peak locations for the different sub-populations. The shift value was chosen to match the peak position in panel (a).

groups as illustrated by the dashed lines in Figure 3.19. Note that the regions in the sections (c), (f), (g), (h) and (i) extend have no upper limits and hence extend beyond the visible area of the plot (e.g. section (c) contains stars with $e \in [0.4, 1.0]$).

Boeche et al. (2013a) found a trend of lower iron abundances for kinematically hotter orbits consistent with previous observations. With the MCM model we can beautifully reproduce this trend. In Figure 3.20 we plot the metallicity distribution of the nine sub-populations. For illustrative reasons we shifted all model iron abundances by -0.25 dex to match the peak location in panel (a). This results in very good agreement in the most of the other panels as well. However, for the most eccentric populations (panels (c), (f) and (i)) the model predicts too high $[\text{Fe}/\text{H}]$. A comparison with an error-free data set (dotted lines in the panels) reveals that panel (i) is dominated by contaminants which contribute about $2/3$ of the population. At this point it is thus unclear whether the model is actually in tension with observations or whether our Gaussian error model is a too crude approximation in this case. The discrepancy in panel (f) is present even in the error-free data and thus reveals a clear mismatch of model and real data. Boeche et al. (2013a) concentrated on panel (c) where they discussed a possible double peaked structure in the $[\text{Fe}/\text{H}]$ distribution. We do not see any hints for such a feature in the model data.

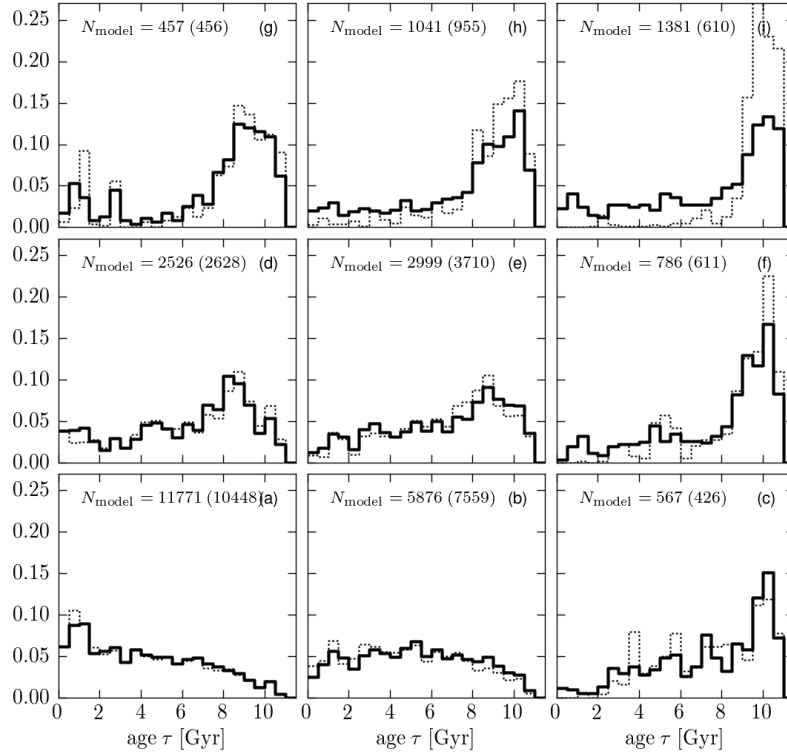


Figure 3.21: Distribution of age in the nine sub-populations defined in Figure 3.19 as predicted by the model. The dotted lines show the distributions of populations selected with the error-free estimates of the eccentricity e and Z_{\max} .

Ages and birth radii The fact, that the model reproduces the correlations between chemistry and kinematics of the stars gives confidence that the stars in our mock survey have indeed similar statistical properties as the real RAVE stars. We can thus go a step further and examine properties of the mock stars that are not or only with great uncertainties accessible via real observations. First, we examine the distribution of stellar ages in the nine sub-populations in Figure 3.21. As expected we find a broad and almost uniform age distribution for the dynamically cool thin disk populations in panels (a) and (b) and a strongly peaked distribution for the hottest orbits in panel (i). In the error-free case the latter panel contains a population with a single age of 10 – 11 Gyr. We can generally see a trend to older populations with increasing Z_{\max} and a similar, but weaker trend with increasing eccentricity. Our input data of the MCM model is based on the cosmological re-simulations by Martig et al. (2012) that thus we know the birth radius, R_{birth} , of the host particle of each star in our sample. For simplicity we identify the birth radii of the stars and their host particle. Figure 3.22 plots the distribution of birth radii for our nine sub-populations. If we compare the birth radius of a star with its present guiding radius R_g we can learn whether the star has migrated radially during its lifetime. Here we use the orbital mean radius $R_m = 0.5(R_{\text{peri}} + R_{\text{apo}})$ as an approximation for R_g .

In all panels most of the stars were born inside the solar radius. This is not surprising given the decreasing stellar density with radius. For the populations with high eccentricities the R_{birth} and R_m distributions agree reasonably well. This means that these populations consist mainly of stars that were dynamically heated, e.g. by giant molecular cloud, spiral arms, the Galactic bar or by passing satellite galaxies. For the stars on more circular orbits in the pan-

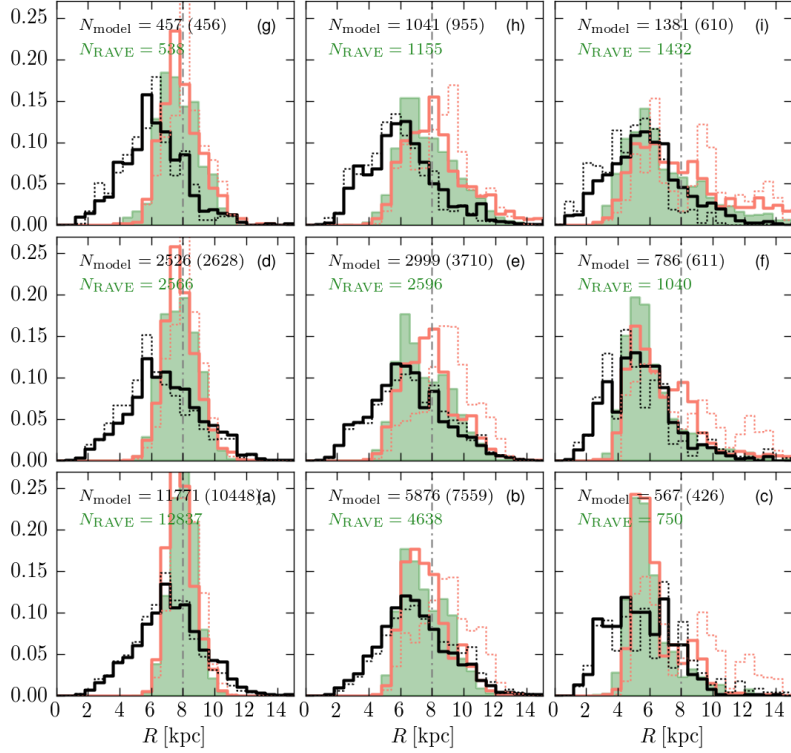


Figure 3.22: Distribution of birth radii (black lines) and current mean radii, R_m (red lines), in the nine sub-populations defined in Figure 3.19 as predicted by the model. The dotted lines show the distributions of populations selected with the error-free estimates of the eccentricity e and Z_{\max} . The green histograms show the distribution of R_m in the real RAVE data.

els (a), (d) and (g) the situation is quite different. By construction the R_m distributions are very narrow, because for these stars the difference between their present (projected) radius R and their mean radius cannot be large⁷. The R_{birth} distributions are broader and their peaks are subsequently shifted to lower values with increasing Z_{\max} . Consequently, almost all stars in panel (g) must have migrated radially via the resonant scattering mechanism described in Sellwood & Binney (2002) that preserves the circularity of their orbit. The fact that we find almost no stars on circular orbits with large Z_{\max} that did not migrate implies that the stars in panel (g) have not acquired their large vertical velocity dispersion after migrating, but were dynamically heated (or born hot) at their location of birth.

We can summarize that the combination of self-consistent dynamical evolution in N -body simulations and a chemical evolution tuned to produce the present state of the Galaxy leads to a very detailed and comprehensive picture of the Milky Way and can help to better understand the consequences of selection criteria and the resulting stellar samples. The hybrid approach of the model is particularly productive in the sense that the model can be made more precise by increasing the resolution in the simulations, even though it will take a lot of improvement to reach the smoothness of analytical distribution functions. We will now turn to a model that is fully self-consistent in the sense that the chemical evolution of the ISM is included in the simulation from the beginning.

⁷The slight broadening with increasing Z_{\max} is most likely reflecting the cone-shaped RAVE survey volume.

3.4 A full cosmological simulation

In the previous sections we studied two models that were explicitly designed to serve as models for our Galaxy. They were tuned to match pre-existing observations and hence their considerable predictive power is not surprising. We will now put our focus on a galaxy model that is based on first principles only, namely a full cosmological simulation of galaxy formation that also follows the chemical evolution of the interstellar medium (ISM). We can hope that it resembles the Milky Way only because the galaxy has roughly the same mass as our Galaxy, it lives in a similar, i.e. quiescent, cosmic environment at redshift $z = 0$ and because it formed a significant stellar disk.

3.4.1 General description of the model

The simulation we will study now is run C from the suite of simulations by Scannapieco et al. (2009). A general introduction to the whole suite of simulations was given in Section 2.2 and, as explained there, we re-scale the simulation such that the galaxy has a circular velocity $v_{\text{circ}}(R_0) = 220 \text{ km s}^{-1}$ at the solar radius $R_0 = 8 \text{ kpc}$. The galaxy in this simulation has a (re-scaled) virial mass $M_{200} \simeq 0.9 \times 10^{12} M_{\odot}$ and a virial radius $R_{200} \simeq 195 \text{ kpc}$. Its total mass is lower but comparable to the mass of the Milky Way (see Chapter 4 and references therein).

We pick simulation C for our study, because in this simulation the galaxy developed the most prominent disk component of all 8 simulations with a disk-to-total mass ratio of 0.213 (Scannapieco et al. 2009) for kinematic disk-bulge decomposition. Compared to observed disk galaxies and the Milky Way in particular, this is a very low value, but Scannapieco et al. (2010) showed that when the decomposition is performed on the basis of the surface brightness distribution a significantly larger value of 0.49 is obtained. As we will see later the massive bulge component in this galaxy has a significant impact on the stellar population in our mock RAVE survey.

It is also worth noting that the ICs of this simulation run were also used in the Aquila comparison project (Scannapieco et al. 2012). In the course of this project a large variety of simulation codes using different prescriptions for star formation, supernova feedback, etc. were compared by running the same initial conditions and comparing the resulting galaxies. Not all codes produced a disk galaxy. Recently, Aumer et al. (2013) and Marinacci et al. (2014) partly re-simulated the suite of Aquarius halos with other simulation codes and found disk-dominated galaxies for almost all halos, including halo C.

The simulations were among the first that produced galaxies with significant disk components *and* self-consistently treated the chemical evolution of the ISM. Because of this they present an ideal opportunity to test our approach. Another advantage is that this simulation was already extensively studied in the past (Scannapieco et al. 2009, 2010, 2011, 2012; Scannapieco & Athanassoula 2012; Tissera et al. 2012, 2013) so that the general structure and its consistency with the general population of disk galaxies and the Milky Way in particular is well known. This means that we can usually relate any features we find in our mock survey directly to known general properties of the galaxy without the need to perform our own global analysis. Before this background it is important to note that we cannot expect a perfect model coming out of this simulation, simply because the spatial resolution is far too low to accurately resolve the vertical structure of the disk. The gravitational softening parameter used in the simulation is 1400 pc. This is more than four times the canonical value

of the scale height of the thin disk (300 pc) and about the same as the thick disk scale height (e.g. 1450 pc in Gilmore & Reid (1983)). The smoothed-out density peak in the disk plane will certainly lead to discrepancies with the observations. It is still an interesting exercise to explore this simulation in the space of observables and see how the well-known short-comings of the numerical simulations in general translate into observations of individual stars.

The simulated galaxy has $\sim 500\,000$ stellar particles within 30 kpc around the center. As done before for the MCM model we increase the resolution of the simulation by superposing the particle distribution with a copy of itself that was rotated by 180° around the rotation axis of the disk (z -axis). For this particle configuration we find mean spatial and velocity smoothing parameters of 340 pc and 40 km s^{-1} .

Elemental abundances For our particular application of the simulation data we need realistic *absolute* values for the metallicities of the stars. This is important because we will not only study the metallicity gradients or correlations, but we will use the values to select the proper isochrones for the stellar population synthesis.

The GALAXIA processing as well as for the later comparison to the RAVE data we need the elemental abundances in the bracket notation as defined in Eq. 2.1. The simulation code provides the mass ratios $m(X)/m(H)$ in the stellar particles for and these relate to the number ratios through their nucleon numbers n_X via

$$\frac{N(X)}{N(H)} = \frac{m(X) n_H}{m(H) n_X} = \frac{m(X)}{m(H)} \frac{1}{n_X} \quad (3.11)$$

If we use for $N_\odot(X)/N_\odot(H)$ the standard values for the Sun as, e.g., given in Asplund et al. (2009) we find that the population of disk particles (defined via the circularity of their orbit as in Scannapieco et al. (2009)) peaks at $[\text{Fe}/\text{H}] \simeq -0.8$ dex, i.e. a much lower value than what is observed in the Milky Way. This was already noticed by Tissera et al. (2012) who studied chemical composition of the galaxies in the same simulations and found that the general chemical *trends* are similar to those in the Milky Way Tissera et al. (see also 2013). The reason for the lower absolute values of the elements abundances lies mostly in the uncertainties of the chemical feedback from supernovae and how this couples with the surrounding ISM (C. Scannapieco, private communication).

For our work the absolute values of the elemental abundances are of importance, because these are used for the selection of the stellar isochrones during the GALAXIA processing. Metal-poor stars are generally more luminous than metal-rich stars, especially in the low temperature regime where heavy elements and molecules absorb a significant fraction of the emitted radiation. A lower average metallicity has hence a profound impact on the population of stars observable by RAVE.

We decided to not to use the real chemical composition of the Sun as a reference, but the mean composition of the stellar particles in the solar annulus⁸. This leaves the simulation not completely self-consistent, because the gas cooling is a function of (absolute) chemical composition in the code. We consider this a minor loss because only in this way we can exploit the full potential of the simulation results. We obtain for our pseudo-solar mass fraction of chemical elements heavier than Helium, Z_\odot , a value of 0.36% instead of the estimate 1.8% in the real Sun (Asplund et al. 2009). Consequently, the distribution of $[\text{Fe}/\text{H}]$ in the solar neighborhood now peaks at -0.1 dex, close to the value of -0.05 dex found by Casagrande et al. (2011) for the stars in the Geneva-Copenhagen survey.

⁸We define the solar annulus as a cylindrical shell of radius 8 kpc and with a thickness and height of 1 kpc, respectively.

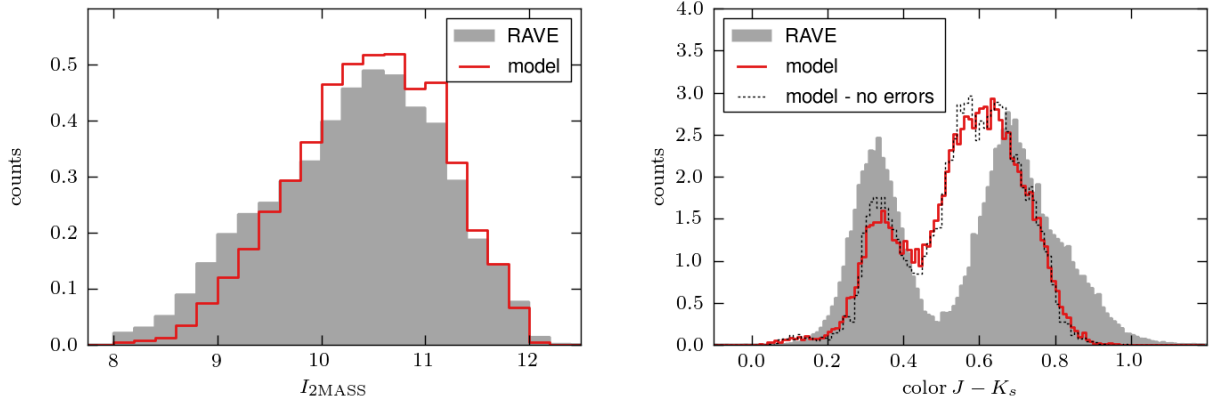


Figure 3.23: Distribution of apparent $I_{2\text{MASS}}$ magnitude (left) and $J - K_s$ color (right) of the real RAVE survey and an equivalent mock star sample based on a cosmological simulation. The black dotted line in the right panel shows the color distribution before observational errors were applied. This figure corresponds to Figure 3.3 and Figure 3.15 for the GALAXIA/Besançon model and the chemodynamical MCM model, respectively.

3.4.2 Comparison to RAVE

After processing the galaxy model with GALAXIA and applying the RAVE selection function we obtain a survey with less than 25 000 stars. This is a factor 6 less than the number of stars in the RAVE sample we tried to reproduce. The reason for this is the mass distribution in the galaxy. The stellar mass surface density at the solar annulus is $\sim 30 M_{\odot} \text{pc}^{-2}$ in the model, which is at the low end of what is observed. However, in the real Galaxy most of the surface density is contributed by the Galactic disk and is hence confined in a volume close to the Galactic plane. If we compute the stellar surface density in the model and only integrate between $z = \pm 1$ kpc the value falls below $15 M_{\odot} \text{pc}^{-2}$. Below 1 kpc the vertical density profile increases only linearly, i.e. is strongly flattened by the strong gravitational softening in the simulation.

Due to the large mismatch in the number of stars the apparent $I_{2\text{MASS}}$ distributions of mock and real data (Figure 3.23, left panel) can only be compared by their shape. The slight deviations can again be interpreted in terms of the smoothed out vertical density profile of the galaxy: the relative under-abundance of bright stars that is balanced by an over-abundance of stars in the fainter bins can to first order⁹ be translated into a too low mass density in vicinity of the Sun and a too slow drop of the density at larger distances. Consistently, the color distribution of the model (Figure 3.23, right panel) shows that there are too many stars of intermediate color between 0.4 and 0.7 dex in the mock sample. This color range contains cool stars, most of which are likely distant giant stars. Nearby hot dwarf stars with $J - K_s < 0.4$ dex are under-represented. The dominant origin of this mismatch hence appears to be the limited force resolution in the simulation, a problem that will surely be alleviated in the next generation of simulations.

Velocities The velocity distributions are similarly affected by the low resolution. The original simulation does not have an explicit velocity resolution, but with EnBiD we get an estimate of the extend of the effect. We have to remember that the smoothing parameter

⁹Assuming all stars to have the same luminosity.

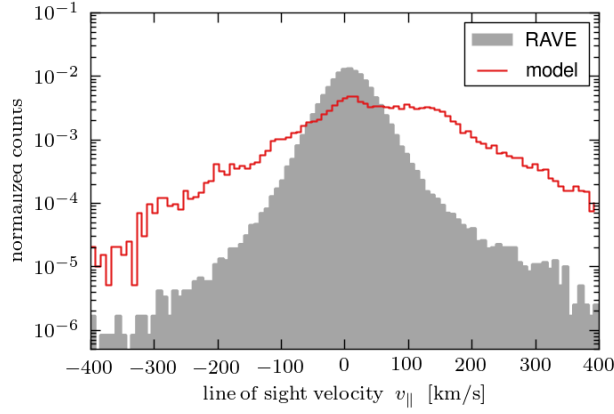


Figure 3.24: Velocity distribution of the RAVE data and the mock sample based on a simulated galaxy. The black dotted line in the right panel shows the metallicity distribution before observational errors were applied.

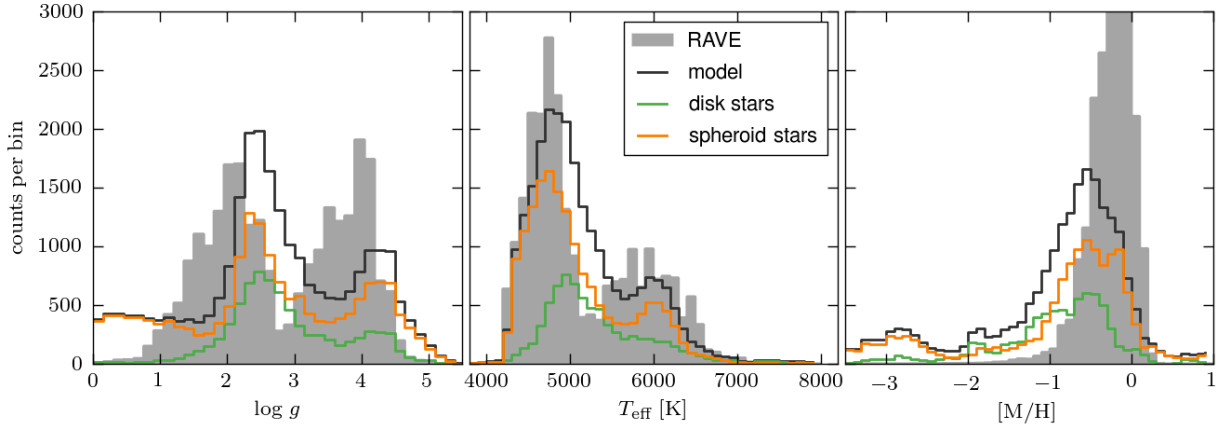


Figure 3.25: Distributions of the stellar parameter of the RAVE input sample and the mock data. The RAVE data was re-scaled to match the number of stars in the mock survey in order to facilitate a better comparison. The mock stars were further sub-divided into a disk and a spheroid population. Please refer to the main text for a further explanation of the division.

$h_v = 40 \text{ km s}^{-1}$ was computed on the basis of the particle distribution superposed with itself, so the actual smoothing in the simulation was even stronger. The latter is determining what structures can be resolved in the simulation. Our method to increase the resolution can not undo this smoothing, but only helps to decrease the shot noise in our mock survey that originates from the finite number of particles tracing a smooth density field and that could produce additional artificial structures. The much broader distribution of line-of-sight velocities in the model compared to the RAVE data (Figure 3.24, left panel) is a clear signature of the velocity smoothing. Note, however, that the asymmetry of the high velocity tails is still detectable in the model data.

Stellar parameters The distribution of surface gravities $\log g$ and effective temperatures T_{eff} in the mock survey exhibit the characteristic two-peaked structure that we already saw in the previous models (Figure 3.25) as well as the overall $\log g$ shift of 0.3 dex. In this case,

the dwarf peak is much reduced compared to the giant peak as well as to the peak in the original RAVE distribution. We further see a flat tail to extremely low $\log g$ values that is clearly not present in the RAVE data. Scannapieco et al. (2009) divided the stellar particles in the simulation into a disk and a spheroid population according to their Galactocentric distance and their circularity parameter. The latter is defined as the ratio of the angular momentum in the z -direction, L_z , and the angular momentum of a circular orbit, L_{circ} , at the position of the particle. If we tag the mock stars according to the classification of their host particles (green and orange lines in Figure 3.25) we find that the low $\log g$ tail consists entirely of stars belonging to the spheroidal component.

The presence of these stars in our mock survey implies that this component, which is commonly associated with the bulge and the stellar halo, is much too prominent in this galaxy. In fact, the presence of a too massive stellar halo is a well-known problem of almost all cosmological simulations. This is generally attributed to inefficient stellar feedback in the simulation that allows the conversion of too much gas into stars in low-mass galaxies at early times (Scannapieco et al. 2009; Guo et al. 2010; Sawala et al. 2011). These galaxies are then accreted and disrupted by the progenitor of the Milky Way. Due to their collisionless dynamics the stars of these satellite galaxies form the stellar halo, while accreted gas would dissipate its orbital energy and settle into the Galactic disk. More recent simulations (Aumer et al. 2013; Stinson et al. 2013) identified early energy feedback by the radiation pressure from young massive stars as an additional source of efficient feedback. Including this effect leads to much more realistic disk-to-bulge ratios.

The low abundance of dwarf stars in the mock sample is again a signature of a too puffed-up stellar disk. This shifts the balance of observable dwarf and giant stars in a given line of sight towards the giants. However, the disk thickness is only one among a number of parameters determining the relative heights of the dwarf and giant peaks. Apart from the disk-spheroid mass ratio there is also the distribution of ages in the population, because the age sets the ratio of dwarfs and giants in the observable magnitude range.

Metallicities Despite our efforts to increase the realism of the metallicity distribution in the simulation we find the mock metal abundances too low compared to the actual RAVE distribution. Interestingly, this model thus deviates in the opposite direction compared to the models discussed in the previous two sections. Since we match the mean metallicity in the immediate solar neighborhood by construction, this result must arise from the spatial distribution of metals that seems to drop too quickly with increased distance from the Galactic plane. In addition to this the massive stellar halo is also largely responsible for the existence of a significant population of extremely metal-poor stars (around -3 dex) in our mock survey.

3.4.3 Effects of the selection function

As already done for the MCM model we can compare the properties of our mock stellar survey to the properties of the sample of host particles that contributed these stars (Figure 3.26). We find an almost flat distribution of heights z above the Galactic plane for the particles that clearly reflects the large spatial smoothing that had to be applied because of the low mass resolution in the simulation. The z distribution of the mock stars still resembles the original RAVE distribution quite well. This again illustrates the important influence of the selection function on our results. In the metallicity distribution we see a prominent peak at extremely low metallicities that has only a very weak counterpart in the stellar distribution.

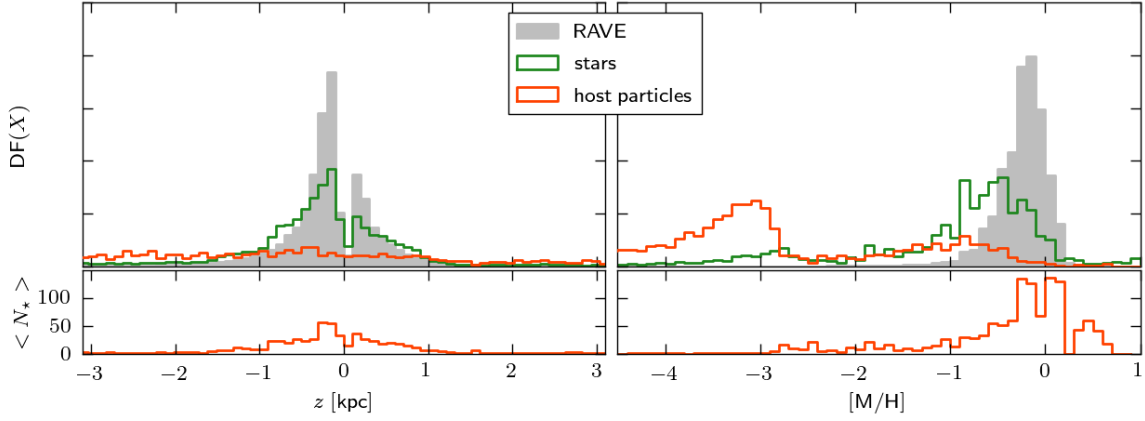


Figure 3.26: Comparison of the distributions of the mock stars and their host particles (upper panels). The left side shows the distributions vertical to the galaxy disk and the right side shows the metallicity distributions. The equivalent distributions found in the real RAVE data are also plotted for comparison. The lower panels show the mean number of mock stars spawned from a particle in a given z or metallicity bin. This figure compares to Figure 3.12 that shows the same for the MCM model.

The latter implies that these particles are very distant and that from the stellar population that they are representing only the very luminous stars, that are rare, can enter the survey. The low metallicity of these particles shows that they belong to the (too massive) stellar halo (cf. Figure 3.25). We can further recognize again the tendency of the mock stars to have the peak of their metallicity distribution at higher values than the peak of the mass particle distribution, even if we ignore the dominant peak at ~ -3 dex and consider only the secondary peak around -1 dex. We found this higher weighting of nearby metal-rich stars already for the MCM model and this appears to be a general implication of the RAVE selection function.

Summarizing, we can state that the studied simulation can not serve as a detailed model for our Galaxy. This result could have been expected, since the simulated galaxy suffers from the well-known problems that affect almost all cosmological simulations of this type, in particular the too massive stellar halo. This generation of simulations is not accurate enough to be seriously analyzed with the sophisticated machinery used in this work. In addition, the simulation we studied was in no way tuned to produce a close match of our galaxy. We repeated the analysis with simulation G from Scannapieco et al. (2009), which hosts also a significant disk component, and found very similar results.

The simulations that form the next generation (Aumer et al. 2013; Stinson et al. 2013; Marinacci et al. 2014) appear not to suffer from the stellar halo problem anymore. The other major obstacle for such simulated galaxies to serve as valid models for the Milky Way is the limited mass and force resolution. If we follow the developments in the field we find a rapid improvement of this issue. Abadi et al. (2003a) reported on their suite of simulations a gas particle mass of $3.3 \times 10^6 M_{\odot}$. Only 6 years later the mass resolution in Scannapieco et al. (2009) has hence increased by a factor of 5 – 15. New standards were set by the Eris simulation (Guedes et al. 2011) who report a gas particle mass of only $2 \times 10^4 M_{\odot}$. We have to remember, however, that this was a single simulation with a total galaxy mass that is on the low side of the mass range in Scannapieco et al. (2009). Still it is clear that in the very near future we will have full cosmological simulations that can resolve the vertical structure

of the Galactic disk in sufficient detail.

This exercise of applying it to this model still has its value, since we have to assess the sensitivity of our approach. An inadequate model of the Galaxy should produce an inadequate mock survey. We showed that we can detect peculiar features in the properties in our mock samples that could be traced back to the known problems of the simulations. This was not clear a priori as there is a significant amount of modeling with external ingredients, like isochrones, between the simulation input and the final mock survey. Finally, we again found that we must not ignore the detailed selection effects in observational data when comparing to simulation results.

3.5 Excursion: designing a selection function for 4MOST

The astrometric space mission Gaia, to be launched in November 2013, is expected to revolutionize our knowledge and perception of the Galaxy in the near future. For the next generation of observing facilities, which will see first light in the post-Gaia era, these results will have to be anticipated during the planning. The successors of RAVE, SEGUE and their likes will clearly outperform their precursors because of advanced technology or merely increased size. But in order to truly maximize the gain in knowledge coming from these instruments the insights obtained from the last and on-going generations of surveys have to be taken into account by developing optimized instrument designs and survey strategies. This also means that a new generation of surveys can choose a more sophisticated survey strategy in the post-Gaia era when a large set of observables will be measured homogeneously for a significant fraction of the stars in the Milky Way.

This is particularly true for high resolution spectroscopic surveys. Here, because of the relatively long exposure times, the number of targets observable during the lifetime of a project is limited and therefore the input catalog has to be strongly optimized in terms of information content. In this section we will describe the outcome of such a process for the 4MOST instrument (4-metre Multi-Object Spectroscopic Telescope; de Jong et al. (2012)), a survey machine that is specifically designed to perform Gaia follow-up observations. The detector will consist of several fiber-fed spectrographs, that divide in low resolution ($R \simeq 7000$; LR) spectrographs and high resolution ($R \simeq 20000$; HR) spectrographs. The project is currently an official study for the European Southern Observatory (ESO) in the preliminary design phase.

In order to ensure that the capabilities of 4MOST meet the scientific requirements several key science cases were identified. The design of the instrument shall allow at minimum the completion of these “design reference surveys” (DRSs) during five years of operations. 4MOST is planned to perform in parallel several massive surveys that overlap on the sky. To cope with the complexity of the endeavor the whole five-year data taking process was simulated including, inter alia, a detailed model of (the through-put of) the actual instrument, the fiber positioning on individual targets, lunation periods and weather statistics from the telescope sight at the Paranal Observatory in Chile (Boller & Dwelly 2012). To facilitate this each DRS provided an input catalog with simulated target data. Here we will briefly describe the work done for the DRSs concerning high-resolution observations of the Galactic disk and bulge component.

The number of fibers feeding the high-resolution spectrographs was not fixed during the planning phase and discussed values ranged from 300 to 1000. The maximum exposure time was

set to 2 hours – a value that allows competitive observations together with a large sky coverage and also keeps the fraction of telescope down-time due to reconfiguration at an acceptable level. Considering the survey duration and the number of exposures per night this results in the observation of several millions of targets. During a 2-hour exposure the spectrum of a star with an apparent V -magnitude of 16 can be measured to a signal-to-noise ratio of 150 (per Å), which was requested as a minimum for a sensible analysis by spectroscopists (Caffau et al. 2013). The bright limit $V = 14$ mag for the range of targets was chosen to be complementary with the GALAH survey that is run on the HERMES instrument (Zucker et al. 2013) that uses this magnitude as a faint limit.

The general science goal of the 4MOST high-resolution surveys is the exploration of the chemical and chemodynamical structure of the Milky Way as well as the identification of sub-structures via chemical tagging (Freeman & Bland-Hawthorn 2002). One requirement was hence to observe stars covering a large range of Galactocentric projected radii, R , and heights above and below the Galactic plane, z . This suggests intrinsically bright giant stars as ideal targets. However, due to their low effective temperatures the spectra of giant stars are often crowded by molecular absorption lines that hamper the analysis. Main sequence (dwarf) stars are generally more suitable for a spectral chemical analysis (E. Caffau, private communication), but are intrinsically fainter. The brightest stars on the main sequence that can be selected without introducing an age bias¹⁰ are F & G dwarf stars. We decided to use a mixture of such dwarf stars and giants. Simulated observations of model spectra by P. Saretto using the 4MOST instrument through-put revealed that observations of dwarf stars with $\log g > 3.5$ dex and $V > 15.5$ did not reach $S/N > 50$ within 2 hours of exposure and so these stars were also excluded from the list of potential targets. Table 3.2 summarizes all target selection criteria.

By adopting these requirements we rely on the assumption that by the time 4MOST will take up operations there is at least a preliminary Gaia data release available. This should provide for all possibly eligible stars the information needed to apply our stellar parameter cuts. The potentially considerable uncertainties on the Gaia should not pose a major problem, but we emphasize that goal of this exercise is to obtain an impression about the number of potential targets and a mock input catalog for the survey simulations. The selection for the actual survey can only be fixed when the Gaia data is available.

We defined three sub-samples for the DRS:

The disk sample With this sample we want to study the chemical and chemodynamical structure of the Galactic disk, both in the radial and in the vertical direction. To facilitate this we selected a sample of stars that is uniformly distributed in the (R, z) -plane. We defined (R, z) -bins of size 2×0.33 kpc² and selected a maximum of 20 000 stars in each bin. This means that we neglect any azimuthal dependencies in our selection process. A further consequence is that the bins close to the Galactic plane and close to the Sun – where most of the potential targets are located – will have a low completeness while the more distant bins we do not find enough targets to fill the bin to the maximum. The maximum number was chosen to allow a good statistical coverage in chemical space, e.g. the $([\text{Fe}/\text{H}]-[\alpha/\text{Fe}])$ -plane.

The Bulge sample We define the Bulge volume to be a Galactocentric sphere of 1.5 kpc and we observe all possible targets in this volume. The number of targets is relatively small, because of the high extinction on the sight-line to and at the Galactic center. Recently several stellar sub-populations in the Bulge (Babusiaux et al. 2010; McWilliam

¹⁰To prevent an age bias the main-sequence lifetime of the stars has to be longer than the age of the Universe.

Table 3.2: Target selection criteria for the 4MOST DRS “disk high-resolution”. The variable r refers to Galactocentric distance.

| Description | Criterion |
|---|---|
| Accessible 4MOST sky | $-70^\circ \leq \delta \leq 20^\circ$ |
| Bright F & G dwarfs | $14 \leq V \leq 15.5$ mag $2.7 \text{ dex} < \log g$ $5200 \leq T_{\text{eff}} \leq 7500$ K |
| Faint F & G dwarfs | $15.5 < V \leq 16$ mag $2.7 < \log g < 3.5$ dex $5200 \leq T_{\text{eff}} \leq 7500$ K |
| Giant stars | $15.5 \leq V \leq 16$ mag $\log g \leq 2.7$ dex |
| Disk sample (2 million stars) | |
| No overlap with bulge region | $r > 1.5$ kpc |
| Bulge sample (250 000 stars) | |
| Bulge region | $r \leq 1.5$ kpc |
| Only giant stars | see above |
| High latitude metal-poor sample (725 000 stars) | |
| No overlap with bulge region | $r > 1.5$ kpc |
| No stars from the disk sample | |
| High latitude | $ b > 30^\circ$ |
| Metal-poor | $[M/H] < -0.5$ dex |

& Zoccali 2010; Bensby et al. 2011, 2013; García Pérez et al. 2013) were reported. With 4MOST we can do a comprehensive study of this issue and thereby gain a better understanding of the formation history of this component.

A high-latitude metal-poor sample This sample complements the disk sample by specifically selecting stars that carry the most information about the history of the Galaxy. This is expected for the metal-poor population, because it tends to have higher ages. The confinement to high Galactic latitudes is owed to the generally low target densities in these sky regions.

To produce the mock input catalog we use the code GALAXIA and the implemented standard (Besançon) model. GALAXIA is an ideal tool for such a project because it efficiently produces all-sky surveys of enormous size. Based on this we found ~ 17 million potential targets for the disk sample of which 2 million entered the final sample, 250 000 bulge giants and 725 000 stars in the high-latitude metal-poor sample. Figure 3.27 illustrates the three sub-catalogs. The left-most panel shows the projection of all samples combined. The irregular shape of the distribution is the result of the limitations to the accessible sky regions for 4MOST because of its planned location at the Paranal Observatory. An important aspect of our selection is that our targets still follow the intrinsic angular distribution of target densities on the sky as close as possible. This is important because the survey will be performed in *parallel* with other surveys, in particular the low-resolution survey of the Galactic disk. We therefore need high target densities for the high-resolution fibers at the same locations where we have

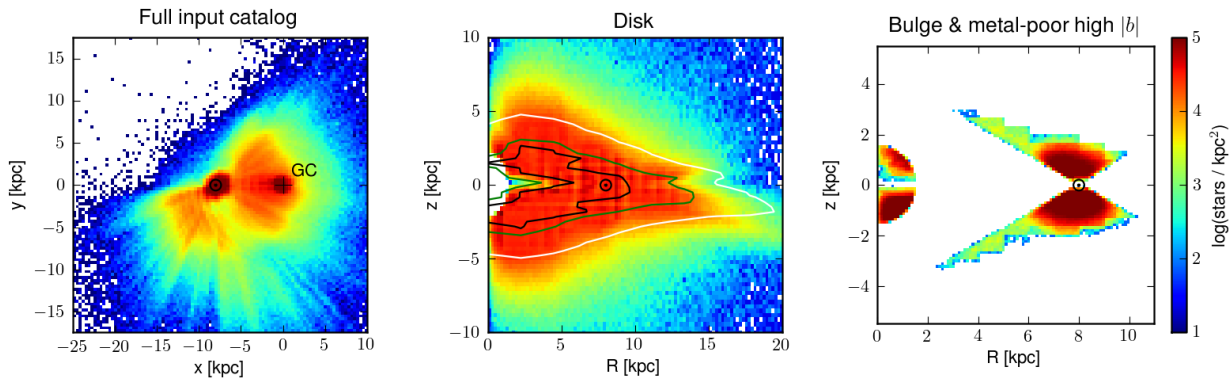


Figure 3.27: Spatial distribution of the mock input catalog for the 4MOST DRS “disk/bulge high-resolution” in different projections. The position of the Sun is marked in all panels with a black ‘ \odot ’. The left-most panel shows all three sub-catalogs combined. The middle panel shows the disk panel in the (R, z) -plane. The sample was specifically selected to have a uniform coverage in this plane. The black, green and white contour lines encircle regions where the target density is larger or equal to 20 000, 14 000 and 2 000 stars per $2 \times 0.33 \text{ kpc}^2$ bin. The right-most panel illustrates the Bulge and the high-latitude metal-poor sample. Note the different scales in the different panels. Color-coding is the same in all panels. This figure was also published in Chiappini et al. (2013).

high target densities for the low-resolution observations. An exception from the high latitude regions where targets are generally sparse. Here we artificially increased our target densities via the high-latitude metal-poor sample.

The mock catalogs contain more targets than we expect to be possibly observed by 4MOST, because this allows a more efficient fiber allocation in the survey simulation. By definition a successful simulation observed 50% of our catalog. Similar considerations using the same GALAXIA output were done for the DRS “Disk/Bulge low-resolution” that contained four sub-samples and also for the DRS “Halo high-resolution” (H. Ludwig). A comprehensive documentation of the preparation of the science cases and DRSs for 4MOST can be found in the scientific report that was included in the 4MOST proposal for ESO (Chiappini et al. 2013).

This example illustrates the likely development to more complex selection functions for massive spectroscopic surveys. Another, real, example for a survey with a complex selection function is the SDSS extension SEGUE that has a multitude of target categories. The most widely used category is the G dwarf sample (Lee et al. 2011; Bovy et al. 2012c; Schlesinger et al. 2012) that has a pure color selection and hence should be kinematically – and to a large degree also chemically – unbiased. Clearly, not all stars in the Galaxy carry the same amount of information about the general structure of the system. An extreme case are the very few stars in thin stellar stream GD-1 that allow to find strong constraints on the global shape of the Galactic gravitational potential (Koposov et al. 2010). It is hence imperative to tune the target list and sort out stars that would add little information to a data base. However, the balance has to be kept for the selection process to be reproducible in order to preserve the statistical validity of the sample. Our selection criteria for the 4MOST targets were specifically defined to obtain a directly recoverable selection function. Due to the expected dramatic increase in a priori knowledge from Gaia and other surveys this selection function can and must be more sophisticated.

3.6 Discussion

The generation of synthetic observations, be it to mimic existing data or to plan future observations, requires contributions from many other fields in addition to the Galaxy model itself. Many of those are still under debate themselves, for example the shape and universality of the IMF. There is also much uncertainty in the stellar atmosphere models and the isochrones, in particular concerning stellar populations with non-solar abundance patterns (e.g. α -enhancement). The shift in the $\log g$ distributions between model and RAVE data illustrates this clearly. The stellar parameters represent characteristic values that are used to classify the stars with respect to each other rather than they are used in their original physical meaning. The problem of differing scales for the stellar parameters is a general one that is always present when different (synthetic or real) surveys are compared. A solution will be needed in the near future if surveys like RAVE and SEGUE which have no stars in common should be productively combined. Synthetic copies of the data set based on the same model might be able to help for this issue.

Another open question is interstellar extinction and its unclear 3-dimensional distribution. By focusing on the RAVE survey we were able to circumvent this problem, because RAVE itself avoided sky regions with high extinction. Other surveys, e.g. APOGEE, that observe in the infrared wavelength region have observations at low Galactic latitudes where a lot of dust is in the lines of sights. If we wanted to model such surveys we need better dust maps of the Galaxy. Efforts to produce such maps have been done (Marshall et al. 2006) or are under way (Sale et al. 2009; Schlafly et al. 2013).

Despite these uncertainties we find good agreement between the models and the RAVE data. While the good performance of the Besançon model could be explained with the fact that the model was fitted to observational data using the exact same set of isochrones etc., this does not hold for the MCM model. The consistency of the two models and the data is hence a remarkable result. The ability of the MCM model to reproduce the chemodynamical results found by Boeche et al. (2013a) rises some hope that the model indeed covers important parts of the evolution our Galaxy. Future observations that allow at least rough age determinations could further test the predictions by the model on the age distributions in the dynamically selected sub-samples.

The deficiency of stars that are moderately metal-poor in the MCM model illustrates, however, that the model is yet incomplete. Minchev et al. (2013a) explicitly neglected a separate thick disk population to test whether a (single-infall) model with only one disk component can already explain the data. Our finding point to a missing component in addition to the stellar halo.

Our test with a full cosmological simulation showed that the detailed structure of the color and stellar parameter distributions contain information on the global structure of the Galaxy. The too low disk-to-bulge ratio in the Galaxy model was clearly detectable in the data as was the too thick disk component. The effect of varying disk thickness could already be seen in our evaluation of the influence of the GALAXIA processing options when we tested different smoothing options. A larger spatial smoothing length effectively thickens the disk and a characteristic change in the relative heights of the dwarf and giant peaks in the $\log g$ distribution could be observed.

A next step for this line of research is clearly an extension to other surveys. A study with the SEGUE survey could clearly shed more light on the structure of the thick disk and the inner stellar halo.

4 The Galactic escape speed and the mass of the Galaxy*

We will now turn to a completely different study that also makes use of the RAVE survey in combination with cosmological simulations. This time, however, the focus is more on the RAVE data and its information content itself. RAVE was specifically designed to provide a kinematically unbiased sample of stars. However, due to its magnitude-limited nature it contains a distance bias favoring stars with a distance between 0.2 and 1.5 kpc (e.g. Figure 3.7). The specific spatial extent of the RAVE stars has to be taken into account even for a purely kinematic study, because velocity is clearly correlated with position in the Galaxy. In the following we will select a sample of high-velocity halo stars for which this correlation is well understood and therefore can be accounted for. This application is hence one of the few examples where we can extract a general property of the Galaxy – the (local) Galactic escape speed and the virial mass – almost without a detour over a comprehensive model of the Galaxy. We write ‘almost’, because in fact we will use a set of simulated galaxies to obtain prior knowledge on a nuisance parameter we want to marginalize over during the analysis.

In the recent years quite a large number of studies concerning the mass of our Galaxy were published. This parameter is of particular interest, because it provides a test for the current cold dark matter paradigm. There is now convincing evidence (e.g. Smith et al. 2007) that the Milky Way (MW) exhibits a similar discrepancy between luminous and dynamical mass estimates as was already found in the 1970’s for other galaxies. A robust measurement of this parameter is needed to place the Milky Way in the cosmological framework. Furthermore, a detailed knowledge of the mass and the mass profile of the Galaxy is crucial for understanding and modeling the dynamic evolution of the MW satellite galaxies (e.g. Kallivayalil et al. (2013) for the Magellanic clouds) and the Local Group (van der Marel et al. 2012b,a). Generally, it can be observed, that mass estimates based on stellar kinematics yield low values $\lesssim 10^{12} M_{\odot}$ (Smith et al. 2007; Xue et al. 2008; Kafle et al. 2012; Deason et al. 2012; Bovy et al. 2012a), while methods exploiting the kinematics of satellite galaxies or statistics of large cosmological dark matter simulations find larger values (Wilkinson & Evans 1999; Li & White 2008; Boylan-Kolchin et al. 2011; Busha et al. 2011; Boylan-Kolchin et al. 2013). There are some exceptions, however. For example, Przybilla et al. (2010) find a rather high value of $1.7 \times 10^{12} M_{\odot}$ taking into account the star J1539+0239, a hyper-velocity star approaching the MW. On the other hand Vera-Ciro et al. (2013) estimate a most likely MW mass of $0.8 \times 10^{12} M_{\odot}$ analyzing the Aquarius simulations (Springel et al. 2008) in combination with semi-analytic models of galaxy formation. Watkins et al. (2010) report an only slightly higher value based on the line of sight velocities of satellite galaxies (see also

*Content and text of this chapter have almost identically been published as Piffil et al. (2014). See also the remarks at the end of the Introduction (Chapter 1). Credit: Piffil et al., A&A, 562, A91, 2014, reproduced with permission ©ESO.

Sales et al. (2007)), but when they include proper motion estimates they again find a higher mass of $1.4 \times 10^{12} M_{\odot}$. Using a mixture of stars and satellite galaxies Battaglia et al. (2005, 2006) also favor a low mass below $10^{12} M_{\odot}$. McMillan (2011) found an intermediate mass of $1.3 \times 10^{12} M_{\odot}$ including also constraints from photometric data. A further complication of the matter comes from the definition of the total mass of the Galaxy which is different for different authors and so a direct comparison of the quoted values has to be done with care. Finally, there is an independent strong upper limit for the Milky Way mass coming from Local Group timing arguments that estimate the total mass of the combined mass of the Milky Way and Andromeda to $3.2 \pm 0.6 \times 10^{12} M_{\odot}$ (van der Marel et al. 2012b).

In this study we attempt to estimate the mass of the MW through measuring the escape speed at several Galactocentric radii. In this we follow up on the studies by Leonard & Tremaine (1990), Kochanek (1996) and Smith et al. (2007) (S07, hereafter). The latter work made use of an early version of the RAVE survey.

The escape speed measures the depth of the potential well of the Milky Way and therefore contains information about the mass distribution exterior to the radius for which it is estimated. It thus constitutes a local measurement connected to the very outskirts of our Galaxy. In the absence of dark matter and a purely Newtonian gravity law we would expect a local escape speed of $\sqrt{2}V_{\text{LSR}} = 311 \text{ km s}^{-1}$, assuming the local standard of rest, V_{LSR} to be 220 km s^{-1} and neglecting the small fraction of visible mass outside the solar circle (Fich & Tremaine 1991). However, the estimates in the literature are much larger than this value, starting with a minimum value of 400 km s^{-1} (Alexander 1982) to the currently most precise measurement by S07 who find $[498, 608] \text{ km s}^{-1}$ as 90% confidence range.

4.1 Methodology

The basic analysis strategy applied in this study initially introduced by Leonard & Tremaine (1990) and later extended by S07. They assumed that the stellar system could be described by an ergodic distribution function (DF) $f(E)$ that satisfied $f \rightarrow 0$ as $E \rightarrow \Phi$, the local value of the gravitational potential $\Phi(\vec{r})$. Then the density of stars in velocity space will be a function $n(v)$ of speed v and tend to zero as $v \rightarrow v_{\text{esc}} = (2\Phi)^{1/2}$. Leonard & Tremaine (1990) proposed that the asymptotic behavior of $n(v)$ could be modeled as

$$n(v) \propto (v_{\text{esc}} - v)^k, \quad (4.1)$$

for $v < v_{\text{esc}}$, where k is a parameter. Hence we should be able to obtain an estimate of v_{esc} from a local sample of stellar velocities. S07 used a slightly different functional form

$$n(v) \propto (v_{\text{esc}}^2 - v^2)^k = (v_{\text{esc}} - v)^k (v_{\text{esc}} + v)^k, \quad (4.2)$$

but, as we will see in Section 4.2, results from cosmological simulations are better approximated by Eq. 4.1.

Currently, the most accurate velocity measurements are line-of-sight velocities, v_{los} , obtained from spectroscopy via the Doppler effect. These measurements have typically uncertainties of a few km s^{-1} , which is an order of magnitude smaller than the typical uncertainties on tangential velocities obtained from proper motions currently available. Leonard & Tremaine (1990) already showed that because of this, estimates from radial velocities alone are as accurate as estimates that use proper motions as well (Fich & Tremaine 1991). The measured velocities v_{los} have to be corrected for the solar motion to enter a Galactocentric rest frame.

Table 4.1: Structural parameters of the baryonic components of our Galaxy model

| disk | | |
|------------------------|----------------------|-----------|
| scale length R_d | 4 | kpc |
| scale height z_d | 0.3 | kpc |
| mass M_d | 5×10^{10} | M_\odot |
| bulge and stellar halo | | |
| scale radius r_b | 0.6 | kpc |
| mass M_b | 1.5×10^{10} | M_\odot |

These corrected velocities we denote with v_{\parallel} .

Following Leonard & Tremaine (1990) we can infer the distribution of v_{\parallel} by integrating over all perpendicular directions:

$$\begin{aligned} n_{\parallel}(v_{\parallel} \mid \vec{r}, k) &\propto \int d\vec{v} n(\vec{v} \mid \vec{r}, k) \delta(v_{\parallel} - \vec{v} \cdot \vec{m}) \\ &\propto \left(v_{\text{esc}}(\vec{r}) - |v_{\parallel}| \right)^{k+1} \end{aligned} \quad (4.3)$$

again for $|v_{\parallel}| < v_{\text{esc}}$. Here δ denotes the Dirac delta function and \vec{m} represents a unit vector along the line of sight.

We do not expect that our approximation for the velocity DF is valid over the whole range of velocities, but only at the high velocity tail of the distribution. Hence we impose a lower limit v_{min} for the stellar velocities. A further important requirement is that the stellar velocities come from a population that is not rotationally supported, because such a population is clearly not described by an ergodic DF. In the case of stars in the Galaxy, this means that we have to select for stars of the Galactic stellar halo component.

We now apply the following approach to the estimation of v_{esc} . We adopt the likelihood function

$$L(v_{\parallel}) = \frac{(v_{\text{esc}} - |v_{\parallel}|)^{k+1}}{\int_{v_{\text{min}}}^{v_{\text{esc}}} dv (v_{\text{esc}} - |v_{\parallel}|)^{k+1}} = \frac{k+2}{2} \frac{(v_{\text{esc}} - |v_{\parallel}|)^{k+1}}{(v_{\text{esc}} - v_{\text{min}})^{k+2}} \quad (4.4)$$

and determine the likelihood of our catalog of stars that have $|v_{\parallel}| > v_{\text{min}}$ for various choices of v_{esc} and k , then we marginalize the likelihood over the nuisance parameter k and determine the true value of v_{esc} as the speed that maximizes the marginalized likelihood.

4.1.1 Non-local modeling

Leonard & Tremaine (1990) (and in a similar form also S07) used Eq. 4.3 and the maximum likelihood method to obtain constraints on v_{esc} and k in the solar neighborhood. This rests on the assumption that the stars of which the velocities are used are confined to a volume that is small compared to the size of the Galaxy and thus that v_{esc} is approximately constant in this volume.

In this study we go a step further and take into account the individual positions of the stars. We do this in two slightly different ways: (1) one can sort the data into Galactocentric radial distance bins and analyze these independently. (2) Alternatively all velocities in the sample are re-scaled to the escape speed at the Sun's position,

$$v'_{\parallel,i} = v_{\parallel,i} \left(\frac{v_{\text{esc}}(\vec{r}_0)}{v_{\text{esc}}(\vec{r}_i)} \right) = v_{\parallel,i} \sqrt{\frac{|\Phi(\vec{r}_0)|}{|\Phi(\vec{r}_i)|}}, \quad (4.5)$$

where \vec{r}_0 is the position vector of the Sun. For the gravitational potential, $\Phi(\vec{r})$, model assumptions have to be made. This approach makes use of the full capabilities of the maximum likelihood method to deal with un-binned data and thereby exploit the full information available.

We will compare the two approaches using the same mass model: a Miyamoto & Nagai (1975) disk and a Hernquist (1990) bulge for the baryonic components and for the dark matter halo an original or an adiabatically contracted NFW profile (Navarro et al. 1996; Mo et al. 1998). As structural parameters of the disk and the bulge we use common values that were also used by S07 and Xue et al. (2008) and are given in Table 4.1. The NFW profile has, apart from its virial mass M_{340} , the (initial) concentration parameter c as a free parameter. In most cases we fix c by requiring the circular speed at the solar radius, $v_{\text{circ}}(R_0)$, to be equal to the local standard of rest, V_{LSR} (after a possible contraction of the halo). As a result our simple model has only one free parameter, namely its virial mass. For our results from the first approach using Galactocentric bins we alternatively apply a prior for c taken from the literature to reduce our dependency on the somewhat uncertain value of the local standard of rest.

4.1.2 General behavior of the method

To learn more about the general reliability of our analysis strategy we created random velocity samples drawn from a distribution according to Eq. 4.3 with $v_{\text{esc}} = 550 \text{ km s}^{-1}$ and $k = 4.3$. For each sample we computed the maximum likelihood values for v_{esc} and k . The left panel of Figure 4.1 shows the resulting parameter distributions for three different sample sizes: 30, 100 and 1000 stars. 5000 samples were created for each value. One immediately recognizes a strong degeneracy between v_{esc} and k and that the method tends to find parameter pairs with a too low escape speed. This behavior is easy to understand if one considers the asymmetric shape of the velocity distribution. The position of the maximum likelihood pair strongly depends on the highest velocity in the sample – if the highest velocity is relatively low the method will favor a too low escape speed. This demonstrates the need for additional knowledge about the power-index k as was already noticed by S07.

4.2 Constraints for k from cosmological simulations

Almost all of the recent estimates of the Milky Way mass made use of cosmological simulations (e.g. Smith et al. 2007; Xue et al. 2008; Busha et al. 2011; Boylan-Kolchin et al. 2013). In particular, those estimates which rely on stellar kinematics (Smith et al. 2007; Xue et al. 2008) make use of the realistically complex stellar velocity distributions provided by numerical experiments. In this study we also follow this approach. S07 used simulations to show that the velocity distributions indeed reach all the way up to the escape speed, but more importantly from the simulated stellar kinematics they derived priors on the power-law index k . This was fundamental for their study on account of the strong degeneracy between k and the escape speed shown in Figure 4.1 (left panel), because their data themselves were not enough to break this degeneracy. As we will show later, despite our larger data set we still face the same problem. However, with the advanced numerical simulations available today we can do a much more detailed analysis.

In this study we make use of the simulations by Scannapieco et al. (2009) that we described

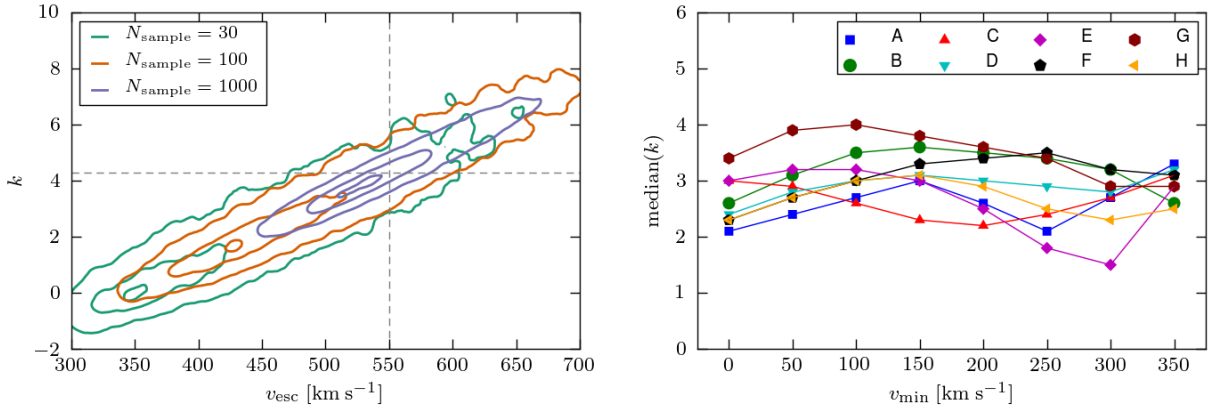


Figure 4.1: *Left panel*: Maximum likelihood parameter pairs computed from mock velocity samples of different size. The dotted lines denote the input parameters of the underlying velocity distribution. The contour lines denote positions where the number density fell to 0.9, 0.5 and 0.05 times the maximum value. *Right panel*: Median values of the likelihood distributions of the power-law index k as a function of the applied threshold velocity v_{min} .

in Section 2.2. An important aspect of the Scannapieco et al. (2009) sample is that the eight simulated galaxies have a broad variety of merger and accretion histories, providing a more or less representative sample of Milky Way-mass galaxies formed in a Λ CDM universe (Scannapieco et al. 2011). Our set of simulations is thus useful for the present study, since it gives us information on the evolution of various galaxies, including all the necessary cosmological processes acting during the formation of galaxies, and at a relatively high resolution.

We remind the reader that we re-scaled the simulations to have a circular speed at the solar radius, $R_0 = 8.28$ kpc, of 220 km s^{-1} to allow a better comparison to the Milky Way. The resulting masses, M_{340} , radii, R_{340} , and velocities, V_{340} as well as the scaling factors are given in Table 2.2. Throughout this study we use a Hubble constant $H = 73 \text{ km s}^{-1} \text{ Mpc}^{-1}$ and define the virial radius to contain a mean matter density $340 \rho_{\text{crit}}$, where $\rho_{\text{crit}} = 3H^2/8\pi G$ is the critical energy density for a closed universe.

Since the galaxies in the simulations are not isolated systems, we have to define a limiting distance above which we consider a particle to have escaped its host system. We set this distance to $3R_{340}$ and set the potential to zero at this radius which results in distances between 430 and 530 kpc in the simulations. This choice is an educated guess and our results are not sensitive to small changes, because the gravitational potential changes only weakly with radius at these distances and in addition, the resulting escape speed is only proportional to the square root of the potential. However, we must not choose a too small value, because otherwise we underestimate the escape speed encoded in the stellar velocity field. On the other hand, we must cut in a regime where the potential is yet not dominated by neighboring (clusters of) galaxies. Our choice is in addition close to half of the distance of the Milky Way and its nearest massive neighbor, the Andromeda galaxy. We further test our choice below. With this definition of the cut-off radius we obtain local escape speeds at R_0 from the center between 475 and 550 km s^{-1} .

Now we select a population of star particles belonging to the stellar halo component. In many numerical studies the separation of the particles into disk and bulge/halo populations is done using a circularity parameter which is defined as the ratio between the particle's angular

momentum in the z -direction² and the angular momentum of a circular orbit either at the particle’s current position (Scannapieco et al. 2009, 2011) or at the particle’s orbital energy (Abadi et al. 2003b). A threshold value is then defined which divides disk and bulge/halo particles. We opt for the very conservative value of 0 which means that we only take counter-rotating particles. Practically, this is equivalent to selecting all particles with a positive tangential velocity w.r.t the Galactic center. This choice allows us to do exactly the same selection as we will do later with the real observational data for which we have to use a very conservative value because of the larger uncertainties in the proper motion measurements. For similar reasons we also keep only particles in our sample that have Galactocentric distances between 4 and 12 kpc which reflects the range of values of the stars in the RAVE survey which we will use for this study. This further ensures that we exclude particles belonging to the bulge component.

Finally, we set the distance R_0 of the observer from the Galactic center to be 8.28 kpc and choose an azimuthal position ϕ_0 and compute the line-of-sight velocity $v_{\parallel,i}$ for each particle in the sample. We further know the exact potential energy Φ_i of each particle and therefore their local escape speed $v_{\text{esc},i}$ is easily computed.

We do this for 4 different azimuthal positions separated from each other by 90° . The positions were chosen such that the inclination angle w.r.t. a possible bar is 45° . The corresponding samples are analyzed individually and also combined. Note that these samples are practically statistically independent even though a particle could enter two or more samples. However, because we only consider the line-of-sight component of the velocities, only in the unlikely case that a particle is located exactly on the line-of-sight between two observer positions it would gain an incorrect double weight in the combined statistical analysis.

Figure 4.2 shows the velocity-space density of star particles as a function of $1 - v_{\parallel}/v_{\text{esc}}$ and we see that, remarkably, at the highest speeds these plots have a reasonably straight section, just as Leonard & Tremaine (1990) hypothesized. The slopes of these rectilinear sections scatter around $k = 3$ as we will see later.

We also considered the functional form proposed by S07 for the velocity DF, that is $n(v) \propto (v_{\text{esc}}^2 - v^2)^k$. Figure 4.3 tests this DF with the simulation data. The curvature implies that this DF does not represent the simulation data as good as the formula proposed by Leonard & Tremaine (1990).

If we fit Eq. 4.3 to the velocity distributions while fixing k to 3 we recover the escape speeds within 6%. This confirms our choice of the cut-off radius for the gravitational potential, $3R_{340}$, that was used during the definition of the escape speeds.

4.2.1 The velocity threshold

We now try to find the best value for the lower threshold velocity v_{min} . S07 had to use a high threshold value for their radial velocities of 300 km s^{-1} , because the threshold had an additional purpose, namely to select for stars from the non-rotating halo component. If one can identify these stars by other means the velocity threshold can be lowered significantly. This adds more stars to the sample and thereby puts our analysis on a broader basis. If the stellar halo had the shape of an isotropic Plummer (1911) sphere the threshold could be set to zero, because for this model our approximated velocity distribution function would be exact. However, for other DFs we need to choose a higher value to avoid regions where our approximation breaks down. Again, we use the simulations to select an appropriate value.

²The coordinate system is defined such that the disk rotates in the $x - y$ -plane.

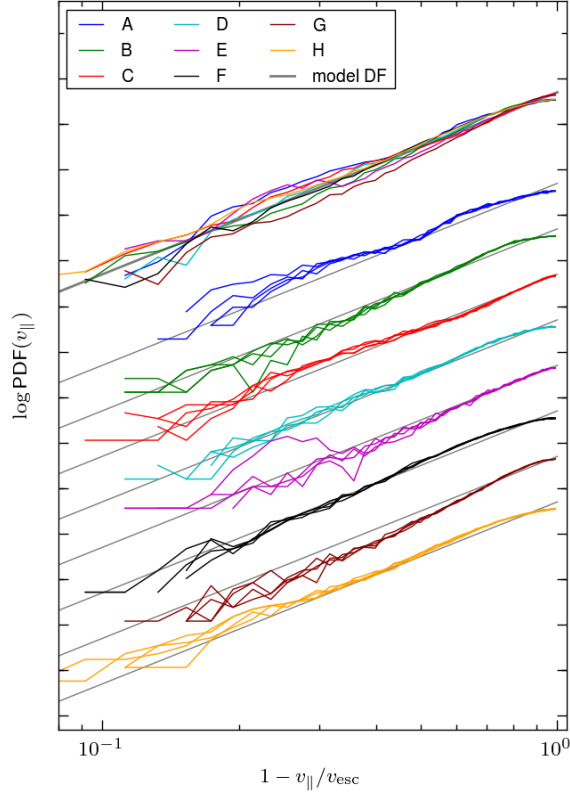


Figure 4.2: Normalized velocity distributions of the stellar halo population in our 8 simulations plotted as a function of $1 - v_{\parallel}/v_{\text{esc}}$. Only counter-rotating particles that have Galactocentric distances r between 4 and 12 kpc are considered to select for halo particles (see Section 4.2.1) and to match the volume observed by the RAVE survey. To allow a comparison each velocity was divided by the escape speed at the particle’s position. Different colors indicate different simulations and for each simulation the v_{\parallel} distribution is shown for four different observer positions. The up-most bundle of curves shows the mean of these four distributions for each simulation plotted on top of each other to allow a comparison. The profiles are shifted vertically in the plot for better visibility. The gray lines illustrate Eq. 4.3 with power-law index $k = 3$.

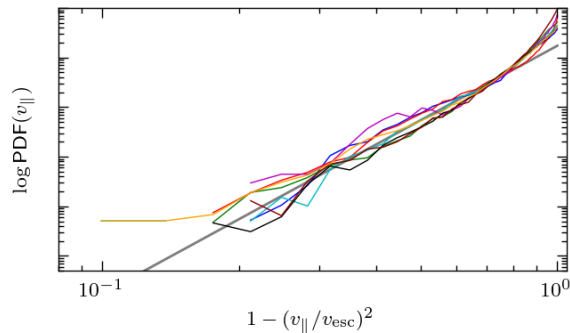


Figure 4.3: Same as the upper bundle of lines in Figure 4.2 but plotted as a function of $1 - v_{\parallel}^2/v_{\text{esc}}^2$. If the data would follow the velocity DF proposed by S07 (gray line) the data should form a straight line in this representation.

We compute the likelihood distribution of k in each simulation using different velocity thresholds using the likelihood estimator

$$L_{\text{tot}}(k | v_{\text{min}}) = \prod_i L(v_{\parallel,i}). \quad (4.6)$$

The right panel of Figure 4.1 plots the median values of the likelihood distributions as a function of the threshold velocity. We see a trend of increasing k for $v_{\text{min}} \lesssim 150 \text{ km s}^{-1}$ and roughly random behavior above. For low values of v_{min} simulation G does not follow the general trend. This simulation is the only one in the sample that has a dominating bar in its center (Scannapieco & Athanassoula 2012) which could contain counter-rotating stars. Before this background a likely explanation for its peculiar behavior is that with a low velocity threshold bar particles start entering the sample and thereby alter the velocity distribution.

Simulation E exhibits a dip around $v_{\text{min}} \simeq 300 \text{ km s}^{-1}$. A spatially dispersed stellar stream of significant mass is counter-orbiting the galaxy and is entering the sample for one of the observer positions. This is also clearly visible in Figure 4.2 as a bump in one of the velocity distributions between 0.2 and 0.3. Furthermore, this galaxy has a rapidly rotating spheroidal component (Scannapieco et al. 2009).

The galaxy in Simulation C has a satellite galaxy very close by. We exclude all star particle in a sphere of 3 kpc around the satellite center from our analysis, but there will still be particles entering our samples which originate from this companion and which do not follow the general velocity DF.

All three cases are unlikely to apply for our Milky Way. Our galaxy hosts a much shorter bar and up to now no signatures of a massive stellar stream were found in the RAVE data (Seabroke et al. 2008; Williams et al. 2011; Antoja et al. 2012). However, it is very interesting to see how our method performs in these rather extreme cases.

We adopt a threshold velocity $v_{\text{min}} = 200 \text{ km s}^{-1}$ and 300 km s^{-1} . Both are far enough from the regime where we see systematic evolution in the k values ($v_{\text{min}} \leq 150 \text{ km s}^{-1}$). For the latter we can drop the criteria for the particles to be counter-rotating because we can expect the contamination by disk stars to be negligible (S07) and thus partly compensate for the reduced sample size.

4.2.1.1 An optimal prior for k

From Figure 4.1 (right panel) it seems clear that the different simulated galaxies do not share exactly the same k , but cover a considerable range of values. Thus in the analysis of the real data we will have to consider this whole range. We fix the extent of this range by requiring that it delivers optimal results for all four observer positions in all eight simulated galaxies. Hence we applied our analysis to the simulated data by computing the posterior probability distribution

$$p(v_{\text{esc}}) \propto \int_{k_{\text{min}}}^{k_{\text{max}}} dk \prod_i L(v'_{\parallel,i} | v_{\text{esc}}, k), \quad (4.7)$$

where L was defined in Eq. 4.4 and $v'_{\parallel,i}$ is the i th re-scaled line-of-sight velocity as defined in Eq. 4.5. We define the median of $p(v_{\text{esc}})$, \tilde{v}_{esc} , as the best estimate. For a comparison of the estimates between different simulations we consider the normalized estimate $\hat{v}_{\text{esc}} = \tilde{v}_{\text{esc}}/v_{\text{esc,true}}$ with $v_{\text{esc,true}}$ being the true local escape speed in the simulation. By varying k_{min} and k_{max} we identify those values that minimize the scatter in the sample of 32 \hat{v}_{esc} values and at the

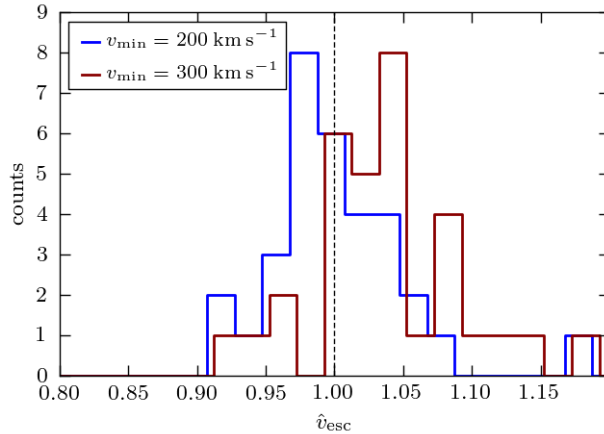


Figure 4.4: Distribution of \hat{v}_{esc} resulting from our 32 test runs of our analysis on simulation data equipped with RAVE-like observational errors and observed in a RAVE-like sky region. In each of the eight simulations four different azimuthal observer positions were tested. A value of unity means an exact recovery of the true local escape speed. The two histograms correspond to our two velocity thresholds applied to the data.

same time leave the median of the sample close to unity. We find very similar intervals for both threshold velocities and adopt the interval

$$2.3 < k < 3.7. \quad (4.8)$$

Reassuringly, this is very close to the lower part of the interval found by S07 (2.7 – 4.7) using a different set of simulations. The scatter of the \hat{v}_{esc} values is smaller than 3.5% (1σ) for both velocity thresholds. This scatter cannot be completely explained by the statistical uncertainties of the estimates, so there seems to be an additional uncertainty intrinsic to our analysis technique itself. We will try to quantify this in the next section.

4.2.1.2 Realistic tests

One important test for our method is whether it still yields correct results if we have imperfect data and a non-isotropic distribution of lines of sight. To simulate typical RAVE measurement errors we attached random Gaussian errors on the parallaxes (distance^{-1}), radial velocities and the two proper motion values with standard deviations of 30%, 3 km s^{-1} and 2 mas, respectively. We computed the angular positions of each particle (for a given observer position) and selected only those particles which fell into the approximate survey geometry of the RAVE survey. The latter we define by declination $\delta < 0^\circ$ and galactic latitude $|b| > 15^\circ$.

Figure 4.4 shows the resulting distributions of \hat{v}_{esc} for the two velocity thresholds. Again, the width of the distributions cannot be solely explained by the statistical uncertainties computed from the likelihood distribution, but an additional uncertainty of $\simeq 4\%$ is required to explain the data in a Gaussian approximation. The distribution for $v_{\text{min}} = 300 \text{ km s}^{-1}$ in addition exhibits a shift to higher values by $\simeq 3\%$. Due to the low number statistics the significance of the shift is unclear ($\sim 3\sigma$). As we will see in Section 4.4, compared to the statistical uncertainties arising when we analyze the real data it would presents a minor contribution to the overall uncertainty and we neglect the shift for this study.

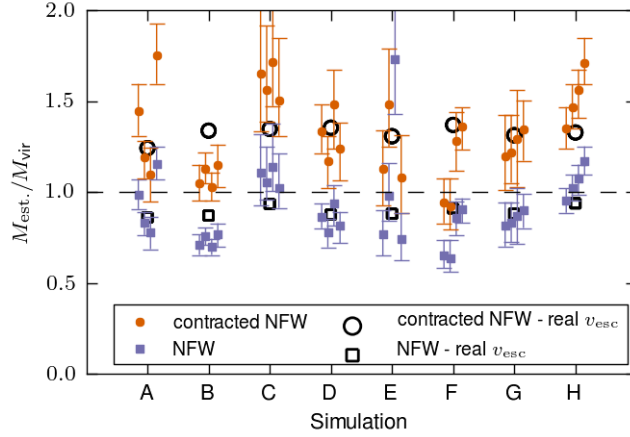


Figure 4.5: Ratios of the estimated and real virial masses in the 8 simulations. For each simulation four mass estimates are plotted based on four azimuthal positions of the Sun in the galaxy. The symbols with error-bars represent the estimates based on the median velocities \tilde{v}_{esc} obtained from the error-prone simulation data, while the black symbols show mass estimates for which the real escape speed was used as an input.

We can go a step further and try to recover the masses of the simulated galaxies using the escape speed estimates. To do this we use the original mass profile of the baryonic components of the galaxies to model our knowledge about the visual parts of the Galaxy and impose an analytic expression for the dark matter halo. As we will do for the real analysis we try two models: an unaltered and an adiabatically contracted NFW sphere. We adjust the halo parameters, the virial mass M_{340} and the concentration c , to match both boundary conditions, the circular speed and the escape speed at the solar radius. Figure 4.5 plots the ratios of the estimate masses and the real virial masses taken from the simulations directly. The adiabatically contracted halo on average over-estimates the virial mass by 25%, while the pure NFW halo systematically understates the mass by about 15%. For both halo models we find examples which obtain a very good match with the real mass (e.g. simulation B for the contracted halo and simulation H for the pure NFW halo). However, the cases where the contracted halo yields better results coincide with those cases where the escape speed was underestimated. The colored symbols in Figure 4.5 mark the mass estimates obtained using the exact escape speed computed from the gravitational potential in the simulation directly. This reveals that the mass estimates from the two halo models effectively bracket the real mass as expected. Note that we also recover the masses of the three simulations C, E and G that show peculiarities in their velocity distributions. Only for simulation E we completely fail to recover the mass for one azimuthal position of the observer. In this case there is a prominent stellar stream moving in the line of sight direction.

4.3 Data

4.3.1 Sample selection in RAVE

The major observational data for this study comes from the fourth data release (DR4) of RAVE survey (see Section 2.1). The wealth of information in the RAVE survey presents an

ideal foundation for our study. Compared to S07 the amount of available spectra has grown by a factor of 10 and at that time there were only velocities derived from the spectra. The number of high-velocity stars has unfortunately not increased by the same factor, which is most likely due to the fact that RAVE concentrated more on lower Galactic latitudes where the relative abundance of halo stars – which can have these high velocities – is much lower. We use only high-quality observations by selecting only stars which fulfill the following criteria:

- the stars must be classified as 'normal' according to the classification by Matijević et al. (2012),
- the Tonry-Davis correlation coefficient computed by the RAVE pipeline measuring the quality of the spectral fit (Steinmetz et al. 2006) must be larger than 10,
- the radial velocity correction due to calibration issues (cf. Steinmetz et al. 2006) must be smaller than 10 km s^{-1} ,
- the signal-to-noise ratio (S/N) must be larger than 25,
- the stars must have a distance estimate by Binney et al. (2014),
- the star must not be associated with a stellar cluster.

The first requirement ensures that the star's spectrum can be well fitted with a synthetic spectral library and excludes, among other things, spectral binaries. The last criterion removes in particular the giant star (RAVE-ID J101742.6-462715) from the globular cluster NGC 3201 that would have otherwise entered our high-velocity samples. Stars in gravitationally self-bound structures like globular clusters, are clearly not covered by our smooth approximation of the velocity distribution of the stellar halo. We further excluded two stars (RAVE-IDs J175802.0-462351 and J142103.5-374549) because of their peculiar location in the physical Hertzsprung-Russell diagram³ (green symbols in Figure 4.7).

In some cases RAVE observed the same target multiple times. In this case we adopt the measurements with the highest S/N, except for the line-of-sight velocities, v_{los} , where we use the mean value. The median S/N of the high-velocity stars used in the later analysis is 56. We then convert the precisely measured v_{los} into the Galactic rest-frame using the following formula:

$$v_{\parallel,i} = v_{\text{los},i} + (U_{\odot} \cos l_i + (V_{\odot} + V_{\text{LSR}}) \sin l_i) \cos b_i + W_{\odot} \sin b_i, \quad (4.9)$$

We define the local standard of rest, V_{LSR} , to be 220 km s^{-1} and for the peculiar motion of the Sun we adopt the values given by Schönrich et al. (2010): $U_{\odot} = 11.1 \text{ km s}^{-1}$, $V_{\odot} = 12.24 \text{ km s}^{-1}$ and $W_{\odot} = 7.25 \text{ km s}^{-1}$.

As mentioned in Section 4.1 we need to construct a halo sample and we do this in the same way as done for the simulation data. We compute the Galactocentric tangential velocities, v_{ϕ} , of all stars in a Galactocentric cylindrical polar coordinate system using the line-of-sight velocities, proper motions, distances and the angular coordinates of the stars. For the distance between the Sun and the Galactic center we use the value $R_0 = 8.28 \text{ kpc}$ (Gillessen et al. 2009). We performed a full uncertainty propagation using the Monte-Carlo technique with 2000 re-samplings per star to obtain the uncertainties in v_{ϕ} . As already done for the simulations we discard all stars with positive v_{ϕ} and also those for which the upper end of the 95% confidence interval of v_{ϕ} reaches above 100 km s^{-1} to obtain a pure stellar halo sample. This is important because a contamination of stars from the rapidly rotating disk

³Including these stars does not significantly affect our results.

component(s) would invalidate our assumptions made in Section 4.1. Note that only for this step we make use of proper motions.

We use the measurements from the UCAC4 catalog (Zacharias et al. 2013) and we avoid entries that are flagged as (projected) double star in UCAC4 itself or in one of the additional source catalogs that are used for the proper motion estimate. In such cases we perform the Monte-Carlo analysis with a flat distribution of proper motions between -50 and 50 mas yr^{-1} , both in Right Ascension, α and declination, δ .

In principle, we could also use a metallicity criterion to select halo stars. There are several reasons why we did not opt for this. First, we want to be able to reproduce our selection in the simulations. Unfortunately, the simulated galaxies are all too metal-poor compared to the Milky Way (Tissera et al. 2012) and are thus not very reliable in this aspect. This is particularly important in the context of the findings by Schuster et al. (2012) who identified correlations between kinematics and metal abundances in the stellar halo that might be related to different origins of the stars (in-situ formation or accretion). Note, however, that despite the unrealistic metal abundances the formation of the stellar halo is modeled realistically in the simulations including all aspects of accretion and in-situ star formation. In the simulated velocity distributions (Figure 4.2) we do not detect any characteristic features that would indicate that the duality of the stellar halo as found by Schuster et al. (2012) is relevant for our study. Second, we would have to apply a very conservative metallicity threshold in order to avoid contamination by metal-poor disk stars. Because of this our sample size would not significantly increase using a metallicity criterion instead of a kinematic one.

It is worth mentioning, that the star with the highest $v_{\parallel} = -448.8 \text{ km s}^{-1}$ in the sample used by S07 (RAVE-ID: J151919.7-191359) did not enter our samples, because it was classified to have problems with the continuum fitting by Matijević et al. (2012). S07 showed via re-observations that the velocity measurement is reliable, however, the star did not get a distance estimate from Binney et al. (2014). Zwitter et al. (2010) estimate a distance of 9.4 kpc which, due to its angular position $(l, b) = (344.6^\circ, 31.4^\circ)$, would place the star behind and above the Galactic center. The star thus clearly violates the assumption by S07 to deal with a locally confined stellar sample and potentially leads to an over-estimate of the escape speed. For the sake of a homogeneous data set we ignored the alternative distance estimate by Zwitter et al. (2010) and discarded the star.

The left-most panel of Figure 4.6 depicts the velocities v'_{\parallel} of all RAVE stars as a function of Galactic longitude l and the two velocity thresholds $v_{\text{min}} = 200$ and 300 km s^{-1} . By selecting for a counter-rotating (halo) population (blue dots) we automatically select against the general sinusoidal trend of the RAVE stars in this diagram. The middle and right panels in Figure 4.6 illustrate the spatial distribution of our high-velocity sample. As a result of RAVE avoiding the low Galactic latitudes, stars with small Galactocentric radii are high above the Galactic plane. Furthermore, because RAVE is a southern hemisphere survey, the stars in the catalog are not symmetrically distributed around the Sun. The stars in our high-velocity sample are mostly giant stars with a metallicity distribution centered at -1.25 dex as can be seen in Figure 4.7.

4.3.2 Including other literature data

To increase our sample sizes we also consider other publicly available and kinematically unbiased data sets. We use the sample of metal-poor dwarf stars collected by Beers et al. (2000,

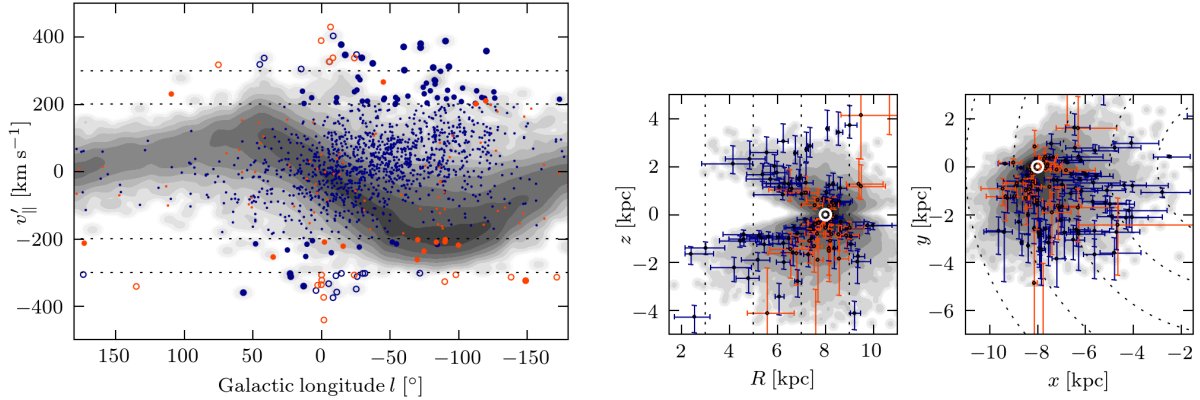


Figure 4.6: *Left panel:* Rescaled radial velocities, v'_r , of our high-velocity samples plotted against their Galactic longitudes, l . The dashed horizontal lines mark our threshold velocities, ± 200 and ± 300 km s^{-1} . Blue and orange symbols represent RAVE stars and B00 stars, respectively. Open circles mark stars that have $|v'_r| > 300$ km s^{-1} , while filled circles represent stars that have $|v'_r| > 200$ km s^{-1} and a classified as halo stars. Colored dots show all stars which we identify as halo stars, i.e. which are on counter-rotating orbits. The small gray dots illustrate the complete RAVE mother sample. *Middle and right panel:* Locations of the stars in our high-velocity sample in the R - z -plane (left panel) and the x - y -plane (right panel) as defined in the left-most panel. Blue and orange symbols represent RAVE stars and B00 stars, respectively. The error bars show 68% confidence regions ($\sim 1\sigma$). Grey dots show the full RAVE catalog and the position of the Sun is marked by a white ' \odot '. The dashed lines in both panels mark locations of constant Galactocentric radius $R = \sqrt{x^2 + y^2}$.

B00 hereafter). The authors also provide the full 6D phase space information including photometric parallaxes. We updated the proper motions by cross-matching with the UCAC4 catalog (Zacharias et al. 2013). We found new values for 2011 stars using the closest counterparts within a search radius of 5 arcsec. For ten stars we found two sources in the UCAC4 catalog closer than 5 arcsec and hence discarded these stars. There were further 5 cases where two stars in the B00 catalog have the same closest neighbor in the UCAC4 catalog. All these 10 stars were discarded as well. Finally, we kept only those stars with uncertainties in the line-of-sight velocity measurement below 15 km s^{-1} .

There is a small overlap of 123 stars with RAVE, 68 of which have a parallax estimate, ϖ , by Binney et al. (2014) with $\sigma(\varpi) < \varpi$. By chance two of these stars entered our high-velocity samples. This, on the first glance, very unlikely event is not so surprising if we consider our selection for halo stars, the strong bias towards metal-poor halo stars of the B00 catalog and the significant completeness of the RAVE survey $>50\%$ in the brighter magnitude bins (Kordopatis et al. 2013).

In order to compare the two distance estimates we convert all distances, d , into distance moduli, $\mu = 5 \log(d/10 \text{ pc})$, because both estimates are based on photometry, so the error distribution should be approximately⁴ symmetric in this quantity. We find that σ_{Beers} should be about 1.3 mag for the weighted differences (Figure 4.8, upper panel) to have a standard deviation of unity. B00 quote an uncertainty of 20% on their photometric parallax estimates,

⁴Note that Binney et al. (2014) actually showed that the RAVE parallax uncertainty distribution is close to normal. However, since both, the RAVE and the B00 distances, are based on the apparent magnitudes of the stars. Comparing the distance moduli seems to be the better choice, even though the uncertainties are not driven by the uncertainties in the photometry.

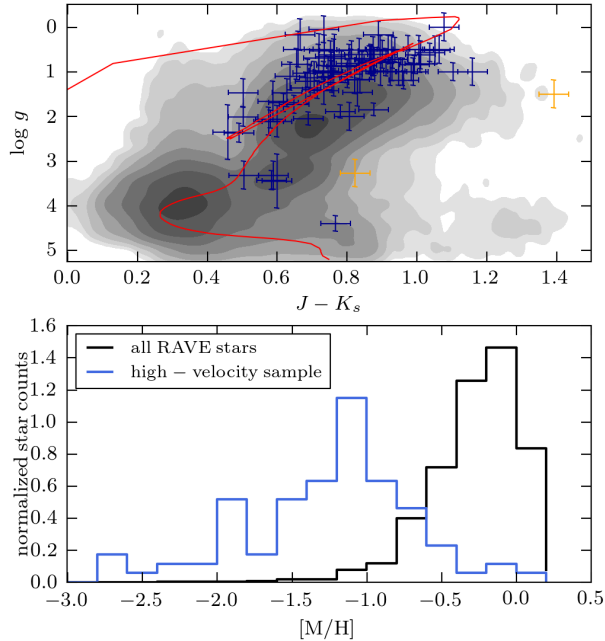


Figure 4.7: *Upper panel:* Distribution of our high-velocity stars as defined in Figure 4.6 in a physical Hertzsprung-Russell diagram (symbols with blue error-bars). For comparison the distribution of all RAVE stars (gray dots) and an isochrone of a stellar population with an age of 10 Gyr and a metallicity of -1 dex (red line) is also shown. The two green symbols represent two stars that were excluded from the samples because of their peculiar locations in this diagram. *Lower panel:* Metallicity distribution of our high-velocity sample (blue histogram). The black histogram shows the metallicity distribution all RAVE stars.

while our estimate corresponds to roughly 60%. We adopt our more conservative value and emphasize that this uncertainty is only used during the selection of counter-rotating halo stars.

We further find a systematic shift by a factor $f_{\text{dist}} = 1.5$ ($\delta\mu = 0.9$ mag) between the two distance estimates, in the sense that the B00 distances are greater. Since more information was taken into account to derive the RAVE distances we consider them more reliable. In order to have consistent distances we decrease all B00 distances by f_{dist}^{-1} and use these calibrated values in our further analysis.

The data set with the currently most accurately estimated 6D phase space coordinates is the Geneva-Copenhagen survey (Nordström et al. 2004) providing Hipparcos distances and proper motions as well as precise radial velocity measurements. However, this survey is confined to a very small volume around the Sun and therefore even stronger dominated by disk stars than the RAVE survey. We find only 2 counter-rotating stars in this sample with $|v_{\parallel}| > 200 \text{ km s}^{-1}$ as well as two (co-rotating) stars with $|v_{\parallel}| > 300 \text{ km s}^{-1}$. For the sake of homogeneity of our sample we neglect these measurements.

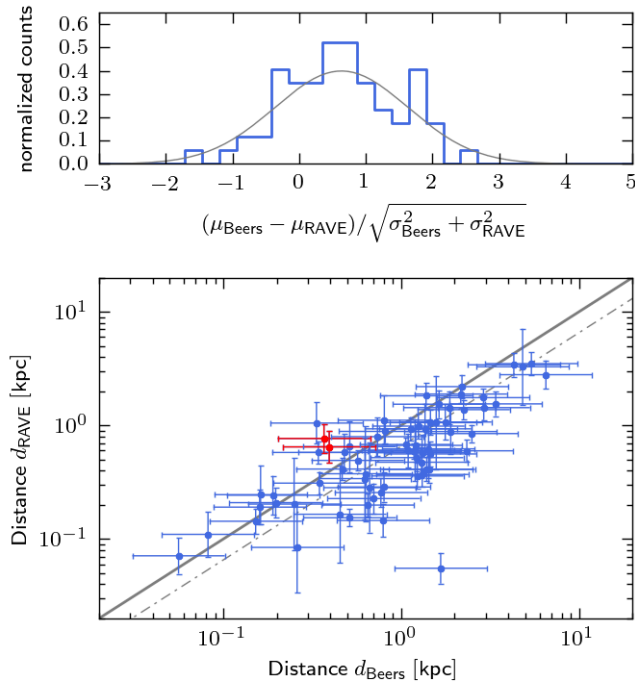


Figure 4.8: *Upper panel:* Distribution of the differences of the distance modulus estimates, μ , by B00 and Binney et al. (2014), divided by their combined uncertainty for a RAVE-B00 overlap sample of 68 stars. With $\sigma_{\text{Beers}} = 1.3$ mag we find a spread of 1σ in the distribution with the median shifted by $0.6\sigma \simeq 0.9$ mag. The gray curve shows a shifted normal distribution. The two red data points mark 2 stars which were also entering our high-velocity samples. *Lower panel:* Direct comparison of the two distance estimates with $1 - \sigma$ error bars. The solid gray line represents equality, while the dashed-dotted line marks equality after reducing the B00 distances by a factor of 1.5.

4.4 Results

4.4.1 Comparison to Smith et al. (2007)

As a first check we do an exact repetition of the analysis applied by S07 to see whether we get a consistent result. This is interesting because strong deviations could point to possible biases in the data due to, e.g., the slightly increased survey footprint of the sky. RAVE contains 76 stars fulfilling the criteria, which is an increase by a factor 5 (3 if we take the 19 stars from the B00⁵ catalog into account). The median values of the distributions are effectively the same (537 km s^{-1} instead of 544 km s^{-1}) and the uncertainties resulting from the 90% confidence interval ($[504, 574]$) are reduced by a factor 0.6 (0.7) for the upper (lower) margin, respectively. If we assume that the precision is proportional to the square root of the sample size we expect a decrease in the uncertainties of a factor $3^{-\frac{1}{2}} \simeq 0.6$.

With the distance estimates available now, we know that this analysis rests on the incorrect assumption that we deal with a local sample. If we apply a distance cut $d_{\text{max}} = 2.5$ kpc

⁵Due to the different values of the solar peculiar motion \vec{U}_{\odot} we have one more star than S07 from this catalog with $|v_{\parallel}| > 300 \text{ km s}^{-1}$. A further difference is our velocity uncertainty criterion.

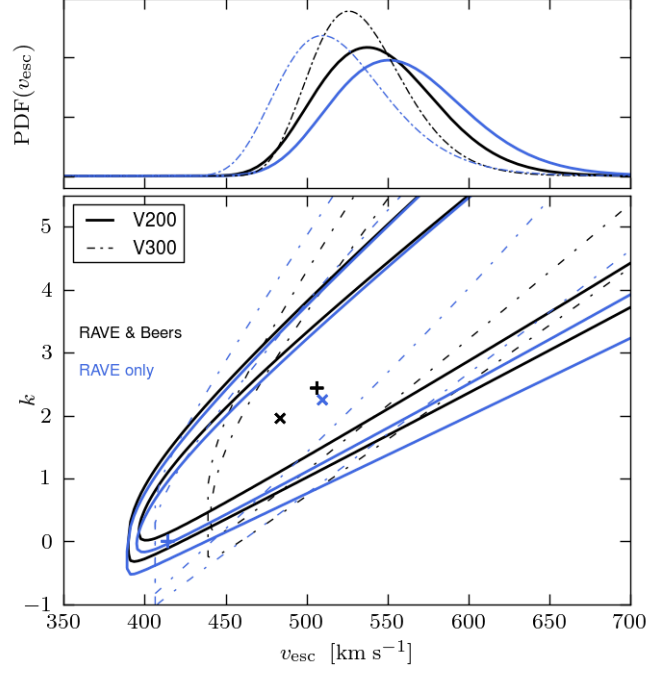


Figure 4.9: Likelihood distributions of parameter pairs v_{esc}, k (lower panel). The positions of the maximum likelihood pairs are marked with the symbols 'x' for the V200 samples and '+' for the V300 samples. Contour lines mark the locations where the likelihood dropped to 10% and 1% of the maximum value. The upper panel shows the likelihood distributions marginalized over the most likely k -interval [2.3,3.7]

onto the data we obtain a sample of 15 RAVE stars and 16 stars from the B00 catalog and we compute a median estimate of 526_{-43}^{+63} km s^{-1} . A lower value is expected because the distance criteria removes mainly stars from the inner Galaxy where stars generally have higher velocities. The reason for this is that RAVE is a southern hemisphere survey and therefore observes mostly the inner Galaxy.

4.4.2 The local escape speed

As described as option (2) in Section 4.1.1 we can estimate for all stars in the catalogs what their radial velocity would be if they were situated at the position of the Sun. We then create two samples using the new velocities. For the first sample we select all stars with re-scaled velocities $v'_{\parallel} > 300 \text{ km s}^{-1}$. S07 showed that such a high velocity threshold yields predominantly halo stars. The resulting sample contains 53 stars (34 RAVE stars) and we will refer to it as V300. The second sample has a lower velocity threshold of 200 km s^{-1} , but stars are pre-selected, in analogy to the simulation analysis, considering only stars classified as 'halo' (Section 4.3.1). This sample we call V200 and it contains 86 stars (69 RAVE stars). Most of the stars are located closer to the Galactic center than the Sun and thus the correction mostly leads to decreased velocity values. In both samples about 7% of the stars have repeat observations. The maximum difference between two velocity measurements is 2.5 km s^{-1} . The resulting likelihood distribution in the (v_{esc}, k) parameter plane is shown in the lower

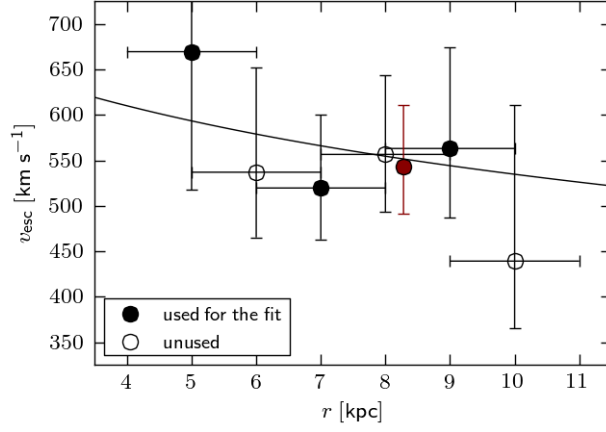


Figure 4.10: Escape speed estimates and 90% confidence intervals in Galactocentric radial bins. The solid black line shows our best-fitting model. Only the filled black data points were used in the fitting process. The red data point illustrates the result of our 'localized' approach.

panel of Figure 4.9. The maximum likelihood pairs for the different samples agree very well, except for the pair constructed from RAVE-only V300 sample, which is located near $v_{\text{esc}} \simeq 410 \text{ km s}^{-1}$ and $k \simeq 0$. In all cases a clear degeneracy between k and the escape speed is visible. This was already seen by S07 and reflects that a similarly curved form of the velocity DF over the range of radial velocities available by different parameter pairs.

We go further and compute the posterior probability DF for v_{esc} , $p(v_{\text{esc}})$ using Eq. 4.7, which effectively means that we marginalize over the optimized k -interval derived in Section 4.2.1.1. For the medians of these distributions we obtain higher values than the maximum likelihood value for all samples. This behavior is consistent with our findings in Section 4.1.2 where we showed that the maximum likelihood analysis tends to yield pair with too low values of k and v_{esc} . These median values can be found in Table 4.2 ("Localized").

4.4.3 Binning in Galactocentric distance

For halo stars with original $|v_{\parallel}| \geq 200 \text{ km s}^{-1}$ we are able to fill several bins in Galactocentric distance r and thereby perform a spatially resolved analysis as described as option (1) in Section 4.1.1. We chose 6 overlapping bins with a radial width of 2 kpc between 4 and 11 kpc. This bin width is larger than the uncertainties of the projected radius estimates for almost all our sample stars (cf. Figure 4.6). The number of stars in the bins are 11, 28, 44, 52, 35 and 8, respectively. The resulting median values (again after marginalizing over the optimal k -interval) of the posterior PDF and the 90% confidence intervals are plotted in Figure 4.10. The values near the Sun are in very good agreement with the results of the previous section. We find a rather flat escape speed profile except for the out-most bins which contain very few stars, though, and thus have large confidence intervals.

4.5 Discussion

4.5.1 Influence of the input parameters

The 90% confidence intervals provided by our analysis technique reflect only the statistical uncertainties resulting from the finite number of stars in our samples. In this section we look for further systematic uncertainties. In Section 4.2.1.2 we already showed that our adopted interval for the power-law index k introduces a systematic scatter of about 5%.

A further source of uncertainties comes from the motion of the Sun relative to the Galactic center. While the radial and vertical motion of the Sun is known to very high precision, several authors have come to different conclusions about the tangential motion, V_{\odot} (e.g. Reid & Brunthaler 2004; Bovy et al. 2012a; Schönrich 2012). In this study we used the standard value for $V_{\text{LSR}} = 220 \text{ km s}^{-1}$ and the $V_{\odot} = 12.24 \text{ km s}^{-1}$ from Schönrich et al. (2010). We repeated the whole analysis using $V_{\text{LSR}} = 240 \text{ km s}^{-1}$ and compared the resulting escape speeds with the values of our standard analysis (cf. the lower part of Table 4.2). The magnitudes of the deviations are statistically not significant, but we find systematically lower estimates of the *local* escape speed for the higher value of V_{LSR} . The shift is close to 20 km s^{-1} and thus comparable to the difference ΔV_{LSR} . This can be understood if we consider that most stars in the RAVE survey and – also in our samples – are observed at negative Galactic longitudes and thus against the direction of Galactic rotation (see Figure 4.6). In this case correcting the measured heliocentric line-of-sight velocities with a higher solar tangential motion leads to lower v_{\parallel} which eventually reflects into the escape speed estimate. Note that this systematic dependency is induced by the half-sky nature of the RAVE survey, while for an all-sky survey this effect might cancel out. In contrast, the exact value of R_0 is not influencing our results, as long as it is kept within the range of proposed values around 8 kpc. The quantity with the largest uncertainties used in this study is the heliocentric distance of the stars. In Section 4.3.2 we found a systematic difference between the distances derived for the RAVE stars and for the stars in the B00 catalog. Such systematic shifts can arise from various reasons, e.g. different sets of theoretical isochrones, systematic errors in the stellar parameter estimates or different extinction laws. Again we repeated our analysis, this time with all distances increased by a factor 1.5, practically moving to the original distance scale of B00. Again we find a systematic shift to lower local escape speeds of the same order as for alternative value of V_{LSR} .

We finally also tested the influence of the Galaxy model we use to re-scale the stellar velocities according to their spatial position. We changed the disk mass to $6.5 \times 10^{10} M_{\odot}$ and decreased the disk scale radius to 2.5 kpc, in this way preserving the local surface density of the standard model. The resulting differences in the corrected velocities are below 1% and no measurable difference in the escape speed estimates were found illustrating the robustness of our methods to reasonable changes in the Galaxy parameters.

4.5.2 A critical view on the input assumptions^{||}

Our analysis stands and falls with the reliability of our approximation of the velocity DF given in Eq. 4.1. The conceptual underpinning of this approximation is very weak for four reasons:

^{||}Most of this section was written by James Binney.

- In many analytic equilibrium models of stellar systems at any spatial point there is a non-zero probability density of finding a star right up to the escape speed v_{esc} at that point, and zero probability at higher speeds. For example the Jaffe (1983) and Hernquist (1990) models have this property but King-Michie models (King 1966) do not: in these models the probability density falls to zero at a speed that is smaller than the escape speed. There is hence an important counter-example to the proposition that $n(v)$ first vanishes at $v = v_{\text{esc}}$.
- All theories of galaxy formation, including the standard Λ CDM paradigm, predict that the velocity distribution becomes radially biased at high speed, so in the context of an equilibrium model there must be significant dependence of the DF on the total angular momentum J in addition to E .
- As Spitzer & Thuan (1972) pointed out, in any stellar system, as $E \rightarrow 0$ the periods of orbits diverge. Consequently the marginally-bound part of phase space cannot be expected to be phase mixed. Specifically, stars that are accelerated to speeds just short of v_{esc} by fluctuations in Φ in the inner system take arbitrarily long times to travel to apocenter and return to radii where we may hope to study them. Hence different mechanisms populate the outgoing and incoming parts of phase space at speeds $v \sim v_{\text{esc}}$: while the parts are populated by cosmic accretion (Abadi et al. 2009; Teyssier et al. 2009; Piffil et al. 2011), the outgoing part in addition is populated by slingshot processes (e.g. Hills 1988) and violent relaxation in the inner galaxy. It follows that we cannot expect the distribution of stars in this portion of phase space to conform to Jeans theorem, even approximately. Yet Eq. 4.1 is founded not just on Jeans theorem but a very special form of it.
- Counts of stars in the Sloan Digital Sky Survey (SDSS) have most beautifully demonstrated that the spatial distribution of high-energy stars is very non-smooth. The origin of these fluctuations in stellar density is widely acknowledged to be the impact of cosmic accretion, which ensures that at high energies the DF does not satisfy Jeans theorem.

From this discussion it should be clear that to obtain a credible relationship between the density of fast stars and v_{esc} we must engage with the processes that place stars in the marginally bound part of phase space. Fortunately sophisticated simulations of galaxy formation in a cosmological context do just that. Figure 4.2 illustrated that Eq. 4.1 catches the general shape of the velocity DF very well. The fact that we find a relatively small interval for the power-law index k , that suits for all simulated galaxies with their variety of morphologies, argues for the appropriateness of the functional form by Leonard & Tremaine (1990).

The question remains whether the applied simulation technique influences the range of k -values we find, since all 8 galaxy models were produced with the same simulation code. In particular, the numerical recipes for so-called sub-grid physics like star formation and stellar energy feedback can have a significant impact on the simulation result as was recently demonstrated in the Aquila code comparison project (Scannapieco et al. 2012). However, the main differences were found in the formation of galaxy disks, while in this study we explicitly focus on the stellar halo that was build up from in-falling satellite galaxies. Differing implementations of sub-grid physics might change the amount of stellar and gas mass being brought in by small galaxies, but it appears unlikely that the phase-space structure of Galactic halo will change significantly. This view is confirmed by the very similar k -interval found by S07 using simulations with a completely different implementation of sub-grid physics.

Table 4.2: Median and 90% confidence limits from different analysis strategies. The masses $M_{340,\text{NFW}}$ are estimated assuming an NFW profile for the dark matter halo and the masses $M_{340,\text{contr}}$ are based on an adiabatically contracted NFW profile. The upper part of the table shows the results when V_{LSR} is assumed to be 220 km s^{-1} . In the lower part of the table we show the results if we assume a value of 240 km s^{-1} to facilitate a comparison to other estimates based on this alternative value.

| Strategy | V200 | | | V300 | | |
|---|---|---|---|---|---|---|
| | $v_{\text{esc}}(R_0)$ (km s^{-1}) | $M_{340,\text{NFW}}$ ($10^{12} M_{\odot}$) | $M_{340,\text{contr}}$ ($10^{12} M_{\odot}$) | $v_{\text{esc}}(R_0)$ (km s^{-1}) | $M_{340,\text{NFW}}$ ($10^{12} M_{\odot}$) | $M_{340,\text{contr}}$ ($10^{12} M_{\odot}$) |
| Estimates considering the RAVE and B00 data; $V_{\text{LSR}} = 220 \text{ km s}^{-1}$. | | | | | | |
| Binned | 557^{+87}_{-63} | $1.13^{+0.59}_{-0.35}$ | $1.81^{+1.02}_{-0.62}$ | | | |
| Localized | 543^{+67}_{-52} | $1.06^{+0.66}_{-0.37}$ | $1.71^{+1.14}_{-0.66}$ | 533^{+54}_{-41} | $0.98^{+0.49}_{-0.28}$ | $1.55^{+0.85}_{-0.50}$ |
| Estimates considering the RAVE data only; $V_{\text{LSR}} = 220 \text{ km s}^{-1}$. | | | | | | |
| Binned | 585^{+109}_{-76} | $1.25^{+0.74}_{-0.43}$ | $2.01^{+1.24}_{-0.74}$ | | | |
| Localized | 559^{+76}_{-59} | $1.19^{+0.82}_{-0.45}$ | $1.94^{+1.41}_{-0.79}$ | 517^{+70}_{-46} | $0.86^{+0.60}_{-0.28}$ | $1.35^{+1.05}_{-0.50}$ |
| Estimates considering the RAVE and B00 data; $V_{\text{LSR}} = 240 \text{ km s}^{-1}$. | | | | | | |
| Binned | 541^{+93}_{-65} | $0.88^{+0.54}_{-0.31}$ | $1.32^{+1.02}_{-0.53}$ | | | |
| Localized | 526^{+72}_{-54} | $0.76^{+0.53}_{-0.28}$ | $1.09^{+0.97}_{-0.47}$ | 511^{+48}_{-35} | $0.67^{+0.30}_{-0.17}$ | $0.94^{+0.54}_{-0.29}$ |
| Estimates considering the RAVE data only; $V_{\text{LSR}} = 240 \text{ km s}^{-1}$. | | | | | | |
| Binned | 557^{+107}_{-74} | $0.95^{+0.68}_{-0.35}$ | $1.47^{+1.25}_{-0.63}$ | | | |
| Localized | 535^{+80}_{-57} | $0.81^{+0.64}_{-0.31}$ | $1.18^{+1.17}_{-0.52}$ | 483^{+52}_{-37} | $0.52^{+0.29}_{-0.15}$ | $0.70^{+0.49}_{-0.24}$ |

4.5.3 Estimating the mass of the Milky Way

We now attempt to derive the total mass of the Galaxy using our escape speed estimates. Doing this we exploit the fact that the escape speed is a measure of the local depth of the potential well $\Phi(R_0) = \frac{1}{2}v_{\text{esc}}^2$. A critical point in our methodology is the question whether the velocity distribution reaches up to v_{esc} or whether it is truncated at some lower value. S07 used their simulations to show that the level of truncation in the stellar component cannot be more than 10%. However, to test this they first had to define the local escape speed by fixing a limiting radius beyond which a star is considered unbound. The authors state explicitly that the choice of this radius to be $3R_{\text{vir}}$ is rather arbitrary. More stringent would be to state that the velocity distribution in the simulations point to a limiting radius of $\sim 3R_{\text{vir}}$ beyond which stars do not fall back onto the galaxy or fall back only with significantly altered orbital energies, e.g. as part of an in-falling satellite galaxy.

It is not a conceptual problem to define the escape speed as the high end of the velocity distribution in disregard of the potential profile outside the corresponding limiting radius. Then it is important, however, to use the same limiting radius while deriving the total mass of the system using an analytic profile. This means we have to re-define the escape speed

to

$$v_{\text{esc}}(r \mid R_{\text{max}}) = \sqrt{2|\Phi(r) - \Phi(R_{\text{max}})|}. \quad (4.10)$$

$R_{\text{max}} = 3R_{340}$ seems to be an appropriate value.

This leads to somewhat higher mass estimates. For example, S07 found an escape speed of 544 km s^{-1} and derived a halo mass of $0.85 \times 10^{12} M_{\odot}$ for an NFW profile, practically using $R_{\text{max}} = \infty$. If one consequently applies $R_{\text{max}} = 3R_{\text{vir}}$ the resulting halo mass is $1.05 \times 10^{12} M_{\odot}$, an increase by more than 20%. This is the reason why our mass estimates are higher than those by S07 even though we find a similar escape speed. Note that these values represent the masses of the dark matter halo alone while in the remainder of this study we mean the total mass of the Galaxy when we refer to the virial mass M_{340} . Keeping this in mind it is then straightforward to compute the virial mass corresponding to a certain local escape speed. As already mentioned we use the simple mass model presented in Section 4.1.

In the case of the escape speed profile obtained via the binned data the procedure becomes slightly more elaborate. We have to compute the escape speeds at the centers of the radial bins R_i and then take the likelihood from the probability distributions $\text{PDF}_{R_i}(v_{\text{esc}})$ in each bin. The product of all these likelihoods⁷ is the general likelihood assigned to the mass of the model, i.e.

$$\hat{L}(M_{340}) = \prod_i \text{PDF}_{R_i}(v_{\text{esc}}(R_i \mid M_{340})) \quad (4.11)$$

The results of these mass estimates are presented in Table 4.2. As already seen in Figure 4.5 for the simulations the adiabatically contracted halo model yields always larger results than the unaltered halo.

4.5.4 Fitting the halo concentration parameter

Up to now we assumed a fixed value for the local standard of rest, $V_{\text{LSR}} = 220 \text{ km s}^{-1}$, to reduce the number of free parameters in our Galaxy model to one. Recently several authors found larger values for V_{LSR} of up to 240 km s^{-1} (e.g. Bovy et al. 2012a; Schönrich 2012). If we change the parametrization in the model and use the halo concentration c as a free parameter we can compute the likelihood distribution in the (M_{340}, c) -plane in the same way as described in the previous section. Figure 4.11 plots the resulting likelihood contours for an NFW halo profile (left panel) and the adiabatically contracted NFW profile (right panel). The solid black curves mark the locations where the likelihood dropped to 10% and 1% of the maximum value (which lies near $c \simeq 0$). Grey dotted lines connect locations with common circular velocities at the solar radius.

Navarro et al. (1997) showed that the concentration parameter is strongly related to the mass and the formation time of a dark matter halo (see also Neto et al. 2007; Macciò et al. 2008; Ludlow et al. 2012). With this information we can further constrain the range of likely combinations (M_{340}, c) . We use the relation for the mean concentration as a function of halo mass proposed by Macciò et al. (2008). For this we converted their relation for c_{200} to c_{340} to be consistent with our definition of the virial radius. There is significant scatter around this relation reflecting the variety of formation histories of the halos. This scatter is reasonably well fitted by a log-normal distribution with $\sigma_{\log c} = 0.11$ (e.g. Macciò et al. 2008; Neto et al. 2007). If we apply this as a prior to our likelihood estimation we obtain the black solid contours plotted in Figure 4.11. Note that in the adiabatically contracted case the concentration

⁷We only use half of the radial bins in order to have statistically independent measurements.

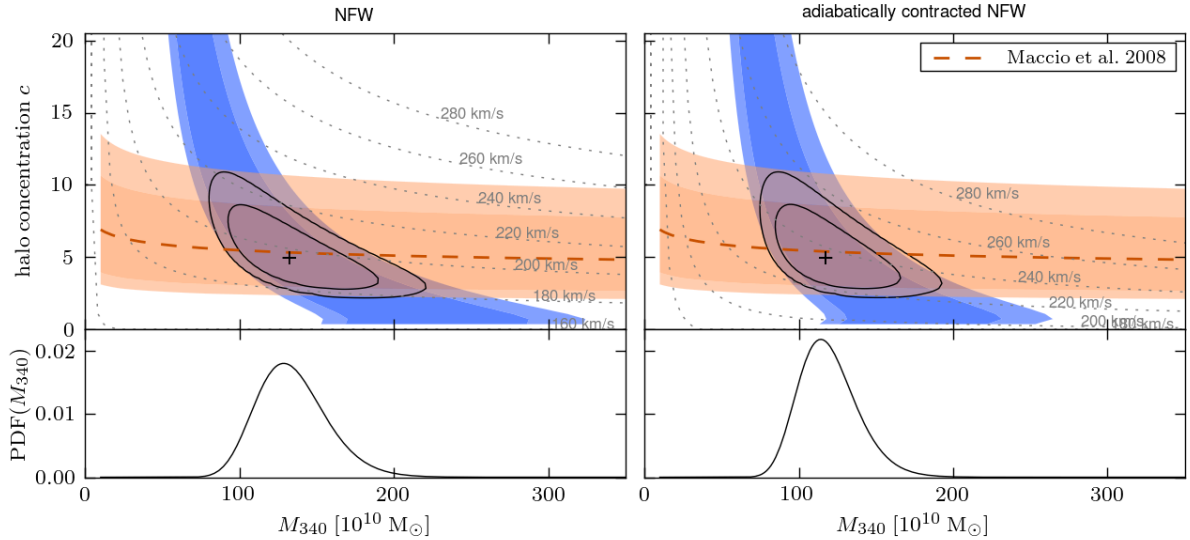


Figure 4.11: Likelihood distribution resulting from our simple Galaxy model when we leave the halo concentration c (and therefore also V_{LSR}) as a free parameter (blue area) for an NFW profile as halo model (left panel) and an adiabatically contracted NFW profile (right panel). The red contours arise when we add the constraints on c from cosmological simulations: the relation of the mean c for a given halo mass found by Macciò et al. (2008) is represented by the thick dashed orange line. The orange area illustrates the spread around the mean c values found in the simulations. The different shades in the blue and orange colored areas mark locations where the probability dropped to 10%, 1% of the maximum value. Dotted gray lines connect locations with constant circular speed at the solar radius.

parameters we are quoting are the *initial* concentrations before the contraction. Only these are comparable to results obtained from dark matter-only simulations.

The maximum likelihood pair of values (marked by a black '+' in the figure) for the adiabatically contracted halo is $M_{340} = 1.09 \times 10^{12} M_{\odot}$ and $c = 5$, which implies a circular speed of 229 km s^{-1} at the solar radius. The unaltered NFW profiles yields the same c but a somewhat larger mass of $1.22 \times 10^{12} M_{\odot}$. Here the resulting circular speed is only 187 km s^{-1} .

If we marginalize the likelihood distribution along the c -axis we obtain the one-dimensional posterior PDF for the virial mass. The median and the 90% confidence interval we find to be

$$M_{340} = 1.3_{-0.3}^{+0.4} \times 10^{12} M_{\odot}$$

for the un-altered halo profile. For the adiabatically contracted NFW profile we find

$$M_{340} = 1.2_{-0.3}^{+0.4} \times 10^{12} M_{\odot}$$

It is worth noting that in this approach the adiabatically contracted halo model yields the lower mass estimate, while the opposite was the case when we fixed the local standard of rest as done in the previous section.

There are several definitions of the virial radius used in the literature. In this study we used the radius which encompasses a mean density of 340 times the critical density for closure in the universe. If one adopts an over-density of 200 the resulting masses M_{200} increase to $1.6_{-0.4}^{+0.5} \times 10^{12} M_{\odot}$ and $1.4_{-0.3}^{+0.4} \times 10^{12} M_{\odot}$ for the pure and the adiabatically contracted halo profile, respectively. For an over-density of $340 \Omega_0 \sim 100$ ($\Omega_0 = 0.3$ being the cosmic mean

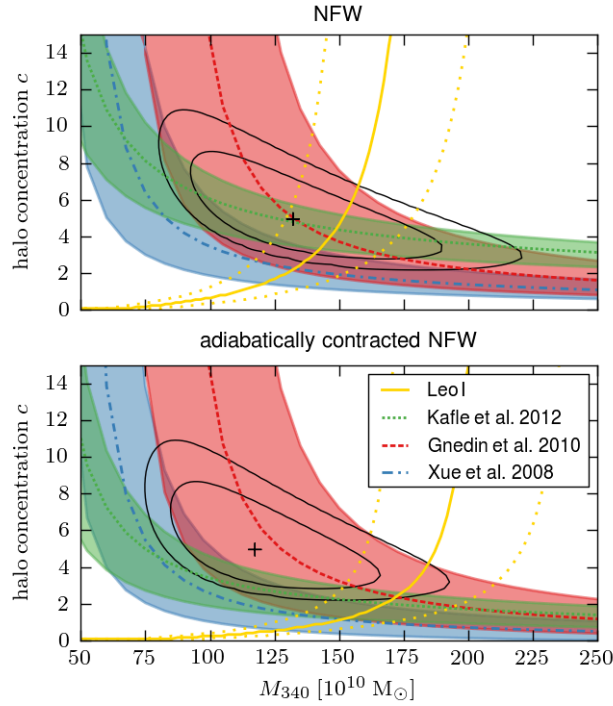


Figure 4.12: Additional constraints on the parameter pairs (M_{340}, c) coming from studies from the literature. The black contours are the same as in Figure 4.11. Gnedin et al. (2010) measured the mass interior to 80 kpc from the GC, Xue et al. (2008) interior to 60 kpc and Kafle et al. (2012) interior to 25 kpc. The yellow solid and dotted line separate models for which the satellite galaxy Leo I is on a bound orbit (below the lines) from those which it is unbound.

matter density), as used, e.g., by Smith et al. (2007) or Xue et al. (2008), the values even increase to $1.9_{-0.5}^{+0.6} \times 10^{12} M_{\odot}$ and $1.6_{-0.4}^{+0.5} \times 10^{12} M_{\odot}$. The corresponding virial radii are

$$R_{340} = 180 \pm 20 \text{ kpc}$$

for both halo profiles ($R_{200} = 225 \pm 20 \text{ kpc}$).

4.5.5 Relation to other mass estimates

We can include as further constraints literature estimates of total masses interior to various Galactocentric radii by Xue et al. (2008), Gnedin et al. (2010) and Kafle et al. (2012). Gnedin et al. (2010) obtained an estimate of a mass of $6.9 \times 10^{11} M_{\odot} \pm 20\%$ within 80 kpc. Xue et al. (2008) found a mass interior to 60 kpc of $4.0 \pm 0.7 \times 10^{11} M_{\odot}$. Kafle et al. (2012) measured a Galactic mass of $2.1 \times 10^{11} M_{\odot}$ interior to 25 kpc from the Galactic center using a similar data set as Xue et al. (2008), but an analysis technique that is less model dependent. We use a 68% confidence interval of $[1.8, 2.3] \times 10^{12} M_{\odot}$ for this last estimate (green shaded area; P. Kafle, private communication). Models fulfilling these constraints are marked in Figure 4.12 with colored shaded areas. In the case of the unaltered NFW halo we find an excellent agreement with Gnedin et al. (2010) and Kafle et al. (2012), while for the adiabatically contracted model the combination of these estimates favor higher virial masses. The estimate by Xue et al.

(2008) is only barely consistent with our results on a 1σ -level for both halo models.

Tests with a different model for the Galactic disk ($M_d = 6.5 \times 10^{10} M_\odot$, $R_d = 2.5$ kpc, similar to the one used by Kafle et al. (2012) and Sofue et al. (2009)) resulted in decreased mass estimates (10%), well within the uncertainties. This model changes the values for the circular speed (223 km s^{-1} and 264 km s^{-1} for the un-altered and the contracted case, respectively) but not the consistency with the mass estimates by Kafle et al. (2012), Gnedin et al. (2010) or Xue et al. (2008).

Another important constraint for the Galactic halo is the space motion of the satellite galaxy Leo I. Boylan-Kolchin et al. (2013) showed that in the Λ CDM paradigm it is extremely unlikely that a galaxy like the Milky Way has an unbound close-by satellite galaxy. If we take the recent estimates for the Galactocentric distance of 261 ± 13 kpc and the absolute space velocity of $200_{-29}^{+22} \text{ km s}^{-1}$ (Sohn et al. 2013) we can identify those combinations of M_{340} and c that leave Leo I on a bound orbit. The line separating models in which Leo I is bound from those where it is not bound is also plotted in Figure 4.12. All models below this line are consistent with a bound orbit of Leo I. The dotted lines show the uncertainties in the sense that they mark the ridge lines for the extreme cases that Leo I is slower and closer by 1σ and that it is farther and faster by 1σ . In the case of the un-altered halo profile our mass estimate is consistent with Leo I being on a bound orbit, while in the contracted case the mass of the Galaxy would be too low.

Finally, Przybilla et al. (2010) found a star, J1539+0239, with a velocity of $694_{-221}^{+300} \text{ km s}^{-1}$ at a Galactocentric distance of ~ 8 kpc moving inwards to the Galaxy. The authors argue that this star should therefore be bound to the Milky Way (see also Irrgang et al. 2013). The star is not in the solar vicinity as its heliocentric distance measured to be 12 ± 2.3 kpc, but its Galactocentric distance is comparable to R_0 . We can therefore directly compare our results. Due to the large uncertainties in the velocity estimate it is not surprising that our most likely value for v_{esc} is consistent with J1539+0239 to be on a bound orbit. However, if their median velocity is correct this star is clearly unbound in our model of the Galaxy and must have obtained its high speed via some other mechanism or be of Extragalactic origin.

4.5.6 On the dark matter halo profile

The two halo models, un-altered and adiabatically contracted NFW halo, are rather extreme cases and the true shape of the Galactic halo is most likely intermediate to these options (Abadi et al. 2010). When we fixed the circular speed at the Sun's position (as done for the estimates shown in Table 4.2) the resulting halo masses were strongly dependent on the shape of the profile. However, when we loosened this constraint using a prior on the halo concentration c (as in Section 4.5.4) our mass estimates become fairly robust to changes of the halo model. In this approach the tension between the constraints coming from the circular speed at the solar radius and the mass estimates at larger distances are likely to be resolved by an intermediate halo model as proposed by Abadi et al. (2010).

4.5.7 Future prospects

The ESO cornerstone mission Gaia Prusti (2012) will soon revolutionize the field of Galactic astronomy. It will deliver the full 6D phase space information for more 100 million stars in

the extended solar neighborhood. With these data we will not be restricted anymore to the use of radial velocities alone as tangential velocities with similar or even smaller uncertainties will be available. Repeating our analysis with Gaia observations will hence deliver much more precise results.

On the other hand we expect that the full complexity of the Galaxy will appear in these data as well. The comparatively sparse RAVE data allowed to neglect many of the details of the Galactic structure, in particular the clumpy nature of the stellar halo. This might be no longer possible with the Gaia data, or in other words, the precision of the estimate might no longer be limited by the data, but by the assumptions in the analysis method itself. It is hence possible that the gain is smaller than one might expect naively if the analysis is repeated in the exact same manner. More robust knowledge about the structure of the inner galaxy obtained, for example, via the analysis of cold tidal streams (Koposov et al. 2010; Sanders & Binney 2013) might allow to refine these assumptions.

5 An alternative origin for hyper-velocity stars*

In the last chapter we used high-velocity halo stars from the RAVE survey to estimate the Galactic escape speed. In this analysis we treated the halo as a smooth spherically symmetric population. The lumpiness of stellar halos, which can be observed in our own Galaxy (Belokurov et al. 2006) as well as in external galaxies (Martínez-Delgado et al. 2010) played only a minor role as a possible disturbance. In this chapter we will direct our focus on the implications of the presence of sub-structure in the Galactic halo.

The growth of galaxies via the accretion of smaller companion systems is one of the major ingredients in the current perception of galaxy formation and evolution. These satellite galaxies are disrupted in the tidal field of their host galaxies and the new material is dispersed near the orbit of the progenitor. Recent theoretical work has shown that especially the outer stellar halo is predominantly made of stars which were born outside the main galaxy (Abadi et al. 2006; Zolotov et al. 2009; Scannapieco et al. 2011). Such stars are thought to have low metallicities and to be old. The small fraction of material born inside the main galaxy reaching these large radii was mostly re-distributed during violent major merger events. As these events were more frequent when the galaxy was still young, these stars are also predominantly old. A third small population of the outer halo are the so-called Hypervelocity stars (HVSs) which are ejected via a three-body interaction involving the super-massive black hole (SMBH) in the Galactic center (Hills 1988). Such stars have no age constraints and should be metal-rich as they originate from the innermost region of the galaxy.

The latter population earned attention since they could serve as an indirect proof for the SMBH in the Galactic center (Hills 1988) and also because they could be used to measure the shape of the Galactic potential (Gnedin et al. 2005; Yu & Madau 2007; Perets et al. 2009). Yu & Tremaine (2003) estimated a HVS ejection rate of 10^{-5} yr^{-1} and Perets et al. (2007) showed that this rate could increase by a magnitude if massive perturbers such as giant molecular clouds or star clusters were considered. Aside from the classical ejection mechanism by Hills (1988) several authors have suggested alternative formation scenarios: a binary black hole of equal (Yu & Tremaine 2003) and un-equal masses (Levin 2006; Sesana et al. 2009), a supernova in a binary near the SMBH (Zubovas et al. 2013) or the accretion of a satellite galaxy (Abadi et al. 2009).

Recent observations of stars in the Galactic halo with unusually high velocities (Brown et al. 2005; Hirsch et al. 2005; Edelmann et al. 2005; Brown et al. 2006a,b, 2007a,b, 2009a; Tillich et al. 2009; Brown et al. 2012; Palladino et al. 2014) raised new interest on the topic. By design of the search strategy these stars have typically blue colors. They move with velocities up to 720 km s^{-1} with respect to the Galactic center and are thought to reside at Galactocentric distances of 20-130 kpc. Interestingly, the targeted HVS survey of Brown et al.

*Content and text of this chapter have almost identically been published as Piffel et al. (2011). See also the remarks at the end of the Introduction (Chapter 1). Credit: Piffel et al., *A&A*, 535, A70, 2011, reproduced with permission ©ESO.

(2009a) only yield out-going HVSs, a fact that is typically attributed to the short lifetimes of the stars compared to the long orbital periods. However, eventually also an in-going star with extremely high velocity was observed (Przybilla et al. 2010).

Despite the small number of HVSs reported to date several peculiarities in the distribution of the observed population were already claimed. Abadi et al. (2009) found that a large part of the population clusters around a certain travel time (~ 130 Myr), i.e. the time a star would need to travel from the GC and arrive at its current radius with its current radial velocity. Such a clustering is not expected from Hills' original SMBH-ejection scenario. It could be explained, however, by a star burst event near the GC triggering an increased ejection rate of HVSs for certain times.

Also the angular distribution on the sky shows signs of anisotropy. Abadi et al. (2009) and Brown et al. (2009b) report a significant over-density of HVSs around the constellation of Leo. Stars ejected by one or more black holes in the GC should appear on the sky in an approximately homogeneous distribution or in a ring-like structure (Levin 2006). However, a preferred ejection direction as found in the data is not naturally explained with this mechanism (however, see Lu et al. (2010)).

The accreted population of stars in the outer halo can also contain stars with large radial velocities. Teyssier et al. (2009) showed that there should exist an energetically loosely or un-bound population of stars originating from disrupted dwarf galaxies. Abadi et al. (2009) commented that a larger total mass of the Galaxy would allow the normal virialized halo population to reach these velocity regimes. The authors further suggested that the peculiarities in the HVS distribution would be naturally explained if part of the observed HVSs would actually belong to a stream of tidal debris of a recently accreted dwarf galaxy. An example for a HVS likely being generated by this mechanism was recently found in M31 (Caldwell et al. 2010).

Several theoretical studies have already investigated properties of the tidal debris of satellite galaxies. Johnston (1998) approximated the energy distribution of tidal debris particles with a triangular shape to build up a stellar halo distribution. Choi et al. (2007) showed that the energy kick obtained by stripped stars via tidal forces and also the deviations between leading and trailing tidal arms are both increasing with the mass of the approaching satellite. Warnick et al. (2008) investigated the relation between observable properties of tidal streams like radial velocity dispersion or thickness to the properties of the progenitor system. D'Onghia et al. (2009, 2010) investigated the effect of resonances during tidal stripping of rotating systems.

In the present study we investigate the kinematic properties of tidal debris stars with a special focus on the fastest stars of this population. For this we systematically study tidal encounters of satellite galaxies with their hosts and investigate the process in detail. We ran a suite of collisionless N -body simulations following the passage of a small companion galaxy through its massive Milky Way-like host galaxy. These simulations are used to obtain an idea of what properties an observer would find in an HVS population generated in a tidal collision. We develop a simple analytical model and test it against the simulations and show in how this model can be used to predict the energy distribution of the tidal debris star.

5.1 Simulation set-up

All simulations were run using the publicly available simulation code Gadget-2 (Springel 2005). For the main galaxy we used the model parameters proposed by Klypin et al. (2002).

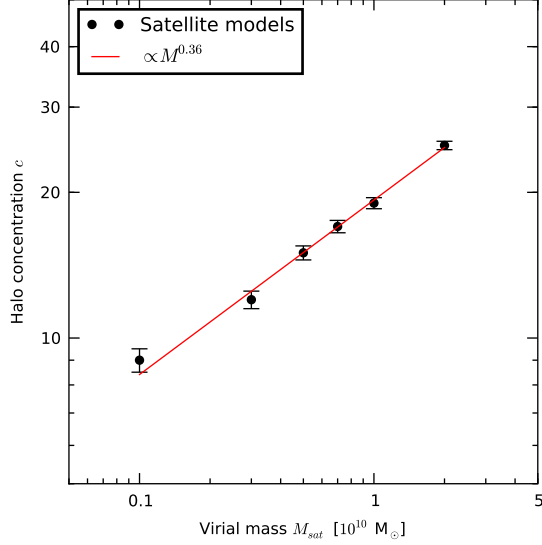


Figure 5.1: Black symbols show the applied values for the halo concentration parameter c for a given satellite mass M_{sat} . The errorbars have a width of 0.5 to reflect the fact that only integer numbers were used for c . The red line shows a power law with exponent 0.36.

The galaxy consists of three components, an adiabatically contracted spherical NFW halo (Navarro et al. 1996), an exponential stellar disk and a spherical stellar bulge with a Hernquist density profile (Hernquist 1990). The disk density profile is

$$\rho_{\text{disk}}(R, z) = \frac{M_{\text{disk}}}{4\pi R_{\text{disk}}^2 z_{\text{disk}}} \exp\left(-\frac{R}{R_{\text{disk}}}\right) \text{sech}^2\left(\frac{z}{z_{\text{disk}}}\right), \quad (5.1)$$

where $R = \sqrt{x^2 + y^2}$. The vertical scale height is set as $z_{\text{disk}} = 0.2R_{\text{disk}}$, as was found in observations of other disk galaxies (Kregel et al. 2002). Table 5.1 presents the parameters used. The dark matter halo is smoothly truncated outside of R_{200} as described in Springel & White (1999). The satellite galaxies are modeled as an adiabatically contracted NFW halo hosting a Hernquist sphere as the spherical baryonic component. The models fulfill the constraints from the Fundamental plane of dE+dSph galaxies given in de Rijcke et al. (2005):

$$\log L_B \sim 4.39 + 2.55 \log \sigma_0 \quad (5.2)$$

$$\log L_B \sim 8.69 + 3.55 \log R_e \quad (5.3)$$

Here, L_B is the B -band luminosity, R_e is the effective radius enclosing half the light of the galaxy and σ_0 is the luminosity-weighted mean velocity dispersion. A Hernquist sphere has an effective radius $R_e \simeq 1.82r_{\text{bulge}}$ (Hernquist 1990). For the velocity dispersion σ_0 , in analogy to the dispersion used by de Rijcke et al. (2005), we computed the mass-weighted mean of the line-of-sight velocity dispersions in different radial annuli of the visible component. Finally, to relate the luminosity L_B to the baryonic mass content of the galaxy we assume a mass-to-light ratio $\Upsilon_B = 2\Upsilon_{B,\odot}$.

The ratio between total, M_{sat} , and baryonic mass, $M_{\text{sat,b}}$, was fixed using the relation found by McGaugh et al. (2010):

$$\log M_{\text{sat,b}} = 4.0 \log v_{\text{circ}} + 1.65. \quad (5.4)$$

To relate the circular velocity of the dark halo, v_{circ} , to the mass of the satellite, M_{sat} , we used the same relation as in McGaugh et al. (2010):

$$M_{\text{sat}} = (1.5 \times 10^5 \text{km}^{-3} \text{s}^3 M_{\odot}) v_{\text{circ}}^3 \quad (5.5)$$

With these constraints the dwarf galaxy is fully determined by only one parameter. In this work we used the total mass M_{sat} as a free parameter which was varied for different simulation runs. The requirement to match all the constraints given above fixes also the concentration parameter c of the satellite dark halo. The obtained mass-concentration relation is given in Figure 5.1. It is best described by a power law:

$$c \simeq 19.3 \left(\frac{M_{\text{sat}}}{10^{10} M_{\odot}} \right)^{0.36} \quad (5.6)$$

Note, that this relation was obtained by fitting our basic satellite model to the observational constraints. Our concentration parameter should thus not be interpreted in the original sense of an evolutionary sequence in the frame-work of Λ CDM cosmology (Navarro et al. 1997). For the initialization of the phase-space positions of the particle samples we followed a method outlined by Springel & White (1999) which is a modified version of the method of Hernquist (1993) which assumes Gaussian velocity distributions. The latter leads to slight deviations from a perfect equilibrium configuration. To account for this both host and satellite galaxies are allowed to relax for 1 Gyr in isolation before they are implemented into the actual simulations. We use a softening length of 0.01 (0.2) kpc for the satellite star (dark matter) particles in all our simulations.

Simulation time All simulations ran until the satellite reached the Apogalacticon after its first pericentric passage or crossed the virial radius of the host galaxy, R_{200} . This was done because we wanted to study the properties of a population of tidal debris particles generated during a single stripping event. As we also have a focus on the stars escaping from the combined satellite and host system we chose to study only the first orbit. We expect this orbit to generate the largest spread in velocities as the initial unperturbed satellite population covers the complete possible phase space regions. At later orbits the satellite will have lost its most energetic population (Choi et al. 2009). Furthermore, considering only the first orbit allows an easier comparison between the different simulation runs as one has the full control over the satellite configuration at the beginning of the orbit.

A suite of simulations To create a suite of comparable simulations we then ran this scenario with varying initial satellite masses $M_{\text{sat}} = 0.1 - 2 \times 10^{10} M_{\odot}$ and different starting positions in the satellite phase space. In the majority of cases the satellite is on a bound polar orbit with respect to the host disk component. To determine the influence of an inclined orbit we also ran a couple of simulations with 0° (planar) and 45° inclination angle. We found that the differences in the results for varying inclinations were small compared to other uncertainties. We thus did not consider inclination as a major parameter and neglect it completely. The initial angular momenta, L_{sat} , of the satellites range between 0 and $15 \times 10^3 \text{ kpc km s}^{-1}$ which corresponds to pericenter distances R_{peri} from 0 to 50 kpc. A list of the initial conditions and some of the analysis results for all runs can be found in the appendix of Piffl et al. (2011).

Table 5.1: Parameters of the host galaxy

| NFW halo | | |
|---|----------------------|--------------------|
| Total mass, M_{halo} | 113×10^{10} | M_{\odot} |
| Virial radius, R_{200} | 258 | kpc |
| Concentration, c | 12 | |
| Virial velocity, $v_{\text{circ}}(R_{200})$ | 129 | km s^{-1} |
| Particle number, N_{halo} | 5×10^5 | |
| Softening, ϵ_{halo} | 0.4 | kpc |
| Exponential disk | | |
| Disk mass, M_{disk} | 4.0×10^{10} | M_{\odot} |
| Scale length, R_{disk} | 3.5 | kpc |
| Scale height, z_{disk} | 0.7 | kpc |
| Particle number, N_{disk} | 10^5 | |
| Softening, ϵ_{disk} | 0.1 | kpc |
| Hernquist bulge | | |
| Bulge mass, M_{bulge} | 0.8×10^{10} | M_{\odot} |
| Scale radius, R_{bulge} | 0.7 | kpc |
| Particle number, N_{bulge} | 2×10^4 | |
| Softening, ϵ_{bulge} | 0.1 | kpc |

5.2 Observable properties from the simulations

Of the 41 simulations performed for this study 23 yielded particles with velocities higher than the local escape speed of the host galaxy. These particles are gravitationally unbound and are the simulated equivalent to HVSSs². However, in the real Milky Way the escape speed is still uncertain to a considerable degree as neither the total mass ($1 - 2 \times 10^{12} M_{\odot}$, e.g. Smith et al. 2007; Xue et al. 2008; Guo et al. 2010; Boylan-Kolchin et al. 2011; Przybilla et al. 2010; McMillan 2011; Piffl et al. 2014) nor the global shape of the gravitational potential (Law et al. 2009) is precisely measured. Moreover, the asymmetry of the Galaxy introduces a direction dependency. Thus the value of the escape speed must not be seen as a sharp limiting velocity dividing bound and unbound stars. It is rather a characteristic value to compare to when evaluating the probability whether a star will eventually fall back onto its host or not. For the dynamics of a star located within the virial radius of the Galaxy it makes no qualitative difference whether it is gravitationally unbound. Because of this, and also to obtain better statistics, we will thus in this section analyze the most energetic 0.1% of the satellite particles, i.e. the Most Energetic Particles (MEPs, for short) regardless whether they reach velocities higher than their local escape speed.

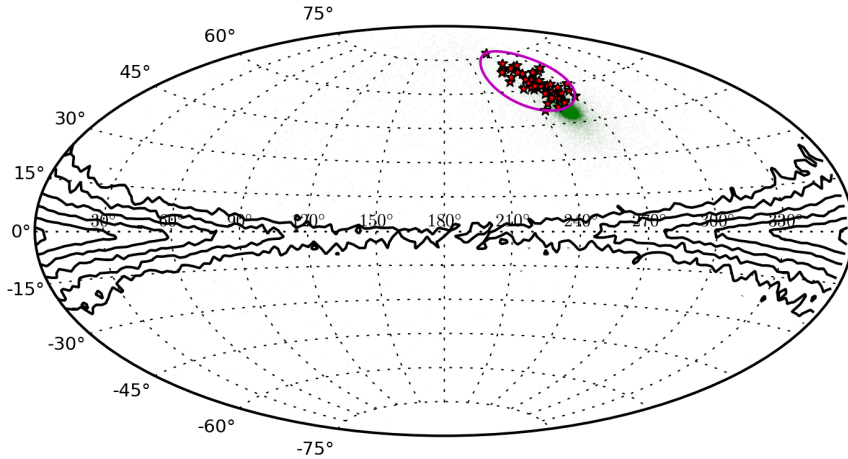


Figure 5.2: Aitoff projection of a simulation run about 200 Myr after Perigalacticon. Green dots represent all satellite particles (only every 5th particle plotted) while the MEPs are marked by red stars. Disk and bulge of the host galaxy is also shown as black mass-density contour-lines. The median distance of the MEPs is ~ 60 kpc, comparable to the Galactocentric distances of the observed HVSs. The MEPs are concentrated to confined area on the sky, in this case enclosed by a circle with angular radius 15° .

5.2.1 Angular distribution

Figure 5.2 shows the angular distribution of the MEPs in one of our simulations (red stars) as seen by an observer on the Sun’s location. The snapshot is taken at a time when the particles have moved from the satellite Perigalacticon out to a galactocentric distance of ~ 60 kpc, similar to the observed HVS population. Green dots indicate the positions of all satellite particles while black dots represent star particles belonging to the host galaxy. As already reported by Abadi et al. (2009) the MEPs are clustered in a tightly confined region on the sky (in Fig. 5.2 marked by the solid magenta circle of radius $\sim 15^\circ$). Averaging over all 39 simulations and over 10 equispaced angular positions of the Sun on the solar circle the mean radius of a circular region encompassing all MEP is 16° and the maximum angular radius is 27° . At a distance of 60 kpc the viewing angle of the observer relative to the orbital plane of the satellite does not play a significant role as the stripped-off particles had not enough time yet to unfold into a prominent stream and are thus observable in a compact area from all directions (cf. the upper left panel of Fig. 5.3).

Furthermore, the position of the satellite relative to the MEPs is not arbitrary. In all our simulations the satellite has a smaller angular distance to the host galactic center than the MEPs. This is due to the fact that the satellite as well as the MEPs have just passed their perigalacticon and now move away from the host. Since the MEPs have higher orbital energies they leave the satellite behind and are thus observed at larger angular distances in the vast majority of cases. The angular distance between the MEPs and the satellite remnant is determined by projection effects depending on the viewing angle relative to the orbital plane of the satellite. In our simulations the satellite core is observed always within 22° (90 percent within 16°) separation to the center of the MEP population.

²In this simulation set-up the escape speed is well defined, because the system is simulated in isolation.

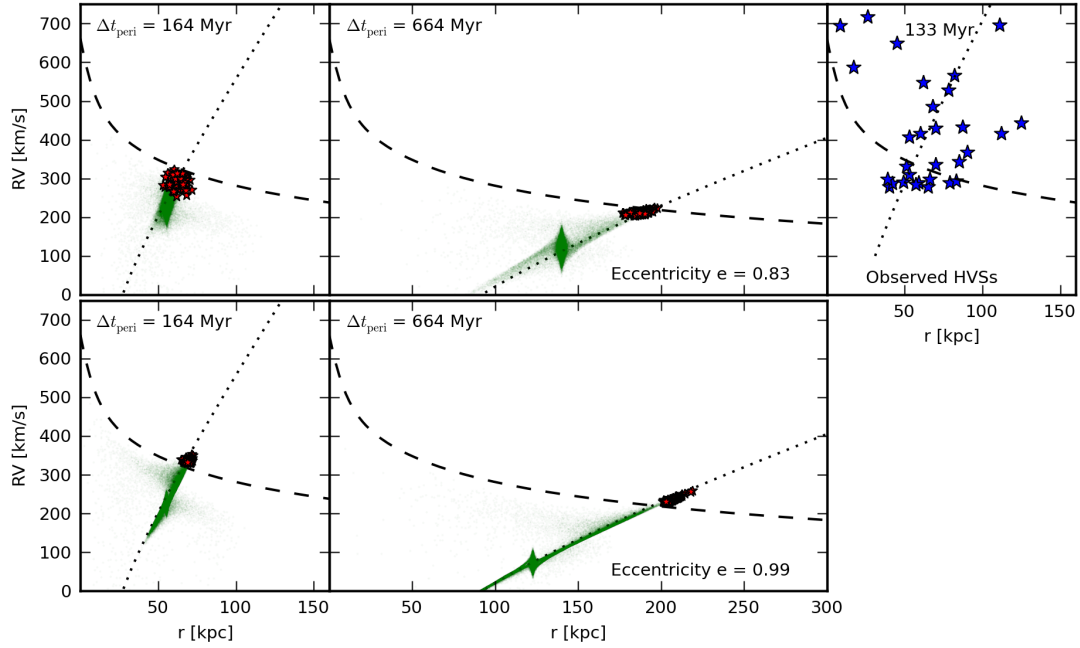


Figure 5.3: Time series of the galactocentric RV-distance plane for two simulation runs. The time elapsed since Perigalacticon, Δt_{peri} , is shown in the upper left corner, respectively. Red stars represent the MEPs, green dots satellite particles and dashed lines the local escape speed of the respective radius. Dotted lines mark lines of constant travel times corresponding to Δt_{peri} . The eccentricity of the satellite orbit is given in the lower right corner of the right most panel, respectively. In the left most panels the mean distance of the MEPs is 60 kpc similar to the observed HVS population which is shown in the right most panel in the upper row for comparison. At this point the MEPs did not have time yet to leave the remaining satellite far behind. Note that none of the simulations were designed to reproduce the observed HVS population.

5.2.2 The radial velocity-distance plane

The particles stripped-off the satellite quickly disperse in physical space and are soon indistinguishable from the already existing Galactic halo population. However, when Galactocentric radial velocities, v_r , are plotted against Galactocentric distance, r , the particles form an elongated pattern reflecting their common origin from the Perigalacticon of the satellite. Figure 5.3 shows time series of two simulations with satellite systems on orbits with different eccentricity. Green dots represent satellite particles while red stars show the MEPs. Particles of the host galaxy are not plotted. The upper series is based on the same simulation that was used for Fig. 5.2 and the upper left most panel shows the same point of time. The lower panel row shows a simulation run with an almost purely radial orbit which has also lower orbital energy. The initial structural properties of the satellite are the same as in the upper run. Note that despite the lower satellite orbital energy the maximum tidal debris velocities are larger than in the run with a lower eccentricity.

The dashed line represents the escape speed from the host system at the respective distance. This corresponds to the trajectory of a test body on a parabolic (purely radial) orbit. Particles below this line are not necessarily bound as part of their motion is hidden in the other velocity components. This explains why particles can cross the dashed line while still con-

serving their energy.

The dotted lines in the panel are lines of constant travel time, i.e. mark positions in the (r, v_r) -plane which are occupied by test bodies which started from a common point with varying initial (radial) velocities. The starting point is usually chosen to be the center of the gravitational potential, as in Fig. 5.3. However, lines from other starting points have similar shapes which explains the good alignment of the tidal debris particles even though the satellite in the upper row run never comes close to the Galactic center (the pericenter distance for this run was 18 kpc).

The width of the tidal debris streams in the (r, v_r) -plane also changes with eccentricity. This can be understood when considering that most of the stripping happens during a short period of time around the pericenter passage. For more circular orbit this period get more extended as more time is spent by the satellite at radii similar to the pericenter distance.

Hence the clustering in travel time already reported by Abadi et al. (2009) has an intrinsic scatter which scales with eccentricity of the orbit of the progenitor system. This is especially so shortly after the pericentric passage, when the distances to the GC are not large and lines of constant travel times have a large slope. At this time the scatter can be stronger than the trend to lines of constant travel time.

The left more panel (upper row) shows the distribution of the observed HVSs in the distance-velocity plane for comparison. The possible tidal debris group in the population proposed by Abadi et al. (2009) clusters around the 133 Myr-line of constant travel time show as dotted black line. Note that none of the two simulation runs was designed to reproduce the observed population as this was not the goal of this more general parameter study.

5.2.3 Maximum velocities

In the classical SMBH sling shot scenario the extremely large ejection velocities are a result of the extreme orbital velocities occurring near a SMBH plus the large orbital velocities of the components of a hard binary system (Yu & Tremaine 2003). Compared to such an environment, collisions of galaxies are much less violent events as the time scales are much larger and potential gradients much shallower. We thus cannot expect the extraordinary velocities up to 3000 km s^{-1} predicted by Hills (1988). Still, the simulations show that stars can be accelerated to their local escape speed and above. The maximum velocities reached by the MEPs at $r \simeq 60 \text{ kpc}$ in our simulations range between 200 and 400 km s^{-1} ($v_{\text{esc}}(60 \text{ kpc}) = 330 \text{ km s}^{-1}$ in our Galaxy model).

5.3 A model for tidal stripping

To guide our further analysis we develop a simple, succinct model to describe the accreted satellite mechanism. It was inspired by the calculations of HVS ejection velocities by Yu & Tremaine (2003) as it treats the galaxy-galaxy encounter similar to an binary-SMBH encounter: a satellite galaxy is moving on an orbit in the gravitational potential $\Phi_{\text{host}}(\vec{r})$ of its much more massive host galaxy. Its specific orbital energy is thus

$$E_{\text{sat}} = \frac{1}{2}v_{\text{sat}}^2 + \Phi_{\text{host}}(\vec{r}_{\text{sat}}) \quad (5.7)$$

Since the satellite is an spatially extended object it is subject to tidal forces which lead to a mass loss of the satellite. Under the assumption of an at least moderately eccentric orbit the majority of this stripping will happen in a short period of time when the satellite is closest to the center of the host galaxy where tidal torques are strongest, i.e., at its perigalacticon, R_{peri} , where it has the velocity $v_{\text{sat}} = V_{\text{peri}}$.

To model the stripping we now assume what we call *instantaneous escape*: a star i with a position \vec{r}_i relative to the satellite center and a velocity \vec{v}_i in the co-moving rest frame of satellite has an orbital energy

$$E_i = \frac{1}{2}(\vec{v}_{\text{sat}} + \vec{v}_i)^2 + \Phi_{\text{host}}(\vec{r}_{\text{sat}} + \vec{r}_i) + \Phi_{\text{sat}}(\vec{r}_i). \quad (5.8)$$

The star is lost to the satellite when the gravitational potential from the satellite, Φ_{sat} is less than the difference in the host potential between the satellite position and the position of the particle, \vec{r}_i ,

$$\Phi_{\text{host}}(\vec{r}_{\text{sat}} + \vec{r}_i) - \Phi_{\text{host}}(\vec{r}_{\text{sat}}) \geq -\Phi_{\text{sat}}(\vec{r}_i), \quad (5.9)$$

which is equivalent for it to be outside of the tidal radius, R_{tidal} . We now assume that this energy transition occurs instantly and the star is left to move in the host potential only. Thus the orbital energy of the star after the stripping is

$$\begin{aligned} E'_i &= \frac{1}{2}(\vec{v}_{\text{sat}} + \vec{v}_i)^2 + \Phi_{\text{host}}(\vec{r}_{\text{sat}}) = \\ &= \vec{v}_{\text{sat}}\vec{v}_i + \frac{1}{2}v_i^2 + \frac{1}{2}v_{\text{sat}}^2 + \Phi_{\text{host}}(\vec{r}_{\text{sat}}) = \\ &= \vec{v}_{\text{sat}}\vec{v}_i + \frac{1}{2}v_i^2 + E_{\text{sat}}. \end{aligned} \quad (5.10)$$

The energy kick obtained by the star compared to the satellite is then

$$\Delta E_i = \vec{v}_{\text{sat}}\vec{v}_i + \frac{1}{2}v_i^2 \quad (5.11)$$

We now ask for the maximum of ΔE . Equation 5.11 leads to the assumption that three conditions need to be fulfilled for the maximum energy kick:

1. The star has the maximum velocity possible which is the local escape speed at the tidal radius: $v_i = v_{\text{esc}}(R_{\text{tidal}})$,
2. Satellite and stellar velocities have to be aligned: $\vec{v}_{\text{sat}} \parallel \vec{v}_i$,
3. The satellite has to be at its maximum velocity, which occurs during the passage of the Perigalacticon: $v_{\text{sat}} = V_{\text{peri}}$.

Moreover, if the star is to gain orbital energy it needs to be at larger Galactocentric radii than the satellite, i.e. $|\vec{r}_{\text{sat}} + \vec{r}_i| > r_{\text{sat}}$, because only then the tidal force pushes the star away from the galactic center and thus from the potential well. This, together with the first condition, requires the star to be on a prograde orbit with respect to the satellite motion. This view is also confirmed by Fig. 5.4. It shows three snapshots of a simulation run shortly before, at and shortly after Perigalacticon. Red stars and blue triangles mark those particles which will have the highest/lowest orbital energy at the end of the simulation, respectively. The two groups are situated at very distinct locations with respect to the satellite. The particles which gain energy move along with the satellite on an orbit prograde with respect to the satellite motion while for particles which lose energy the orbital phase is such that

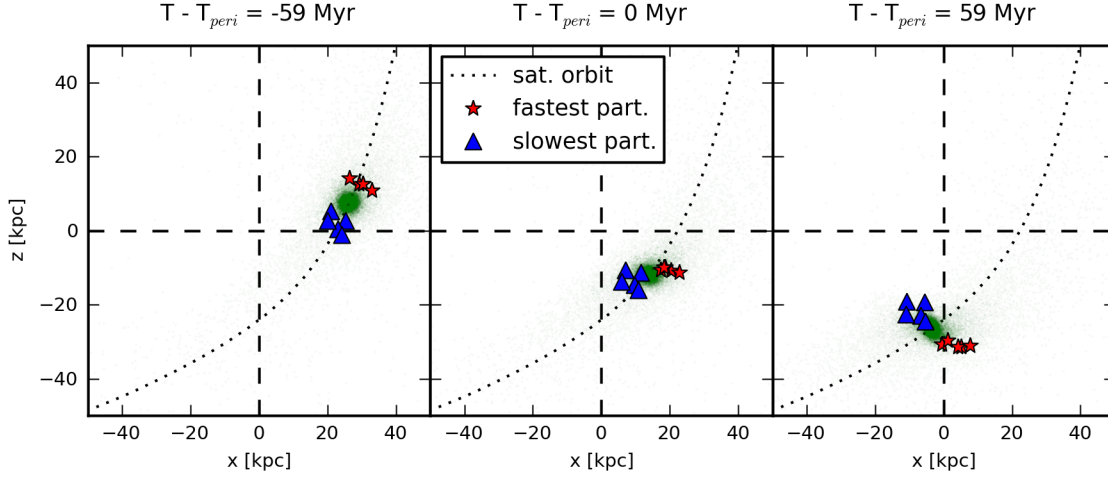


Figure 5.4: Snapshots of the satellite (small green dots) shortly before, during and shortly after its pericentric passage. Red stars show the positions of those particles which will have the highest orbital energy at the end of the simulation. Blue triangles show those with the lowest energy. The latter have a relative motion opposite to the satellite motion and are on retrograde orbits. The high energy particles move with the satellite and are on prograde orbits.

their motion is contrary to the direction of the system velocity.

Thus we arrive at

$$\Delta E_{\max} = V_{\text{peri}} v_{\text{esc}}(R_{\text{tidal}}) + \frac{1}{2} v_{\text{esc}}(R_{\text{tidal}})^2. \quad (5.12)$$

The quantities V_{peri} and $v_{\text{esc}}(R_{\text{tidal}})$ can be estimated if we know

- the radial mass profile of the host galaxy,
- the radial dark matter and baryonic mass profile of the satellite galaxy,
- the parameters of the satellite orbit, namely the initial angular momentum L_{sat} and the initial orbital energy E_{sat} .

In a first step we estimate the minimum distance to which the satellite approaches the host center, i.e. the pericenter distance R_{peri} . For this we use the effective potential $\Phi_{\text{eff}} = L_{\text{sat}}^2/(2r^2) + \Phi_{\text{host}}(r)$ exploiting

$$E_{\text{sat}} - \frac{1}{2} \Delta E_{\text{DF}} = \Phi_{\text{eff}}(R_{\text{peri}}), \quad (5.13)$$

where we compute the energy loss from dynamical friction ΔE_{DF} using Eq. 5.19. Further we compute the satellite velocity in the Perigalacticon via

$$V_{\text{peri}} = \sqrt{2(E_{\text{sat}} - \frac{1}{2} \Delta E_{\text{DF}} - \Phi_{\text{host}}(R_{\text{peri}}))}. \quad (5.14)$$

To compute the escape velocity $v_{\text{esc}}(R_{\text{tidal}})$ from the satellite system we first have to determine the tidal radius R_{tidal} which we assume to be equal to the Jacobi radius at the distance R_{peri} :

$$R_{\text{tidal}} = \left(\frac{M'_{\text{sat}}}{3M_{\text{host}}(R_{\text{peri}})} \right)^{\frac{1}{3}} R_{\text{peri}}. \quad (5.15)$$

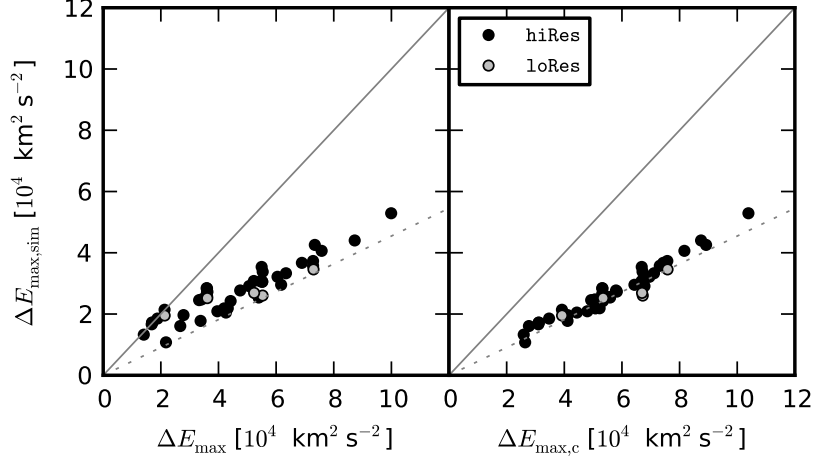


Figure 5.5: Energy gain with respect to E_{sat} predicted by our simplified model ΔE_{max} compared to the maximum energy gain found in each simulation. The latter are by a factor of ~ 0.45 (slope of the gray dotted lines) lower than the estimates, which is most likely due to oversimplification of the model. Phase-space sampling due to the limited particle number does not play a significant role as can be seen from the gray circles which mark the runs with 10 times lower resolution. *Left panel:* the estimated energy gain as obtained from our model. *Right panel:* the energy gain from our model corrected for an additional dependency on the angular momentum of the satellite. See text for a discussion.

However, we do not take the total satellite mass M_{sat} for the final radius. We also take into account that due to its much larger extension the dark matter halo of the satellite is stripped much earlier than the baryonic component. Consequently in a first step we compute the tidal radius using the total satellite mass M_{sat} and assume that all material outside this “dark matter tidal radius” $R_{\text{tidal,DM}}$ is lost. We then compute the “baryonic tidal radius” using Equation 5.15 with the mass $M'_{\text{sat}} = M_{\text{sat}}(r < R_{\text{tidal,DM}})$. Finally we obtain the escape speed

$$v_{\text{esc}}(R_{\text{tidal}}) = \sqrt{2|\Phi_{\text{sat}}(R_{\text{tidal}})|}. \quad (5.16)$$

Note that the tidal radius computed in this two-step process also allows a very good estimate of the baryonic mass loss of the satellite when it is assumed that all mass outside this tidal radius is lost, i.e.

$$f_{\text{unbound}} = \frac{M_{\text{lost}}}{M_{\text{sat}}} = \frac{M_{\text{sat}}(r > R_{\text{tidal}})}{M_{\text{sat}}}. \quad (5.17)$$

In the left panel of Fig. 5.5 we compare this model prediction obtained from Equation 5.12 to simulation results. For the latter we analyzed our simulations at Apogalacticon after the satellite’s passage through the host system and the particle with the highest orbital energy $\max(E_i)$ was identified. The energy gain $\Delta E_{\text{max,sim}}$ is then defined as $\max(E_i) - E_{\text{sat}}$. Solid lines in Fig. 5.5 indicates equality. Equation 5.12 *systematically* overestimates the maximum energy kick by a (constant) factor of 2.2, as indicated by the dashed line with slope $\alpha = 2.2^{-1} \simeq 0.45$. The overestimation are most likely due to oversimplification of our estimate, e.g. the neglect of the structural evolution of the satellite in the tidal field. Surprisingly, the mass resolution only plays a minor role in the sense that simulation runs with lower particle numbers do not yield significantly smaller maximum energy differences. This is most likely due to the steep slope of the energy distribution of the tidal debris stars

(see Sect. 5.4).

Much of the scatter in the left panel of Fig. 5.5 turned out to be a residual dependency on the initial angular momentum of the respective satellites in the simulation. We obtain a tighter relation (right panel) when we use

$$\Delta E_{\max,c} = \Delta E_{\max} \sqrt{\frac{L_{\text{sat}} + L_{\text{char}}}{L_{\text{char}}}}, \quad (5.18)$$

with $L_{\text{char}} = 6300 \text{ kpc kms}^{-1}$. Thus the value $\alpha \Delta E_{\max,c}$ gives a robust estimate of the maximum energy gain occurring during a satellite-host galaxy encounter.

Dynamical friction In the course of its orbit the satellite galaxy is also subject to dynamical friction. This means that it will sink deeper into the potential well of the host system. By the time it reaches its Perigalacticon stripped-off stars might have to get over an energy gap much wider to become HVSs. The extent of the energy loss depends mainly on the mass M_{sat} and the orbit of the satellite, in a way which is counterproductive to the ejection energies ΔE_{\max} : a more massive satellite ejects stars at higher energies as its internal velocities are larger. This energy gain for the stripped-off stars goes roughly spoken with $\sqrt{M_{\text{sat}}}$ since $v_{\text{esc}}(r) \propto \sqrt{M_{\text{sat}}}$ which goes into our estimate (Eq. 5.12). On the other hand a higher mass results in stronger dynamical friction which roughly goes $\propto M_{\text{sat}}$ (Chandrasekhar 1943). In fact in our simulations we find that the loss in orbital energy after one orbit is

$$\Delta E_{\text{DF}} = 2 \times 10^{-4} \left(\frac{M_{\text{sat}}}{M_{\odot}} \right)^{0.78} \left(1 + \frac{L_0}{5900 \text{ kpc kms}^{-1}} \right)^{-1}, \quad (5.19)$$

which reflects the dependency of the physical extent of the satellite on its mass and also the change of the orbital trajectories with changing orbital angular momentum. We use this simplistic approach as it covers best the effect of a possible reaction of the host galaxy on the intruder (however, see Taylor & Babul (2001) and Gan et al. (2010) for a more elaborated approach to model dynamical friction).

Thus above a certain mass the satellite will not be able to eject any HVSs since the energy loss of the whole system is larger than the energy gain of the single stars. However, judging from our simulations this will only happen at masses $> 10^{11} M_{\odot}$. Extrapolating our results into this (major merger) mass regime is not meaningful as a massive intruder will significantly perturb the host galaxy. We can thus just state that this scenario does not occur for minor mergers in the present work.

Hypervelocity stars In the context of hypervelocity stars which are unbound to the total system we have to compare ΔE with E_{sat} , the orbital energy of the satellite, since the energy E of such an unbound object must be

$$E = E_{\text{sat}} - \Delta E_{\text{DF}} + \Delta E \geq 0. \quad (5.20)$$

Thus the condition

$$\alpha \Delta E_{\max,c} \geq -E_{\text{sat}} + \Delta E_{\text{DF}}. \quad (5.21)$$

must be full-filled to allow unbound stars to be generated during such a satellite-host galaxy encounter with $\alpha \simeq 0.45$.

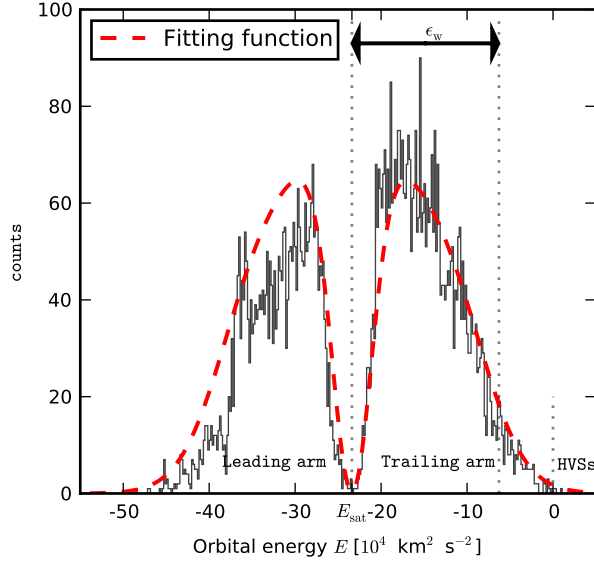


Figure 5.6: A histogram of the orbital energies of all particles which initially belonged to the satellite but became unbound to it in the course of the first orbit (tidal debris particles). The two peaks correspond to the two tidal arms torn out of the satellite. The central gap coincides with the orbital energy E_{sat} of the remaining satellite system. The dashed red line shows the fitting function (Eq. 5.22) which is used to characterize the distribution. The meaning of the fitting parameter ϵ_w which is used to determine the width of the high energy peak is also indicated. Note that throughout this work we only consider the high energy peak, as this is where HVSs would reside.

5.4 The energy distribution

A more robust measure of range of orbital energies covered by the stripped-off stars can be obtained when looking on the overall width of the energy distribution of all particles gravitationally unbound to the satellite. We determine these stars using an iterative method described by Tormen et al. (1998). The energy distribution is plotted in Fig. 5.6. The two peaks represent the leading and trailing tidal arm, respectively. The gap between them is centered on the orbital energy of the satellite. We apply an empirical fitting function

$$f_{\text{fit}}(E) = \frac{f_{\text{high}}}{C} \left[\frac{1}{(1 + \exp(\gamma(\frac{\Delta E}{\epsilon_w} - 1)))^2} - f_{\text{inner}} \exp\left(-\left(\frac{\Delta E}{\epsilon_{\text{inner}}}\right)^2\right) \right], \quad (5.22)$$

again with $\Delta E = E - E_{\text{sat}}$. To normalize the function we use the factor f_{high}/C , where f_{high} is the number of particles in the high energy (trailing) arm divided by the initial number of satellite particles and

$$\begin{aligned} C &= \frac{1}{f_{\text{high}}} \int_{E_{\text{sat}}}^{\infty} f_{\text{fit}}(E) dE \\ &= \epsilon_w \left[1 + \frac{1}{\gamma} \left(\ln(1 + e^{-\gamma}) - \frac{1}{1 + \exp(-\gamma)} \right) \right] - \frac{\sqrt{\pi} f_{\text{inner}} \epsilon_{\text{inner}}}{2}. \end{aligned} \quad (5.23)$$

The function is shown in Fig. 5.6 as red dashed line. For the fitting procedure we only consider the high energy peak of the distribution, i.e. where $E \geq E_{\text{sat}}$. The fitting parameters provide us with some characteristics of respective distribution: the width or typical energy, ϵ_w , the

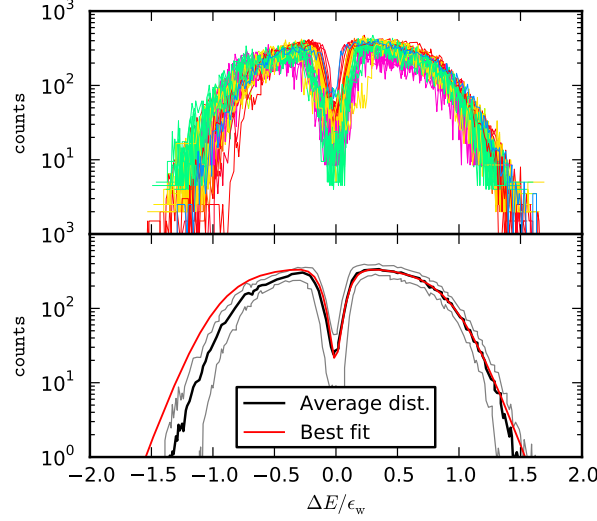


Figure 5.7: *Upper panel:* The histograms of the energies differences $\Delta E = E_i - E_{\text{sat}}$ of the tidal debris particles of all simulations used in this work over-plotted. The distributions are plotted as functions of ΔE in units of the width of the high energy peak ϵ_w . The histograms are also renormalized so that the high energy peak covers the same area. The lines are color-coded according to the initial angular momentum of the progenitor system (from red representing more radial orbits to blue for more circular orbits) *Lower panel:* The mean distribution obtained from the distribution plotted in the upper panel (solid black line). The standard deviation is also indicated with the thin gray lines. Over-plotted in red is our fitting function using the parameters given in Eqs. 5.25 and $\epsilon_w = 1$.

width of the central minimum, ϵ_{inner} , a measure of how fast the distribution drops off with increasing energy, γ , and the relative depth of the central minimum, f_{inner} .

A composite distribution Following an idea by Johnston (1998) we assume the general shape of the distributions to be invariant and only the width and the normalization to be specific to the respective orbit and satellite parameters. This means that the parameters $\epsilon_{\text{inner}}, \gamma, f_{\text{inner}}$ are either constant for all situations or a function of ϵ_w . To compare the distribution shapes we rescaled the particle energies into units of their specific typical energy ϵ_w via

$$\Delta \hat{E}_i = \frac{E_i - E_{\text{sat}}}{\epsilon_w}. \quad (5.24)$$

The resulting energy distributions were then renormalized to eliminate the influence of the number particles in the respective (trailing) tidal arm. The upper panel of Fig. 5.7 plots the energy distributions of all our simulations onto each other. Note that these include satellites varying over more than a magnitude in mass and angular momentum. The resulting mean distribution (black line) with the standard deviation (gray line) is also plotted. Applying our fitting function Eq. 5.22 results in the following parameter values:

$$\begin{aligned} \epsilon_{\text{inner}} &= 0.14\epsilon_w, \\ \gamma &= 5.21, \\ f_{\text{inner}} &= 0.94. \end{aligned} \quad (5.25)$$

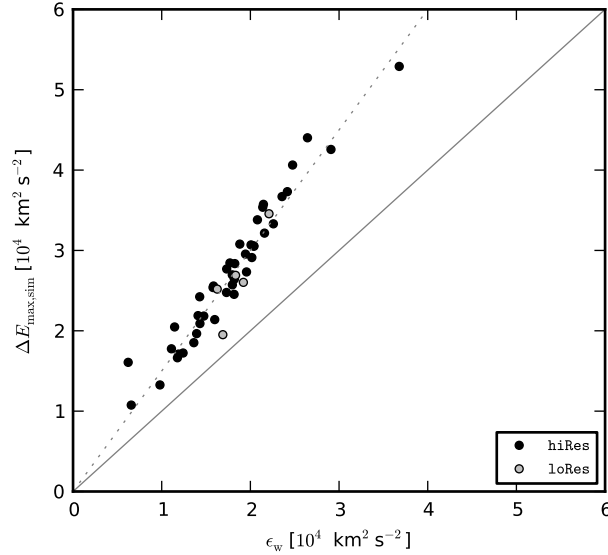


Figure 5.8: Relation between the maximum energy gain $\Delta E_{\max,\text{sim}}$ and the width ϵ_w of the energy distribution of all tidal debris stars obtain via fitting Equation 5.22. The gray dotted line has a slope of 1.5.

The fit is shown as a dashed red line in Fig. 5.7. We then repeat the fitting procedure for all single distributions with only ϵ_w as a free parameter. The resulting widths are plotted in Fig. 5.8 against the highest energy of all satellite particles, $\Delta E_{\max,\text{sim}}$. Grey dots represent the lower resolution runs. The tight correlation

$$\Delta E_{\max,\text{sim}} = \beta \epsilon_w \quad (5.26)$$

with $\beta \simeq 1.5$ (which is not strongly affected by the resolution in the simulations) is a result of the steep drop at the high energy tip of the distribution. Using the simple model developed in the previous section we can thus obtain an estimate for the width of the high energy peak via

$$\begin{aligned} \epsilon_w &= \beta^{-1} \Delta E_{\max,\text{sim}} \simeq \frac{\alpha}{\beta} \Delta E_{\max,c} \\ &= 0.3 \Delta E_{\max,c}. \end{aligned} \quad (5.27)$$

Note that $v_{\text{esc}}(r)$ is a proxy for the mass of the satellite. Thus more massive satellites will produce a larger energy spread in the stripped-off stars. One could also say that the higher velocity dispersion of a more massive galaxy directly translates into a larger energy dispersion in the tidal debris.

5.5 Discussion

It is now straightforward to compute the maximum velocities generated during a tidal collision at certain galactocentric radius $r > R_{\text{peri}}$:

$$\begin{aligned} v_{\max}(r) &= [2(E_{\max} - \Phi_{\text{host}}(r))]^{\frac{1}{2}} \\ &= [2(E_{\text{sat,apo}} + 0.45 \Delta E_{\max,c} - \Phi_{\text{host}}(r))]^{\frac{1}{2}}, \end{aligned} \quad (5.28)$$

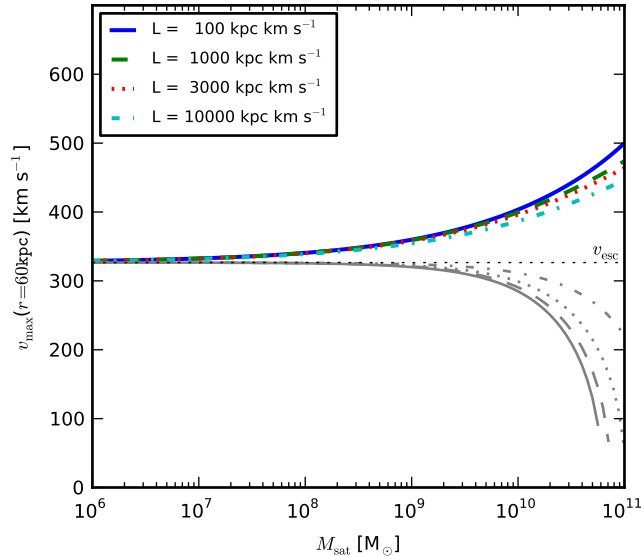


Figure 5.9: The maximum ejection velocities at a galactocentric distance of 60 kpc as a function of initial satellite mass as computed from Eq. 5.28 assuming an initial orbital energy of the satellite $E_{\text{sat}} = 0 \text{ km}^2 \text{ s}^{-2}$. The energy loss due to dynamical friction was computed using the empirical law (Eq. 5.19) obtained from our simulations. The lower gray lines show the velocity of the satellite remnant at the same distance.

where $E_{\text{sat,apo}} = E_{\text{sat}} - \Delta E_{\text{DF}}$ is the orbital energy of the remaining satellite after the passage. To obtain a quantitative idea we assume again a Galactocentric distance of $r = 60 \text{ kpc}$ to be comparable to the observations of HVSs. For the energy loss via dynamical friction ΔE_{DF} for simplicity we use the loss law (Eq. 5.19) found in our simulations. The velocities obtained in this way are plotted in Fig. 5.9 as a function of the initial satellite mass M_{sat} and for four different initial angular momenta L_{sat} . The satellite system was assumed to approach the host galaxy on a parabolic orbit, i.e. $E_{\text{sat}} = 0 \text{ km}^2 \text{ s}^{-2}$. Only the most massive satellite galaxies eject HVSs with substantial velocities comparable to the radial velocities of the observed HVSs. Less massive galaxies could, in principal, also yield such large velocities if they move on more energetic orbits themselves. For example, a satellite with mass $M_{\text{sat}} = 10^9 M_{\odot}$ would have to cross the virial radius of our parent galaxy³ with a velocity of $\sim 660 \text{ km s}^{-1}$ to eject a star with 720 km s^{-1} at 60 kpc comparable to the fastest HVSs known. Such a system would not lose enough energy to become bound to the larger galaxy. In this case one hardly would speak about an ejected star since the galaxy would move along with the star for a long period of time.

We now consider the subsample of observed HVSs with travel times $\sim 133 \text{ Myr}$ pointed out by Abadi et al. (2009, cf. their Fig. 1). The spread in velocities is roughly⁴ 400 km s^{-1} . Such strong variations in the velocities translate into a progenitor mass of $\simeq 10^{11} M_{\odot}$. If we select only stars within the over-density region defined by Abadi et al. (2009) the spread reduces to $\sim 250 \text{ km s}^{-1}$ resulting in a minimum progenitor mass still larger than $10^{10} M_{\odot}$. Concerning the known satellite galaxies the respective authors of the HVS discovery papers already excluded a kinematic connection to them (Brown et al. 2005, 2006a, 2009a; Edelmann et al.

³In our Galaxy model $R_{200} \simeq 260 \text{ kpc}$.

⁴We ignore the fact that the stars reside at different galactocentric radii. Taking this into account would enlarge the spread even further.

2005; Hirsch et al. 2005). Since we do not expect such a system to have escaped observations to date we conclude that a satellite origin for the sub-sample to be unlikely.

However, one should keep in mind that a more massive host galaxy (our host model has a total mass of $1.1 \times 10^{12} M_{\odot}$) would shift the lines in Fig. 5.9 upwards and would, in principal, allow also very small galaxies to produce stars with velocities, e.g. $> 500 \text{ km s}^{-1}$. However, the fact that only massive galaxies can eject stars with velocities significantly larger than their own velocities remains unaffected by this.

5.5.1 The bound HVS population and the outer stellar halo

Several recent studies have shown that the outer stellar halo is almost purely made of accreted stars (Abadi et al. 2006; Zolotov et al. 2009; Scannapieco et al. 2009). As smooth gas accretion via cold flows plays only a minor role for Milky Way-type galaxies at low red shifts (Brooks et al. 2009), we can assume the Galaxy has not grown significantly since its last major merger. Our simulations now demonstrate that satellite accretion will inevitably produce stars with velocities up to and exceeding their local escape speed. This means that the phase space distribution of stellar halo stars reaches all velocities up to the local escape speed at all times. For example, Smith et al. (2007) used this as a critical assumption for their technique to estimate the mass of the Galaxy.

However, this also means that a classification of a star as a HVS ejected from the SMBH based on its velocity is only valid for extremely large velocities. Without a confirmation of their young ages the “bound” HVS population in the compilation of Brown et al. (2009a) is indistinguishable from the normal (accreted) stellar halo population. To date only three stars in the survey have clear spectroscopic identification as main sequences B stars (Fuentes et al. 2006; López-Morales & Bonanos 2008; Przybilla et al. 2008) while others could be old blue stragglers or blue horizontal branch stars (Perets et al. 2009).

5.5.2 An intragalactic stellar population

With our results we can also address the question on what kind of satellites are the main contributors to a possible intragalactic stellar population (ISP) or Wandering stars (Teyssier et al. 2009). For this we assume the in-falling satellite galaxies to be initially on parabolic orbits, i.e. $E_{\text{sat}} = 0$. Via dynamical friction the satellites will be shifted onto bound orbits during their first passage. Thus not all stars in the trailing (high energy) tidal arm will become unbound, but only those which gained more energy than is lost by their progenitor system.

By integrating our fitting formula (Eq. 5.22) using the proper value for ϵ_w obtained via Equations 5.18 and 5.26 over energies larger than the frictional energy loss ΔE_{DF} we obtain the fraction of the baryonic mass which became HVSs. In the upper panel of Fig. 5.10 this fraction multiplied by the baryonic mass content of the satellite is shown as a function of the total satellite mass. For the estimation an initial angular momentum L_0 had to be set. The plot shows the results for four different L_0 (color coding is the same as in Fig. 5.9).

We then convolve this mass ejection function with an observational mass function of dwarf galaxies. We therefore used the luminosity function obtained by Koposov et al. (2008) and converted it into a mass function using the same relations used to create our satellite models for the simulations. As a result we obtained the cumulative HVS mass production function

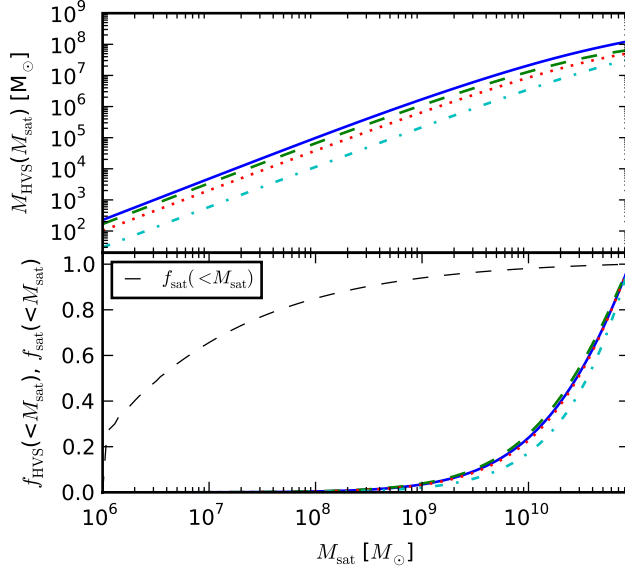


Figure 5.10: *Upper panel:* Mass ejected at unbound velocities during one satellite orbit as a function of initial progenitor mass. The satellite is assumed to have zero initial orbital energy, i.e. to be on a parabolic orbit. Different lines correspond to four different initial angular momenta of the satellite. The vertical dashed line indicates the mass of a single star particle in our simulations. *Lower panel:* mass fraction of an unbound intergalactic population originating from satellites with masses below M_{sat} . The fraction were computed using satellite mass function based on the satellite luminosity function of Koposov et al. (2008). The mass function is also shown as thin dashed line. More than 95 percent of the population is created by satellites more massive than $10^9 M_{\odot}$.

shown in the lower panel of Fig. 5.10. Color coding is the same as in the upper panel. The dashed black line indicates the cumulative mass function of satellite galaxies. Consistent with the results of Teyssier et al. (2009) obtained via cosmological simulations we find that a tiny minority of massive satellites produces the overwhelming majority of HVSs. Given the fact that more massive galaxies usually are also more metal-rich (Tamura et al. 2001) we conclude that an intragalactic stellar population should have at least on average a higher metallicities than the surviving dwarf galaxy population.

6 Summary and conclusions

In the previous three chapters we led the reader in almost a zigzag course from theoretical models to observational data and backwards. Doing this we explored several possibilities for a productive combination of individual stellar observations and numerical simulations. It is clear that there is no one general approach that is superior to everything else, but that each question needs a tailored analysis strategy that fits the problem and the available data. In the following we will summarize the analyses presented. Finally we attempt to formulate a few more general conclusions.

6.1 Synthetic stellar surveys

The aim of the study presented in Chapter 3 was to explore the capabilities of various Galaxy models by means of synthetic stellar surveys. As a testing ground we used the rich data base of the Radial Velocity Experiment (RAVE), one of the first representatives of the new generation of massive spectroscopic stellar surveys that provide velocities and astrophysical stellar parameters for a substantial amount of stars. Before we could conduct this study we had to complete the important preparatory task to evaluate the RAVE selection function. This is described in the first section of Chapter 2 where we show the selection function can be well recovered despite its complex structure in the space of position angles and apparent magnitudes. Our major tool to facilitate the analysis of the Galaxy models into the space of observables was the code GALAXIA that provides a flexible framework to combine these models with the insights of stellar physics and evolution (i.e. stellar model atmospheres and evolutionary tracks) and thereby allows to transfer the models into the space of observables. The code could not be used “out of the box”, but we also had to adapt it for our purposes as we described in Section 2.3.

As a first step we produced a mock RAVE survey based on the widely-used Besançon model (Robin et al. 2003) and confronted it with the real data. An interesting aspect of this exercise is that the Besançon model was created just at the time when the RAVE observations started and thus presents pure prior knowledge. With this in mind we can state that the model performs very well in reproducing the velocity and stellar parameter distributions in RAVE. In the metallicity distribution we find significant discrepancies pointing to a too prominent and possibly also a too metal-poor thick disk component in the model. A higher mean metallicity of the thick disk would also be more consistent with the high-resolution measurements by Soubiran et al. (2003). Nevertheless, the good agreement between model and real data in the aspects where it is expected gives us confidence in the validity of our input assumptions and especially in our modeling of the RAVE selection function. Finally, as we explore the correlations between the properties of the stars, in particular, the relation between kinematics and chemistry, we reach the limits of the Besançon model that assigns metallicities and kinematics to a large degree independently.

From here we move on and for the first time transform a full N -body model of the Milky Way

into the space of observables to compare it with real stellar data on an equal footing. As an input we use the hybrid model by Minchev et al. (2013a), the MCM model, that combines a cosmological re-simulation with a chemical evolution model for the Galaxy. Resolved stellar population synthesis with a discrete model is a novel approach and we extensively tested our input set-up to understand the role of the different ingredients.

For this model it is straightforward to evaluate the selection effects in the RAVE data. We find clear discrepancies in the metallicities distributions of the stars in the mock survey and the underlying distribution in the survey volume. This clearly illustrates the need to model the detailed selection function, as we do in this study, if the intrinsic properties of the stars in the survey (metallicities, ages, etc.) are analyzed.

We find that the model is competitive in relation to the Besançon model in matching the magnitude, color and stellar parameter distributions. Some aspects of the model are, however, clearly hampered by the coarse representation of the smooth phase space distribution function (DF) via mass particles. On the one hand we have the velocity distribution, where the large phase space smoothing broadens the DF. On the other hand, we find a patchy structure in the star counts as a function of position on the sky that is caused by the nearby mass particles that are heavily over-sampled during the generation of the mock stars. To prevent this an even stronger smoothing would be required. Both caveats could be resolved by improving the mass, spatial and velocity resolution by increasing the number of particles in the input model. We finally showed that the model is capable to reproduce the chemodynamical correlations found in the RAVE data. Here the self-consistent dynamic history of all stars in the model reveals its full power. From this point we head off and find predictions of the model in the sense that we explore statistical properties for RAVE sub-samples, that are not available from the real data, like ages and birth locations of the stars. We can show that we can identify stars that have migrated radially via the mechanism described by Sellwood & Binney (2002) by selecting a stellar population that combines large vertical motions with close to circular orbits.

Finally, we studied the outcome of a full cosmological simulation of the evolution of a disk galaxy using our machinery. Within the same volume this galaxy is represented by a number of particles that is a factor of 5 less than in the MCM model, so the effects of limited resolution are much stronger in this model. But even when we take this into account we find strong discrepancies between model and real data, mostly in the surface gravity and metallicity distributions. These can be traced back to the presence of a too massive metal-poor spheroidal component in the galaxy. The too low disk-to-bulge ratio in this galaxy was already known from previous analyses of this galaxy and is a common problem in simulations of this type. The fact that we could detect it in our synthetic RAVE survey illustrates the sensitivity of our approach to the global structure of a Galaxy model, i.e. that the signatures of the global structure are not lost in the complex interplay of the stellar evolutionary tracks, stellar atmosphere models, phase space smoothing and the selection function in the stellar synthesis process. Our technique is hence suitable to discriminate between 'good' and 'bad' models of the Galaxy or even to fit a model to data.

In the general context, our study represents the first step to (re-)connect two important astrophysical lines of research via a common frame-work: simulations of (disk) galaxy formation and Galactic Astronomy with its massive stellar surveys already available now or in the near future. Recently a number of successful simulations of disk galaxies were reported (Governato et al. 2010; Guedes et al. 2011; Aumer et al. 2013; Marinacci et al. 2014) and with the rapid developments in simulation techniques and computational power, it seems clear that at least the next generation of simulations will provide close counter-parts of our

Galaxy including also reliable information about the distribution of chemical elements (the latter is currently often missing in the simulations). Pseudo-cosmological approaches like the MCM model (Minchev et al. 2013a) provide already today excellent models for our Galaxy with a self-consistent dynamic history.

At the same time the developments in observational astronomy, i.e. the realization of massive spectroscopic survey projects, like RAVE, SEGUE, APOGEE, HERMES and eventually Gaia and 4MOST, allow the statistical exploration of the stellar content of the Galaxy far beyond the solar neighborhood into volumes well resolved by the above mentioned simulations. Furthermore, stellar properties like the chemical abundances, precise kinematics, distances and especially the correlations of those contain information about the past history of the Galaxy. However, this information is masked in the data by the unavoidable selection effects. Even an completely automated (and therefore well predictable) mission like the Gaia satellite will have an extremely complicated selection function coming from the non-trivial scanning law (e.g. Prusti 2012). It will hence in many cases be impossible to distillate information about the Galaxy directly from the data. Our technique to transform physical models into observational space presents a straightforward approach to deal with the selection effects and recover the underlying information. Our discussion on the planning of the 4MOST instrument in Section 3.5 illustrates that the trend to more sophisticated selection criteria will extend into the future.

Ad hoc models of the present state of the Galaxy based on photometry are clearly insufficient to cope with the comprehensive data delivered by current and future surveys. In particular the link between stellar dynamics and their elemental abundances appears to play a key role in the recovery the formation history of the Milky Way (e.g. Minchev et al. 2013b) and it is a difficult and yet unsolved problem to implement such trends into an analytic model. With our method we gain access to the computationally relatively cheap models like the hybrid MCM model – that could be used in a fitting process – as well as to the above mentioned fully self-consistent cosmological models that naturally give rise to these chemodynamic correlations. Such models are required to proof the consistency of the Λ CDM paradigm on scales of galaxies like the Milky Way or even smaller. Proofing this consistency could be the next major success of numerical astrophysics comparable to the reproduction of the large scale filamentary structure of the Universe.

Before this problem can be actually tackled another issue has to be resolved. Current simulations rely heavily on the largely phenomenological modeling of physical processes that yet cannot be resolved or are not well understood (star formation, feedback, etc., see Springel (2012) for an overview). Rix & Bovy (2013) recently asked whether there is “testable evidence that the feedback implemented in the simulations actually took place”. Synthetic stellar observations of such simulations can certainly help answering this question.

An interesting type of discrete models that we have not considered in this thesis, are massive test particle simulations that allow the study of kinematic sub-structure induced by non-axis-symmetric features in the Galaxy (Monari et al. 2013). These simulations allow extremely high particle numbers and are from this point of view well suited for the creation of synthetic observations. A drawback is that these simulation do not have a real evolutionary dynamic and chemical history, so only the effects of the current structure of the Galactic disk (like bar resonances) can be tested. Exploring these models through the eyes of RAVE could possibly clarify the nature of the velocity gradients found by Siebert et al. (2012) and Williams et al. (2013) in this survey.

With the machinery to generate synthetic surveys set-up we are not restricted to concentrate on a specific survey – as we have done in this thesis. Different surveys probe different aspects

of the Galaxy and therefore we will dramatically increase our leverage to evaluate models if we consider more than one survey. A simultaneous analysis of the complementary surveys RAVE and SEGUE appears to be the next logical step. Another powerful addition could be a stellar sample with precise age determinations via astroseismology coming from the Corot and Kepler missions (Chaplin & Miglio 2013). An obstacle for such a simultaneous analysis is currently that different surveys often have systematic shifts between their parameter estimates, for example in distance or metallicity. These shifts have to be well understood before a sensible combined analysis can be done.

6.2 The Galactic escape speed and the mass of the Milky Way

In Chapter 4 we analyzed the the RAVE survey together with additional literature data, to estimate the Galactic escape speed (v_{esc}) at various Galactocentric radial bins and through this the virial mass of our Galaxy. For this we define the escape speed as the minimum speed required to reach $3R_{340}$. In order to break a degeneracy between our fitting parameters we had to calibrate our method on a set of cosmological simulations of disk galaxy formation. The 90% confidence interval for our best estimate of the local escape speed is $492 < v_{\text{esc}} < 587 \text{ km s}^{-1}$, with a median value of 533 km s^{-1} .

Our estimate is very close to the previous measurement by Smith et al. (2007) (544 km s^{-1}) who used a much earlier version of the RAVE survey that included only radial velocities. In this work we could use available distance estimates for the stars and take the fact into account that many of the RAVE stars are located far from the Sun and closer to the Galactic center where the velocity distribution is shifted to higher values. These stars violated the implicit assumption made by Smith et al. (2007) to have a local sample.

With our new v_{esc} value we can estimate the virial mass of the Galaxy (baryons and dark matter) by assuming a simple mass model of the baryonic content of the Galaxy and a spherical (adiabatically contracted) NFW halo profile and fixing the local standard of rest to 220 km s^{-1} . The resulting values can be found in Table 4.2. Despite the very similar value for the escape speed we find a slightly higher mass for the Galaxy, because we consistently apply the definition of the escape speed mentioned above.

The local standard of rest (V_{LSR}) is still under debate. If we loosen our constraint on V_{LSR} and use a prior on the halo concentration parameter, c , coming from large cosmological simulations we find a most likely value for the virial mass $M_{340} = 1.3_{-0.3}^{+0.4} \times 10^{12} M_{\odot}$ for the pure NFW profile and $1.2_{-0.3}^{+0.4} \times 10^{12} M_{\odot}$ for an adiabatically contracted halo profile. We also provide estimates for other definitions of the virial mass, M_{200} and M_{100} , that are often used in the literature and for which the values are higher for an equivalent Galaxy model.

The mass measurements within 25 and 80 kpc recently published by Kafle et al. (2012) and Gnedin et al. (2010) are in better agreement with our model with an unaltered NFW profile. However, this model predicts a circular speed at the solar radius of only 187 km s^{-1} , in strong disagreement with recent estimates favoring values larger than 220 km s^{-1} (Schönrich 2012; Bovy et al. 2012a). The adiabatically contracted halo model predicts a more realistic value of 229 km s^{-1} , but agrees worse with the measurements by Kafle et al. (2012) and Gnedin et al. (2010). The un-contracted halo model is further consistent with the requirement that the satellite galaxy Leo I is on a bound orbit. A halo model with a more moderate contraction

due to the condensation of baryons as proposed by Abadi et al. (2010) in its center might mitigate the tensions introduced by the various constraints.

In this study we could not address all properties that define the Galactic dark matter halo from a dynamical point of view. We had to assume a spherically symmetric halo, because the kinematics of our locally confined stellar sample do not contain any information about the geometrical shape. Theoretical predictions (e.g. Allgood et al. 2006; Vera-Ciro et al. 2011) as well as observations (Law et al. 2009; Vera-Ciro & Helmi 2013) favor a triaxial configuration. Long thin stellar streams in the halo hold information on the flattening of the halo and hence an analysis as done by Koposov et al. (2010) for GD-1 is complementary to our results. Accurate distances and proper motions are key for these studies.

Another open question is the amount of sub-structure in the halo. Simulations predict a large number of sub-halos in our Galaxy (Gao et al. 2004; Klypin et al. 1999), many of which are unobservable, because they lost their gas content before they could form stars. Again, thin stellar streams could shed light into this problem, because these should be visibly perturbed and heated by the constant passages of these dark matter over-densities Johnston et al. (2002); Carlberg et al. (2012). Note that our tests with cosmological simulation showed that neither the non-spherical shape nor the existence of dark sub-halos do invalidate our results on the Milky Way mass.

The space mission Gaia will provide substantial data for studies like ours as well as for studies of thin stellar streams. This should allow to pin down the mass of the Galaxy much more accurately, even though our approach might brush over too many details of the Galaxy to be the best choice for a data set with the precision and completeness of the Gaia results. The constraints on the shape of the Galactic potential might be accessible only for the inner halo, because of the relatively bright limit of the Gaia spectrograph. It is, however, expected that the shape is changing with radial distance (Kazantzidis et al. 2010; Vera-Ciro et al. 2011). A global assessment of the shape profile might be only possible with the data coming from 4MOST that can will provide radial velocities and spectro-photometric distances for much more distant stars in the halo and thereby complete the set of phase space coordinates for these stars.

6.3 Hypervelocity stars in galactic tidal tails

In Chapter 5 we have used a suite of 41 N -body simulations to study the tidal debris of satellite galaxies interacting with their much more massive host systems. Abadi et al. (2009) suggested that a fraction of the stripped-off stars can reach significant velocities and could be confound with Hypervelocity stars (HVSs) ejected from the Galactic center by a super-massive black hole. We find that, as suggested by these authors, the stripped-off stars are in fact observed in a confined region on the sky. However, for stars at distances still observable from the solar position the reason for this is not only the projection of a collimated stellar stream along the line of sight, but in addition that so shortly after the stripping event the stars had not yet enough time to disperse in physical space. We further developed a simple analytic model to predict the maximum possible ejection velocities via estimating the maximum possible energy kick a star can obtain during such a tidal encounter (Eq. 5.18). Following Johnston (1998) we suggest that the general shape of the energy distribution of particles stripped-off during one orbit is self-similar and can be described quite accurately by Equation 5.22. There are only two free parameters in the distribution, its width and its

normalization. The first represent a characteristic energy and is tightly connected to the maximum energy kick described by our stripping model. The normalization simply reflects the fraction of mass lost by the satellite. Both can be predicted knowing only the initial properties of the host and satellite galaxy without the need of computationally expensive N -body simulations.

We also address the recently reported Hypervelocity star population. Velocities larger than 500 km s^{-1} are only generated by massive satellite galaxies ($> 10^{11} M_{\odot}$) or by galaxies with very large in-fall velocities in which case these galaxies stay unbound from the host and leave the parent galaxy together with the HVSs. Furthermore the larger spread in velocities of HVSs with common travel times also requires a massive progenitor ($> 10^{10} M_{\odot}$). The absence of the remnant of such a massive system makes a tidal debris origin for the HVSs unlikely even from a kinematic point of view.

Convolving our formalism with a satellite mass function allows us to determine the masses of the progenitors of the main contributors to a potential intergalactic stellar population (ISP). We find that stars originating from satellite galaxies with masses $> 10^9 M_{\odot}$ form about 95 percent of the population. This is consistent with the findings of Teyssier et al. (2009) who traced back the origin of unbound particles in the cosmological simulations of Bullock & Johnston (2005). We thus conclude that such an ISP should tend to have the same or even a higher metallicity than the outer halo population and also as the present population of Milky Way satellites. An interesting aspect of this topic is added by the fact that most Galactic satellite galaxies orbit in a “disk of satellites” (Metz et al. 2008; Pawlowski et al. 2012). If the early Galactic satellites also followed this distribution, the ISP should also exhibit a highly anisotropic distribution (see also Pawlowski et al. 2013).

6.4 Closing remarks

If we remove our focus on the individual questions addressed in our three studies we can try to find their place in a more holistic research strategy. But what is the general question we are asking? The ultimate goal of Astrophysical research (or fundamental research in general) appears to be open to one’s personal opinion, but the study of the Milky Way as a galaxy is clearly motivated from a cosmological point of view. We want to learn about the formation and history of these objects and thereby about the history of the Universe as a whole. The Milky Way provides the unique opportunity to study the individual constituents of a galaxy in finest detail.

The *current* Galactic structure should be accessible via direct inference methods, like we have applied to obtain the virial mass of the Milky Way (other examples are Kafle et al. (2012), Bovy et al. (2012c) or Golubov et al. (2013)), or via dedicated simulations, e.g. to model the Sagittarius stream (Law et al. 2009; Vera-Ciro & Helmi 2013) and our study on a accretion origin of the hypervelocity star population. To do this we do not need a comprehensive model of the Galaxy including detailed information about the individual histories of the stars.

We can then search for evolutionary models that lead to a galaxy with structural parameters similar to those of the Milky Way, be it full cosmological simulations or hybrid models like the MCM model. The great question here is the uniqueness of such a model. The high degrees of stochasticity and non-linearity of galaxy evolution implied by the Λ CDM paradigm make it seem plausible that there will be many scenarios leading to the same galaxy. This is particularly clear since the discovery of radial migration as an important mechanism in the secular evolution of galaxy disks (Roškar et al. 2008; Schönrich & Binney 2009; Minchev

et al. 2012). Here our approach to generate synthetic stellar observations unfolds its power. For example, the chemical tagging approach (Freeman & Bland-Hawthorn 2002) will identify signatures of merging history of the Galaxy. With synthetic observations we are able to predict the number of sub-structures detectable in the GALAH survey (Zucker et al. 2013) for a given Galaxy model – in analogy to the missing satellite problem – and might be able to discard many of these models. The complex structure of the Galactic disk revealed by Bovy et al. (2012c) in the SEGUE survey is also difficult to interpret without model predictions that consistently cover the effects of radial mixing.

It is hence a combination of various approaches that we will eventually lead us to a coherent picture of our Galaxy and its evolution. Synthetic stellar observations might play the key role in connecting Galactic Astronomy with physical cosmology.

Bibliography

- Abadi, M. G., Navarro, J. F., Fardal, M., Babul, A., & Steinmetz, M. 2010, MNRAS, 407, 435
- Abadi, M. G., Navarro, J. F., & Steinmetz, M. 2006, MNRAS, 365, 747
- Abadi, M. G., Navarro, J. F., & Steinmetz, M. 2009, ApJ, 691, L63
- Abadi, M. G., Navarro, J. F., Steinmetz, M., & Eke, V. R. 2003a, ApJ, 591, 499
- Abadi, M. G., Navarro, J. F., Steinmetz, M., & Eke, V. R. 2003b, ApJ, 597, 21
- Alexander, J. B. 1982, MNRAS, 201, 579
- Allende Prieto, C., Majewski, S. R., Schiavon, R., et al. 2008, *Astronomische Nachrichten*, 329, 1018
- Allgood, B., Flores, R. A., Primack, J. R., et al. 2006, MNRAS, 367, 1781
- An, D., Beers, T. C., Johnson, J. A., et al. 2013, ApJ, 763, 65
- Antoja, T., Helmi, A., Bienaymé, O., et al. 2012, MNRAS, 426, L1
- Asplund, M., Grevesse, N., Sauval, A. J., & Scott, P. 2009, ARA&A, 47, 481
- Aumer, M., White, S., Naab, T., & Scannapieco, C. 2013, accepted for publication in MNRAS, astro-ph 1304.1559
- Babusiaux, C., Gómez, A., Hill, V., et al. 2010, A&A, 519, A77
- Barnes, J. & Hut, P. 1986, Nature, 324, 446
- Battaglia, G., Helmi, A., Morrison, H., et al. 2005, MNRAS, 364, 433
- Battaglia, G., Helmi, A., Morrison, H., et al. 2006, MNRAS, 370, 1055
- Beers, T. C., Chiba, M., Yoshii, Y., et al. 2000, AJ, 119, 2866, (B00)
- Belokurov, V., Zucker, D. B., Evans, N. W., et al. 2006, ApJ, 642, L137
- Bensby, T., Adén, D., Meléndez, J., et al. 2011, A&A, 533, A134
- Bensby, T., Yee, J. C., Feltzing, S., et al. 2013, A&A, 549, A147
- Bienaymé, O., Robin, A. C., & Creze, M. 1987, A&A, 180, 94
- Binney, J., Burnett, B., Kordopatis, G., et al. 2014, MNRAS, 437, 351
- Boeche, C., Chiappini, C., Minchev, I., et al. 2013a, A&A, 553, A19
- Boeche, C., Siebert, A., Piffl, T., et al. 2013b, A&A, 559, A59
- Boeche, C., Siebert, A., Williams, M., et al. 2011, AJ, 142, 193
- Boller, T. & Dwelly, T. 2012, in Society of Photo-Optical Instrumentation Engineers (SPIE) Conference Series, Vol. 8448
- Bovy, J., Allende Prieto, C., Beers, T. C., et al. 2012a, ApJ, 759, 131
- Bovy, J., Rix, H.-W., & Hogg, D. W. 2012b, ApJ, 751, 131
- Bovy, J., Rix, H.-W., Liu, C., et al. 2012c, ApJ, 753, 148
- Boylan-Kolchin, M., Besla, G., & Hernquist, L. 2011, MNRAS, 414, 1560

- Boylan-Kolchin, M., Bullock, J. S., Sohn, S. T., Besla, G., & van der Marel, R. P. 2013, *ApJ*, 768, 140
- Breddels, M. A., Smith, M. C., Helmi, A., et al. 2010, *A&A*, 511, A90
- Brooks, A. M., Governato, F., Quinn, T., Brook, C. B., & Wadsley, J. 2009, *ApJ*, 694, 396
- Brown, W. R., Geller, M. J., & Kenyon, S. J. 2009a, *ApJ*, 690, 1639
- Brown, W. R., Geller, M. J., & Kenyon, S. J. 2012, *ApJ*, 751, 55
- Brown, W. R., Geller, M. J., Kenyon, S. J., & Bromley, B. C. 2009b, *ApJ*, 690, L69
- Brown, W. R., Geller, M. J., Kenyon, S. J., & Kurtz, M. J. 2005, *ApJ*, 622, L33
- Brown, W. R., Geller, M. J., Kenyon, S. J., & Kurtz, M. J. 2006a, *ApJ*, 640, L35
- Brown, W. R., Geller, M. J., Kenyon, S. J., & Kurtz, M. J. 2006b, *ApJ*, 647, 303
- Brown, W. R., Geller, M. J., Kenyon, S. J., Kurtz, M. J., & Bromley, B. C. 2007a, *ApJ*, 660, 311
- Brown, W. R., Geller, M. J., Kenyon, S. J., Kurtz, M. J., & Bromley, B. C. 2007b, *ApJ*, 671, 1708
- Bruzual, G. & Charlot, S. 2003, *MNRAS*, 344, 1000
- Bullock, J. S. & Johnston, K. V. 2005, *ApJ*, 635, 931
- Burnett, B., Binney, J., Sharma, S., et al. 2011, *A&A*, 532, A113
- Busha, M. T., Marshall, P. J., Wechsler, R. H., Klypin, A., & Primack, J. 2011, *ApJ*, 743, 40
- Caffau, E., Koch, A., Sbordone, L., et al. 2013, *Astronomische Nachrichten*, 334, 197
- Caldwell, N., Morrison, H., Kenyon, S. J., et al. 2010, *AJ*, 139, 372
- Carlberg, R. G., Grillmair, C. J., & Hetherington, N. 2012, *ApJ*, 760, 75
- Carollo, D., Beers, T. C., Lee, Y. S., et al. 2007, *Nature*, 450, 1020
- Casagrande, L., Schönrich, R., Asplund, M., et al. 2011, *A&A*, 530, A138
- Chabrier, G. 2001, *ApJ*, 554, 1274
- Chandrasekhar, S. 1943, *ApJ*, 97, 255
- Chaplin, W. J. & Miglio, A. 2013, *ARA&A*, 51, 353
- Chiappini, C. 2009, in *IAU Symposium*, Vol. 254, *IAU Symposium*, ed. J. Andersen, B. Nordström, & J. Bland-Hawthorn, 191–196
- Chiappini, C., de Jong, R. S., Schwobe, A., et al. 2013, 4MOST Scientific report - Milestone 2, for access please contact 4MOST PI Roelof S. de Jong
- Choi, J., Weinberg, M. D., & Katz, N. 2007, *MNRAS*, 381, 987
- Choi, J., Weinberg, M. D., & Katz, N. 2009, *MNRAS*, 400, 1247
- Cioni, M.-R. L., Girardi, L., Moretti, M. I., et al. 2014, *A&A*, 562, A32
- Coşkunoğlu, B., Ak, S., Bilir, S., et al. 2011, *MNRAS*, 412, 1237
- Dalton, G., Trager, S. C., Abrams, D. C., et al. 2012, in *Society of Photo-Optical Instrumentation Engineers (SPIE) Conference Series*, Vol. 8446
- de Jong, R. S., Bellido-Tirado, O., Chiappini, C., et al. 2012, in *Society of Photo-Optical Instrumentation Engineers (SPIE) Conference Series*, Vol. 8446
- de Rijcke, S., Michielsen, D., Dejonghe, H., Zeilinger, W. W., & Hau, G. K. T. 2005, *A&A*, 438, 491
- Deason, A. J., Belokurov, V., Evans, N. W., et al. 2012, *MNRAS*, 425, 2840

- Dehnen, W. 1998, *AJ*, 115, 2384
- Dehnen, W. & Binney, J. 1998, *MNRAS*, 294, 429
- D’Onghia, E., Besla, G., Cox, T. J., & Hernquist, L. 2009, *Nature*, 460, 605
- D’Onghia, E., Vogelsberger, M., Faucher-Giguere, C.-A., & Hernquist, L. 2010, *ApJ*, 725, 353
- Edelmann, H., Napiwotzki, R., Heber, U., Christlieb, N., & Reimers, D. 2005, *ApJ*, 634, L181
- Epchtein, N., de Batz, B., Capoani, L., et al. 1997, *The Messenger*, 87, 27
- Ferrara, A. & Tolstoy, E. 2000, *MNRAS*, 313, 291
- Fich, M. & Tremaine, S. 1991, *ARA&A*, 29, 409
- Flynn, C., Holmberg, J., Portinari, L., Fuchs, B., & Jahreiß, H. 2006, *MNRAS*, 372, 1149
- Freeman, K. & Bland-Hawthorn, J. 2002, *ARA&A*, 40, 487
- Fuentes, C. I., Stanek, K. Z., Gaudi, B. S., et al. 2006, *ApJ*, 636, L37
- Fuhrmann, K. 2011, *MNRAS*, 414, 2893
- Gan, J., Kang, X., van den Bosch, F. C., & Hou, J. 2010, *MNRAS*, 408, 2201
- Gao, L., White, S. D. M., Jenkins, A., Stoehr, F., & Springel, V. 2004, *MNRAS*, 355, 819
- Gao, S., Just, A., & Grebel, E. K. 2013, *A&A*, 549, A20
- García Pérez, A. E., Cunha, K., Shetrone, M., et al. 2013, *ApJ*, 767, L9
- Gillessen, S., Eisenhauer, F., Fritz, T. K., et al. 2009, *ApJ*, 707, L114
- Gilmore, G. & Reid, N. 1983, *MNRAS*, 202, 1025
- Gingold, R. A. & Monaghan, J. J. 1977, *MNRAS*, 181, 375
- Girardi, L., Groenewegen, M. A. T., Hatziminaoglou, E., & da Costa, L. 2005, *A&A*, 436, 895
- Gnedin, O. Y., Brown, W. R., Geller, M. J., & Kenyon, S. J. 2010, *ApJ*, 720, L108
- Gnedin, O. Y., Gould, A., Miralda-Escudé, J., & Zentner, A. R. 2005, *ApJ*, 634, 344
- Golubov, O., Just, A., Bienaymé, O., et al. 2013, *A&A*, 557, A92
- Górski, K. M., Hivon, E., Banday, A. J., et al. 2005, *ApJ*, 622, 759
- Gottlöber, S., Hoffman, Y., & Yepes, G. 2010, *ArXiv e-prints*
- Governato, F., Brook, C., Mayer, L., et al. 2010, *Nature*, 463, 203
- Governato, F., Mayer, L., Wadsley, J., et al. 2004, *ApJ*, 607, 688
- Gratton, R. G., Carretta, E., Claudi, R., Lucatello, S., & Barbieri, M. 2003, *A&A*, 404, 187
- Guedes, J., Callegari, S., Madau, P., & Mayer, L. 2011, *ApJ*, 742, 76
- Guo, Q., White, S., Li, C., & Boylan-Kolchin, M. 2010, *MNRAS*, 404, 1111
- Hambly, N. C., Davenhall, A. C., Irwin, M. J., & MacGillivray, H. T. 2001, *MNRAS*, 326, 1315
- Hernquist, L. 1990, *ApJ*, 356, 359
- Hernquist, L. 1993, *ApJS*, 86, 389
- Hills, J. G. 1988, *Nature*, 331, 687
- Hirsch, H. A., Heber, U., O’Toole, S. J., & Bresolin, F. 2005, *A&A*, 444, L61
- Høg, E., Fabricius, C., Makarov, V. V., et al. 2000, *A&A*, 355, L27
- Hogg, D. W. & Lang, D. 2011, in *EAS Publications Series*, Vol. 45, *EAS Publications Series*, 351–358

- Irrgang, A., Wilcox, B., Tucker, E., & Schiefelbein, L. 2013, *A&A*, 549, A137
- Ivezić, Ž., Beers, T. C., & Jurić, M. 2012, *ARA&A*, 50, 251
- Jaffe, W. 1983, *MNRAS*, 202, 995
- Johnston, K. V. 1998, *ApJ*, 495, 297
- Johnston, K. V., Spergel, D. N., & Haydn, C. 2002, *ApJ*, 570, 656
- Just, A. & Jahreiß, H. 2010, *MNRAS*, 402, 461
- Kafle, P. R., Sharma, S., Lewis, G. F., & Bland-Hawthorn, J. 2012, *ApJ*, 761, 98
- Kallivayalil, N., van der Marel, R. P., Besla, G., Anderson, J., & Alcock, C. 2013, *ApJ*, 764, 161
- Kauffmann, G., Colberg, J. M., Diaferio, A., & White, S. D. M. 1999, *MNRAS*, 303, 188
- Kazantzidis, S., Abadi, M. G., & Navarro, J. F. 2010, *ApJ*, 720, L62
- Kim, J.-h., Abel, T., Agertz, O., et al. 2014, *ApJS*, 210, 14
- King, I. R. 1966, *AJ*, 71, 64
- Klypin, A., Kravtsov, A. V., Valenzuela, O., & Prada, F. 1999, *ApJ*, 522, 82
- Klypin, A., Zhao, H., & Somerville, R. S. 2002, *ApJ*, 573, 597
- Kochanek, C. S. 1996, *ApJ*, 457, 228
- Koposov, S., Belokurov, V., Evans, N. W., et al. 2008, *ApJ*, 686, 279
- Koposov, S. E., Rix, H.-W., & Hogg, D. W. 2010, *ApJ*, 712, 260
- Kordopatis, G., Gilmore, G., Steinmetz, M., et al. 2013, *AJ*, 146, 134
- Kregel, M., van der Kruit, P. C., & de Grijs, R. 2002, *MNRAS*, 334, 646
- Kroupa, P. 2007, *ArXiv Astrophysics e-prints*
- Law, D. R., Majewski, S. R., & Johnston, K. V. 2009, *ApJ*, 703, L67
- Lee, Y. S., Beers, T. C., An, D., et al. 2011, *ApJ*, 738, 187
- Leonard, P. J. T. & Tremaine, S. 1990, *ApJ*, 353, 486
- Levin, Y. 2006, *ApJ*, 653, 1203
- Li, Y.-S. & White, S. D. M. 2008, *MNRAS*, 384, 1459
- López-Morales, M. & Bonanos, A. Z. 2008, *ApJ*, 685, L47
- Lu, Y., Zhang, F., & Yu, Q. 2010, *ApJ*, 709, 1356
- Lucy, L. B. 1977, *AJ*, 82, 1013
- Ludlow, A. D., Navarro, J. F., Li, M., et al. 2012, *MNRAS*, 427, 1322
- Macciò, A. V., Dutton, A. A., & van den Bosch, F. C. 2008, *MNRAS*, 391, 1940
- Mamajek, E. E. & Hillenbrand, L. A. 2008, *ApJ*, 687, 1264
- Marigo, P., Girardi, L., Bressan, A., et al. 2008, *A&A*, 482, 883
- Marinacci, F., Pakmor, R., & Springel, V. 2014, *MNRAS*, 437, 1750
- Marshall, D. J., Robin, A. C., Reylé, C., Schultheis, M., & Picaud, S. 2006, *A&A*, 453, 635
- Martig, M., Bournaud, F., Croton, D. J., Dekel, A., & Teyssier, R. 2012, *ApJ*, 756, 26
- Martig, M., Bournaud, F., Teyssier, R., & Dekel, A. 2009, *ApJ*, 707, 250
- Martínez-Delgado, D., Gabany, R. J., Crawford, K., et al. 2010, *AJ*, 140, 962
- Matijevič, G., Zwitter, T., Bienaymé, O., et al. 2012, *ApJS*, 200, 14
- McGaugh, S. S., Schombert, J. M., de Blok, W. J. G., & Zagarosky, M. J. 2010, *ApJ*, 708, L14

- McMillan, P. J. 2011, MNRAS, 414, 2446
- McWilliam, A. & Zoccali, M. 2010, ApJ, 724, 1491
- Metz, M., Kroupa, P., & Libeskind, N. I. 2008, ApJ, 680, 287
- Miglio, A., Chiappini, C., Morel, T., et al. 2013, MNRAS, 429, 423
- Minchev, I., Chiappini, C., & Martig, M. 2013a, accepted by A&A, astro-ph 1208.1506
- Minchev, I., Chiappini, C., Martig, M., et al. 2013b, ArXiv e-prints
- Minchev, I. & Famaey, B. 2010, ApJ, 722, 112
- Minchev, I., Famaey, B., Quillen, A. C., et al. 2012, A&A, 548, A126
- Minchev, I. & Quillen, A. C. 2006, MNRAS, 368, 623
- Miyamoto, M. & Nagai, R. 1975, PASJ, 27, 533
- Mo, H. J., Mao, S., & White, S. D. M. 1998, MNRAS, 295, 319
- Monari, G., Antoja, T., & Helmi, A. 2013, submitted, astro-ph 1306.2632
- Navarro, J. F., Frenk, C. S., & White, S. D. M. 1996, ApJ, 462, 563
- Navarro, J. F., Frenk, C. S., & White, S. D. M. 1997, ApJ, 490, 493
- Navarro, J. F. & Steinmetz, M. 1997, ApJ, 478, 13
- Navarro, J. F. & Steinmetz, M. 2000, ApJ, 538, 477
- Neto, A. F., Gao, L., Bett, P., et al. 2007, MNRAS, 381, 1450
- Nordström, B., Mayor, M., Andersen, J., et al. 2004, A&A, 418, 989
- Palladino, L. E., Schlesinger, K. J., Holley-Bockelmann, K., et al. 2014, ApJ, 780, 7
- Pasetto, S., Chiosi, C., & Kawata, D. 2012a, A&A, 545, A14
- Pasetto, S., Grebel, E. K., Zwitter, T., et al. 2012b, A&A, 547, A70
- Pawlowski, M. S., Kroupa, P., & Jerjen, H. 2013, accepted for publication in MNRAS, astro-ph 1307.6210
- Pawlowski, M. S., Pflamm-Altenburg, J., & Kroupa, P. 2012, MNRAS, 423, 1109
- Perets, H. B., Hopman, C., & Alexander, T. 2007, ApJ, 656, 709
- Perets, H. B., Wu, X., Zhao, H. S., et al. 2009, ApJ, 697, 2096
- Piffl, T. 2009, Diplomarbeit, Universität Leipzig, available under http://www.aip.de/groups/publications/piffl_dipl.pdf
- Piffl, T., Scannapieco, C., Binney, J., et al. 2014, A&A, 562, A91
- Piffl, T., Williams, M., & Steinmetz, M. 2011, A&A, 535, A70
- Piontek, F. & Steinmetz, M. 2011, MNRAS, 410, 2625
- Plummer, H. C. 1911, MNRAS, 71, 460
- Press, W. H., Teukolsky, S. A., Vetterling, W. T., & Flannery, B. P. 2007, Numerical Recipes 3rd Edition: The Art of Scientific Computing, 3rd edn. (New York, NY, USA: Cambridge University Press)
- Prusti, T. 2012, Astronomische Nachrichten, 333, 453
- Przybilla, N., Nieva, M. F., Tillich, A., et al. 2008, A&A, 488, L51
- Przybilla, N., Tillich, A., Heber, U., & Scholz, R. 2010, ApJ, 718, 37
- Reid, M. J. & Brunthaler, A. 2004, ApJ, 616, 872
- Reylé, C., Marshall, D. J., Robin, A. C., & Schultheis, M. 2009, A&A, 495, 819
- Rix, H.-W. & Bovy, J. 2013, A&A Rev., 21, 61
- Robin, A. C., Luri, X., Reylé, C., et al. 2012, A&A, 543, A100

- Robin, A. C., Reylé, C., Derrière, S., & Picaud, S. 2003, *A&A*, 409, 523
- Roškar, R., Debattista, V. P., Quinn, T. R., Stinson, G. S., & Wadsley, J. 2008, *ApJ*, 684, L79
- Sale, S. E., Drew, J. E., Unruh, Y. C., et al. 2009, *MNRAS*, 392, 497
- Sales, L. V., Navarro, J. F., Abadi, M. G., & Steinmetz, M. 2007, *MNRAS*, 379, 1464
- Sanders, J. L. & Binney, J. 2013, *MNRAS*, 433, 1826
- Sawala, T., Guo, Q., Scannapieco, C., Jenkins, A., & White, S. 2011, *MNRAS*, 413, 659
- Scalo, J. M. 1986, *Fund. Cosmic Phys.*, 11, 1
- Scannapieco, C. & Athanassoula, E. 2012, *MNRAS*, 425, L10
- Scannapieco, C., Gadotti, D. A., Jonsson, P., & White, S. D. M. 2010, *MNRAS*, 407, L41
- Scannapieco, C., Tissera, P. B., White, S. D. M., & Springel, V. 2005, *MNRAS*, 364, 552
- Scannapieco, C., Tissera, P. B., White, S. D. M., & Springel, V. 2006, *MNRAS*, 371, 1125
- Scannapieco, C., Wadepuhl, M., Parry, O. H., et al. 2012, *MNRAS*, 423, 1726
- Scannapieco, C., White, S. D. M., Springel, V., & Tissera, P. B. 2009, *MNRAS*, 396, 696
- Scannapieco, C., White, S. D. M., Springel, V., & Tissera, P. B. 2011, *MNRAS*, 417, 154
- Schlafly, E., Green, G., & Finkbeiner, D. P. 2013, in *American Astronomical Society Meeting Abstracts*, Vol. 221, 145.06
- Schlegel, D. 2012, Letter submitted to the NSF Astronomy Portfolio Review, astro-ph/1203.0591
- Schlegel, D., Abdalla, F., Abraham, T., et al. 2011, *ArXiv e-prints*
- Schlegel, D. J., Finkbeiner, D. P., & Davis, M. 1998, *ApJ*, 500, 525
- Schlesinger, K. J., Johnson, J. A., Rockosi, C. M., et al. 2012, *ApJ*, 761, 160
- Schönrich, R. 2012, *MNRAS*, 427, 274
- Schönrich, R. & Binney, J. 2009, *MNRAS*, 399, 1145
- Schönrich, R., Binney, J., & Dehnen, W. 2010, *MNRAS*, 403, 1829
- Schuster, W. J., Moreno, E., Nissen, P. E., & Pichardo, B. 2012, *A&A*, 538, A21
- Seabroke, G. M., Gilmore, G., Siebert, A., et al. 2008, *MNRAS*, 384, 11
- Sellwood, J. A. & Binney, J. J. 2002, *MNRAS*, 336, 785
- Sesana, A., Madau, P., & Haardt, F. 2009, *MNRAS*, 392, L31
- Sharma, S., Bland-Hawthorn, J., Binney, J., et al. 2013, submitted
- Sharma, S., Bland-Hawthorn, J., Johnston, K. V., & Binney, J. 2011, *ApJ*, 730, 3
- Sharma, S. & Steinmetz, M. 2006, *MNRAS*, 373, 1293
- Siebert, A., Famaey, B., Binney, J., et al. 2012, *MNRAS*, 425, 2335
- Siebert, A., Williams, M. E. K., Siviero, A., et al. 2011, *AJ*, 141, 187
- Skrutskie, M. F., Cutri, R. M., Stiening, R., et al. 2006, *AJ*, 131, 1163
- Smith, M. C., Ruchti, G. R., Helmi, A., et al. 2007, *MNRAS*, 379, 755, (S07)
- Sofue, Y., Honma, M., & Omodaka, T. 2009, *PASJ*, 61, 227
- Sohn, S. T., Besla, G., van der Marel, R. P., et al. 2013, *ApJ*, 768, 139
- Soubiran, C., Bienaymé, O., & Siebert, A. 2003, *A&A*, 398, 141
- Spitzer, Jr., L. & Thuan, T. X. 1972, *ApJ*, 175, 31
- Springel, V. 2005, *MNRAS*, 364, 1105

Springel, V. 2012, *Astronomische Nachrichten*, 333, 515

Springel, V., Frenk, C. S., & White, S. D. M. 2006, *Nature*, 440, 1137

Springel, V., Wang, J., Vogelsberger, M., et al. 2008, *MNRAS*, 391, 1685

Springel, V. & White, S. D. M. 1999, *MNRAS*, 307, 162

Steinmetz, M. & Müller, E. 1993, *A&A*, 268, 391

Steinmetz, M., Zwitter, T., Siebert, A., et al. 2006, *AJ*, 132, 1645

Stinson, G. S., Brook, C., Macciò, A. V., et al. 2013, *MNRAS*, 428, 129

Tamura, N., Hirashita, H., & Takeuchi, T. T. 2001, *ApJ*, 552, L113

Taylor, J. E. & Babul, A. 2001, *ApJ*, 559, 716

Teyssier, M., Johnston, K. V., & Shara, M. M. 2009, *ApJ*, 707, L22

Tillich, A., Przybilla, N., Scholz, R., & Heber, U. 2009, *A&A*, 507, L37

Tissera, P. B., Scannapieco, C., Beers, T. C., & Carollo, D. 2013, *MNRAS*, 432, 3391

Tissera, P. B., White, S. D. M., & Scannapieco, C. 2012, *MNRAS*, 420, 255

Tonry, J. & Davis, M. 1979, *AJ*, 84, 1511

Toomre, A. & Toomre, J. 1972, *ApJ*, 178, 623

Tormen, G., Diaferio, A., & Syer, D. 1998, *MNRAS*, 299, 728

Žerjal, M., Zwitter, T., Matijevič, G., et al. 2013, *ApJ*, 776, 127

van der Marel, R. P., Besla, G., Cox, T. J., Sohn, S. T., & Anderson, J. 2012a, *ApJ*, 753, 9

van der Marel, R. P., Fardal, M., Besla, G., et al. 2012b, *ApJ*, 753, 8

Vera-Ciro, C. & Helmi, A. 2013, *ApJ*, 773, L4

Vera-Ciro, C. A., Helmi, A., Starkenburg, E., & Breddels, M. A. 2013, *MNRAS*, 428, 1696

Vera-Ciro, C. A., Sales, L. V., Helmi, A., et al. 2011, *MNRAS*, 416, 1377

Warnick, K., Knebe, A., & Power, C. 2008, *MNRAS*, 385, 1859

Watkins, L. L., Evans, N. W., & An, J. H. 2010, *MNRAS*, 406, 264

Widrow, L. M., Gardner, S., Yanny, B., Dodelson, S., & Chen, H.-Y. 2012, *ApJ*, 750, L41

Wilkinson, M. I. & Evans, N. W. 1999, *MNRAS*, 310, 645

Williams, M. E. K., Steinmetz, M., Binney, J., et al. 2013, *MNRAS*

Williams, M. E. K., Steinmetz, M., Sharma, S., et al. 2011, *ApJ*, 728, 102

Xue, X. X., Rix, H. W., Zhao, G., et al. 2008, *ApJ*, 684, 1143

Yu, Q. & Madau, P. 2007, *MNRAS*, 379, 1293

Yu, Q. & Tremaine, S. 2003, *ApJ*, 599, 1129

Yuan, H. B., Liu, X. W., & Xiang, M. S. 2013, *MNRAS*, 430, 2188

Zacharias, N., Finch, C. T., Girard, T. M., et al. 2013, *AJ*, 145, 44

Zolotov, A., Willman, B., Brooks, A. M., et al. 2009, *ApJ*, 702, 1058

Zubovas, K., Wynn, G. A., & Gualandris, A. 2013, *ApJ*, 771, 118

Zucker, D. B., De Silva, G., Freeman, K. C., Bland-Hawthorn, J., & HERMES Team. 2013, in *American Astronomical Society Meeting Abstracts*, Vol. 221, 234.06

Zwitter, T., Matijevič, G., Breddels, M. A., et al. 2010, *A&A*, 522, A54+

Zwitter, T., Siebert, A., Munari, U., et al. 2008, *AJ*, 136, 421

Acknowledgments

I want to thank Matthias Steinmetz for providing me the chance to write my dissertation at the AIP and for taking time whenever I expressed the need for help and advice, but otherwise giving me all the freedom I wanted. I also thank my colleagues at the AIP and elsewhere for their support and friendship.

I thank Cecilia Scannapieco for granting me access to her suite of simulations plus all the additional analysis products and for giving advice and support for my own various projects. Similarly I have to thank Ivan Minchev and Cristina Chiappini for providing me their chemodynamical model for my study of mock surveys in Chapter 3 and many helpful discussions on the topic. I thank Sanjib Sharma for generously providing me with a pre-release version of his GALAXIA code and making the code EnBiD¹ publicly available.

I acknowledge support by the German Research Foundation under grant DFG-STE-710/4-3. Funding for RAVE has been provided by: the Australian Astronomical Observatory; the Leibniz-Institut für Astrophysik Potsdam (AIP); the Australian National University; the Australian Research Council; the French National Research Agency; the German Research Foundation (SPP 1177 and SFB 881); the European Research Council (ERC-StG 240271 Galactica); the Istituto Nazionale di Astrofisica at Padova; The Johns Hopkins University; the National Science Foundation of the USA (AST-0908326); the W. M. Keck foundation; the Macquarie University; the Netherlands Research School for Astronomy; the Natural Sciences and Engineering Research Council of Canada; the Slovenian Research Agency; the Swiss National Science Foundation; the Science & Technology Facilities Council of the UK; Opticon; Strasbourg Observatory; and the Universities of Groningen, Heidelberg and Sydney. The RAVE web site is at <http://www.rave-survey.org>.

This publication makes use of data products from the Two Micron All Sky Survey, which is a joint project of the University of Massachusetts and the Infrared Processing and Analysis Center/California Institute of Technology, funded by the National Aeronautics and Space Administration and the National Science Foundation.

This research made use of the cross-match service, the SIMBAD database and the VizieR catalog access tool provided by CDS, Strasbourg.

Some of the results in this work have been derived using the HEALPix (Górski et al. 2005) package. The orbital integrations in Section 3.3.6 were done using the Python package GALPY² by Jo Bovy.

This document was typeset by L^AT_EX.

¹<http://sourceforge.net/projects/enbid>

²<https://github.com/jobovy/galpy>